Photophysical Studies On Hybrid Nanomaterials For Manifold Applications

THESIS

SUBMITTED FOR THE DEGREE OF

DOCTOR OF PHILOSOPHY (SCIENCE)

IN

NANOSCIENCE AND NANOTECHNOLOGY

BY

NIVEDITA PAN

CENTRE FOR RESEARCH IN NANOSCIENCE AND NANOTECHNOLOGY

UNIVERSITY OF CALCUTTA

2024

To My Family

Acknowledgements

The journey towards my research life would not have been possible unless I have been blessed with the unconditional support and encouragement from countless people.

First of all, on successful completion of my PhD work, I humbly express my deepest gratitude to my research supervisor, Professor (Dr.) Samir Kumar Pal, by whom I have been supervised throughout these seven years of my research life starting from my master's days. This work would not have been possible without his warm encouragement, support, thoughtful guidance, constant motivation, and constructive criticism. I feel myself extremely fortunate to have such an energetic supervisor who has sacrificed all his comfort for our academic success and for me he is all-in-one. I always find him answering instantaneously every silly question raised by any student even if he or she has not studied the subject deeply. I deeply feel that the term depression which is the biggest problem nowadays in student life, can't touch us who are working under his dynamic supervision, because even if you are somehow depressed you will always find him with his motivational words beside you which will instantaneously direct you towards your goal. Sir has patiently guided me during crucial moments in my work while simultaneously allowing me to express my ideas and work independently. I am grateful to him for allowing me to explore new areas of research, and interact and collaborate with various researchers from several different research fields. I also thank him for providing me with the opportunity to work with a talented team of researchers and an excellent research environment.

I would like to deeply thank Dr. Debjani Karmakar, who has patiently made me learn different computational techniques, that helped me a lot to explain many research problems. I would like to thank Dr. Arpita Chattopadhyay, Techno International, Kolkata, Dr. Mala Mitra, Sister Nivedita University, Kolkata, Prof. Saleh A. Ahmed, Umm Al-Qura University, Makkah, Saudi Arabia, to whom I worked on various collaborative projects during my initial research days. I would like to thank Dr. Chinmoy Bhattacharya, IIEST Shibpur, from whom I learned electrochemical techniques, and Dr. Ranjan Das for his physical chemistry perspective.

The workplace would not be smooth without the presence of such lovely lab mates, supportive seniors, and friends. A special thanks to Dr. Jayita Patwari, who always encouraged me to join sir's lab and her positive viewpoint towards AOSL lab attracted me. I am thankful to Susmita di for assisting enormously in thesis writing and her special care towards me, Nur da for being helpful whenever required, Lopamudra di, for sharing funny and serious moments, Monojit da, Ria di, Amrita, Neha, Deepshikha for spending good lab time, Arka da, Tuhin da, Probir da for being mentors during my project works. My appreciation and regards go to all my other colleagues and seniors: Dr. Dipanjan Mukherjee, Dr. Arpan Bera, Dr. Pritam Biswas, Dr. Aniruddha Adhikari, Dr. Soumendra Singh, Dr. Animesh Halder, Dr. Damayanti Bagchi, Dr. Priya Singh, Dr. Soumendra Darbar, Late Debanjana Singh Roy, Sumona di, Mahasweta, Debdutta, Rama, Sayantika, Manali and Aman.

I express my gratitude to my MSc. Teachers, all the faculty members, and the staff of S. N. Bose National Centre for Basic Sciences for their assistance in my research career. I acknowledge S. N. Bose National Centre for Basic Sciences and Department of Science and Technology (DST), India for providing the research fellowship.

Furthermore, I express my gratitude to Dr. Anjani Kumar Singh, Late Dr. Anil Kumar Singh, Dr. Ashutosh Kumar Shukla, and Late Dr. Vikas Gupta; from the Department of Physics, Ewing Christian College, Allahabad, for their valuable advice and guidance.

I thank Manjari for being the perfect friend and my spiritual partner who provided me endless support during my time in S. N. Bose, Harmit, Shubham, Samir, Riju, and Parthpratim for sharing a very good time on class days, Ria for sharing a happy time, I always find you beside me whenever needed. Rajdeep for keeping faith in me, Anirban and Shoham for being cute and benevolent.

Finally, my parents, grandparents, and sister for them words are not enough. I would like to pay high regard to my parents for inculcating their active ideal-centric values in me and my sister. Without their sacrifices, moral support, and blessings, this would not have been possible. Nandita being my soulmate and backbone, is a positive competitor from childhood, without her the journey would have been boring. All family members who have supported me through thick and thin, with love and affection. Thank you all.

Nivedita Pan

CONTENTS

CHAPTER 1

Introduction

1.1. Background:

As the human population and industries are growing rapidly, alongside improvements in human living standards, environmental pollution, and energy shortages are escalating steadily [1-3]. Due to rapid urbanization, an extra burden environment has accounted in terms of releasing non-biodegradable products, several chemical wastes, and toxic gases along with high energy consumption demand [4, 5]. Clean water to drink, clean air to breathe, and minimum energy requirements are the few basic requirements that a person needs to survive. However, toxic heavy metals such as lead, cadmium, and arsenic have increased significantly than their permissible limit [6, 7]. Several other categories of pollutants affect the environment; among them, toxic heavy metals pose significant ecosystem-related challenges because of their persistent presence in the environment, capacity to infiltrate the food chain, and high levels of toxicity, which largely endanger the environmental milieu [8]. The sources of release of toxic heavy metals in the environment include burning and submersion of non-biodegradable substances, burning of automobile fuels, toxic gases from the excessive use of coolant devices to combat global warming, etc. [9, 10]. These not only affect the environmental and ecological conditions but raise a high energy demand.

The sustainable objective of technological progress is to bridge the gap between laboratory-based solutions and on-site applications by developing sensitive, specific, and portable sensors for pollution monitoring and the development of renewable energy sources. Thus, there is an urgent need for mankind to deal with the energy crisis and environmental pollution. As we know, the current energy needs, are still covered by conventional energy resources such as coal, oil, etc.,

which are limited to a specific time frame, after that they will be consumed entirely [11].

Among all alternative and renewable energy sources, solar energy stands out as the most abundant and environmentally friendly [12]. The total solar power reaching the Earth's surface is underutilized. If just 0.1% of the total available solar energy could be converted to electrical energy, with an average efficiency of 10%, it would be sufficient to meet the world's entire energy demand. Nevertheless, the high cost associated with conventional silicon-based photovoltaics hinders their competitiveness against other energy sources [13]. The demand for affordable and sustainable energy solutions has spurred intensive research into various other solar energy conversion technologies, including dye-sensitized solar cells (DSSCs), hydrogen generation by photoelectrochemical (PEC) water splitting, etc. However, a significant drawback of the materials involved in the process, is their toxicity and inability to absorb infrared (IR) radiation from the solar spectrum, which accounts for 52% of the total solar energy. This limitation represents a major mechanism for energy loss in solar conversion processes [14] and, therefore, triggered the research in the direction of organic dyes and NIR-sensitive materials that can be used as light-harvesting materials. Despite significant advancements in renewable energy technologies, the persistent energy shortage remains a cause for concern. Therefore, keeping in mind the above challenges, focused research by developing appropriate materials that address such environmental pollution and energy crisis issues is the need of the hour.

1.2. Nanomaterials and Their Hybrids: A Brief Overview:

Nanomaterials and their hybrid formation continue to play a growing interest in academic and technological aspects [15]. The field of nanotechnology, due to the emergence of novel nanomaterials is likely to overtake other industries and will soon become the dominant building block. Nanomaterials consist of an assembly of atoms and molecules having at least a geometrical dimension of less than 100 nm. Quantum confinement in nanomaterials is widely used, they include 0D, 1D,

2D, 3D metal nanoparticles, wide band gap semiconductors as well as narrow band gap-based quantum well or dots, carbon based nanostructures such as carbon dots, carbon nanotubes, etc. However, to spread the varsity and application of nanomaterials, their hybrid formation with other materials is important, which may be broadly classified into different categories such as inorganic-organic, inorganic-inorganic, organic-organic metal-organic nanohybrids, etc. [16, 17]. Organic-inorganic hybrid formation through nanomaterial capping with suitable ligands, especially metal-based nanoparticles, and metal-oxide nanoparticles, has attracted more attention because capping introduces physical stability, reduces toxicity, and increases solubility in the desired medium [18, 19].

Colloidal ligand-capped nanoparticles have seen significant commercial success in a wide range of industries, such as food, paint, pharmaceuticals, soap, and photography [17, 19]. They are utilized for various purposes, including improving taste and texture in food, enhancing color stability and durability in paint, enabling targeted drug delivery in pharmaceuticals, acting as emulsifiers and stabilizers in soap production, and contributing to finer resolution and image quality in photography. Their versatile properties have made them indispensable across these sectors. Purely Organic-organic self-assemblies find application specially in the field of photocatalysis. Along with it, core-shell structures serve several purposes, including protection, facilitating further chemical modification, and ensuring compatibility with the surrounding environment.

These structures consist of a core material surrounded by a shell, typically made of a semiconductor on semiconductor, metal on metal, metal on semiconductor, and vice versa, as well as oxide on metal and semiconductor and organic on metal or semiconductor. Each combination caters to different applications, offering unique properties and functionalities; hence a suitable hybrid material synthesis can find application in any required field of interest according to the need.

1.3. Scope of the Photophysical Investigation on Hybrid Nanomaterials for Manifold Applications:

Upon interaction with light, materials and molecules can undergo specific physicochemical changes, like the resonance of nanomaterial internal electromagnetic field in the presence of an external field; photoexcitation can bring material to an electronically excited state. The processes, which include changes in material's behaviour upon light interaction, such as dipoles and electron-hole pair generation, are generally described by the so-called photophysical processes. The photophysical behavior of nanomaterials has gone through drastic changes upon hybrid formation. For instance, the excited stated fluorescence of a dye can drastically be quenched upon hybrid formation with some other relevant semiconductor nanomaterial. Hybrid formation can lead to several other processes, such as ligand-to-metal charge transfer in ligan-capped metal-oxides nanoparticles, plasmon delocalization upon hybrid formation with heavy metal ions, etc. Therefore, a photophysical understanding of such hybrid nanomaterials opens the field to investigation in different fields, including photovoltaics, photocatalysis, plasmon-induced sensing, environmental pollution monitoring, and remediation.

1.3.1. Environmental Pollution Monitoring: Ligand capped metal nanoparticles, being plasmonic in nature, emerge as a class of optically active nanomaterials not only appealing for basic studies but have revolutionary applications in several fields including energy conversion, electronics, photonics, biomedical and specially in environmental sensing applications [20-22]. The plasmonic nature of such nanoparticles exhibits a particular photophysical property known as 'Localized Surface Plasmon Resonance' (LSPR), where the coherent oscillations of electrons on the nanoparticle surface upon photon incidence can bring the enhancement in the optical cross-sections [23]. LSPR resonance condition is susceptible to external stimuli. It can be perturbed when its surrounding environment changes leading to change in its resonance condition, which can be utilized as markers to detect several pollutants present in the environment. Most

of these nanomaterials exhibit high optical absorbance cross-sections in the UV-Visible region, making them highly effective in sensing and identifying environmental contaminants [24, 25]. The presence of pollutants specially in the form of heavy metals in the system, led to the self-aggregation or agglomeration of the NPs into different non-spherical geometry and clusters, driven by forces such as van der Waals interaction, ligand coupling, electrostatic attraction, and repulsion between the charged particles, etc. [26-29]. These spectral changes can indeed be detected using simple UV-Visible spectroscopy, making it a valuable tool for pollutant detection. In some cases, the changes may be noticeable even to the naked eye, further simplifying the detection process and expanding its accessibility as a crucial tool for low-cost environmental monitoring and analysis. [30, 31]. In this direction, paper-based nanoparticle-impregnated sensors strip finds greater application.

1.3.2. Environmental Pollution Remediation: The reactive oxygen species (ROS) takes part in antimicrobial activities [32-34] and eventually degradation of organic-inorganic pollutants [35, 36] present in the water. Recent studies have highlighted the potential of ROS as a tool to address water toxicity issues [37]. By focusing on ROS-based treatment methods, one can aim to mitigate water toxicity by breaking down harmful organic compounds, pathogens, and heavy metals, thus improving water quality and safety. Organic sensitizers, being able to harvest a wide range of solar spectrum, can be used to produce ROS in the medium. The photophysical behavioral study of the multiple sensitizer system can help to understand how the ultimate efficiency of ROS generation can be increased when they closely interact with each other [38]. Nevertheless, choosing the proper host material is equally important in determining the photophysical interactions between the sensitizers [39]. Self-assembled surfactant media, such as micelles and vesicles, hold promise as potential hosts for solubilizing hydrophobic sensitizers by forming organic-organic hybrids. Additionally, they can provide a restricted environment that can lead to additional photophysical phenomena such as Förster resonance energy transfer (FRET), which can be

advantageous in terms of enhanced ROS production and herby lead to efficient pollution remediation.

1.3.3. Solar Light Harvesting: The use of semiconductor-based hybrid materials for energy and carrier transfer across their interfaces is important in view of enhanced photocatalytic processes, solar energy conversion into chemical energy, and water splitting applications. Metal-organic frameworks based on hybrid nanomaterials in combination with semiconductors could also be used for efficient light harvesting assemblies [40]. Titanium oxide (TiO_2) and zinc oxide (ZnO) are the widely used electron transporting wide band gap semiconducting metal oxides that find application in photocatalytic and photovoltaic processes. However, these wide band gap semiconducting materials harvest very little of the solar spectrum, so utilization of longer wavelength photons, photocatalytic and photovoltaic efficiency, etc., is a matter of concern. A successful strategy to deal with this is 'dye sensitization', thereby enhancing the optical response to the visible region or even near-infrared (NIR) region [41]. Therefore, metal-free organic sensitizers have become the current trend due to their tuneable structure, low cost, and spectral responsive ability [42].

Moreover, low band gap semiconductor quantum dots (QD) have shown promising responses in harvesting the NIR range of solar spectrum [43]. However, exciton recombination in low-band gap semiconductors is a prevalent problem that has to be dealt with. In contrast, the hybrid formation of low-bandgap semiconducting QDs with wide-band-gap semiconductor/ 1D nanostructures can lead to efficient charge separation and transportation, thereby finding applications in photovoltaics, photocatalysis, and quantum dot-sensitized photoelectrochemical water splitting [44, 45].

1.4. Objective:

In the proposed research work, we are mainly focused on investigating the detailed photophysical, optical, and electrochemical properties of plasmonic metal nanostructures, semiconductor heterostructures, and light-harvesting self-

assemblies. Although many studies have been performed with plasmonic nanostructures, the field of sensing still needs cheaper, faster spectroscopic tools and field deployable devices. We have chosen citrate functionalized silver and gold plasmonic metal nanoparticles and done a detailed photophysical study of LSPR upon interaction with heavy metal pollutants, which we have here chosen lead (Pb). Detailed spectroscopic and microscopic understanding have been done to establish the underlying sensing mechanism. Apart from spectroscopic studies, we have done some analytical and computational work that includes relevant photophysical aspects. Based on the underline mechanism, we have also focused on detecting real-world lead samples present in the atmosphere; for that, several methods have been discussed to bring the real-world samples into detection conditions and match them with lab parameters to quantify the amount of pollutant present. Using spectroscopy and based on the results further we translated these colorimetric and spectral findings to develop sensor strips which could detect the pollution level on the field.

We have also investigated the semiconductor nanostructured materials that can be successfully applied to enhance the photocatalytic activity and H_2 production under solar light irradiation. We have worked with biologically relevant organic dyes (eg. porphyrin, squarine, RK1, etc.). We are interested in implementing broadband light harvesting with techniques such as co-sensitization leading to FRET [46], surface ligand-to-metal charge transfer (LMCT) [47] of adsorbates in association with TiO_2, ZnO metal oxides or with different self-assembled micellar systems. In order to fulfill our objectives, we would be focused on detailed charge transfer dynamics at dye-micellar, dye-semiconductor, metal-organic, inorganic-organic interface of nanoparticle (NP) or Quantum dot nanomaterial assemblies.

Quantum dots (such as CdSe, PbS etc.) have highly tuneable absorbance and photoluminescence bands depending on size and surface properties [48]. However, NIR light harvesting ability QDs is a matter of concern concerning the utilization of full solar spectrum. In this regard, we have included studies on NIR active PbS quantum dots. We have explored the faster electron transporting

mechanism with the help of the hybrid formation of PbS QDs with suitable materials for their beneficiary use in reducing back recombination and easy charge separation processes. For, that we have proposed the synthesis of NIR active tri-hybrid material and found its application in photoelectrochemical water splitting.

1.5. Summary of the Work Done:

1.5.1. Spectroscopic and Theoretical Studies on Ligand Capped Metal Nanohybrids for Environmental Pollution Monitoring:

1.5.1.1. A Combined Spectroscopic and Theoretical Analysis of Plasmonic Silver Nanoparticle Sensor Towards Detailed Microscopic Understanding of Heavy Metal Detection [49]: Plasmonic nanoparticles are of great importance owing to their highly responsive 'Localized Surface Plasmon Resonance' (LSPR) behaviour to self-agglomeration/ aggregation leading to the development of various nanosensors. Herein, we demonstrated the definite self-assembly of citrate functionalized silver nanoparticles (AgNPs) into a one-dimensional linear chain in the presence of charged lead ions (Pb^{2+}), one of the most toxic heavy metal pollutants. We have explored detail mechanism using various spectroscopic tools and electron microscopy. The self-aggregation of AgNPs leads to the generation of new LSPR modes due to coupling of nearby existing modes. The conclusion of our experimental findings is duly supported by our developed numerical modeling based on the quasi-static approximation that the generated new LSPR modes are solely due to the formation of chain-like aggregation of AgNPs. We have also monitored the LSPR spectra in presence of other metal ions, however, only Pb^{2+} found to give such unique self-assembled geometry may due to its high interaction affinity with citrate. These findings play a key role in citrate functionalised AgNPs being used as a low-cost, highly selective, sensitive lead ion sensor for potential application in industrial lead pollution monitoring. We have further varied several sensor parameters such as AgNPs size, concentration, and the allowed reaction time for it to be practically

implemented as an efficient lead sensor meeting the Environmental Protection Agency recommendations.

1.5.1.2. Paper-based Plasmonic Nanosensor Monitors Environmental Lead Pollution in Real Field [50]: The sustainable goal of technological advancement is to go from lab to site by developing a sensitive, specific and portable sensor for pollution monitoring. Herein, we report a completely portable colorimetric prototype device for the selective monitoring of lead (Pb) pollution, mainly in air, which relies on a new aspect of analysing the colorimetric assays on paper strips by the direct measurement of the retroreflective information, other than the available tedious image analysis methods. Our indigenously developed citrate-functionalized silver nanoparticles (AgNPs) embedded in cellulose paper strips showed significant localized surface plasmonic resonance (LSPR) peaks in the blue region and with the increase in the Pb concentration, the LSPR band in the blue region decreased and a new peak appeared in the green region of the electromagnetic spectrum due to the formation of larger aggregates. The prototype device monitored these spectral changes and accordingly gave the Pb content present in the sample. In this work, we made the sample under study by the acid digestion of one of the widely present air-suspended particulates, i.e., PbO_2. The prototype device is a suitable field-deployable technique for environmental Pb sensing towards low-cost paper-based sensing.

1.5.1.3. A Nanosensor-based Prototype Development for Heavy Metal Detection: A Combined Spectroscopic and Theoretical Study [51]: With the advent of technology, nanosensors have proved to be an important tool that provides a sustainable solution for environmental pollution monitoring. Herein, we report a spectroscopic detection of lead (Pb), one of the toxic heavy metal pollutants, with the help of citrate functionalized gold nanoparticles (AuNPs), followed by the development of a low-cost prototype device. Self-aggregation of citrate functionalized AuNPs in the presence of lead has been observed spectroscopically. The longitudinal mode of Surface Plasmon Resonance (SPR) of AuNPs increases as the Pb concentration increases. Consequently, a new peak in

the red region of the EM spectrum emerges, which is a clear indication of self-aggregation of NPs. We have used quasi-static approximation based numerical modelling to determine the percentage of aggregation of the AuNPs, which could be used to determine the amount of Pb^{2+} ions present in the solution. These key findings can be utilized for the development of low-cost prototype for monitoring lead pollution in the environment.

1.5.2. Spectroscopic Studies on Broadband Light Harvesting Using Organic Sensitizer-based Micellar Self-assemblies for Environmental Remediation Applications:

1.5.2.1. Broad Light Harvesting Under Restricted Environment: Photophysical Understanding Leading to Enhanced Reactive Oxygen Species Generation [46]: Surfactant self-assemblies are of great importance due to their suitable attachment affinity with the hydrophobic organic sensitizers in aqueous media. In this work, the two organic photo-sensitizers protoporphyrin (PPIX) and squaraine (SQ2), absorbing in the visible and near-infrared region of the solar spectrum, respectively, have been used simultaneously as dual sensitizers. These two sensitizers behave as donor-acceptor pairs for Förster resonance energy transfer (FRET) in close proximity to a restricted micellar environment. This process of dual sensitization on the surface of cationic (CTAB) micelle has been found to generate enhanced reactive oxygen species (ROS) under white light irradiation due to the resonance energy transfer from a donor to an acceptor molecule. The choice of the cationic micellar solution has also been justified on the basis of proper sensitizer attachment position with the micelle due to its suitable electrostatic interaction affinity with the sensitizers. The attachment position of the sensitizers with cationic, anionic, and nonionic micellar solutions has been confirmed by picosecond resolve fluorescence transients of the sensitizers in solvents of different polarities. Several control studies have been performed with the respective sensitizers alone in presence of white light irradiation and separately in their own absorption regions to confirm the enhanced ROS generation with dual sensitizers under white light irradiation.

This positively charged host micelle and generation of ROS can be helpful in potential photo remediation applications towards selective anionic pollutants. Some preliminary results regarding the possibility of anionic pollutant degradation are also discussed.

1.5.3. Spectroscopic Studies on Photoinduced Charge Separation, Excitonic Behaviour at the Interfaces of the Hybrid Nanomaterials:

1.5.3.1. Plasmon-coupled Donor−acceptor Type Organic Sensitizer-based Photoanodes for Enhanced Photovoltaic Activity: Key Information from Ultrafast Dynamical Study [52]: Environment-friendly purely organic dye-sensitized based solar cells and photoelectrochemical cells have emerged as primary photovoltaic technologies due to their stability, cost-effectiveness, and equally high efficiency compared to the conventional ruthenium-based dyes. Nevertheless, back electron-hole recombination, fast electron injection, wide-band light harvesting, and environmental hazards are crucial aspects that govern the advancement in photovoltaic technology. Organic photosensitizers having a delocalized π system of electrons end-capped with electron acceptors (A) and donors (D), have easy synthesis methods, excellent abilities to confine solar energy, and exceptional tunable absorbances and have the potential to overcome the above-mentioned crucial aspects in combination with semiconductor-metal (plasmonic) nanohybrids. Here, we have reported enhanced photovoltaic activity of organic D-π-A type photosensitizer (RK1) based plasmonic Au nanoparticle decorated hybrid mesoporous TiO_2 photoanodes in dye-sensitized solar cells (DSSCs) and dye-sensitized photoelectrochemical (DSPEC) water splitting. The presence of plasmonic material not only reduces the back electron-hole recombination but also the spectral overlap of its Localized Surface Plasmon Resonance (LSPR) band with that of organic sensitizer RK1 in close proximity to the TiO_2 surface, leading to the possibility of Förster Resonance Energy Transfer (FRET) which further enhances the device performance. Further, an ultrafast spectroscopic study has been performed to study the excited-state charge and energy transfer dynamics of the interfaces of the nanohybrids. Our analysis

demonstrates the identification of a specific unique combination of the nanohybrid, which is useful in designing a new generation of solar light harvesting material, especially in the case of DSPECs.

1.5.3.2. Unraveling an Ultrafast Electron Transport Mechanism in a Photocatalytic "Micromachine" for Their Potential Light Harvesting Applications [53]: Following the seminal discovery of Richard Feynman, several micromachines have been made that are capable of several applications, such as solar energy harvesting, remediation of environmental pollution, etc. Here we have synthesized a nanohybrid combining TiO_2 nanoparticle and light harvesting robust organic molecule RK1 (2-cyano-3-(4-(7-(5-(4-(diphenylamino)phenyl)-4- octylthiophen-2-yl)benzo[c][1,2,5] thiadiazol-4-yl)phenyl) acrylic acid) as a model micromachine having solar light harvesting ability potential for application in photocatalysis, preparation of solar active devices, etc. Detailed structural characterization has been performed on the nanohybrid, including High-Resolution Transmission Electronic Microscopy (HRTEM) and Fourier-transform infrared spectroscopy (FTIR). We have studied the excited-state ultrafast dynamics of the efficient push-pull dye RK1 in solution, on mesoporous semiconductor nanoparticles, and in insulator nanoparticles by streak camera (resolution of the order of 500 fs). The dynamics of such photosensitizers in polar solvents have been reported, and it has been observed that completely different dynamics occur when they are attached to the surface of the semiconductor/insulator nanosurface. A femtosecond-resolved fast electron transfer has been reported when photosensitizer RK1 has been attached to the surface of the semiconductor nanoparticle, which plays a crucial role in developing an efficient light harvesting material. The generation of reactive oxygen species as a result of femtosecond-resolved photoinduced electron injection in the aqueous medium is also investigated in order to explore the possibility of redox-active micromachines, which are found to be crucial for efficient and enhanced photocatalysis.

1.5.4. Spectroscopic Studies on Quantum Dot-Based Hybrid Nanomaterials for Manifold Applications:

1.5.4.1. Near-infrared Active Tri-nanohybrid for Enhanced Energy Harvesting [54]: Efficient energy harvesting through full solar spectrum utilization has been considered a promising solution to world energy and environmental issues. In this direction, lead sulphide (PbS) quantum dot (QD) based hybrid materials find greater application due to their near-infrared (NIR) active photo response. Slower charge injection and inefficient charge separation limit the photoactive response of such NIR active low band gap semiconductors like PbS QDs. Moreover, constructing dual charge transfer pathways in a PbS QDs based nanocomposite through the formation of hybrids with suitable materials can be advantageous in suppressing the charge recombination. In this work, we have synthesized a nanocomposite after decorating the PbS-QDs with semiconducting TiO_2 nanoparticles modified with multiwall carbon nanotubes (MWCNT) and thus forming the tri-hybrid (PbS-TiO_2-MWCNT) nanocomposites. The enhanced photo-activities of the tri-hybrid, as compared to di-hybrids like PbS-TiO_2, PbS-MWCNT were confirmed by the steady state, time-resolved photoluminescence (TRPL) measurements, and reactive oxygen species (ROS) generation measurements. Higher ROS generation in the tri-hybrid has been correlated with a faster interfacial electron transfer due to the dual charge injection pathway of PbS QD to TiO_2 and MWCNT. The enhanced activity of the tri-hybrid has also been analyzed from the first principal calculations in light of an efficient interfacial electron transfer as a result of the dual charge injection pathway. The photoelectrochemical water-spilling response of the photoanodes in terms of photocurrent density, electrochemical impedance, and Mott–Schottky measurements on PbS-TiO_2 and PbS-TiO_2-MWCNT photoanodes reveal that a combination of MWCNT and TiO_2 exhibits an increase in electrical double layer capacitance, decrease in series resistance and enhancement of carrier density with NIR illumination at the heterojunction. Overall, all the dynamical studies at the interface of the tri-hybrid based photoanodes demonstrate its potential of

utilization as a futuristic NIR- active photoelectrochemical water-splitting material.

1.6. Plan of the Thesis:

The plan of the thesis is as follows:

Chapter 1: This chapter provides a concise introduction to the scope and motivation behind the thesis. A summary of the work done, the objective, and an overview of the key findings and contributions of the thesis have been included.

Chapter 2: This chapter provides a brief overview of the steady-state, dynamical, computational tools and the structural aspects of the quantum-confined nanostructures, dyes, and fluorescent probes used in the experiments.

Chapter 3: This chapter includes the details of instrumentation, data analysis, and experimental procedures that have been used during the entire thesis work. A summary of the instruments working principle and materials synthesis procedure has been described here.

Chapter 4: This chapter contains the details of plasmon physics and how the unique aggregation geometry of silver nanoparticles can be used as a cost-effective tool for heavy metal detection. This study also investigates the exact aggregation mechanism using our developed analytical equation based on quasi-static approximation. Further, it has been investigated how lab-based experimental understanding is directly translated to on-site pollution monitoring through the development field of deployable portable devices. Here, the tunable physicochemical and colorimetric properties of the functionalized silver and gold nanoparticles have been utilized to detect heavy metal ion on a paper-based substrate.

Chapter 5: In this chapter, we have explored how broad solar light harvesting starting from visible to NIR region using dual organic sensitizers can efficiently produce ROS. Our present study can be beneficial to deal with the particular

problem of converting the entire solar spectra as much as possible and hence focused on utilizing this energy to generate enhanced ROS for potential photocatalytic activity. To maximize the light-harvesting the chosen sensitizers are such that FRET is occurring between them and have bring in close proximity to each other using a suitable restricted micellar environment.

Chapter 6: The chapter will be of general interest of in direction of renewable energy that how an organic donor (D) – π bridge - acceptor (A) type photosensitizer in combination with plasmonic nanomaterial can be utilized in photovoltaic and in photocatalysis-enhanced device performance. Here, we have shown the dual application of dye-sensitized TiO_2-Au photoanode in Dye-sensitized Solar Cells (DSSCs) as well as in Dye-sensitized Photoelectrochemical Cells (DSPECs) for water splitting application. It has been shown that the presence of plasmonic material not only reduces the back electron recombination, but also the spectral overlap of its Localized Surface Plasmon Resonance (LSPR) band with that of organic sensitizer RK1 in close proximity of TiO2 surface, leading to the possibility of Förster Resonance Energy Transfer (FRET) which further enhances the device performance. A dilated femtosecond-resolved ultrafast time-resolved dynamical study has been done to verify the charge and electron transfer across the hybrid interfaces. This study is expected to provide a futuristic aspect of new generation of solar light harvesting material, especially in the case of DSPECs.

Chapter 7: In this chapter, we reported a synthesis of a NIR active PbS QD-based tri-hybrid material having interest in direction of renewable energy that how near PbS quantum dots (QDs) in proximity with multiwall carbon nanotube (MWCNT) on the surface of wide band gap semiconducting TiO_2 can be utilized as an active tri-hybrid (PbS-TiO_2-MWCNT) photoanodes for broadband photoelectrochemical water splitting. Here, we proposed a dual-channel charge transfer pathway from photoexcited PbS QDs to TiO_2 as well as to MWCNT, which ultimately reduces the well-known fast charge recombination phenomena in such low band gap semiconducting QDs. Incorporating MWCNT as a dopant

with TiO_2 has been shown to have additional benefits in enhancing the light harvesting activity of PbS QDs.

References

[1] B. Chen, H. Kan, Air pollution and population health: A global challenge, *Environ. Health Prev. Med.* 13 (2008) 94.

[2] G. M. Grossman, A. Krueger, Pollution and growth: What do we know?, *Cambridge University Press*, Cambridge, 1993.

[3] W. Fyfe, M. Powell, B. Hart, B. Ratanasthien, A global crisis: Energy in the future, *Nonrenewable Resour.* 2 (1993) 187.

[4] M. Arfanuzzaman, B. Dahiya, Sustainable urbanization in Southeast Asia and beyond: Challenges of population growth, land use change, and environmental health, *Growth and Change* 50 (2019) 725.

[5] R. A. Begum, K. Sohag, S. M. S. Abdullah, M. Jaafar, CO_2 emissions, energy consumption, economic and population growth in Malaysia, *Renew. Sustain. Energy Rev.* 41 (2015) 594.

[6] K. H. Vardhan, P. S. Kumar, R. C. Panda, A review on heavy metal pollution, toxicity and remedial measures: Current trends and future perspectives, *J. Mol. Liq.* 290 (2019) 111197.

[7] G. Zhao, J. Li, X. Ren, C. Chen, X. Wang, Few-layered graphene oxide nanosheets as superior sorbents for heavy metal ion pollution management, *Environ. Sci. Technol.* 45 (2011) 10454.

[8] J. Briffa, E. Sinagra, R. Blundell, Heavy metal pollution in the environment and their toxicological effects on humans, *Heliyon* 6 (2020) e04691.

[9] S. V. Shaik, S. Shaik, K. Gorantla, D. Mahapatra, A. B. P. Setty, Investigation on thermodynamic performance analysis and environmental effects of various new refrigerants used in air conditioners, *Environ. Sci. Pollut. Res. Int.* 27 (2020) 41415.

[10] S. Dey, N. Mehta, Automobile pollution control using catalysis, *Resour. Environ. Sustain.* 2 (2020) 100006.

[11] S. Shafiee, E. Topal, When will fossil fuel reserves be diminished?, *Energy policy* 37 (2009) 181.

[12] C. Acar, I. Dincer, Comparative assessment of hydrogen production methods from renewable and non-renewable sources, *Int. J. Hydrogen Energy.* 39 (2014) 1.

[13] F. Priolo, T. Gregorkiewicz, M. Galli, T. F. Krauss, Silicon nanostructures for photonics and photovoltaics, *Nat. Nanotechnol.* 9 (2014) 19.

[14] M. Q. Yang, M. Gao, M. Hong, G. W. Ho, Visible-to-NIR photon harvesting: Progressive engineering of catalysts for solar-powered environmental purification and fuel production, *Adv. Mater.* 30 (2018) 1802894.

[15] F. Bensebaa, Nanoparticle technologies: From lab to market, *Academic Press*, Oxford, 2012.

[16] Y. Yu, Y. Shi, B. Zhang, Synergetic transformation of solid inorganic–organic hybrids into advanced nanomaterials for catalytic water splitting, *Acc. Chem. Res.* 51 (2018) 1711.

[17] A. Heuer-Jungemann, N. Feliu, I. Bakaimi, M. Hamaly, A. Alkilany, I. Chakraborty, A. Masood, M. F. Casula, A. Kostopoulou, E. Oh, The role of ligands in the chemical synthesis and applications of inorganic nanoparticles, *Chem. Rev.* 119 (2019) 4819.

[18] D. Meroni, S. Ardizzone, Preparation and application of hybrid nanomaterials, *Nanomater.* 8 (2018) 891.

[19] Y. Zhang, A. M. Schnoes, A. R. Clapp, Dithiocarbamates as capping ligands for water-soluble quantum dots, *ACS Appl. Mater. Interfaces.* 2 (2010) 3384.

[20] P. K. Jain, X. Huang, I. H. El-Sayed, M. A. El-Sayed, Review of some interesting surface plasmon resonance-enhanced properties of noble metal nanoparticles and their applications to biosystems, *Plasmonics* 2 (2007) 107.

[21] N. Wu, Plasmonic metal–semiconductor photocatalysts and photoelectrochemical cells: A review, *Nanoscale* 10 (2018) 2679.

[22] D. O'Connor, A. V. Zayats, The third plasmonic revolution, *Nat. Nanotech.* 5 (2010) 482.

[23] S. K. Gray, Surface plasmon-enhanced spectroscopy and photochemistry, *Plasmonics* 2 (2007) 143.

[24] S. A. Maier, Plasmonics: Fundamentals and applications, *Springer Science & Business Media*, New York, 2007.

[25] K. Khurana, N. Jaggi, Localized surface plasmonic properties of Au and Ag nanoparticles for Sensors: A review, *Plasmonics* 16 (2021) 981.

[26] H. Zhang, K.-H. Fung, J. r. Hartmann, C. T. Chan, D. Wang, Controlled chainlike agglomeration of charged gold nanoparticles via a deliberate interaction balance, *J. Phys. Chem. C* 112 (2008) 16830.

[27] H. Zhang, D. Wang, Controlling the growth of charged-nanoparticle chains through interparticle electrostatic repulsion, *Angew. Chem.* 120 (2008) 4048.

[28] Y. W. Lin, C. C. Huang, H. T. Chang, Gold nanoparticle probes for the detection of mercury, lead and copper ions, *Analyst* 136 (2011) 863.

[29] D. Vilela, M. C. González, A. Escarpa, Sensing colorimetric approaches based on gold and silver nanoparticles aggregation: Chemical creativity behind the assay. A review, *Anal. Chim. Acta.* 751 (2012) 24.

[30] P. K. Sarkar, A. Halder, N. Polley, S. K. Pal, Development of highly selective and efficient prototype sensor for potential application in environmental mercury pollution monitoring, *Water Air Soil Pollut.* 228 (2017) 314.

[31] A. Alizadeh, M. Khodaei, C. Karami, M. Workentin, M. Shamsipur, M. Sadeghi, Rapid and selective lead (II) colorimetric sensor based on azacrown ether-functionalized gold nanoparticles, *Nanotechnol.* 21 (2010) 315503.

[32] M. N. Karim, M. Singh, P. Weerathunge, P. Bian, R. Zheng, C. Dekiwadia, T. Ahmed, S. Walia, E. Della Gaspera, S. Singh, Visible-light-triggered reactive-oxygen-species-mediated antibacterial activity of peroxidase-mimic CuO nanorods, *ACS Appl. Nano Mater.* 1 (2018) 1694.

[33] F. Vatansever, W. C. de Melo, P. Avci, D. Vecchio, M. Sadasivam, A. Gupta, R. Chandran, M. Karimi, N. A. Parizotto, R. Yin, Antimicrobial strategies centered around reactive oxygen species–bactericidal antibiotics, photodynamic therapy, and beyond, *FEMS Microbiol. Rev.* 37 (2013) 955.

[34] Y. Min, X. F. Qi, Q. Xu, Y. Chen, Enhanced reactive oxygen species on a phosphate modified C_3N_4/graphene photocatalyst for pollutant degradation, *CrystEngComm* 16 (2014) 1287.

[35] P. Dunlop, J. Byrne, N. Manga, B. Eggins, The photocatalytic removal of bacterial pollutants from drinking water, *J. Photochem. Photobiol. A* 148 (2002) 355.

[36] X. Yang, J. Qin, Y. Jiang, K. Chen, X. Yan, D. Zhang, R. Li, H. Tang, Fabrication of P25 /Ag_3PO_4< 4 chyuery./graphene oxide heterostructures for enhanced solar photocatalytic degradation of organic pollutants and bacteria, *Appl. Catal. B.* 166 (2015) 231.

[37] D. Chatterjee, S. Dasgupta, Visible light induced photocatalytic degradation of organic pollutants, *J. Photochem. Photobiol. C* 6 (2005) 186.

[38] P. Pallavi, B. Sk, P. Ahir, A. Patra, Tuning the förster resonance energy transfer through self-assembly approach for efficient white-light emission in aqueous aedium, *Chem. A. Eur. J.* (2017).

[39] S. Chatterjee, S. Nandi, S. C. Bhattacharya, Fluorescence resonance energy transfer from fluorescein to safranine T in solutions and in micellar medium, *J. Photochem. Photobiol. A* 173 (2005) 221.

[40] H. Tada, T. Mitsui, T. Kiyonaga, T. Akita, K. Tanaka, All-solid-state Z-scheme in CdS–Au–TiO_2 three-component nanojunction system, *Nat. Mater* 5 (2006) 782.

[41] A. Hagfeldt, G. Boschloo, L. Sun, L. Kloo, H. Pettersson, Dye-sensitized solar cells, *Chem. Rev.* 110 (2010) 6595.

[42] C. P. Lee, R. Y. Y. Lin, L. Y. Lin, C. T. Li, T. C. Chu, S. S. Sun, J. T. Lin, K. C. Ho, Recent progress in organic sensitizers for dye-sensitized solar cells, *RSC Adv.* 5 (2015) 23810.

[43] E. M. Miller, D. M. Kroupa, J. Zhang, P. Schulz, A. R. Marshall, A. Kahn, S. Lany, J. M. Luther, M. C. Beard, C. L. Perkins, Revisiting the valence and conduction band size dependence of PbS quantum dot thin films, *ACS nano* 10 (2016) 3302.

[44] J. Patwari, H. Joshi, H. Mandal, L. Roy, C. Bhattacharya, P. Lemmens, S. K. Pal, Exciton dissociation in an NIR-active triohybrid nanocrystal leading to efficient generation of reactive oxygen species, *Phys. Chem. Chem. Phys.* 21 (2019) 10667.

[45] S. Sardar, P. Kar, S. Sarkar, P. Lemmens, S. K. Pal, Interfacial carrier dynamics in PbS-ZnO light harvesting assemblies and their potential implication in photovoltaic/ photocatalysis application, *Sol. Energy Mater.* 134 (2015) 400.

[46] S. A. Ahmed, N. Pan, H. M. Altass, J. Patwari, R. J. Obaid, H. Alessa, R. S. Jassas, S. K. Pal, Broad light harvesting under restricted environment: Photophysical understanding leading to enhanced reactive oxygen species generation, *J. Photochem. Photobiol. A: Chem.* 418 (2021) 113422.

[47] A. Giri, N. Goswami, M. Pal, M. T. Zar Myint, S. Al-Harthi, A. Singha, B. Ghosh, J. Dutta, S. K. Pal, Rational surface modification of Mn_3O_4 nanoparticles to induce multiple photoluminescence and room temperature ferromagnetism, *J. Mat. Chem. C* 1 (2013) 1885.

[48] S.-Y. Joo, D.-W. Jeong, C.-G. Lee, B.-S. Kim, H.-S. Park, W.-B. Kim, Room-temperature processing of CdSe quantum dots with tunable sizes, *J. Appl. Phys.* 121 (2017) 223102.

[49] N. Pan, T. K. Maji, S. Bandyopadhyay, P. Biswas, A. Chatterjee, M. Mitra, A. Chatterjee, S. K. Pal, A combined spectroscopic and theoretical analysis of plasmonic silver nanoparticle sensor towards detailed microscopic understanding of heavy metal detection, *Plasmonics* 17 (2022) 223.

[50] N. Pan, N. Bhattacharyya, A. Banerjee, P. Biswas, L. Roy, A. Chatterjee, R. Bhattacharjee, S. Singh, S. A. Ahmed, A. Chattopadhyay, M. Mitra, S. K. Pal, Paper based plasmonic nanosensor monitors environmental lead pollution in real field, *New J. of Chem.* 46 (2022) 8177.

[51] N. Pan, R. Ghosh, D. Mukherjee, N. Bhattacharyya, L. Roy, A. Banerjee, S. Singh, R. T. Goswami, M. Mitra, A. Chattopadhyay, S. K. Pal, A Nanosensor-based prototype development for heavy metal detection: A combined spectroscopic and theoretical study, *IEEE Sens. Lett.* 7 (2023) 1.

[52] N. Pan, S. Ghosh, M. N. Hasan, S. A. Ahmed, A. Chatterjee, J. Patwari, C. Bhattacharya, J. Qurban, A. S. Khder, S. K. Pal, Plasmon-Coupled donor–acceptor type organic sensitizer-basedp hotoanodes for enhanced photovoltaic activity: Key Information from ultrafast dynamical study, *Energy Fuels* 36 (2022) 9272.

[53] N. Pan, L. Roy, M. N. Hasan, A. Banerjee, R. Ghosh, M. A. Alsharif, B. H. Asghar, R. J. Obaid, A. Chattopadhyay, R. A. Das, Saleh A., S. K. Pal, Unraveling an utrafast electron tansport mechanism in a photocatalytic "Micromachine" for their potential light Harvesting Applications, *Micromachines* 14 (2023) 980.

[54] N. Pan, M. N. Hasan, S. Ghosh, L. Roy, C. Bhattacharya, D. Karmakar, S. K. Pal, Near-infrared active tri-nanohybrid for enhanced energy harvesting, *ChemistrySelect* 9 (2024) e202400968.

CHAPTER 2

An Overview of Experimental, Computational Techniques and Systems

Various steady-state and dynamic techniques have been employed to explore the synthesis, characterization of hybrid nanomaterials and their potential in various fields such as solar-light harvesting, and environmental pollution monitoring. These include photoinduced electron transfer (PET), Förster resonance energy transfer (FRET) on hybrid materials, photocurrent−voltage (I−V) characterization, sweep voltammetric and impedance measurement photoanodes, etc., In order to investigate the microscopic phenomena involved in hybrid materials computational calculations based on density functional theory have been employed. In this chapter, a brief discussion about the above-mentioned tools has been included. An overview of the various systems, probes, and dyes used in the studies has also been provided.

2.1. Steady-state and Dynamical Tools:

2.1.1. Quenching of Fluorescence: Fluorescence quenching refers to the process wherein the excitation energy of a fluorophore is lost non-radiatively due to interaction with another molecule, termed a quencher, leading to a reduction in fluorescence intensity.

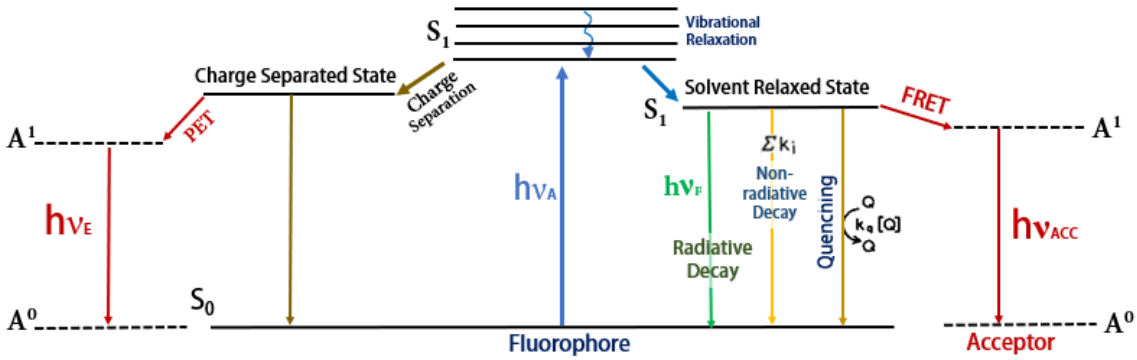

Figure 2.1: *The modified Jablonski diagram with collisional quenching fluorescence resonance energy transfer (FRET) and PET. Other non-radiative paths to the ground state are included in the term Σki.*

Static quenching occurs when fluorophore forms a non-fluorescent complex in the ground state with the other molecules present in the solution called quencher. On the other hand, collisional quenching happens when the excited-state fluorophore and quencher diffuse in the solution and collide with each other. In this scenario, the two molecules do not form a complex, and return to the ground state after a diffusive encounter with the quencher.

2.1.2. Photoinduced Electron Transfer (PET): PET can be described as the movement of an electron caused by the absorption of light from an electron-rich species (D) to an electron deficient species (A), as shown in equation 2.1.

$$D + A \rightarrow D^{+} + A^{-} \qquad 2.1$$

The first law of photochemistry tells us that a photoinduced process must be initiated by the absorption of light. In PET, the absorbing species can either be a donor, the acceptor, or a ground-state complex between the donor and acceptor, often referred to as a charge transfer complex. These possibilities are shown in equations 2.2−2.4.

$$D \xrightarrow{h\upsilon} D^{*} + A \longrightarrow D^{+} + A^{-} \qquad 2.2$$

$$A \xrightarrow{h\upsilon} A^{*} + D \longrightarrow D^{+} + A^{-} \qquad 2.3$$

$$(D \cdots A) \xrightarrow{h\upsilon} (D \cdots A)^{*} \longrightarrow D^{+} + A^{-} \qquad 2.4$$

Transport of charges or excitons is commonly seen as fundamental processes in many optoelectronic devices as well as biological systems. The creation, diffusion, and annihilation of excitons and the mobility of charges are some of the key processes in many devices that interconvert electric and light energies [1, 2]. PET is an essential process in many biochemical systems, such as those in respiration and photosynthesis [3, 4]. To gain a deep understanding of these systems, it is important to describe the rates of these processes with a few empirically derived parameters [5, 6]. In our systems, the apparent rate constants, k_{nr}, were determined for the nonradiative processes by comparing the

lifetimes of donor in the absence (τ_0) and the presence (τ) of an acceptor, using equation 2.5 [7].

$$k_{nr} = 1/\langle \tau \rangle - 1/\langle \tau_0 \rangle \qquad 2.5$$

This thesis demonstrates various interfacial electron transfer processes processes, particularly in light-harvesting materials. In heterogeneous photocatalysis, the photoinduced charge separation in the photocatalyst is necessary and several strategies have been employed to facilitate the charge separation. In sensitizer/quantum dot-sensitized (QD) based photoanodes having applications in solar cells (DSSC) and in photoelectrochemical (PEC) water splitting, a series of charge transfer processes had to occur cooperatively so that the electrical output can be harvested efficiently. These include (i) electron injection from excited sensitizer /QD into metal oxides and (ii) electron transport to the collecting electrode surface. The positions of the band energies of the sensitizer/QD-semiconductors should be such that they facilitate desired functionality either to induce electron−hole recombination (e.g., light-emitting diodes) or to improve charge separation by driving electrons and holes in two different nanoparticles. In each instance where semiconductor nanocrystals are implemented into a practical device, PET reactions are intimately involved and dictate overall functionality. This thesis focuses on the recent progress made in understanding the kinetics and mechanistic aspects of various PET processes at the semiconductor interface and their role in optimizing solar cell and PEC water-splitting performance.

2.1.3. Förster Resonance Energy Transfer (FRET): FRET is an electrodynamic phenomenon involving the nonradiative transfer of the excited state energy from the donor dipole (D) to an acceptor dipole (A) in the ground state (Figure 2.2a). Basically, FRET is of two types: (i) homo-molecular FRET and (ii) hetero-molecular FRET. In the former case, the same fluorophore acts both as energy donor and acceptor, while in the latter case, two different molecules act as donor and acceptor. Each donor-acceptor (D-A) pair participating in FRET is characterized by a distance known as Förster distance (R_0), i.e., the D-A

separation at which energy transfer is 50% efficient. The rate of resonance energy transfer (k_T) from a donor to an acceptor is given by [8],

$$k_T = \frac{1}{\tau_D}\left(\frac{R_0}{r}\right)^6 \qquad 2.6$$

where τ_D is the donor's lifetime in the absence of acceptor and r is the donor to acceptor (D-A) distance. The rate of transfer of donor energy depends upon the extent of overlap of the emission spectrum of the donor with the absorption spectrum of the acceptor ($J(\lambda)$), the quantum yield of the donor (Q_D), the relative orientation of the donor and acceptor transition dipoles (κ^2) and the distance between the donor and acceptor molecules (r) (Figure 2.2b). In order to estimate the FRET efficiency of the donor and hence to determine distances between donor-acceptor pairs, the methodology described below is followed [8]. R_0 is given by,

$$R_0 = 0.211\left[\kappa^2 n^{-4} Q_D J(\lambda)\right]^{1/6} \text{ (in Å)} \qquad 2.7$$

where n is the refractive index of the medium, Q_D is the quantum yield of the donor and $J(\lambda)$ is the overlap integral. κ^2 is defined as,

$$\kappa^2 = \left(\cos\theta_T - 3\cos\theta_D \cos\theta_A\right)^2 = \left(\sin\theta_D \sin\theta_A \cos\varphi - 2\cos\theta_D \cos\theta_A\right)^2 \qquad 2.8$$

where θ_T is the angle between the emission transition dipole of the donor and the absorption transition dipole of the acceptor, θ_D, and θ_A are the angles between these dipoles and the vector joining the donor and acceptor and is angle between the planes of the donor, and acceptor (Figure 2.2b). κ^2 value can vary from 0 to 4. For collinear and parallel transition dipoles, $\kappa^2 = 4$; for parallel dipoles, $\kappa^2 = 1$; and for perpendicularly oriented dipoles, $\kappa^2 = 0$. For donors and acceptors that randomize by rotational diffusion prior to energy transfer, the magnitude of κ^2 is assumed to be 2/3. However, in systems with a definite site of attachment of the donor and acceptor molecules, to get physically relevant results, the value of κ^2 has to be estimated from the angle between the donor emission and acceptor absorption dipoles [9].

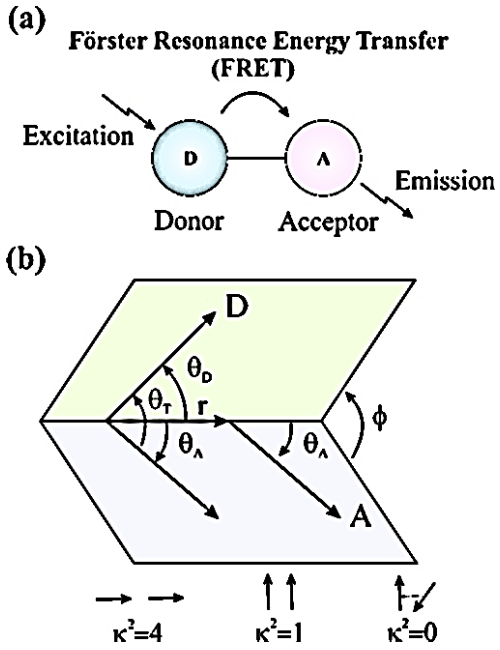

Figure 2.2: *(a) Schematic illustration of the FRET process. (b) The orientation factor 2 depends on the directions of the emission and absorption dipoles of the donor and acceptor, respectively.*

$J(\lambda)$, the overlap integral, which expresses the degree of spectral overlap between the donor emission and the acceptor absorption, is given by,

$$J(\lambda) = \frac{\int_0^\infty F_D(\lambda)\varepsilon_A(\lambda)\lambda^4 d\lambda}{\int_0^\infty F_D(\lambda) d\lambda} \qquad 2.9$$

where $F_D(\lambda)$ is the fluorescence intensity of the donor in the wavelength range of to $\lambda+d\lambda$ and is dimensionless. $\varepsilon_A(\lambda)$ is the extinction coefficient (in $M^{-1}cm^{-1}$) of the acceptor at λ. If λ is in nm, then $J(\lambda)$ is in units of $M^{-1}\,cm^{-1}\,nm^4$. Once the value of R_0 is known, the efficiency of energy transfer can be calculated. The efficiency of energy transfer (E) is the fraction of photons absorbed by the donor which are transferred to the acceptor and is defined as,

$$E = \frac{k_T(r)}{\tau_D^{-1} + k_T(r)} \qquad 2.10$$

$$\text{Or, } E = \frac{R_0^6}{r^6 + R_0^6} \qquad 2.11$$

For D-A systems decaying with multiexponential lifetimes, E is calculated from the amplitude weighted lifetimes $\langle\tau\rangle = \sum_i \alpha_i \tau_i$ of the donor in the absence (τ_D) and presence (τ_{DA}) of the acceptor as,

$$E = 1 - \frac{\tau_{DA}}{\tau_D} \qquad 2.12$$

The D-A distances can be measured using equations 2.11 and 2.12.

2.1.4. Data Analysis of Time-Resolved Fluorescence Transients: Curve fitting of the time-resolved fluorescence transients was carried out using a nonlinear least square fitting procedure to a function 2.13 comprised of convolution of the IRF

$$(X(t) = \int_0^t E(t')R(t - t')dt') \qquad 2.13$$

(E(t)) with a sum of exponentials (2.14) with pre-exponential factors (B_i),

$$(R(t) = A + \sum_{i=1}^{N} B_i e^{-t/\tau_i}) \qquad 2.14$$

characteristic lifetimes (τ_i) and a background (A). Relative concentration in a multiexponential decay is expressed as 2.15.

$$c_n = \frac{B_n}{\sum_{i=1}^{N} B_i} \times 100 \qquad 2.15$$

The average lifetime (amplitude-weighted) of a multiexponential decay is expressed as,

$$\tau_{av} = \sum_{i=1}^{N} c_i \tau_i \qquad 2.16$$

2.1.5. Dye-Sensitized Solar Cells (DSSC): DSSC [10-12] is a potentially inexpensive alternative to traditional semiconductor solar cells. The essential components of a DSSC are semiconductor metal oxides attached to sensitizing

dyes (mostly, ruthenium) and an electrolyte medium (iodine-based). A schematic of the interior and operating principle of a DSSC is shown in Figure 2.3. The typical basic configuration is as follows: at the heart of the device is the metal oxide layer (mostly ZnO/TiO_2), which is deposited on a fluorine-doped tin oxide (FTO) coated glass substrate. Attached to the surface of the nanocrystalline film is a monolayer of the charge transfer sensitizer/QDs.

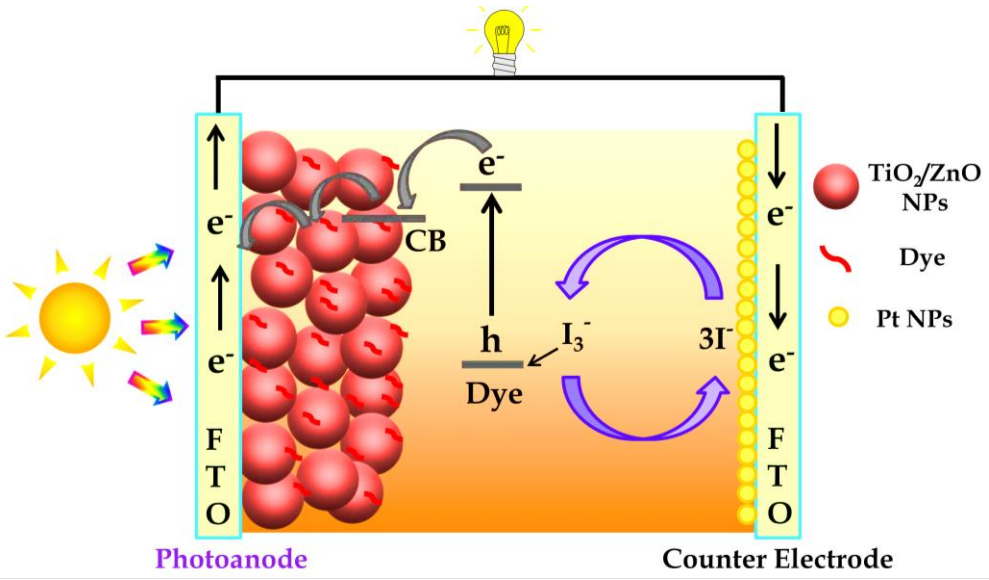

Figure 2.3: *Schematic representation of a DSSC showing different charge migration processes.*

Photoexcitation of the latter results in the injection of an electron into the conduction band of the oxide, leaving the dye in its oxidized state. The dye is restored to its ground state by electron transfer from the electrolyte, usually an organic solvent containing the iodide/triiodide (I^-/I_3^-) redox system. The regeneration of the sensitizer by iodide intercepts the recapturing of the conduction band electron by the oxidized dye. The I_3^- ions formed by oxidation of I^- diffuse a short distance (~ 60 μm) through the electrolyte to the cathode, which is coated with a thin layer of platinum catalyst, where the regenerative cycle is completed by electron transfer to reduce I_3^- to I^-. In order to quantitatively measure the efficacy of a DSSC, photocurrent–voltage (*I–V or J–V*) measurements under simulated sunlight, incident photon-to-current conversion efficiency (IPCE) under monochromatic light and photovoltage decay measurement under dark conditions following a brief illumination of light are important.

2.1.5.1. Photocurrent−Voltage (I−V) Measurements: Many solar cell parameters can be obtained from current-voltage (I-V) measurements of a cell. The I-V characteristics measurement can be done using Source-Measure Units (SMUs), which can source and measure both current and voltage. A DSSC can be represented by an equivalent electric circuit shown in Figure 2.4, where, I_L is the photocurrent, R_S is the series resistance (describes the resistances of the materials) and R_{sh} the shunt resistance.

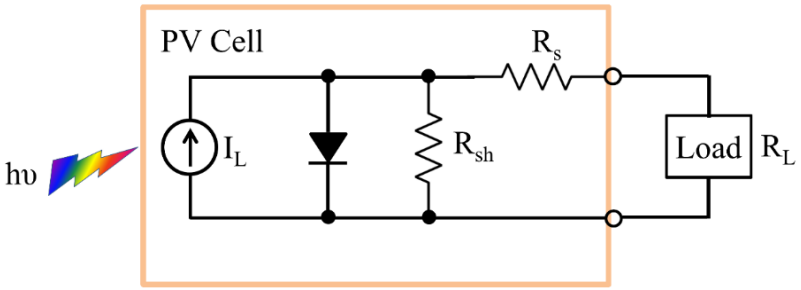

Figure 2.4: *Idealized equivalent electric circuit of a DSSC.*

Short-Circuit Current (I_{SC} or J_{SC}): The current equals the short-circuit current when the applied bias potential is zero:

$$I = I_{ph} - I_S \left[\exp\left(\frac{V + I.R_S}{\eta.V_{th}} \right) - 1 \right] \qquad 2.17$$

Open-Circuit Voltage (V_{OC}): When no current is flowing through the cell the potential equals the open-circuit potential, using equation 2.18 one can find:

$$V_{OC} = \eta.V_{th} \ln\left(\frac{I_{ph}}{I_c} + 1 \right) \qquad 2.18$$

Maximum Power Output (P_{max}): The power delivered from a solar cell at a certain potential equals the product of the current at this potential times the potential:

$$P(V) = I(V).V \qquad 2.19$$

To obtain a graphic representation of the power, one has to vary the potential between V_{OC} and 0. The point where the power is maximum (P_{max}) corresponds

to the peak power point (PPP) for the $I-V$ curve. These are the optimal current and potential conditions (I_m, V_m) for the operating cell.

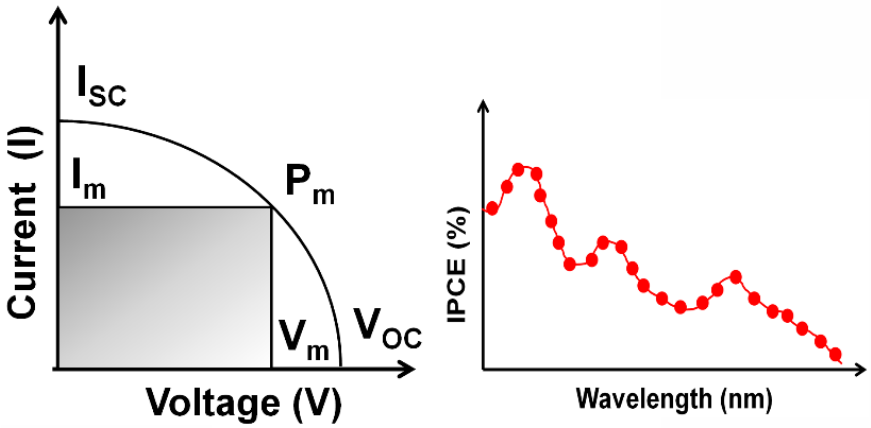

Figure 2.5: *Schematic representation of conventional I−V characteristic diagram (left). Typical IPCE characteristic diagram of a DSSC (right).*

Fill Factor (*FF*): The *FF* quantifies the quality of the solar cell, which is the ratio of actual power output ($V_m \times I_m$) versus its 'dummy' power output ($V_{OC} \times I_{SC}$) of a solar cell, as shown in equation 2.20:

$$FF = \frac{V_m I_m}{V_{OC} I_{SC}} \qquad 2.20$$

The *FF* lies between 0.6 and 0.85 for an efficient DSSC. These values are influenced by the values of the series and the shunt resistances. To obtain high *FF* values the shunt resistance has to be as small as possible and the series resistance as high as possible.

Photo-conversion Efficiency (η): The overall photo-conversion efficiency is given by the following equation:

$$\eta = \frac{V_m I_m}{P_{in}} = \frac{V_{OC} I_{SC} FF}{P_{in}} \qquad 2.21$$

It expresses the ratio of produced power and the incoming power (P_{in}). The experimental conditions have been fixed worldwide, in order to compare results coming from different places. A power density value of 100 mW/cm^2, at air mass 1.5 global (AM 1.5 G) condition has been set for the incident solar radiation, and

the temperature of the cell should be 25 °C. The AM is the ratio of the path-length of incoming sunlight through the atmosphere when the sun is at an angle to the zenith, and the path-length when the sun is at the zenith.

2.1.5.2. Incident Photon-to-Current Conversion Efficiency (IPCE) Measurements: The sensitivity of a solar cell varies with the wavelength of the incoming light. The IPCE value corresponds to the photocurrent density produced in the external circuit under monochromatic illumination of the cell divided by the photon flux that strikes the cell. From such an experiment the IPCE as a function of wavelength can be calculated from:

$$IPCE(\lambda) = \frac{n_{electrons}(\lambda)}{n_{photons}(\lambda)} = \frac{I(\lambda)/e}{P_{in}(\lambda)/h.\nu} = \frac{I(\lambda)}{\lambda.P_{in}(\lambda)} \cdot \frac{hc}{\nu} \qquad 2.22$$

Or, $$\mathrm{IPCE\%} = \left[1240 \times J_{SC}\left(\mathrm{A/cm^2}\right)\right] / \left[\lambda(\mathrm{nm}) \times P\left(\mathrm{W/cm^2}\right)\right] \times 100 \qquad 2.23$$

where, $I(\lambda)$ is the current given by the cell at wavelength λ, $P_{in}(\lambda)$ the incoming power at wavelength λ and I_p is the incident light power striking the device. IPCE values provide practical information about the monochromatic quantum efficiencies of a solar cell. Figure 2.5 (right) shows a typical IPCE spectrum of a standard DSSC.

2.1.5.3. Photovoltage Decay Measurement: The open circuit voltage of a DSSC generated under illumination is equivalent to the separation between the quasi-Fermi level of electrons in the TiO_2 film and the rest potential of the counter electrode, which remains in equilibrium with the redox couple. The forward electron injection from the sensitizer to TiO_2 is terminated upon stopping the illumination, thus discharging of electrons occurs through the back electron transfer or recombination with the oxidized electrolytes. The open circuit voltage decay reflects the timescales for the recombination processes.

2.1.6. Photoelectrochemical (PEC) Water Splitting: Photoelectrochemical [13] (PEC) water splitting with sunlight is a promising and environmentally friendly technology garnering considerable attention for renewable hydrogen

production. The choice of semiconductor electrode materials in PEC water-splitting cells significantly influences the efficiency of solar-to-hydrogen conversion in the device. The essential components of a PEC are a semiconductor photoelectrode, an electrolyte medium, a reference, and a counter electrode. A schematic of the interior and operating principle of a PEC is shown in Figure 2.6. The typical configuration is as follows: a semiconductor layer that is deposited on a fluorine-doped tin oxide (FTO) coated glass substrate. Here mainly, we have worked with TiO2 metal-oxide semiconductors.

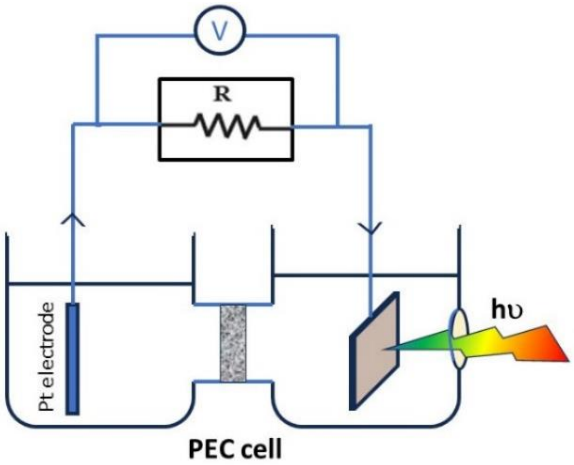

Figure 2.6: *Photoelectrochemical cell in which, the semiconductor electrode is connected with Pt electrode.*

Upon photoexcitation, the TiO_2 electrode facilitated a flow of current from the platinum electrode to the TiO_2 electrode via the external circuit. The current direction indicates that oxidation (oxygen evolution) takes place at the TiO_2 electrode, while reduction (hydrogen evolution) occurs at the platinum black electrode. We propose that water can undergo decomposition into oxygen and hydrogen under visible light without the need for any external voltage, as outlined in the following schemes (2.24 - 2.26):

$$TiO_2 + 2h\nu \longrightarrow 2e^- + 2p^+ \qquad 2.24$$

(photoexcitation on TiO_2 surface)

$$2p^+ + H2O \longrightarrow \frac{1}{2}O_2 + 2H^+ \qquad 2.25$$

(at TiO_2 electrode)

$$2e^- + 2H^+ \longrightarrow H_2 \qquad 2.26$$

(at the platinum electrode)

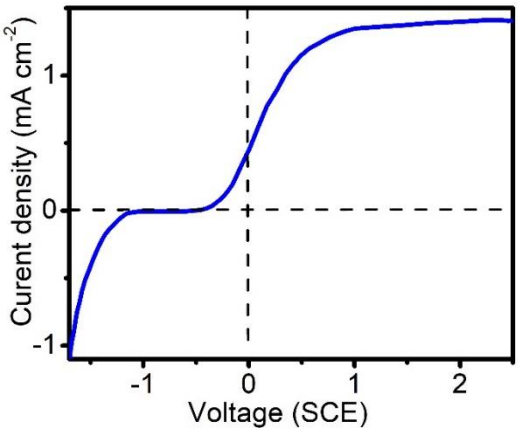

Figure 2.7: *Current-voltage curves for typical TiO_2 n-type semiconductor photoanode under light excitation.*

2.1.6.1. Photoelectrochemical Impedance Measurement: Impedance measurement is important given PEC device performance in view of impedance. In Electrochemical Impedance Spectroscopy (EIS) studies, the interface of an electrode undergoing an electrochemical reaction is commonly likened to an electronic circuit. This analogy involves a particular arrangement of resistors and capacitors. By obtaining an impedance plot from a given electrochemical system using an equivalent circuit, one can relate it to the physical and chemical properties of the system. Extracting numerical values involves fitting the data to the circuit model, thereby allowing for a deeper understanding of the system's behavior. An ideal three-electrode PEC cell can be modelled as a circuit shown in Figure 2.8, where R_s is electrolyte resistance, and C_{dl} is electrical double-layer capacitance at the working electrode-electrolyte junction, R is the reaction resistance at the semiconductor interface.

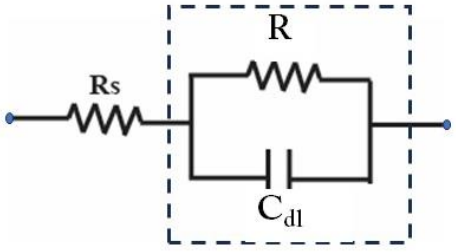

Figure 2.8: *A simplified equivalent circuit of PEC cell.*

The fundamental principle behind impedance methods involves subjecting the system under investigation to a small amplitude sinusoidal excitation signal and

then measuring the response i.e., current, voltage, or another relevant signal. The impedance, Z (ω), as mentioned above, is a complex quantity and can be represented in cartesian as well as polar coordinates. In polar coordinates, the impedance of the data is represented by,

$$Z(\omega) = |z(\omega)|e^{\varphi\omega} \qquad 2.27$$

Where, $|z(\omega)|$ is the magnitude of the impedance, and φ is the phase shift. In cartesian coordinates, the impedance is given by,

$$Z(\omega) = z_r(\omega) + jz_i(\omega) \qquad 2.28$$

where Z_r is the real part of the impedance, and Z_j is the imaginary part, and $j = 1$. In impedance spectroscopy, we measure the impedance as a function of frequency. The data set is called the impedance spectrum, consisting of the frequency of the real and imaginary parts of impedance. In such impedance measurements, the frequency varies from low frequency (LF), around 1 MHz, and goes up to 1 μHz. While recording data, it takes more time at a low-frequency range, which accounts for the more time taken to complete a full cycle. For example, if we measure at 1 MHz, it takes 1000 seconds to complete a cycle measurement. The plot of the real part of impedance against the imaginary part gives a *Nyquist Plot.* At LF and HF limit, the above circuit will behave as a purely resistive circuit with resistance values of Rs+R and Rs, respectively, since at HF, the capacitive impedance would behave as a short circuit and will offer almost zero resistance.

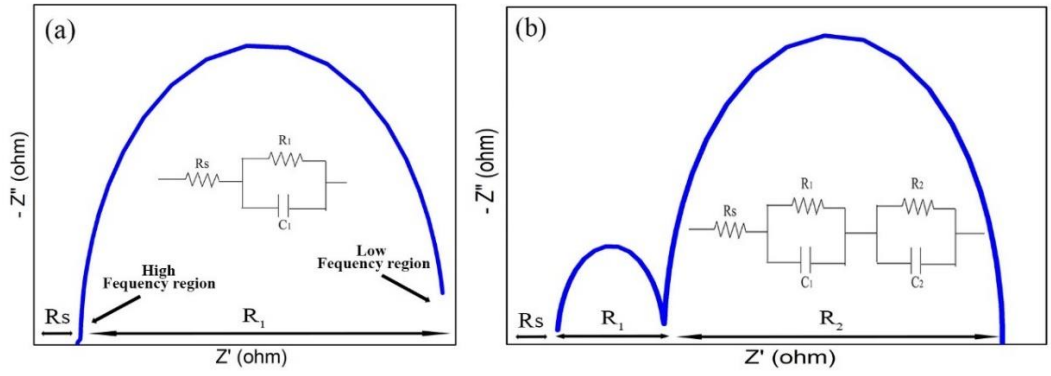

Figure* 2.9: The Nyquist plots for (a) a typical dye-sensitized photoanode and (b) a dye-sensitized solar cell with their corresponding equivalent circuits.*

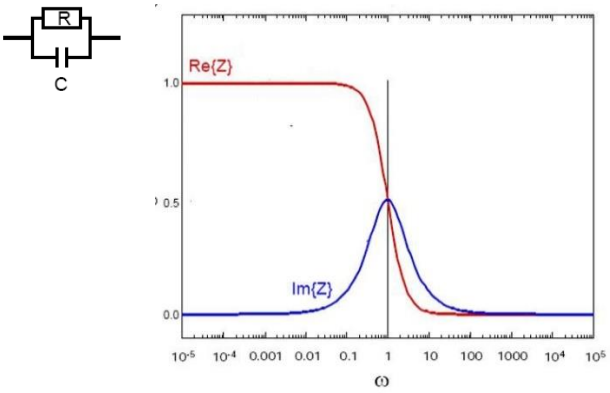

Figure 2.10: *Bode plot representation of simple RC circuit.*

In contrast, at LF limit capacitive impedance would offer almost infinite resistance and will not allow current to pass. While plotting data in the Nyquist format, the real axis must be equal to the imaginary axis so as not to distort the shape of the curve. The shape of the curve is important in making qualitative interpretations of the data. A drawback of the Nyquist representation is the loss of the frequency dimension in the data. One approach to address this limitation is by annotating the frequencies directly onto the curve. The other type of representation, including the frequency data, is the *Bode plot*. The relation between phase and frequency is expressed below by equation 2.29.

$$\varphi = \tan^{-1}\frac{\mathrm{Im\ Z}}{\mathrm{Re\ Z}} \qquad 2.29$$

The Bode plot facilitates a clear understanding of how impedance varies with frequency. By using the logarithm of frequency, a wide range of frequencies can be depicted on a single graph while ensuring each decade receives equal emphasis. Additionally, the Bode plot displays impedance magnitude ($|Z|$) on a logarithmic scale, enabling the representation of a broad range of impedance values on the same set of axes. This feature is advantageous, particularly when impedance exhibits significant frequency dependence, such as with capacitors.

2.1.6.2. Mott-Schottky Analysis: To quantitatively measure the carrier concentration associated with the increased capacitance upon light irradiation, the capacitance-voltage (C-V) characterization is performed**.**

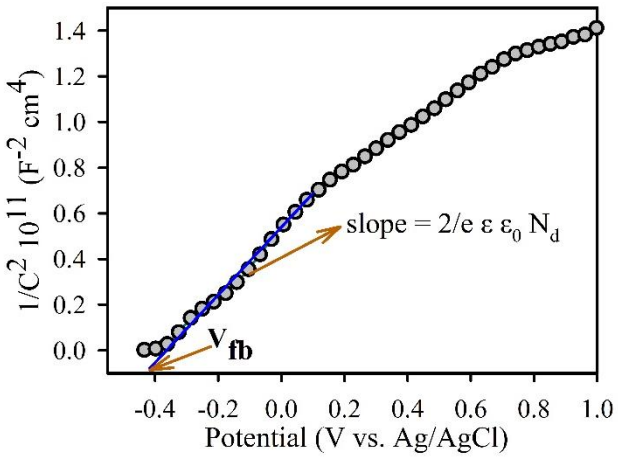

Figure 2.11: *The Mott-Schottky plot of n-type-TiO_2 photoanode.*

The method involves measuring the apparent capacitance as a function of potential under depletion conditions and is based on the Mott- Schottky relationship.

$$1/C^2_{sc} = (2/e\ \varepsilon\ \varepsilon_0\ N_d)\ (E\text{-}E_{fb}\text{-}kT/e) \qquad 2.30$$

Where C_{sc} is the space charge capacitance in units of F cm^{-2}, ε denotes the dielectric constant of the photoelectrode material, e is the electron charge, ε_0 denotes the permittivity of vacuum, N_d is the carrier density in units of cm^{-3}, E in Volt (V) is the applied bias voltage at the electrode; E_{fb} in V represents the flat band potential, T is temperature in Kelvin and k denotes Boltzmann constant. M-S (Mott-Schottky) analysis allows for the determination of both the flat band potential (V_{fb}) and the density of free charge carriers (either donors or acceptors, N_d / N_a). The flat band potential of the photoelectrode material is also calculated from the Mott-Schottky plot by the intercept of the applied biased axis. The capacitance-voltage (C-V) characterization of the TiO_2 anode is shown in Figure 2.11.

2.2. Computational Techniques:

There are Numerous computational techniques, such as Molecular Dynamics (MD), Monte Carlo (MC), Density Functional Theory (DFT), Monte Carlo Renormalization Group (MCRG), Quantum Monte Carlo (QMC), and Time-Dependent Density Functional Theory (TDDFT), have significantly advanced

the fields of condensed matter physics, chemistry, and materials science. These methodologies enable researchers to investigate and comprehend intricate materials and phenomena that may be challenging or impractical to study experimentally. Among them, we have used computational DFT, which involves translating theoretical principles and mathematical frameworks into computer programs, facilitating the exploration and analysis of material properties and behaviours at the atomic and molecular levels.

2.2.1. Density Functional Theory: The term density functional theory refers to all methods that express the ground-state energy as a function of the electronic density ρ(r). The DFT is presently the most successful (and the most promising) approach to computing the electronic structure of matter. Its applicability ranges from atoms, molecules, and solids to nuclei and quantum and classical fluids. The idea of DFT can be attributed to the Thomas-Fermi theory of electron density concept [14]. In this way, a function of the 3N variable, where N is the number of electrons, can be reduced to a lower dimension. According to that model, the electron density can be written as equation 2.31. The Thomas-Fermi model, however, was too crude because the approximation used for the kinetic energy of the electrons, as well as errors in the exchange energy, was unable to sustain bound states.

$$\rho(\boldsymbol{r}) = N \int \psi(r_1, r_2, \dots, r_N)\psi^*(r_1, r_2, \dots, r_N)dr_1 dr_2 \dots dr_N \qquad 2.31$$

Nevertheless, it showed the pathway for the development of DFT by Hohenberg and Kohn in [6] to deal with many electron problems more efficiently. In 1964, Hohenberg and Kohn put forth two crucial theorems [15] that provided a practical approach for reducing the many-electron problems to an effective one-electron problem. These two theorems are considered the backbone for electronic structure calculations in condensed matter physics.

The primary advantages of taking electronic density as the basic variable are: (i) it is a function of 3 variables, unlike the wave function which is a function of 3N

variables and is simpler to tabulate and plot; (ii) it is a function in 3D space in which we live, and it provides better visualization, (iii) it is an experimental variable. In the next section, we briefly discuss the mathematical formulation of the density of states. It is important to note that the accuracy of DFT calculations depends on the choice of exchange-correlation functional, which is not well-known in general.

2.2.2. Exchange Correlation Functional: The exchange-correlation (XC) functional is a key component of DFT calculations. It is a mathematical function that accounts for the effects of electron exchange and electron correlation, which are not explicitly included in the Kohn-Sham equation. The XC functional is used to calculate the exchange-correlation energy, which is a measure of the interaction between the electrons in a system. The exchange energy arises from the antisymmetry of the wave function of a system of indistinguishable particles. It describes the energy change when two electrons exchange places, and it can be calculated exactly for some simple systems. However, for more complex systems, the exact exchange energy is not known, and an approximation must be used. The correlation energy arises from the fact that electrons repel each other due to their Coulombic interactions. This repulsion leads to a reduction in the energy of the system, known as the correlation energy. Like the exchange energy, the exact correlation energy is not known for most systems and must be approximated. Many different forms of XC functionals have been developed, ranging from simple local approximations to more complex non-local functionals that include the effects of electron density gradients. The choice of XC is functional depends on the properties of the system being studied and the accuracy required for the calculations. Although DFT is accurate in principle, the main drawback of the Kohn-Sham formulation comes due to its inexplicit exchange-correlation term. The exact expression of the E_{XC} is complex and unknown. So, to solve the equation one needs to choose a good approximation of the exchange-correlation function. In practice, the utility of the theory lies in the approximations used for E_{XC}. Even though the exact formulation of E_{XC} is

very complex, great progress has been made with a remarkably simple approximation to encounter the problem. the various approximation formulas, the local density approximation (LDA) and generalized gradient approximation (GGA) are the most commonly used approximation methods. The development of more accurate and efficient XC functionals is an active area of research in computational chemistry and materials science. The goal is to develop functionals that can accurately predict the properties of complex systems with reasonable computational costs. The different approximate functionals for exchange correlation are discussed next section.

2.2.2.1. Local Density Approximation (LDA): The Local Density Approximation (LDA) is a widely used theoretical framework in condensed matter physics, materials science, and related fields for calculating the electronic structure of solids. In the LDA, the energy of the system is expressed as a functional of the electron density, which is the probability density of finding an electron at a given point in space. The electron density is calculated self-consistently by solving the Kohn-Sham equations, which are a set of partial differential equations that describe the behavior of non-interacting electrons in an external potential. This approximation is based on the idea that the electronic structure of a solid is determined by the local environment around each atom, rather than the global structure of the crystal. It was first introduced by Kohn and Sham in 1965, but the basic idea existed in the theory by Thomas-Fermi-Dirac. Under the LDA approximation, it is assumed that the charge density varies very slowly at any point $\mathbf{r}$ in space so that the electron gas in a small volume element $d^3\mathbf{r}$ could be considered locally uniform.

2.2.2.2. Generalized Gradient Approximation (GGA): We have seen that the LDA was derived by assuming that the electron density varies very slowly in space. Thus, it was argued that LDA could be improved if we expanded the exchange-correlation functional in terms of the gradient of the density in the Taylor series and truncated it to some order. Such an approximation is known as generalized gradient expansion approximation and was implemented by

Herman et al. (1969) [16]. While GGA retains the core features of LDA, it also takes into account the spatial variations in the charge density, which are important. One that has been widely used is by Perdew and Wang, known as PW86 and PW91 [17, 18]. Later on, Perdew *et al.* (1996) proposed another functional (PBE) [19], which retains important features of PW91. In this thesis, we have mostly used the GGA-PBE exchange-correlation function, which is briefly described below. GGA retains the correct features of LDA and combines them with the inhomogeneity features that are energetically most important. Although the GGA method works much more precisely over LDA in terms of predicting the binding energies, electronic and magnetic properties of the materials, it does have a few drawbacks. It is also known to overestimate the electric polarization for polar materials [20]. Finally, both GGA and LDA fail for strong electron-electron correlated systems and present research is continuing in search of a better functional.

2.2.3. Basis Set: To solve the Kohn-Sham equations, a choice of an appropriate basis set to expand the one-electron Kohn-Sham orbitals is necessary. The choice of basis set is dependent on the attributes of the system under study. Over the years, various basis-set methods have been developed to predict the electronic properties of solids with reasonable accuracy. Depending on the choice of basis sets, different methods can be broadly classified into two categories:

2.2.3.1. The Projector-Augmented-Wave (PAW) Formalism: The projector augmented-wave (PAW) method was developed by Blochl in 1994 [21] as a method to accurately and efficiently calculate the electronic structure. The advantage of this formalism is it contains the numerical advantages of pseudopotential calculations while retaining the physics of all-electron calculations, including the correct nodal behavior of the valence-electron wave functions and the ability to include upper core states in addition to valence states in the self-consistent iterations. Later, Kresse and Joubert modified this PAW method and implemented it within the plane-wave code of the Vienna Ab-initio Simulation Package(VASP) [22, 23]. Within this formalism, the drawback arising

due to oscillations of valence-state wave functions is addressed by transforming the physical wave functions $\psi_n(r)$ into smooth auxiliary wave functions $\tilde{\psi}_n(r)$ that can be represented in a plane wave expansion. The PAW formalism as implemented within the VASP software by Kresse and Joubert, has been primarily used for the work described within this thesis.

2.2.4. Electronic Structure and Orbital Analysis: The first-principles electronic structure is calculated with the help of plane-wave calculations with norm-conserving projector augmented wave (PAW) pseudopotentials. We have used generalized gradient approximation (GGA) with Ceperley-Alder (CA) and Perdew-Burke-Ernzerhof (PBE) [19] exchange-correlation functionals, respectively, as implemented in the Vienna ab initio simulation program (VASP) [24]. A monkhorst-Pack *k*-grid of dimension 3×3×2 is used for sampling the Brillouin zone and the cut-off for the plane wave expansion is kept at 500 eV. The energy convergences for all self-consistent field calculations are kept as 10^{-5} eV and the structural optimizations were performed using the conjugate gradient algorithm, till the Hellmann-Feynmann force on each ion is less than 0.01 eV/Å. We calculated spin-polarised plane-wave pseudopotentials using the norm-conserving projector augmented wave pseudopotentials as implemented in the Vienna ab initio simulation programme (VASP) [22]. Interface-induced dipolar interactions are included after taking care of van der Waals corrections after incorporating a semiempirical dispersion potential to the density functional theory (DFT) using the Grimme DFT-D3 method [25]. On the other hand, the density functional theory calculations were also, performed using the B3LYP exchange-correlation functional and 6-311G basis set in Gaussian 16 software. Molecules (to be optimized) structure was obtained from PubChem Database, and using the geometry optimization method, the electronic ground state of the structures. In geometry optimization, the geometry is adjusted until a stationary minimum is reached in the potential surface. In case of the complexes, geometry optimization for several configurations has been performed, and the lowest energy structure was used for further electronic calculation.

2.3. Systems:

2.3.1. Quantum Confined Nanostructures: The quantum confinement effect arises when a particle's size is small, typically less than 10 nanometres, compared to the wavelength of its electron. This phenomenon significantly impacts the optical and electronic characteristics as well as the bandgap of the material. When the movement of an electron or hole is confined in any dimension, the energy band becomes discretized into energy states. This discreteness in energy states becomes apparent when a particle's confinement to a region of space is comparable to or smaller than its de Broglie wavelength. In contrast to the continuous absorption spectrum of a bulk semiconductor, this discretization results in a discrete absorption spectrum. Depending on the number of spatial dimensions in which particles are confined, quantum-confined structures can be categorized as quantum wells (confined along one dimension - 1D), quantum wires (confined along two dimensions - 2D), and quantum dots (confined along three dimensions - 3D). In our research, we have utilized various quantum confinement structures such as nanotubes (NTs), and colloidal QDs for near-infrared (NIR) light harvesting. This section will explore the structures employed in our study.

2.3.1.1. Lead Sulphide Quantum Dots (PbS QDs): PbS QDs among all lead chalcogenide colloidal nanocrystals as the most promising material for solution-processable optoelectronics. PbS belongs to the class of IV-VI semiconductor NCs, drawing significant scientific interest in recent years. PbS QDs exhibit compelling electrical and optical characteristics, making them suitable for various applications such as diode lasers, light-emitting diodes, infrared detectors, photovoltaics, and incoherent up/down conversion of infrared light. The unique features of PbS QDs include tunable band gap, strong absorption across a broad wavelength spectrum encompassing the near and short-wavelength infrared (NIR 700-1000 nm and SWIR 1000-1600 nm), thus expanding their utility beyond silicon's band gap. Additionally, PbS QDs possess a significant dipole moment, enhanced multiple exciton generation

(MEG), and the advantage of being cost-effectively processed via solution methods.

2.3.1.2. Multi-wall Carbon Nanotubes (MWCNTs): Carbon, one of the most abundant elements, exhibits excellent charge transport properties superior to its inorganic counterparts [26]. Graphene sheets in their low-dimensional form, i.e., carbon nanotubes (CNTs), whether single-walled or multiwalled, exhibit a wide range of applications owing to their delocalized π-electrons, exceptional electrical and thermal conductivity, hollow, high surface area, and stability [26-28]. MWCNTs are increasingly targeting applications in alternative energy and infrastructure, such as pipes and elements of building structures, as well as in automotive and aircraft structural materials. These sectors demand lightweight and robust materials with enhanced physical properties, essential for components like wind power generator blades, boat hulls, aircraft parts, and vessels. Here, we have addressed the conjunction of CNTs with semiconductor nanoparticles that can be utilized efficiently for efficient charge transportation and separation of photoexcitation charge carriers.

2.3.2. Molecular Probes: In this section, we will discuss the different probe molecules that have been used in the course of the study.

2.3.2.1. 3, 7, 12, 17-Tetramethyl- 8, 13-divinyl- 2, 18-porphinedipropionic acid (Protoporphyrin IX, PPIX): PP is a necessary precursor to biologically essential prosthetic groups such as heme, cytochrome c, and chlorophylls. PP is a very well-known cancer drug and efficient hydrophobic photosensitizer (PS) for photodynamic therapies (PDT) [29]. The efficiency of PDT depends on the photoactivation of the photosensitizers accumulated at the target site and the pharmacokinetic properties of the photosensitizer to achieve the desired biological response.

2.3.2.2. 5- carboxy- 2- [[3- [(2, 3-dihydro-1, 1-dimethyl- 3-ethyl- 1H-benzo [e] indol- 2-ylidene) methyl]-2-hydroxy- 4-oxo- 2-cyclobuten- 1-ylidene] methyl]- 3, 3 dimethyl- 1-octyl-3H-indolium (Squaraine, SQ2): Squaraine SQ2 (Figure

2.12) is a condensation product of electron-rich substrate and squaric acid derivatives, with a four-membered squarine ring present into the polymethine chain structure consist of absorption maxima in longer wavelength region [30, 31]. SQ2 imposes greater light-absorption ability (molar extinction co-efficient 319 000 M-1 cm-1) at lowenergy region (~665 nm absorption maxima) and higher photo-stability with respect to other available commercial dyes. Due to the extended absorption in the near 47 infra-red (NIR) region, SQ2 is considered an important photoactive materials in the field of organic photovoltaic devices [32], dye-sensitized solar cell (DSSC) [33], biomedical imaging, and photomedicine [31].

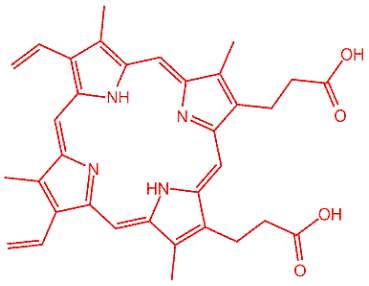

Protoporphyrin (PPIX)

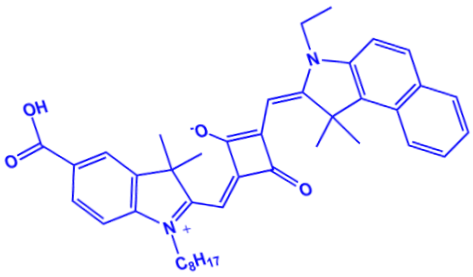

Squarine (SQ2)

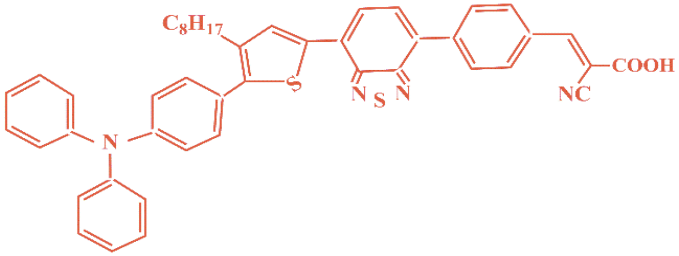

RK1

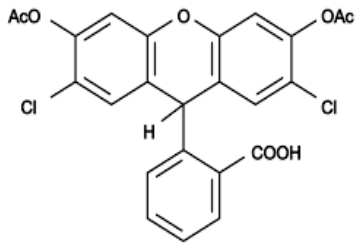

DCFH

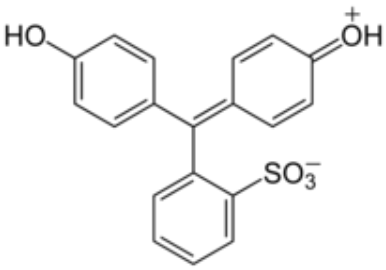

Phenol Red

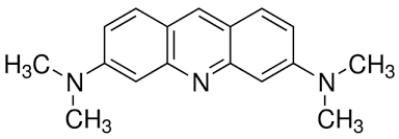

Acridine Orange (AO)

Figure 2.12: *Chemical structure of all molecular probes used.*

2.3.2.3. 2′-7′-Dichlorofluorescin diacetate (DCFH-DA): Dichlorofluorescin (DCFH) is a probe that belongs to the organic compounds of the fluorescein family, the structure shown in Figure 2.12 [34]. DCFH can be oxidized to dichlorofluorescein (DCF), which has an intense green 46 fluorescence. The molecular structure of DCFH is shown in Figure 2.12. Dichlorofluorescein (DCFH) is non-fluorescent, which converts to fluorescent dichlorofluorescein (DCF) upon oxidation through reacting with reactive oxygen species (ROS). This quantifies the amount of ROS as well as cellular oxidative stress.

2.3.2.4. 2-cyano-3-(4-(7-(5-(4- (diphenylamine) phenyl)-4- octylthiophen-2-yl) benzo[c] [1,2,5] thiadiazol-4-yl) phenyl) acrylic acid (RK1): RK1 [35] is a purely organic doner-bridge-acceptor type dye (Figure 2.12)exhibits a PCE of 10.20%, which is comparable to that of the Ru-metal-based industrial standard, N719 (10.19%), under identical conditions [36]. Moreover, devices based on RK1 show excellent stability under standard irradiation conditions. The dye has directional electron distribution with electron delocalization of the highest occupied molecular orbital (HOMO) in the triphenylamine group and of the lowest unoccupied molecular orbitals (LUMO) in the benzothiadiazole and cyanoacrylic acid group. The calculated HOMO (-3.184 eV), and LUMO (-5.242) positions are favourable for electron injection into the conduction band (CB) of wide band gap semiconductor such asTiO_2.

2.3.2.5. Acridine Orange (AO): AO is an organic dye with molecular formula $C_{17}H_{19}N_3$. AO is widely used as a nucleic acid-selective fluorescent cationic dye which is commonly used to determine cell cycle [37]. AO has a strong absorption at λ_{max} = ~480 nm [38]. As AO is cell-permeable, it interacts with DNA and RNA by intercalation or electrostatic attractions, respectively. When bound to DNA, it is very similar spectrally to fluorescein, with an excitation maximum of 502 nm and an emission maximum of 525 nm (green) [37]. In association with RNA, the excitation maximum of AO shifts to 460 nm (blue), and the emission maximum shifts to 650 nm (red). AO can be used in conjunction with ethidium bromide or propidium iodide to differentiate between viable, apoptotic, and necrotic cells.

Additionally, AO may be used to detect nuclear damage or chromatin condensation, aiding in clinical diagnosis [39]. Its structure is given in Figure 2.12.

2.3.2.6. Phenolsulfonphthalein (Phenol Red): Phenol Red is stable in air, meaning it doesn't readily degrade or react with oxygen or moisture in the atmosphere under normal conditions. Therefore, phenol red is one of the model pollutants and is produced from chemical waste products. It's most commonly used as a pH indicator frequently used in cell culture media and other biological assays. However, like many compounds, it can degrade over time if exposed to extreme conditions such as high temperatures, strong acids or bases, or prolonged exposure to light.

References

[1] H. Spanggaard, F. C. Krebs, A brief history of the development of organic and polymeric photovoltaics, *Sol. Energy Mater. Sol. Cells*, 83 (2004) 125.

[2] Y. Shirota, H. Kageyama, Charge carrier transporting molecular materials and their applications in devices, *Chem. Rev.*, 107 (2007) 953.

[3] H. B. Gray, J. R. Winkler, Electron tunneling through proteins, *Q. Rev. Biophys.*, 36 (2003) 341.

[4] G. McLendon, R. Hake, Interprotein electron transfer, *Chem. Rev.*, 92 (1992) 481.

[5] H. Bassler, Charge transport in disordered organic photoconductors: A monte carlo simulation study, *Phys. Status Solidi. B*, 175 (1993) 15.

[6] V. M. Kenkre, J. D. Andersen, D. H. Dunlap, C. B. Duke, Unified theory of the mobilities of photoinjected electrons in naphthalene, *Phys. Rev. Lett.*, 62 (1989) 1165.

[7] J. H. Bang, P. V. Kamat, Quantum dot sensitized solar cells. A tale of two semiconductor nanocrystals: CdSe and CdTe, *ACS Nano*, 3 (2009) 1467.

[8] J. R. Lakowicz, Principles of fluorescence spectroscopy, *Kluwer Academic/Plenum*, New York, 2006.

[9] D. Banerjee, S. K. Pal, Simultaneous binding of minor groove binder and intercalator to dodecamer DNA: Importance of relative orientation of donor and acceptor in FRET, *J. Phys. Chem. B*, 111 (2007) 5047.

[10] B. O'Regan, M. Grätzel, A low-cost, high-efficiency solar cell based on dye-sensitized colloidal TiO_2 films, *Nature*, 353 (1991) 737.

[11] M. Grätzel, Conversion of sunlight to electric power by nanocrystalline dye-sensitized solar cells, *J. Photochem. and Photobiol. A*, 164 (2004) 3.

[12] M. Grätzel, Photoelectrochemical cells, *Nature*, 414 (2001) 338.

[13] A. Fujishima, K. Honda, Electrochemical photolysis of water at a semiconductor electrode, *Nature*, 238 (1972) 37.

[14] E. Fermi, A statistical method for the determination of alcune priorieta dell'atom, *Rend. Accad. Naz. Lincei*, 6 (1927) 32.

[15] P. Hohenberg, W. Kohn, Inhomogeneous electron gas, *Phys. Rev.*, 136 (1964) B864.

[16] F. Herman, J. P. Van Dyke, I. B. Ortenburger, Improved statistical exchange approximation for inhomogeneous many-electron systems, *Phys. Rev. Lett.*, 22 (1969) 807.

[17] J. P. Perdew, W. Yue, Accurate and simple density functional for the electronic exchange energy: Generalized gradient approximation, *Phys. Rev. B*, 33 (1986) 8800.

[18] J. P. Perdew, Y. Wang, Accurate and simple analytic representation of the electron-gas correlation energy, *Phys. Rev. B*, 45 (1992) 13244.

[19] J. P. Perdew, K. Burke, M. Ernzerhof, Generalized gradient approximation made simple, *Phys. Rev. Lett.*, 77 (1996) 3865.

[20] Y. Umeno, B. Meyer, C. Elsässer, P. Gumbsch, Ab initio study of the critical thickness for ferroelectricity in ultrathin Pt/ $PbTiO_3$ /Pt films, *Phys. Rev. B*, 74 (2006) 060101.

[21] P. E. Blöchl, Projector augmented-wave method, *Phys. Rev. B*, 50 (1994) 17953.

[22] G. Kresse, J. Furthmüller, Efficient iterative schemes for ab initio total-energy calculations using a plane-wave basis set, *Phys. Rev. B*, 54 (1996) 11169.

[23] G. Kresse, D. Joubert, From ultrasoft pseudopotentials to the projector augmented-wave method, *Phys. Rev. B*, 59 (1999) 1758.

[24] G. Kresse, J. Furthmüller, Efficiency of ab-initio total energy calculations for metals and semiconductors using a plane-wave basis set, *Comput. Mater. Sci.*, 6 (1996) 15.

[25] S. Grimme, Semiempirical GGA-type density functional constructed with a long-range dispersion correction, *J. Comput. Chem.*, 27 (2006) 1787.

[26] A. Hirsch, Functionalization of single-walled carbon nanotubes, *Angew. Chem. Int. Ed.*, 41 (2002) 1853.

[27] W. Feng, C. Qin, Y. Shen, Y. Li, W. Luo, H. An, Y. Feng, A layer-nanostructured assembly of PbS quantum dot/multiwalled carbon nanotube for a high-performance photoswitch, *Sci. Rep.*, 4 (2014) 3777.

[28] Y. Hou, F. Zuo, A. Dagg, P. Feng, Visible light-driven α-Fe_2O_3 nanorod/graphene/BiV_1–x $MoxO_4$ core/shell heterojunction array for efficient photoelectrochemical water splitting, *Nano Lett.*, 12 (2012) 6464.

[29] W. E. Grant, A. MacRobert, S. G. Bown, C. Hopper, P. M. Speight, Photodynamic therapy of oral cancer: Photosensitisation with systemic aminolaevulinic acid, *Lancet*, 342 (1993) 147.

[30] S. Sreejith, P. Carol, P. Chithra, A. Ajayaghosh, Squaraine dyes: A mine of molecular materials, *J. Mater. Chem.*, 18 (2008) 264.

[31] J. H. Yum, P. Walter, S. Huber, D. Rentsch, T. Geiger, F. Nüesch, F. De Angelis, M. Grätzel, M. K. Nazeeruddin, Efficient far red sensitization of nanocrystalline TiO_2 films by an unsymmetrical squaraine dye, *J. Am. Chem. Soc.* , 129 (2007) 10320.

[32] G. Chen, H. Sasabe, Y. Sasaki, H. Katagiri, X. F. Wang, T. Sano, Z. Hong, Y. Yang, J. Kido, A series of squaraine dyes: Effects of side chain and the number of hydroxyl groups on material properties and photovoltaic performance, *Chem. Mater.*, 26 (2014) 1356.

[33] H. Choi, P. K. Santra, P. V. Kamat, Synchronized energy and electron transfer processes in covalently linked CdSe–squaraine dye–TiO_2 light harvesting assembly, *ACS nano*, 6 (2012) 5718.

[34] S. Sardar, S. Chaudhuri, P. Kar, S. Sarkar, P. Lemmens, S. K. Pal, Direct observation of key photoinduced dynamics in a potential nano-delivery vehicle of cancer drugs, *Phys. Chem. Chem. Phys.*, 17 (2015) 166.

[35] H. Chen, Y. Gong, A. l. Vázquez-Mayagoitia, J. Zhang, J. M. Cole, Dye aggregation, photostructural reorganization and multiple concurrent dye $\cdots TiO_2$ binding modes in dye-sensitized solar cell working electrodes containing benzothiadiazole-based dye RK-1, *ACS Appl. Energy Mater.*, 3 (2019) 423.

[36] D. Joly, L. Pellejà, S. Narbey, F. Oswald, J. Chiron, J. N. Clifford, E. Palomares, R. Demadrille, A robust organic dye for dye sensitized solar cells based on iodine/iodide electrolytes combining high efficiency and outstanding stability, *Sci. Rep.*, 4 (2014) 4033.

[37] N. Atale, S. Gupta, U. Yadav, V. Rani, Cell-death assessment by fluorescent and nonfluorescent cytosolic and nuclear staining techniques, *J. Microscopy*, 255 (2014) 7.

[38] A. Pitchaimani, A. Renganathan, S. Cinthaikinian, K. Premkumar, Photochemotherapeutic effects of UV-C on acridine orange in human breast cancer cells: Potential application in anticancer therapy, *RSC Adv.*, 4 (2014) 22123.

[39] E. E. M. Mohammed, E. Mosad, A. M. Zahran, D. A. Hameed, E. A. Taha, M. A. Mohamed, Acridine orange and flow cytometry: Which is better to measure the effect of varicocele on sperm DNA integrity?, *Adv. Urology*, 2015 (2015).

CHAPTER 3

Instrumentation and Sample Preparation

In this chapter, the details of the instrumental setup and sample preparation techniques used in our studies have been described.

3.1. Instrumental Setups:

3.1.1. Steady-state UV-Vis Absorption and Emission Measurement: Steady-state UV-Vis absorption and emission spectra were measured with Shimadzu UV-2600 spectrophotometer and Horiba Fluorolog, respectively. Schematic ray diagrams of these two instruments are shown in Figures 3.1 and 3.2.

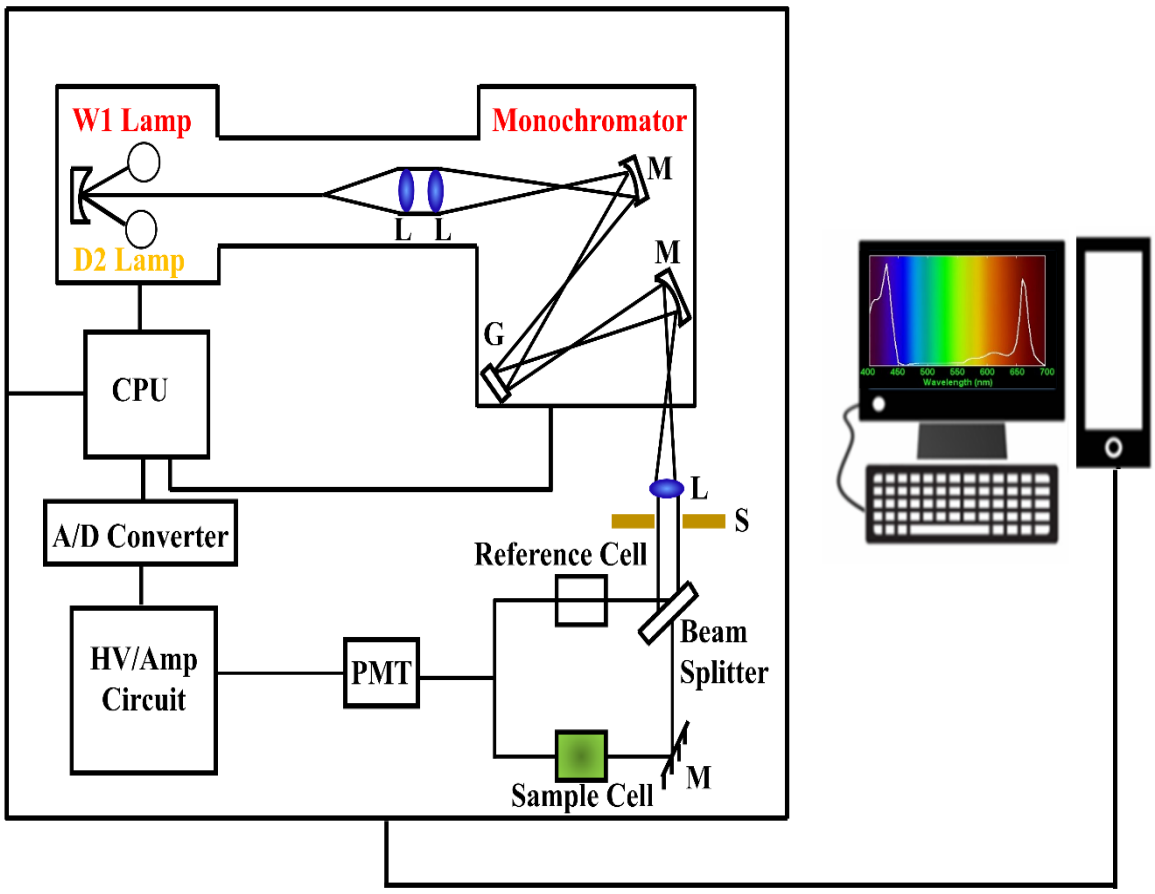

Figure 3.1: *Schematic ray diagram of an absorption spectrophotometer. Tungsten halogen (W1) and deuterium lamps (D2) are used as light sources in the visible and UV regions, respectively. M, G, L, S, PMT designate mirror, grating, lens, shutter, and photomultiplier tube, respectively. CPU, A/D converter and HV/amp indicate central processing unit, analog to digital converter and high-voltage/amplifier circuit, respectively.*

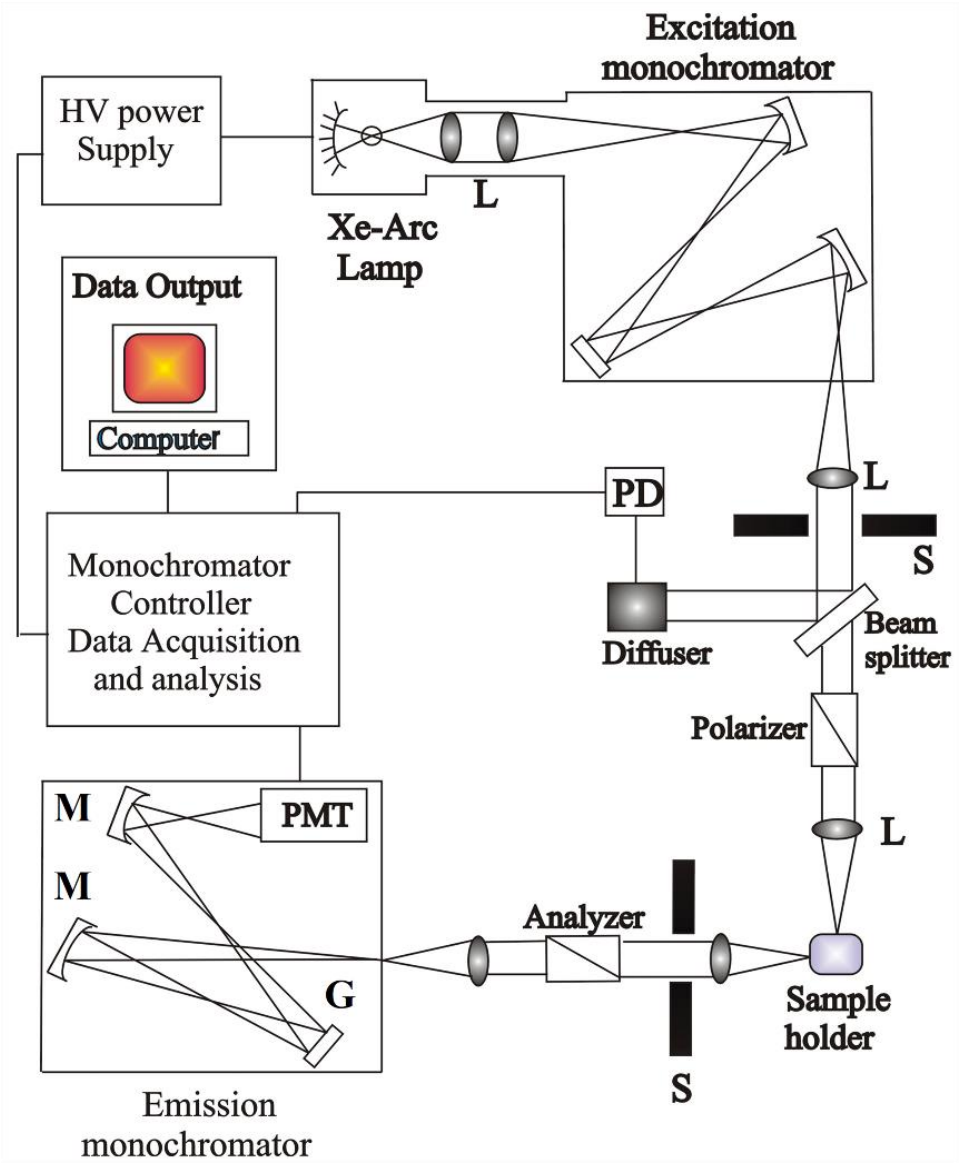

Figure 3.2: *Schematic ray diagram of an emission spectrofluorimeter. M, G, L, S, PMT, and PD represent mirror, grating, lens, shutter, and photomultiplier tube and reference photodiode, respectively.*

A Jobin Yvon FL1057 UV-VIS-NIR spectrofluorometer was used for the optical measurement of paper substrate samples, using the 60 mm integrating sphere and a solid sample holder for specular, diffuse, total reflectance, and transmittance measurements of solid samples. However, a very small amount of light entered to the detector when the light is diffusely scattered by samples such as suspended liquid, opaque solid or powders. An integrating sphere captures most of the light from the sample offering a more representative measurement of the sample. The 60 mm integrating spheres fit directly into the sample compartment and are used to measure a small number of samples, providing a

larger sampling area and thereby good signal-to-noise performance. All 60 mm integrating spheres include a Spectralon reference tile and a specular reflectance exclusion sample holder. Figure 3.3 represents the block diagram of the integrating sphere based absorption spectrophotometer setup.

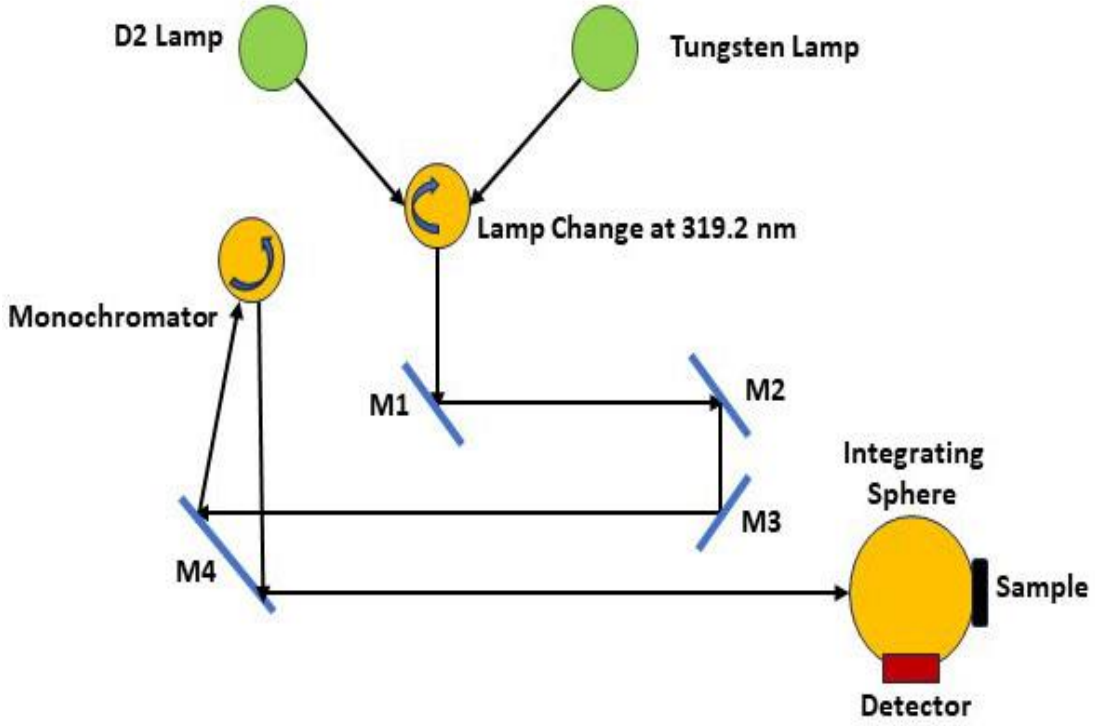

Figure 3.3: *Schematic ray diagram of integrating sphere-based absorption spectrophotometer. Tungsten halogen and deuterium lamps (D2) are used as light sources in the visible and UV regions, respectively.*

3.1.2. Time-correlated Single Photon Counting (TCSPC) Technique: All the picosecond-resolved fluorescence transients were recorded using TCSPC technique. The schematic block diagram of a TCSPC system is shown in Figure 3.3. TCSPC setup from Edinburgh instruments, U.K., was used during fluorescence decay acquisitions. The instrument response functions (IRFs) of the laser sources at different excitation wavelengths varied between 70 ps to 80 ps. The fluorescence from the sample was detected by a photomultiplier after dispersion through a grating monochromator [1]. For all transients, the polarizer on the emission side was adjusted to be at 54.70 (magic angle) with respect to the polarization axis of excitation beam.

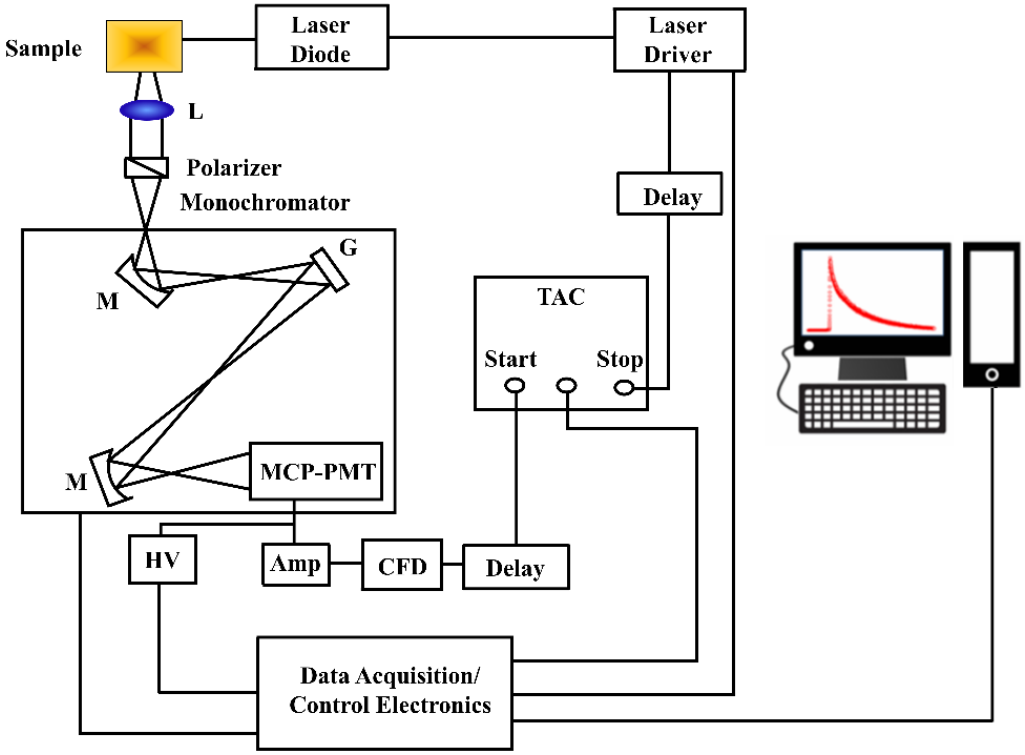

Figure 3.4: *Schematic ray diagram of a time correlated single photon counting (TCSPC) spectrophotometer. A signal from microchannel plate photomultiplier tube (MCP-PMT) is amplified (Amp) and connected to start channel of time to amplitude converter (TAC) via constant fraction discriminator (CFD) and delay. The stop channel of the TAC is connected to the laser driver via a delay line. L, M, G and HV represent lens, mirror, grating and high voltage source, respectively.*

3.1.3. Femtosecond Resolved Transients Fluorescence Measurements Using Streak Camera: Femtosecond-resolved fluorescence lifetime decay measurements were carried out by capturing the streak camera images in a custom-made steak camera-based setup (Figure 3.5). The customized streak camera system consists of 3.5 ps FWHM LASER source (Mai Tai HP 1040S from Spectra Physics, Mode-Locked Ti: sapphire LASER, 2.5 W, repetition rate 80 MHz, working temperature 20-25°C), sample compartment, monochromator (SpectraPro HRS-300, scan range 0-1500 nm, 300 mm triple grating, grating change repeatability 0.2 nm), spectra-physics second and third harmonic generator and a streak sweep unit along with a Charge Coupled Device (CCD) camera (Optronics OPTOSCOPE SC-10). The probe pulse of 440 nm, generated by doubling the 880 nm by sending 2.5 W, 880 nm mother LASER pulse to the input of the second/ third harmonic generator, was guided to the sample chamber, and the fluorescence light from the chamber was collected through a

lens and then to a polarizer. The light was then entered into the monochromator, thereafter from the exit slit of the monochromator it is guided to the photocathode of the streak camera to produce a horizontal linear spectral image [2].

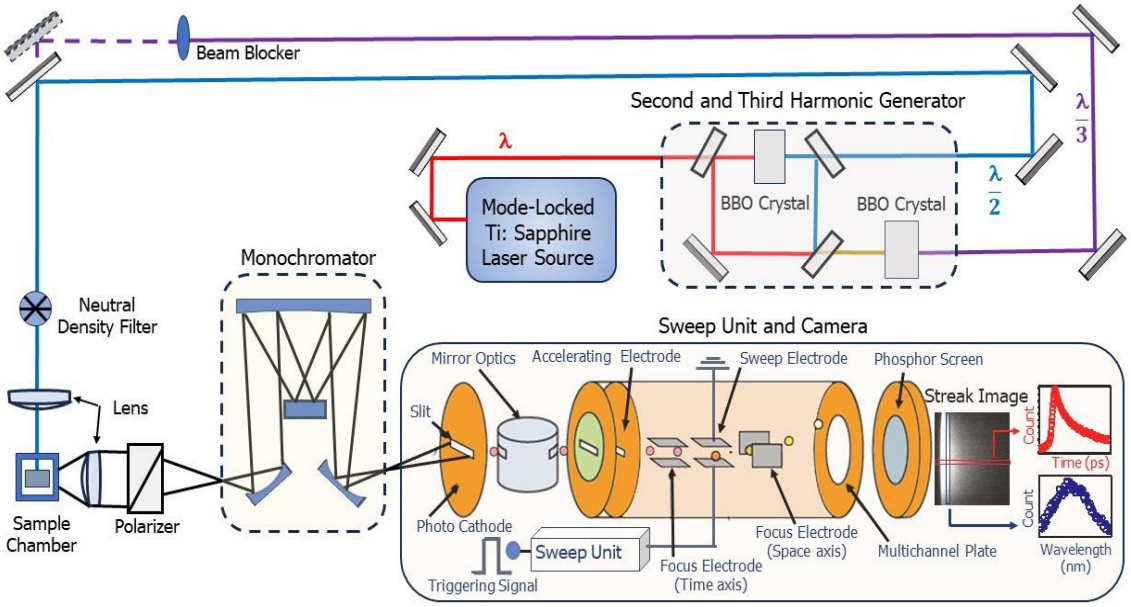

Figure 3.5: *Schematic diagram and working principle of the custom-made femtosecond resolved streak camera setup. The streak on the horizontal and vertical sides of the collected streak image represents the count versus time and count versus wavelength.*

The produced photoelectrons are then accelerated further by the electrical field and biased to the vertical direction under a variable electrical field through a streak sweep unit. These photoelectrons impinge on the multichannel plate (MCP) inside the streak camera and make multiple electrons that give a single spot on the target phosphor screen [3]. The field scan and the LASER pulse flashing are synchronized through a triggering signal from the mother LASER pulse. These spots are then recorded by CCD and the corresponding pixel information is transferred to a computer for further data processing. The streak camera produces 2-dimensional (2D) spectrum-time images (290 ps time, along x-axis for 15 ps/mm sweep rate span and 150 nm wavelength span of wavelength along y-axis). Streak image helps to detect of both wavelength and time from the same laser pulse shot. The decay of the fluorescence intensity in the excited state could be represented as $\mathbf{I(t)} = \mathbf{I_0 e^{-t/\tau}}$, where I(t) is the recorded

intensity, I_0 is the initial intensity, and τ is the fluorescence lifetime. The above expression gets changed for multiexponential fluorescence decays. Here, to fit the decay multiple decay components were used as the decays were multiexponential in nature. Detailed fitting procedures are explained in the "Principles of Fluorescence Spectroscopy" by Lakowicz [4]. Micromath Scientist software, which employs deconvolution via the iterative reconvolution technique based on a nonlinear least-squares process, was used to fit fluorescence transients.

3.1.4. Transmission Electron Microscopy (TEM): A FEI TecnaiTF-20 field-emission high-resolution TEM (Figure 3.6) equipped with energy dispersive X-ray

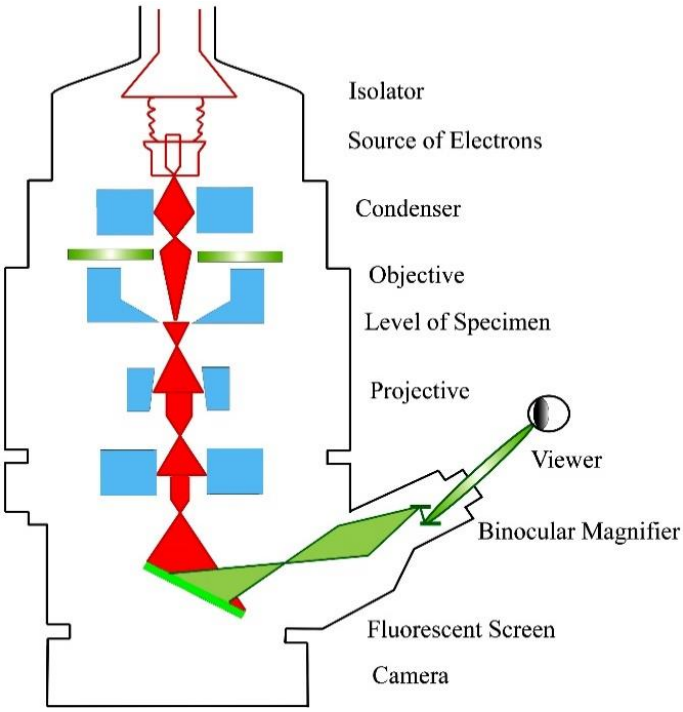

Figure 3.6: *Schematic diagram of a typical transmission electron microscope (TEM). After the transmission of an electron beam through a specimen, the magnified image is formed either on the fluorescent screen or can be detected by a CCD camera.*

(EDAX) spectrometer was used to characterize the microscopic structures of samples and to analyze their elemental composition. The sizes of the nanostructures were determined from the TEM images obtained at 200 kV acceleration voltage of the microscope. Samples for TEM were prepared by

placing a drop of the colloidal solution on a carbon-coated copper grid and allowing the film to evaporate overnight at room-temperature.

3.1.5. Scanning Electron Microscopy (SEM): Surface characterization of nanomaterials was done by scanning electron microscope FE (field emission)-SEM; JEOL. Ltd., JSM-6500F. An electron-gun is attached to the SEM and the electrons from filament are triggered by 0 KV to 30 KV voltages. These electrons go first through a condenser lens and then through an objective lens, then through an aperture and finally reach to the specimen. The high energy electrons go a bit in the sample and back again give secondary electrons. The signal from secondary electrons are detected by detector and amplified. The ray diagram of the SEM setup is shown in Figure 3.7.

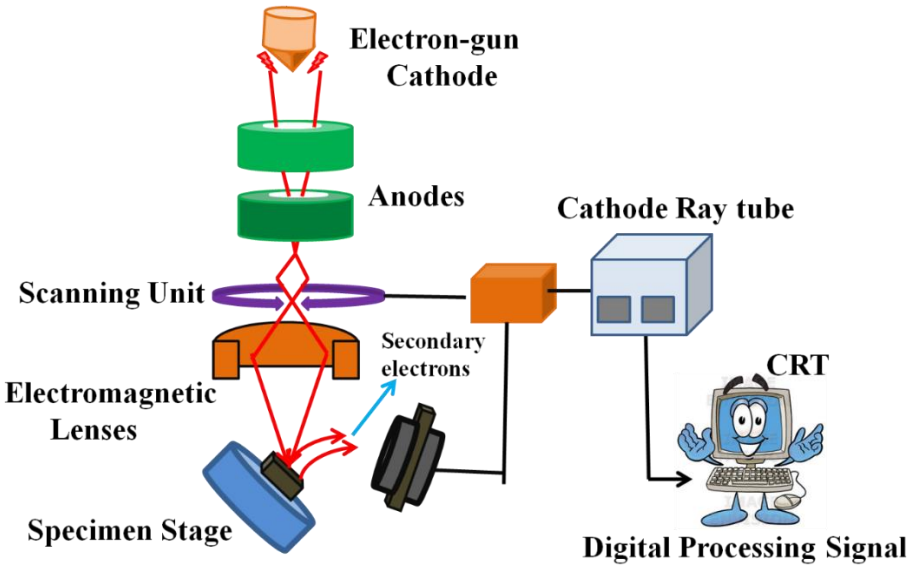

Figure 3.7: *Schematic diagram of a typical scanning electron microscope (SEM).*

3.1.6. Dynamic Light Scattering (DLS): Dynamic light scattering (DLS), also known as Photon Correlation Spectroscopy (PCS) or Quasi-Elastic Light Scattering (QELS), is one of the most popular techniques used to determine the hydrodynamic size of the particle. DLS measurements were performed on a Nano S Malvern instrument, U.K. employing a 4 mW He-Ne laser (λ= 632.8 nm) and equipped with a thermostatted sample chamber. The instrument allows DLS measurements in which all the scattered photons are collected at 173˚ scattering angle (Figure 3.8). The instrument measures the time-dependent fluctuation in

intensity of light scattered from the particles in solution at a fixed scattering angle. The ray diagram of the DLS setup is shown in Figure 3.8.

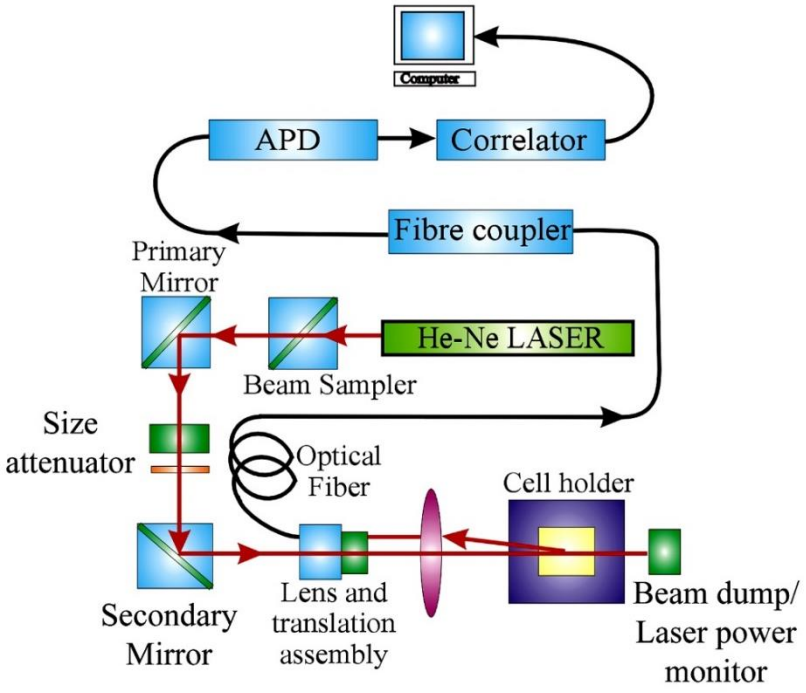

Figure 3.8: *Schematic ray diagram of dynamic light scattering (DLS) instrument. The avalanche photodiode (APD) is connected to the preamplifier/amplifier assembly and finally to the correlator. It has to be noted that lens and translational assembly, laser power monitor, size attenuator, and laser are controlled by the computer.*

It has been seen that particles in dispersion are in a constant, random Brownian motion and this causes the intensity of scattered light to fluctuate as a function of time. The correlator used in a DLS instrument constructs the intensity autocorrelation function G(τ) of the scattered intensity,

$$G(\tau) = \langle I(t)I(t+\tau)\rangle \qquad 3.1$$

where τ is the time difference (the sample time) of the correlator. For a large number of monodisperse particles in Brownian motion, the correlation function (given the symbol G) is an exponential decay function of the correlator time delay τ,

$$G(\tau) = A[1 + B\exp(-2\Gamma\tau)] \qquad 3.2$$

where A is the baseline of the correlation function, B is the intercept of the correlation function. Γ is the first cumulant and is related to the translational diffusion coefficient as, $\Gamma = Dq^2$, where q is the scattering vector and its magnitude is defined as,

$$q = \left(\frac{4\pi n}{\lambda_0}\right)\sin\left(\frac{\theta}{2}\right) \qquad 3.3$$

where n is the refractive index of dispersant, λ_0 is the wavelength of the laser and θ, the scattering angle. For polydisperse samples, the equation can be written as,

$$G(\tau) = A\left[1 + B\left|g^{(1)}(\tau)\right|^2\right] \qquad 3.4$$

where the correlation function $g^{(1)}(\tau)$ is no longer a single exponential decay and can be written as the Laplace transform of a continuous distribution G(Γ) of decay times,

$$g^{(1)}(\tau) = \int_0^\infty G(\Gamma)\exp(-\Gamma\tau)d\Gamma \qquad 3.5$$

The scattering intensity data in DLS are processed using the instrumental software to obtain the hydrodynamic diameter (d_H) and the size distribution of the scatterer in each sample. In a typical size distribution graph from the DLS measurement, X-axis shows a distribution of size classes in nm, while the Y-axis shows the relative intensity of the scattered light. The diffusion coefficient (D) can be calculated using the hydrodynamic diameter (d_H) of the particle by using the Stoke-Einstein relation,

$$D = \frac{k_B T}{3\pi\eta d_H} \qquad 3.6$$

where k_B, T, d_H, η are Boltzmann constant, temperature in Kelvin, hydrodynamic diameter, and viscosity, respectively.

3.1.7. Zeta Potential Measurement Setup: Zeta potential (ζ) is measures a effective surface charge on a charged particle. The stability of a colloidal system depends on the balance between two counteracting forces: Van der Waals, and electrical double layer (EDL). An EDL is structure that appears on the surface of an object when it is exposed to a fluid. The object might be a solid particle, a gas bubble, a liquid droplet, or a porous body. The EDL refers to two parallel layers of charge surrounding the object. The zeta potential is the electric potential in the interfacial double layer at the location of the slipping plane relative to a point in the bulk fluid away from the interface. In other words, zeta potential is the potential difference between the dispersion medium and the stationary layer of fluid attached to the dispersed particle (Figure 3.9). When an electric field is applied across an electrolyte, charged particles suspended in the electrolyte are attracted towards the electrode of opposite charge. Viscous forces acting on the particles tend to oppose this movement. When equilibrium is reached between these two opposing forces, the particles move with constant velocity. The velocity is dependent on the strength of electric field or voltage gradient, the dielectric constant of the medium, the viscosity of the medium and the zeta potential. The velocity of a particle in a unit electric field is referred to as its electrophoretic mobility. Zeta potential is related to the electrophoretic mobility by the Henry equation (Equation 3.7) [5]

$$U_e = \frac{2\varepsilon\zeta f(\kappa a)}{3\eta} \qquad 3.7$$

Where U_e is the electrophoretic mobility, ε is the dielectric constant, ζ is the zeta potential, η is the viscosity of the dispersant, f(κa) is the Henry's function. As κ is the thickness of the EDL and a is the radius of the particle, the term κa measures the ratio of the particle radius to electrical double layer thickness. The most frequently used zeta potential analyzers are based on phase analysis (PALS). In PALS, a phase variation is measured from which the electrophoretic velocity can be measured. Light from the LASER is splitted into two portions and a small portion of the initial beam (the reference beam) is re-routed such that

once recombined with the scattered beam, it is the disparity that is noted. This permits the phase shift to be examined for positive and negative mobility and relate it with ζ potential.

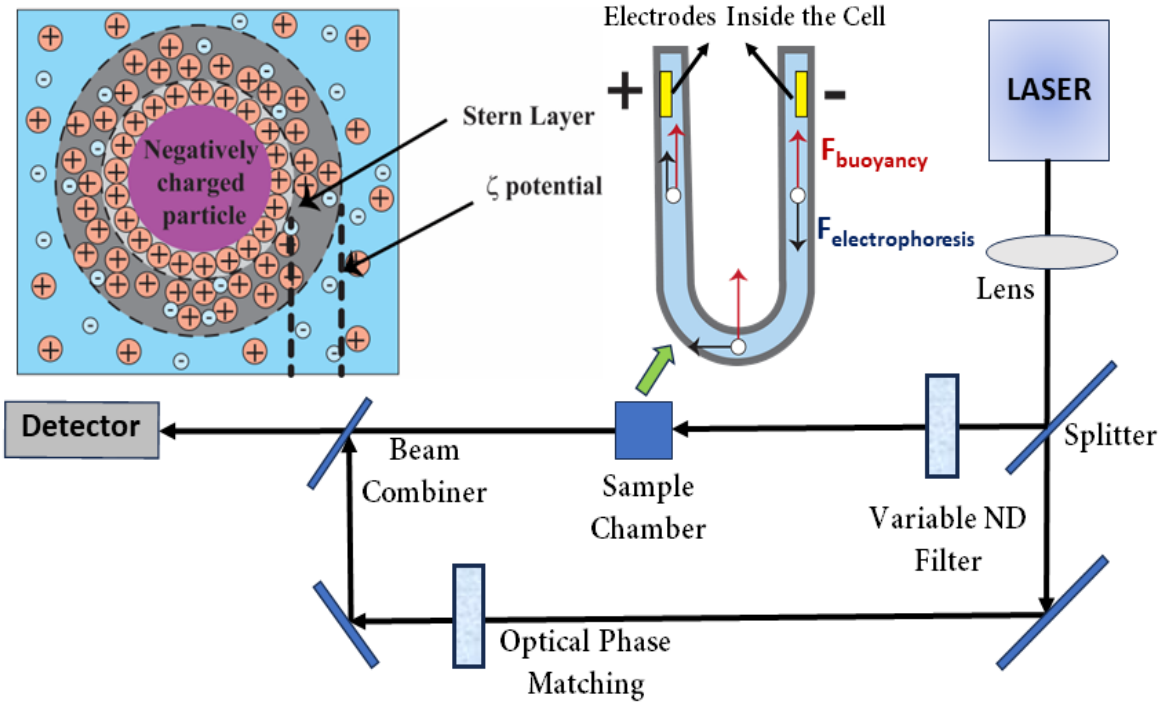

Figure 3.9: *The formation of electrical double layer and zeta potential on the surface of a charged particle. The Zeta potential measurement setup and the direction of forces inside the sample chamber.*

3.1.8. X-ray Diffraction (XRD) Measurement: XRD is a popular and a powerful technique for determining crystal structure of crystalline materials. By examining the diffraction pattern, one can identify the crystalline phase of the material. Small angle scattering is useful for evaluating the average interparticle distance while wide-angle diffraction is useful for refining the atomic structure of nanoclusters. The widths of the diffraction lines are closely related to strain and defect size and distribution in nanocrystals. As the size of the nanocrystals decreases, the line width is broadened due to loss of long-range order relative to the bulk. This XRD line width estimate the size of the particle by using the Debye-Scherrer formula,

$$D = \frac{0.9\lambda}{\beta \cos\theta} \qquad 3.8$$

where, D is the nanocrystal diameter, λ is the wavelength of light, β is the full-width half-maximum (FWHM) of the peak in radians, and θ is the Bragg angle. XRD measurements were performed on a PANalytical XPERT-PRO diffractometer (Figure 3.10) equipped with CuKα radiation (λ = 1.5418 Å at 40 mA, 40 kV). XRD patterns were obtained by employing a scanning rate of 0.02° s^{-1} in the 2θ range from 15° to 75°.

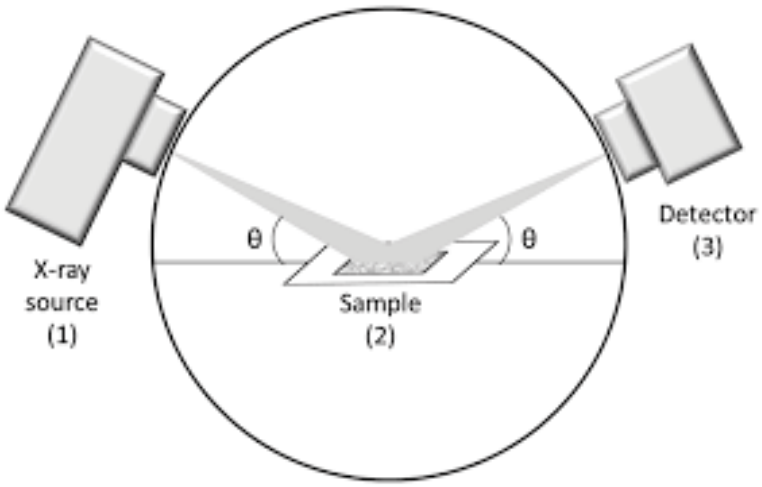

Figure 3.10: *Schematic diagram of X-ray Diffraction (XRD) instrument. By varying the angle θ, the Bragg's Law conditions, nλ=2dsinθ are satisfied by different d-spacings in polycrystalline materials. Plotting the angular positions and intensities of the resultant diffracted peaks of radiation produces a pattern, which is characteristic of the sample.*

3.1.9. Thermogravimetric-Differential Thermal Analyzer (TG-DTA) Setup: The thermogravimetric (TG) analysis was carried out using Diamond thermogravimetric (TG)-differential thermal analyzer (DTA) from Perkin Elmer. The TG determines the weight change of a sample whereas the DTA measures the change in temperature between a sample and the reference as a function of temperature and/or time. The schematic of the TG-DTA setup is shown in Figure 3.11. When a weight change occurs on the sample side, the beam holding the platinum pans is displaced. This movement is detected optically and the driving coil current is changed to return the displacement to zero. The detected driving coil current change is proportional to the sample weight change and the output is the TG signal. The DTA detects the temperature difference between the sample holder and the reference holder using the electromotive force of thermocouples.

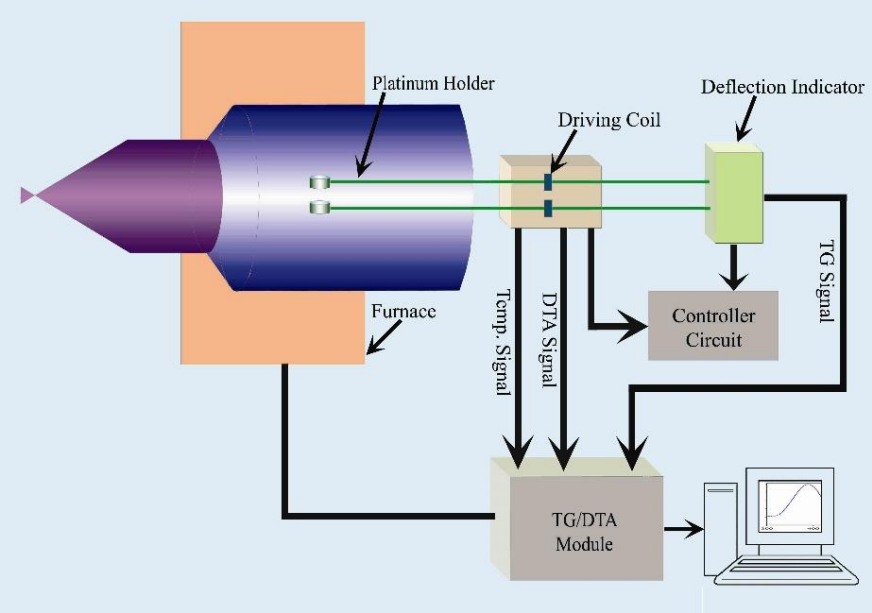

Figure 3.11: *The schematic representation of TG-DTA setup.*

3.1.10. Fourier Transform Infrared (FTIR) Measurement: FTIR spectroscopy is a technique that can provide very useful information about functional groups in a sample. An infrared spectrum represents the fingerprint of a sample with absorption peaks which correspond to the frequencies of vibrations between the bonds of the atoms making up the material. Because each different material is a unique combination of atoms, no two compounds produce the exact same infrared spectrum. Therefore, infrared spectroscopy can result in a positive identification (qualitative analysis) of every different kind of material. In addition, the size of the peaks in the spectrum is a direct indication of the amount of material present. The two-beam Michelson interferometer is the heart of FTIR spectrometer. It consists of a fixed mirror (M4), a moving mirror (M5) and a beam-splitter (BS1), as illustrated in Figure 3.12. The beam-splitter is a laminate material that reflects and transmits light equally. The collimated IR beam from the source is partially transmitted to the moving mirror and partially reflected to the fixed mirror by the beam-splitter. The two IR beams are then reflected back to the beam-splitter by the mirrors. The detector then sees the transmitted beam from the fixed mirror and reflected beam from the moving mirror, simultaneously. The two combined beams interfere constructively or

destructively depending on the wavelength of the light (or frequency in wavenumbers) and the optical path difference introduced by the moving mirror.

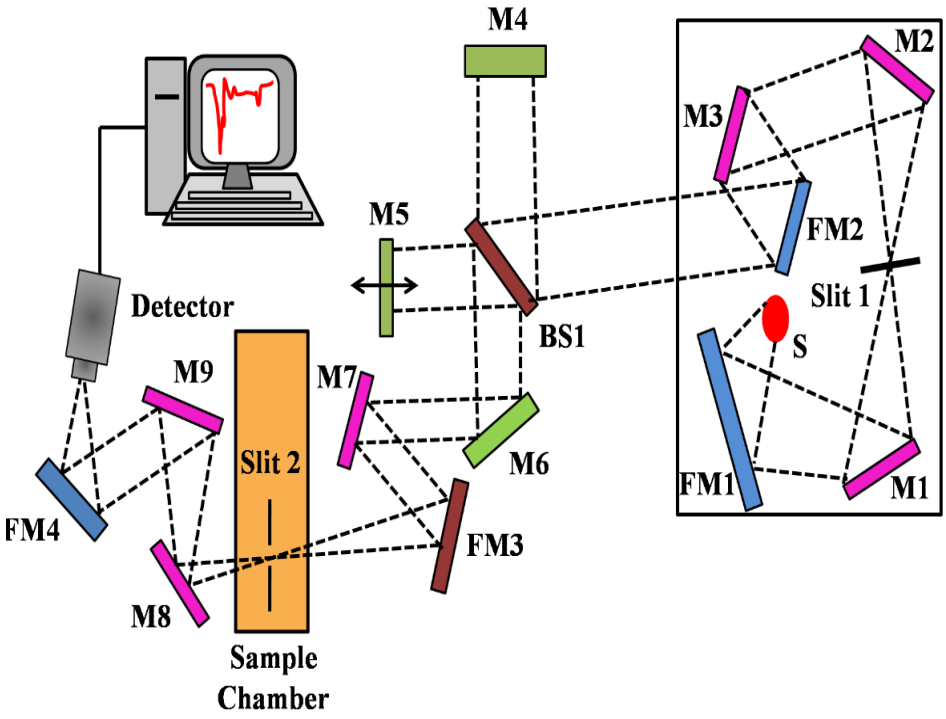

Figure 3.12: *Schematic of Fourier Transform Infrared (FTIR) spectrometer. It is basically a Michelson interferometer in which one of the two fully-reflecting mirrors is movable, allowing a variable delay (in the travel-time of the light) to be included in one of the beams. M, FM and BS1 represent the mirror, focussing mirror and beam splitter, respectively. M5 is a moving mirror.*

The resulting signal is called an interferogram which has the unique property that every data point (a function of the moving mirror position) which makes up the signal has information about every infrared frequency which comes from the source. Because the analyst requires a frequency spectrum (a plot of the intensity at each individual frequency) in order to make identification, the measured interferogram signal cannot be interpreted directly. A means of "decoding" the individual frequencies is required. This can be accomplished *via* a well-known mathematical technique called the Fourier transformation. This transformation is performed by the computer which then presents the user with the desired spectral information for analysis. FTIR measurements were performed on a JASCO FTIR-6300 spectrometer (transmission mode). For the FTIR measurements, powdered samples were mixed with KBr powder and pelletized. The background correction was made using a reference blank of KBr pellet.

3.1.11. Laser Raman Spectroscopy: Raman spectroscopy is a useful technique for the identification of a wide range of substances− solids, liquids, and gases. It is a straightforward, non-destructive technique requiring no sample preparation. Raman spectroscopy involves illuminating a sample with monochromatic light and using a spectrometer to examine light scattered by the sample.

At the molecular level photons can interact with matter by absorption or scattering processes. Scattering may occur either elastically, or inelastically. The elastic process is termed Rayleigh scattering, whilst the inelastic process is termed Raman scattering. The electric field component of the scattering photon perturbs the electron cloud of the molecule and may be regarded as exciting the system to a 'virtual' state. Raman scattering occurs when the system exchanges energy with the photon and the system subsequently decays to vibrational energy levels above or below that of the initial state. The frequency shift corresponding to the energy difference between the incident and scattered photon is termed the Raman shift. Depending on whether the system has lost or gained vibrational energy, the Raman shift occurs either as an up or down-shift of the scattered photon frequency relative to that of the incident photon. The down-shifted and up-shifted components are called, respectively, the Stokes and anti-Stokes lines. A plot of detected number of photons versus Raman shift from the incident laser energy gives a Raman spectrum. Different materials have different vibrational modes, and therefore characteristic Raman spectra. This makes Raman spectroscopy a useful technique for material identification. There is one important distinction to make between the Raman spectra of gases and liquids, and those taken from solids− in particular, crystals. For gases and liquids, it is meaningful to speak of the vibrational energy levels of the individual molecules which make up the material. Crystals do not behave as if composed of molecules with specific vibrational energy levels; instead, the crystal lattice undergoes vibration. These macroscopic vibrational modes are called phonons. In modern Raman spectrometers (LabRAM HR, Jobin Yvon), lasers are used as a photon source due to their highly monochromatic nature, and high beam fluxes

(Figure 3.13). This is necessary as the Raman effect is weak, typically the Stokes lines are ~10^5 times weaker than the Rayleigh scattered component. In the visible spectral range, Raman spectrometers use notch filters to cut out the signal from a very narrow range centred on the frequency corresponding to the laser radiation. Most Raman spectrometers for material characterization use a microscope to focus the laser beam to a small spot (<1−100 μm diameter). Light from the sample passes back through the microscope optics into the spectrometer. Raman shifted radiation is detected with a charge-coupled device (CCD) detector, and a computer is used for data acquisition and curve fitting. These factors have helped Raman spectroscopy to become a very sensitive and accurate technique.

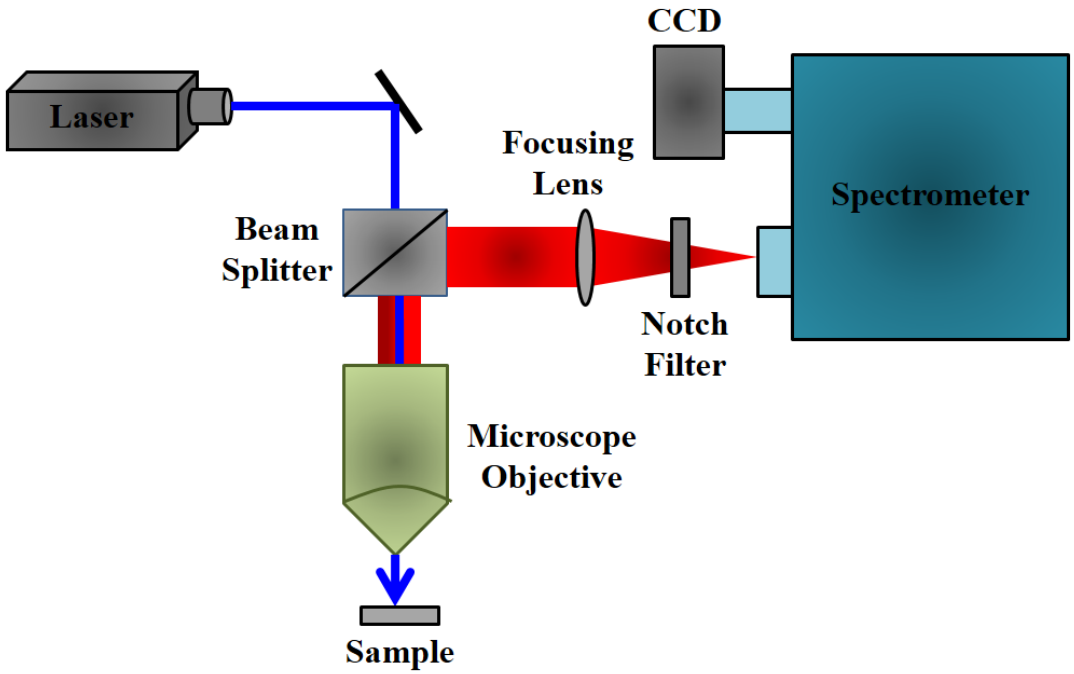

Figure 3.13: *Schematic diagram of a Raman spectrometer is shown.*

3.1.12. Linear Sweep Voltammetry (LSV): LSV is a useful technique for studying electrochemical reactions. In case of LSV, the voltage is applied at a fixed rate, the current response is plotted as a function of the applied potential. Electrochemical experiments were performed using a CHI-650E potentiostat (CH Instrument, Austin, TX). A three-electrode system consisting of a platinum working electrode, a platinum counter electrode, and a reference electrode were employed.

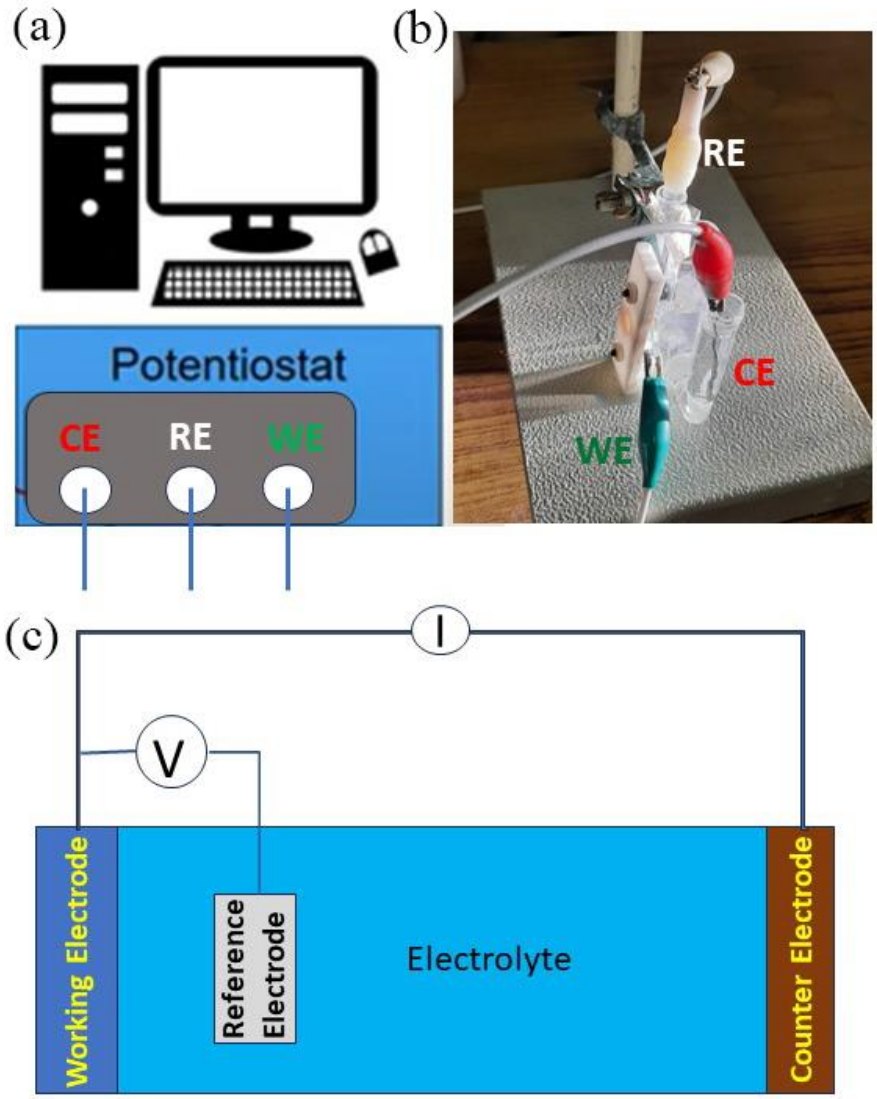

Figure 3.14: *(a) Schematic diagram of a for performing linear sweep voltammetry (LSV), (b) The three-electrode setup under white light illumination. (c) The schematic diagram of a simplified measurement circuit.*

All the potentials reported in this thesis are referenced to the Ag/Ag+ couple. Electrolyte is usually added to the sample solution to ensure sufficient conductivity. The solvent, electrolyte, and material composition of the working electrode will determine the potential range that can be accessed during the experiment. The schematic presentation of the LSV set up is shown in Figure 3.14. A typical electrochemical measurement circuit is made up of an electrochemical cell, an adjustable voltage source (V_S), an ammeter (A_M) and a voltmeter (V_M). The three electrodes of the electrochemical cell are the working electrode (WE), reference electrode (RE) and the counter (or auxiliary) electrode

(CE). The voltage source (V_S) for the potential scan is applied between the working electrode and the counter electrode. The potential (E) between the reference electrode and the working electrode is measured with the voltmeter and the overall voltage (Vs) is adjusted to maintain the desired potential at the working electrode with respect to the reference electrode. The resulting current (i) flowing to or from the working electrode is measured with the ammeter (A_M). The photoanodes, with a geometric area of 0.27 cm^2, were employed as the working electrode and exposed to the electrolyte solution under light irradiation.

Here, Pt electrode works as counter, and the semiconductor as working electrode. For the PEC water oxidation measurement, Na_2SO_4 solution (at a concentration of 0.1 M) is generally used as the supporting electrolyte, which improves the overall conductivity of the solution and eliminates the migration current. However, during the water splitting process, due to either oxygen evolution ($H_2O \rightarrow O_2$) or hydrogen evolution ($H^+ \rightarrow H_2$), the pH of the solution may get altered, and subsequently the kinetics of the process and stability of the materials get affected. Thus, to maintain the neutral aqueous solution, pH 7 phosphate buffer solution (i.e. Na_2HPO_4 and NaH_2PO_4 0.1 M) is used. Xenon lamp as a white light source (Excelitas, USA) under 100 mW cm^{-2} beam intensity and IR lamp source having a wavelength span of 600 nm to 1000 nm with a beam intensity of 470 lux was used for observing the UV-Vis and NIR activity of the photoelectrodes respectively. An ultraviolet cut-off filter (having, $\lambda > 420$ nm) is placed in front of a Xe-lamp for measuring visible response. The photoanodes (working electrode) were used with active area of 0.27 cm^2 exposed to the electrolyte solution under illumination.

3.1.13. Electrochemical Impedance Spectroscopy (EIS): Electrochemical Impedance Spectroscopy (EIS) is a powerful technique to investigate the electronic and ionic processes in dye/QD sensitized solar cells (DSSC) and photoanodes. Electrochemical impedance is usually measured by applying an ac potential to an electrochemical cell and then measuring the current through the cell. An important advantage of EIS over other techniques is the possibility of

using tiny ac voltage amplitudes exerting a very small perturbation on the system. A Nyquist plot can be made by plotting the real part of the transfer function on the X-axis and the imaginary part on the Y-axis.

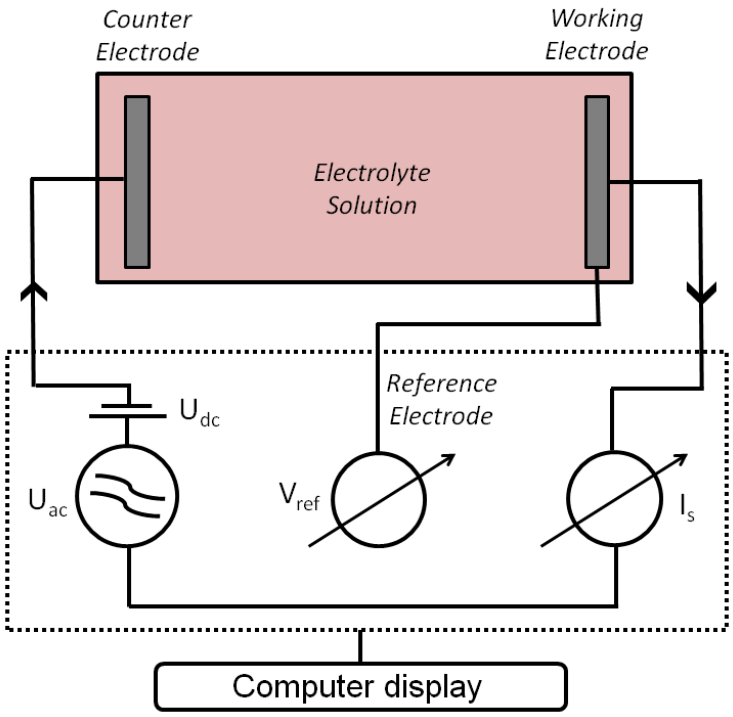

Figure 3.15: *Schematic diagram of a simplified measurement circuit for performing Electrochemical Impedance Spectroscopy (EIS).*

The Nyquist diagram for DSSC features typically three semicircles that in the order of increasing frequency are attributed to the Nernst diffusion within the electrolyte, the electron transfer at the oxide/electrolyte interface and the redox reaction at the platinum counter electrode. While, the Nyquist plot of photoanodes consist of two semicircles, corresponds to the first two processes as mentioned in case of DSSCs. From applying appropriate equivalent circuits, the transport rate and lifetime of the electron in the mesoscopic film are derived. Electrochemical impedance spectroscopy (EIS) was performed on an electrochemical workstation CHI650E (CH instruments) with a frequency range from 100 kHz to 0.1 Hz in the open circuit condition. The schematic presentation of the EIS setup is shown in Figure 3.15. All impedance measurements were carried out under a bias illumination of 100mW/cm^2. The obtained spectra were fitted using the CHI650E software in terms of appropriate equivalent circuits.

Capacitance experiments were done in an Autolab-302, PG Stat, FRA-II (Metrohm, The Netherlands) in the same three-electrode glass (borosilicate) cell configuration containing a standard Ag/AgCl as the reference electrode and Pt rod counter electrode.

3.1.14. Solar Cell Characterization: The characterization of DSSCs involves the electrical current−voltage (I−V) characteristics, incident photon to current conversion efficiency (IPCE) measurements, and photovoltage decay measurements. The current density-voltage characteristics of the cells were recorded by a keithley multimeter under irradiance of 100 mW cm^{-2} (AM 1.5 simulated illuminations, Photo Emission Tech).

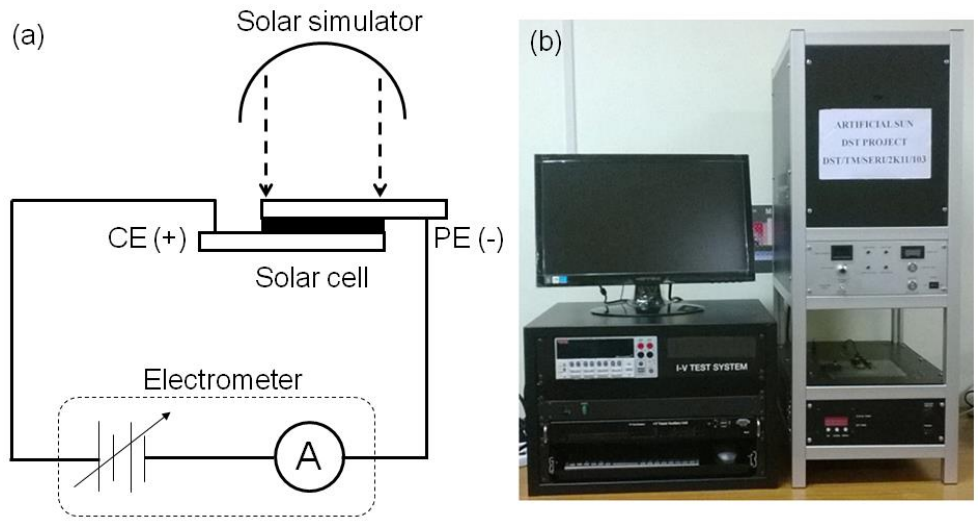

Figure 3.17: *(a) Electrical setup and (b) photograph of the solar simulator used for the solar cell characterization.*

The electrical circuit used to measure the I−V characteristics of the solar cells is shown in Figure 3.17. The short-circuit current (I_{SC}) and open-circuit voltage (V_{OC}) of the solar cells were determined from their respective I−V characteristic curves. The fill factor (FF) and efficiency (η) of the solar cells were calculated by using equations 2.20 and 2.21, respectively. The IPCE of the DSSCs was measured by using a homemade setup with a Bentham monochromator and dual light (deuterium and xenon) sources. The monochromatic light was allowed to fall on the solar cells and the respective current from the solar cell at every incident wavelength of light was measured.

Finally, the IPCE was calculated by using equation 2.23. The set up used to measure the IPCE of the solar cells is shown in Figure 3.18.

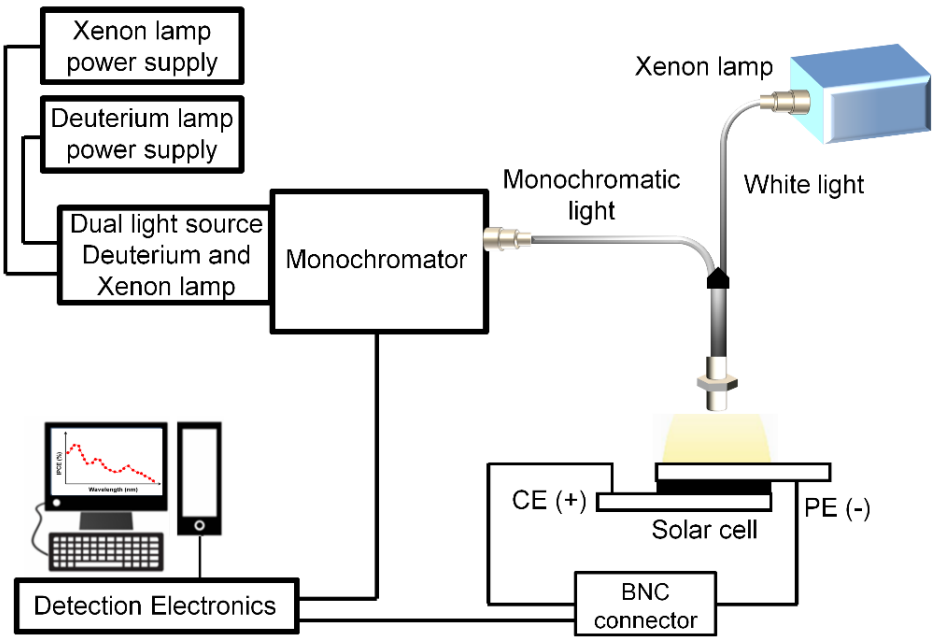

Figure 3.18: *Schematic diagram of a simplified measurement circuit for performing IPCE measurements.*

Photovoltage decay measurements were carried out after illuminating the cells under 1 Sun condition. The photovoltage decays after switching off the irradiation were monitored by an oscilloscope (Owon) through computer interface as shown in Figure 3.19. The decays were fitted with exponential decay functions.

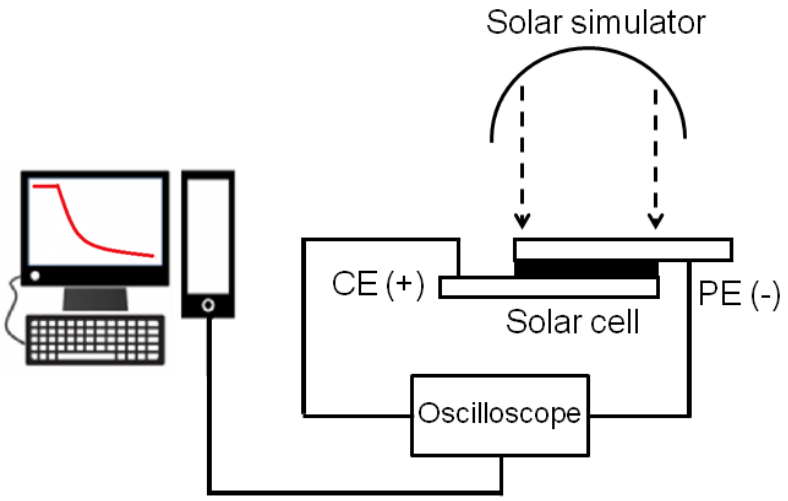

Figure 3.19: *Schematic diagram of the photovoltage decay measurement setup.*

3.1.15. Fiber-Optic Coupled System for Photocatalytic Measurements: Increased sensitivity in the signal detection in the presence of strong ambient light in our experimental setup lies on the confocal geometry of the excitation and detection sides [6]. As shown in the schematic ray-diagram of the experimental setup (Figure 3.20) the excitation fiber (400 µM core diameter) carrying laser light is connected to an optical coupler (Ocean Optics, USA, model: 74-UV) in order to focus excitation light at the middle of a sample holder, which is an all-side polished quartz-cuvette from Starna cells (U.S.A).

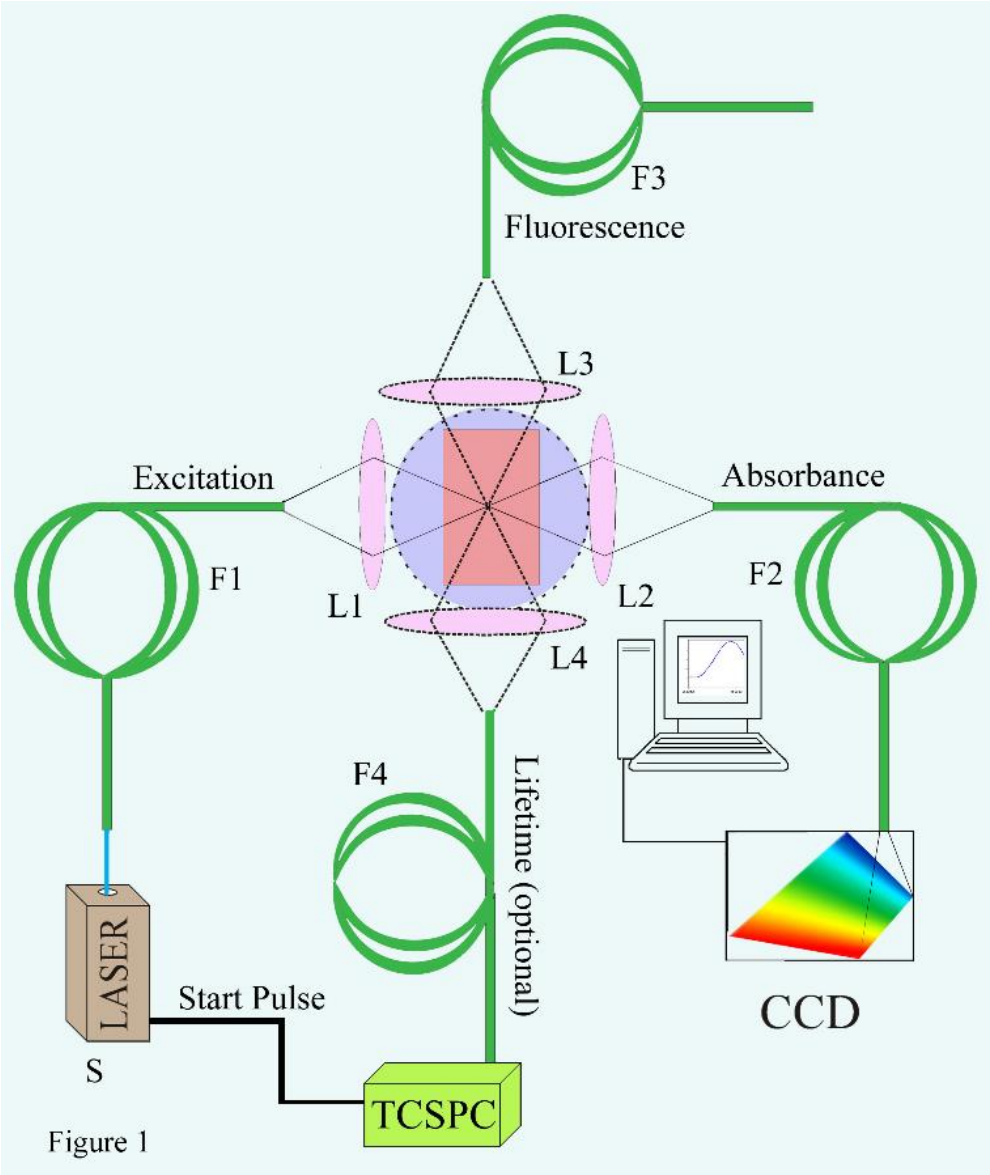

Figure 3.20: *Schematic diagram of the universal setup. S is the source, F1-F4 are the optical fibers, L1-L4 are the fiber coupler lenses, the violate circle represents the ambient light around the sample (reddish rectangle). CCD is the photo-signal detector, connected with computer.*

The numerical aperture (NA) of the excitation fiber (NA=0.45) and focal length of the optical coupling lens (0.5 cm) systems are to achieve out-of-focus rejection by two strategies: firstly by illuminating a single point of the specimen at any one time with a focused beam, so that illumination intensity drops off rapidly above and below the plane of focus and secondly by the use of optical fiber as a collecting unit with similar coupling lens so that light emitted away from the point in the specimen being illuminated is blocked from reaching the detector. The collection fiber is arranged in 'I' geometry and connected with the commercially available CCD based miniaturized spectrograph (Ocean Optics, USA, model: HR4000) in order to measure absorption of the sample of interest. More flexibility in the measurement can also be achieved by using Shimadzu spectrophotometer (UV-2600) or Jobin Yvon (Fluoromax-3) fluorimeter to measure absorption and photoluminescence, respectively. In order to establish the fact that the absorption of a sample can be measured in presence of strong ambient light effectively, we have placed the quartz cell containing test sample on a home-made UV bath (8W).

3.2. Sample Preparation: In this section the different sample preparation methods have been discussed.

3.2.1. Chemicals Used: The chemicals and spectroscopic probes were procured from the following sources. Analytical-grade chemicals were used for synthesis without further purification. Deionized (DI) water, obtained from Millipore, was used to prepare all aqueous solutions. The probes RK1 (Solaronix, Switzerland), protoporphyrin IX (Sigma Aldrich), squarine (Solaronix, Switzerland), and dichlorofluorescen diacetate DCFH-DA (Sigma) have been used. nm), TiO_2 NPs (~ 21 nm), Al_2O_3 NPs (~ 40 nm) were purchased from Sigma Aldrich. Trisodium citrate ($Na_3C_6H_5O_7$), gold chloride ($HAuCl_4$), silver nitrate ($AgNO_3$), lead oxide and all other metal salts (either in the form of chloride or nitrate) were purchased from Sigma Aldrich. PbS quantum dots were purchased from Evident Technology. Carboxylic acid functionalized multiwall carbon nanotubes (MWCNT, powder, average size; L 9.5 nm × 1.5 μm) was purchased from Sigma

Aldrich. Other solvents such as toluene, dimethyl sulfoxide (DMSO), ethanol; acids such as nitric acid (HNO_3), and hydrochloric acid (HCl) were purchased from Merck. Whatman filter papers for measurement on the paper substrate were purchased from Sigma Aldrich.

3.2.2. Synthesis of Citrate-functionalized Silver Nanoparticles (AgNPs): Citrate functionalized silver nanoparticles (AgNPs) have been synthesized in aqueous solution by reduction method taking $NaBH_4$ as a reducing agent [7]. Briefly, 1 mL of 5mM $AgNO_3$ was added to 16 mL of 1 mM trisodium citrate under constant stirring in an ice/water bath at around 0°C, to this solution 100 µL of a freshly prepared 5 mM $NaBH_4$ over 5 minutes (min). The colourless solution gradually changed its colour upon the addition of the reducing agent and finally gained an intense yellow colour. This yellow-coloured colloidal solution was kept under stirring for 2 h at almost 0^oC. The as-prepared citrate functionalized silver NPs were stabilized for several weeks.

3.2.3. Synthesis of Citrate-functionalized Gold Nanoparticles (AuNPs): Stock solution of 100 mM of $HAuCl_4$ was prepared, from this stock 200 µl was added to distilled water and the solution was heated to boiling. In this boiling solution 400 µl of 0.5 M trisodium citrate was added and kept for heating for 15-20 minutes until the colour of the solution changes from yellow to colourless to finally gradually wine red indicating the formation of AuNPs. Here, trisodium citrate was used as reducing as well as stabilizing agent. This solution is ready for use without further purification and is stable of many days.

3.2.4. Procedure for Pb^{2+} Induced Sensing Experiments Using AgNPs and AuNPs: All the UV-Visible (UV-Vis) absorbance spectra measurements of the AgNPs were carried out at room temperature. For Pb^{2+} measurement purposes, the required amount of as-prepared colloidal solution of the AgNPs (nanosensor) was added in the water maintaining the net volume equal to 2 mL. Stock solutions of varying concentrations of Pb^{2+} ions were prepared (suitable amount of lead nitrate $Pb(NO_3)_2$ was added to Millipore water to prepare the

Pb^{2+} aqueous solution) and every time the same amount of the sensor was added into it. The temporal evolution of the plasmon resonance bands of AgNPs was also monitored and for this purpose, the mixture samples were stood for a definite time.

3.2.5. Methods for Acid Digestion of the Real World Lead samples: The real lead samples in atmosphere were generally found in the form of lead dioxide samples. The collected lead samples were acid-digested using a mixture of 12 ml of HNO_3 and 4 ml of HCl and allowed to boil for 1 h [8]. This dry Pb residue was then dissolved in water and pH balanced to around 6.5. This Pb extract was then filtered for further experimental use.

3.2.6. Fabrication and Design of the Paper-based AgNPs and AuNPs Impregnated Sample Strips and Pb^{2+} Drop-caste Method: We have used Whatman filter paper (grade 4) as the base for drop casting the AgNPs nanosensor. To measure the colorimetric changes of the sample for different Pb concentrations, in retro-reflective way, the filter paper bases were supported with a reflecting layer consisting of an aluminium foil layer at the bottom. These whole fabricated filter paper pads along with a reflecting layer were abbreviated as RPP (reflecting paper pad). These RPPs were further used for drop-casting of the nanosensor. The effective area of the RPPs were kept to be 1 cm^2 for all the cases. All the information from the RPPs were collected in a retro-reflected geometry. For that every time ~30 mL of the prepared ion (heavy metal) solutions were dropcasted on RPPs and then the 20 mL of the sensor was added into it. The paper strips were then kept for 15 minutes so that the prominent colour change on RPPs were observed. For invitro measurement purposes, the required amount of prepared colloidal AgNPs solution (nanosensor) was added in the 2 mL of the Pb aqueous solutions.

For AuNPs, the information from the paper substrate were collected in transmission geometry. For that, every time 20μL of the prepared ion (heavy

metal) solution and 50μL of ~180nM of AuNPs were mixed priorly and then 5 μL of solution was dropcasted on the paper substrate for measurement.

3.2.7. Procedure for AgNPs-Pb^{2+} Complex Spectral Monitoring Through Diffuse Reflectance Spectra (DRS) Measurement: We have used a Xenon lamp source (HPX-2000) (Ocean Insight) starting from 200 to 2000 nm, a spectrometer (HR4000) (Ocean Optics), and a lab-grade diffuse reflectance probe (Ocean Optics, Florida) to design the experimental setup. The reflectance probe includes one excitation fibre, surrounded by six collection fibres. The light from the source is transmitted through the excitation fibre and six collection fibres collect the retro reflected light from the sample under test and send the signal to the spectrometer. A LabVIEW (software) based graphic user interface was developed for data acquisition and data analysis.

3.2.8. Synthesis of the Sensitizer Entrapped Surfactant Systems: Three types of surfactant solutions CTAB, SDS and Triton X-100 were prepared in an aqueous medium above their critical micellar concentration. Stock solutions of 40 mM for each micelle (CTAB, Triton X-100 and SDS) were prepared by adding the required amount of surfactant in ultrapure water under constant stirring for 10 minutes. This stock solution of 40 mM micellar solution has been used for future analysis. At first stock solutions of 0.15 mM of the sensitizers (PPIX and SQ2) were prepared separately in three micellar environments. For that required amount of the sensitizers were added in 10 ml of the 40 mM previously prepared surfactant solution and these solutions were put under constant stirring for 2 h at room temperature. After continuous stirring, the colourless surfactant solutions were changed gradually to coloured solutions indicating the formation of surfactant conjugated sensitizer system. These sensitizers conjugated micellar solutions were then stored in dark for further use.

3.2.9. Preparation of DCFH Assay: DCFH solution was prepared [9] by mixing 0.5 mL of 1.0 mM DCFH-DA with 2.0 mL of 0.01 N NaOH in methanol. The de-esterification reaction was continued for 30 min at room temperature under

stirring condition. Finally, the mixture was neutralized with 10 mL of 25 mM NaH_2PO_4 at pH 7.4. This solution was stored in dark and used further to perform the assay.

3.2.10. Quantitative Estimation of Reactive Oxygen Species (ROS) Generation in the Sensitizer Entrapped Surfactant System by DCFH Assay: DCHF assay for all the samples and controls were carried out in a total volume of 2.0 mL micelle water that contained 10 µL of DCFH solution and the sensitizer-micelle solutions were added in such a volume so that the effective optical density at the peak of the sensitizer remains 0.2. The assay was performed for 10 mins under dark and then 40 mins under light irradiation of different wavelength and intensity. A white light (~11830 lux), red light (~780 lux) and blue light (~20,000 lux) LEDs were used for the irradiation.

3.2.11. Methods for Photo Remediation Activity in Sensitizer Entrapped Surfactant System: The photo remediation activity of the CTAB_sensitizer system under visible light illumination was examined by monitoring the time-dependent photo-decomposition of the model pollutant phenol red (PR), a negatively charged heterocyclic structure having a sulphur trioxide attaching group. The decrease in absorption intensity of the PR was recorded with respect to time and the percentage of degradation was measured accordingly.

3.2.12. Preparation TiO_2-Au Nanohybrid and of Sensitization of RK1 on TiO_2 Al_2O_3, NPs, TiO_2-Au, Al_2O_3-Au Nanohybrid Surface: The RK1_TiO_2 nanohybrid was synthesized by addition of TiO_2 NPs to 10 mL of 0.3 mM solution of RK1 in toluene under constant magnetic stirring at room temperature (RT) for 12 hr. The solution was then put under centrifugation for 30 minutes and successively washed with toluene four times so that no extra unreacted dye remained in the sample. The Au decorated TiO_2 nanoparticles were prepared by the chemical reduction method of gold (III) on TiO_2 nanoparticle surface. At first aqueous colloidal suspension of TiO_2 is prepared by sonication for 20 min. Then 20µL of 25mM of $HAuCl_4$ was added under constant stirring for 5 minutes. A

stock solution 10 mM of $NaBH_4$ was prepared by adding required amount of $NaBH_4$ salt to 2 mL of water. From this freshly prepared stock, 200µl of $NaBH_4$ has been added to the stirring solution of TiO_2 and $HAuCl_4$. The reaction was allowed for further 30 minutes. The as-prepared Au decorated TiO_2 nanohybrid (TiO_2_Au) was centrifuged and dried at ~80^oC. The synthesis of RK1_TiO_2_Au nanohybrid was done prepared by addition of the Au_TiO_2 nanohybrid to 10 mL of 0.3 mM solution of RK1 in toluene under constant magnetic stirring at RT for 14 hr. After that solution was centrifuged for 20 min and successively washed with toluene three to four times so that no extra unreacted dye remains in the system.

The RK1_Al_2O_3 and RK1_Al_2O_3_Au nanohybrids were synthesised using the same procedure as RK1_TiO_2, only instead of TiO_2, Al_2O_3 has been used.

3.2.13. Preparation of Dye-sensitized Photoanodes and Fabrication of Dye-Sensitized Solar Cells: For DSSCs fabrication, the counter electrodes were prepared by casting 5 mM of chloroplatinic acid (prepared in isopropanol) on FTO followed by thermal deposition at 385^oC for 30 min. These Pt counter electrodes were then placed on top of the dye-sensitized photoanode es and assembled with the help of a sealing layer of 60 µm thick Surlyn. An electrolyte couple I/I^{3-} composed of 0.5 M, 0.05 M iodine (I_2), lithium iodide (LiI) and 0.5 M 4-tert-butylpyridine (TBP) in acetonitrile was filled between the inter electrode space through the predrilled small holes made on the counter electrode. The active area of measurement was kept to be 0.64 cm^2.

The photoanodes were fabricated using the following procedure. The mixer was stirred for 5 h. Then triton X-100 was added to the mixer and stirred for a few minutes. Finally, the paste was coated on a conducting side of the ITO using the doctor-blade technique. The films were dried at room temperature, were put for annellation at 450^oC for 1 hr in a muffle furnace then allowed to cool at 80^oC and then photoactivated by immersing them in dye solution for the duration of 24 hrs.

The photoanodes were withdrawn from the solution and immediately rinsed with ethanol. The two electrodes were placed on top of each other with a single

layer of thick Surlyn (Solaronix) as a spacer between the two electrodes as mentioned above. The dye solution we used was prepared in toluene having an optimized RK1 concentration of 0.3 mM.

3.2.14. Quantitative Estimation of Reactive Oxygen Species (ROS) Generation in the Dye-sensitized Nanohybrids: Using steady-state fluorescence emission after excitation at the frequency of 488 nm, the fluorescence intensity of DCF at about 520 nm can be measured. The experiment is in a 1 cm optical path length quartz cuvette containing 3 mL of solution having 1 g L^{-1} concentration of each nanohybrid. Fresh DCFH was introduced to the system every hour during the recyclability assay, which was carried out three times in a row. Warm white light (Havlock, 12W) of 42800 Lux was used to illuminate the samples.

3.2.15. Methods for Photocatalysis Test in Dye-sensitized Nanohybrids: Under visible light illumination, the photocatalytic activity of the nanohybrids was tested to detect the photo-decomposition of acridine orange (AO), a model pollutant with a nitrogen-containing heterocyclic structure in aqueous media. The degradation of AO under light illumination (initial concentration C = 0.5 X 10^{-4} M) was performed in a 1 cm optical path length quartz cuvette containing 3 mL of solution having 1 g L^{-1} concentration of each nanohybrid. The solution was illuminated with a warm white light (Havlock, 12W) of 42800 Lux. The degradation percentage (%DE) of AO in 1 h was calculated by using the equation.

$$\% DE = \frac{I_0 - I}{I_0} \times 100 \qquad 3.9$$

where I_0 represents the initial absorption intensity of AO at its maximum absorbance peak, λ_{max} = 491 nm and I represents the absorption intensity after getting irradiated for 1 h.

3.2.16. Preparation Methods of TiO_2-MWCNT, TiO_2-PbS QD Hybrid and PbS-TiO_2-MWCNT Tri-hybrid Materials: The TiO_2-MWCNT nanocomposite was prepared by continuously stirring 2 mg of MWCNT 50 mg of TiO2 in water for 12 hrs. The hybridization of PbS quantum dots (QDs) with TiO_2 nanoparticles

(NPs) and MWCNT was accomplished through continuous stirring of a 100 mL stock colloidal solution containing PbS QDs and 10 mg of TiO_2 NPs or TiO_2-MWCNT hybrid in 5 mL of toluene. This procedure was carried out in the dark at room temperature for a duration of 6 hours. The solution containing colloidal hybrid solution was then undergone centrifugation, and the resulting clear supernatant was separated from the prepared hybrid nanocomposite. Subsequently, the PbS-TiO_2 and PbS-TiO_2-MWCNT hybrid material was obtained through three to four successive washes with toluene solvent, collected after drying in a water bath.

3.2.17. Quantitative Estimation of Reactive Oxygen Species (ROS) Generation in the PbS-QD Sensitized Nanohybrids: The DCFH oxidation experiment utilized the DCFH marker, prepared through the de-esterification procedure from the DCFH-DA probe, as reported in prior literature[10]. The oxidation of DCFH results in the generation of fluorescent DCF in the presence of light. The concentrations of the samples were checked from the optical density (OD) of absorption spectra before ROS measurement. Fluorescence emissions at 525 nm were recorded upon excitation at 488 nm. Reactive oxygen species (ROS) experiments were conducted in the absence of light for 10 minutes, followed by exposure to irradiation of 470 lux with a wavelength span from 600 to 1000 nm for 70 minutes.

3.2.18. Preparation of PbS-QD Sensitized Photoanodes for Photoelectrochemical Measurements: The photoanodes thin film was first prepared following the standard doctor-blading protocol [11, 12]. At first, the respective colloidal paste of TiO2 and TiO2-MWCNT nanocomposite was uniformly spread over the FTO substrate and allowed to dry at 60^0C. The process was repeated several times to achieve the 500 nm thickness of the film. Subsequently, the photo-electrodes were annealed at 350^0C for 1 hour in atmospheric conditions. Thereafter, followed by cooling to 80°C then photo-activated by immersion in a 10 ml PbS QD solution in toluene for a period of 18 hours and by the process of adsorption, the TiO_2 and TiO_2-MWCNT films were

sensitized to form the respective PbS-TiO_2 and PbS-TiO_2-MWCNT films. The film preparation procedure makes the fact more evident that PbS QDs are adsorbed on top of the TiO_2-MWCNT nanocomposites.

References

[1] D. V. O'Conner, D. Philips, Time correlated single photon counting, *Academic Press*, London, 1984.

[2] R. Krishnan, H. Saitoh, H. Terada, V. Centonze, B. Herman, Development of a multiphoton fluorescence lifetime imaging microscopy system using a streak camera, *Rev. Sci. Instrum.* 74 (2003) 2714.

[3] M. Komura, S. Itoh, Fluorescence measurement by a streak camera in a single-photon-counting mode, *Photosynth. Res.* 101 (2009) 119.

[4] J. Lakowicz, Kluwer Academic, *New York* (1999).

[5] A. J. Bard, L. R. Faulkner, H. S. White, Electrochemical methods: Fundamentals and applications, *Wiley*, Oxford, 2022.

[6] S. S. Sinha, P. K. Verma, A. Makhal, S. K. Pal, A Versatile fiber-optic coupled system for sensitive optical spectroscopy in strong ambient light, *Rev. Sci. Instrum.* 80 (2009) 053109.

[7] C. Flores, C. Diaz, A. Rubert, G. Benítez, M. Moreno, M. F. L. de Mele, R. Salvarezza, P. Schilardi, C. Vericat, Spontaneous adsorption of silver nanoparticles on Ti/TiO2 surfaces. Antibacterial effect on Pseudomonas aeruginosa, *J. Colloid. Interface Sci.* 350 (2010) 402.

[8] A. Halder, D. Shikha, A. Adhikari, R. Ghosh, S. Singh, T. Adhikari, S. K. Pal, Development of a nano-sensor (FeNSOR) based device for estimation of iron ions in biological and environmental samples, *IEEE Sens. J.* 20 (2019) 1268.

[9] J. Patwari, H. Joshi, H. Mandal, L. Roy, C. Bhattacharya, P. Lemmens, S. K. Pal, Exciton dissociation in an NIR-active triohybrid nanocrystal leading to efficient generation of reactive oxygen species, *Phys. Chem. Chem. Phys.* 21 (2019) 10667.

[10] X. Chen, Z. Zhong, Z. Xu, L. Chen, Y. Wang, 2′,7′-Dichlorodihydrofluorescein as a fluorescent probe for reactive oxygen species measurement: Forty years of application and controversy, *Free Radic. Res.* 44 (2010) 587.

[11] S. Sarkar, A. Makhal, T. Bora, S. Baruah, J. Dutta, S. K. Pal, Photoselective excited state dynamics in ZnO–Au nanocomposites and their implications in photocatalysis and dye-sensitized solar cells, *Phys. Chem. Chem. Phys.* 13 (2011) 12488.

[12] M. K. Nazeeruddin, A. Kay, I. Rodicio, R. Humphry-Baker, E. Müller, P. Liska, N. Vlachopoulos, M. Grätzel, Conversion of light to electricity by cis-X_2 bis (2, 2'-bipyridyl-4, 4'-dicarboxylate) ruthenium (II) charge-transfer sensitizers (X= Cl-, Br-,I-, CN-, and SCN-) on nanocrystalline titanium dioxide electrodes, *J. Am. Chem. Soc.* 115 (1993) 6382.

CHAPTER 4

Spectroscopic and Theoretical Studies on Ligand Capped Metal Nanohybrids for Environmental Pollution Monitoring

4.1. Introduction:

As the industries and population are growing rapidly, the amount of environmental pollution is increasing exponentially with every passing day. Substantial progress has yet to be achieved in eliminating or combating environmental pollution, hence several field deployable, low-cost techniques are proven to be of great help [1, 2] for pollution monitoring.

Plasmonic nanomaterials being one of the emerging classes of optically active nanomaterials not only appealing for basic studies, but have revolutionary application in several other fields including energy conversion, electronics, photonics, sensors and biomedical applications [3-5]. The plasmonic nature of metallic nanostructures exhibit a special property known as 'Localized Surface Plasmon Resonance' (LSPR) through the coherent electron oscillations in presence of photon incidence, which can bring the enhancement in the optical cross-sections, hot carrier generation, and so forth, at their surface [6]. The LSPR modes are known to be highly sensitive to the external dielectric environment of nanoparticles [7]. Modulation of LSPR band based on its sensitivity to the nearby medium has led to development of several nanosensors. Nanosensors based on nanoparticles (NPs) have proven to meet the age-old challenges in the field of chemical and biological sensing, as well as to tackle tremendous environmental pollution due to their highly sensitive and tuneable LSPR bands to its external environment [8]. Especially there are tremendous effort has been made in cleaning and monitoring of industrial as well as mining waste which contains high amount of various toxic and nonbiodegradable heavy metal pollutants (Hg, Cd, Zn, Ni, As, Pb etc.) [9, 10]. Among various pollutants, nonbiodegradable toxic heavy metal ions such as lead, cadmium, arsenic have put serious

ecosystem related problems due to their persistent nature in the environment, ability to enter food chain and high toxicity . Of these, our specific focus is on the detection of Pb^{2+} ions, which is one of the most toxic and worrisome pollutants [11]. Lead is of particular interest, because of its toxicity and its widespread presence in the environment and appraised as a priority pollutant [12]. It is one of the devastating industrial pollutants, which enters the ecosystem through soil, air and water. Here, lead (Pb) is our primary concern due to its low melting point, durability, hence, widely used as a multipurpose construction material and also used as a gasoline additive in automobiles [11]. Despite its use as an important industrial material, not only Pb has drastic ecological risk even at lower level of exposure but also exerts adverse effects on human health [13, 14]. Although the use exposure of Pb has been restricted since the very much than 1960s, it is found that even lower exposure can affect the brain development and nervous system, especially among children. While in adults it causes heart diseases, blood pressure, neurological disorder etc. [15]. Today the major exposures of lead into the environment are through human's action as mining, grinding and crushing of the ores, lead-based products such as lead-acid batteries [16], paints, cosmetics [17-19] petrol additive, lead pipes and industrial wastage [11, 20]. The industrial waste water contains upto 500 mg/L of Pb(II) which is very high compared to the Environmental Protection Agency (EPA) recommendations which is 0.05 mg/L [21]. So, it is highly desirable to detect lead from industrial waste-water before discharging into the environment. Greater concern is the emission of lead to the air in the form of fine aerosol particulates which can travel very lager distances far from their origin. Lead pollution in air can occur through automobiles, burning coal-based fuel, roasting of minerals, lead based fire crackers specially the situation is alarming in developing countries [22, 23]. Thus, there is an urgent need for constant monitoring of lead level in air and in industrial wastes and segments as well.

Nanomaterials of noble metal such as silver (Ag) and gold (Au) nanoparticles are the two most widely used plasmonic nano-markers with various surface modification to detect environment polluting heavy metals from different

systems, possessing a high optical absorbance cross-section in UV-Visible region [24, 25]. These two plasmonic nanoparticles (NPs) are extensively studied for environmental sensing applications due to their highly selective and sensitive tuneable LSPR properties [26]. The presence of heavy metal ions in the system led to the self-aggregation or agglomeration of the NPs into different non-spherical geometry and clusters, driven by forces such as van der Waals interaction, ligand coupling, electrostatic attraction and repulsion between the charged particles, etc [27-30]. As a result, the size shape, and physical environment of the NPs change drastically, which leads to a change in the shape of the LSPR band [31]. It is possible to detect these spectral changes using simple UV-Vis spectroscopy, or even in naked eye as a crucial tool for heavy metal ion detection [32, 33]. Along with spectroscopy, several microscopy techniques such as electron and scanning microscopy have been regularly used for the visualization and characterization of the formed NP aggregates [34].

Despite substantial progress made by engineers, scientists and environmentalists to combat environmental pollution; more facile, low-cost, field-deployable techniques are the need of the era. Nowadays, paper-based colorimetric techniques have gained much attention due to their low cost, portability, and wide application in various areas such as industry, public health, food safety, and environmental monitoring. In this direction, low-cost paper-based sensors more importantly nanosensors are emerging as a very effective tool. Analytical measurements of colorimetric assays have led to the development of paper based devices, which fulfil all these requirements simultaneously [1, 2, 35-37]. Recently, some of the studies have been reported with cellulose based paper sensors fabricated via atomic stamp printing, techniques such as electrochemical and microfluidics [38-41]. Yet the paper based filed deployable low cost devices are seldom explored. One of the most widely used paper based sensing techniques is colorimetry, which depending on the concentration of analyte present in the sample gives different absorbance at specific wavelengths and hence the colorimetric changes appear. As such paper-based colorimetric low-cost devices for heavy metal ion detection need to be

explored. Several silver nanoparticles-based studies have already been reported with different surface modifications based on Pb^{2+} interaction, however, investigation on the exact aggregation mechanism is still sparse in the literature [42-44]. Recently, some theoretical studies have been done in this direction which reveals that when two or more nanoparticles assemble new LSPR properties are observed [45-48]. Mei's theory has been used extensively to understand colloidal NP systems and their complex aggregates. Although, we can emphasise the use of electrostatic models based on a quasi-static approximation to deal with the optical cross-section of NPs and their simpler aggregates. Keeping in mind this fact, we have done combined experimental and theoretical approaches to establish the exact mechanism of interaction of Pb^{2+} with citrate-functionalized silver NPs.

In the first part of the work, we have synthesized and characterized citrate functionalized silver nanoparticles (AgNPs) and done spectroscopic as well as analytical studies to understand the underlined aggregation mechanism after its interaction with Pb^{2+}. We have utilized the prominent changes in LSPR spectra of the AgNPs as a central sensing tool for Pb^{2+} detection, mostly due to the formation of one dimensional (1D) self-assembled chain-like geometry of NPs. The mechanism is based on the simultaneous quenching of the existing LSPR peak and generation of a new red shifted LSPR peak. For further details for the aggregation type, we have performed transmission electron microscopy (TEM) to visualize the corresponding geometrical changes and based on the findings of the TEM results we performed basic theoretical studies on nanoparticle and its aggregates. To establish the formation of self-assembled chain-like aggregated structures, fitting of the experimental data with analytically calculated optical cross-section equations have been done. Our study finds application in industrial Pb^{2+} monitoring for that we have varied several nanoparticle parameters for better sensitivity towards lower Pb^{2+} concentrations. Due to their tuneable LSPR properties in visible region, these noble nanoparticles possess tuneable colorimetric properties. The self-assembly and aggregation of NPs upon interaction with heavy metal ions lead to the generation of new LSPR

modes and hence the colorimetric changes appear which can be used as an instant detection tool for heavy metal ion sensing [49].

In the second part of this work, we have focused on Pb detection in air, through the development of colorimetric paper sensor. Pb may be present in the environment in various forms but the common ones are ionic and oxide forms, also several pigments and acid batteries discharges oxide forms [11]. The most occurring forms includes Pb^{2+} (ionic) and in oxides it exists as lead dioxide (PbO_2), litharge (PbO) and red lead (Pb_2O_3). Several traditional methods have been in use for its monitoring and detection as atomic absorption spectrometry [50], atomic emission spectrometry [51], inductively coupled plasma mass spectrometry, etc.; which involve tedious, time-consuming and costly operative procedures. Therefore, they have some limitations to their practical implementation. According to EPA guidelines, the standard protocol for pollutant quantification in ambient air evolves collection of samples in standard filter papers (borosilicate based) through high volume samplers [52, 53]. The extraction of metal ions from filter paper is done through acid digestion methods. According to the available data of Central Pollution Control Board (CPCB), India, the Pb concentration in ambient air is 0.5 mg/m^3 [54] . If the sampling is done with the average sampling rate of 1 liters/min for the duration of 24 hour, then the Pb concentration when converted to ppm is ~ 80 ppm [54]. Here we have calibrated our device from 0 to 600 ppm, which covers sufficiently good range for Pb monitoring in air as well as areas where a much higher amount of Pb (upto 1000 ppm) can be found such as sediments and industrial waste. Herein, we have chosen AgNPs as a plasmonic nanosensors due to their tuneable LSPR properties even if dropcasted in paper substrate. The nanosensor embedded in paper substrate shows significant colorimetric response selectively for Pb in its ionic form. A prototype device is designed to measure these colorimetric changes by the direct measurement of the retro-reflective signal from the paper substrate. Particularly for the oxide forms of Pb, acid digestion technique has been implemented so that the oxide sample under study can bring into its ionic form. We have also done in vitro studies to confirm the underlined

mechanism behind the colorimetric changes of the sensor upon Pb interaction. Our synthesized nanosensor embedded in a cellulose paper based system followed by a prototype device finds application in real field atmospheric Pb detection in an cost effective way.

In the next part of this work, we have synthesized citrate functionalized Gold nanoparticles (AuNPs) for detecting lead. We have explored spectroscopic techniques to understand the underlying mechanism behind the interaction of Pb^{2+} ions with AuNPs. We have further performed numerical studies on AuNPs and their aggregates after its interaction with the Pb^{2+} ions to establish the formation of rod-like aggregates. The amount of aggregation of the AuNPs on Pb^{2+} interaction along with the persistence of single NPs have also been calculated. We have further developed a low-cost prototype to monitor Pb^{2+} ions at the point of interest.

4.2. Results and Discussion:

4.2.1. A Combined Spectroscopic and Theoretical Analysis of Plasmonic Silver Nanoparticle Sensor Towards Detailed Microscopic Understanding of Heavy Metal Detection [55]: The as-prepared citrate functionalized silver nanoparticle's (AgNPs) aqueous colloidal solution has been characterized by UV-Vis spectrophotometry. The UV-Vis absorbance spectra of the AgNPs in increasing order of concentration of nanosensor shown in Figure 4.1a indicate that the optical density (O.D.) increases with an increase in the concentration of the NPs. Inset of Figure 4.1a shows the pictorial image of yellow coloured colloidal AgNPs solution. The characteristic LSPR absorbance band of AgNP is found to be peaking at around 395 nm which is consistent with previously reported literature for citrate functionalized silver nanoparticles [49]. Dynamic light scattering has been performed for an idea of average hydrodynamic diameter of the AgNPs. Figure 4.1b shows the volume distribution of hydrodynamic diameter of the AgNPs having an average hydrodynamic diameter equal to 15 nm. The exact size distribution and characterization of the AgNPs have been done using TEM. From the TEM image of AgNPs shown in

Figure 4.1c, we confirm the almost spherical shape and uniform size distribution of the NPs.

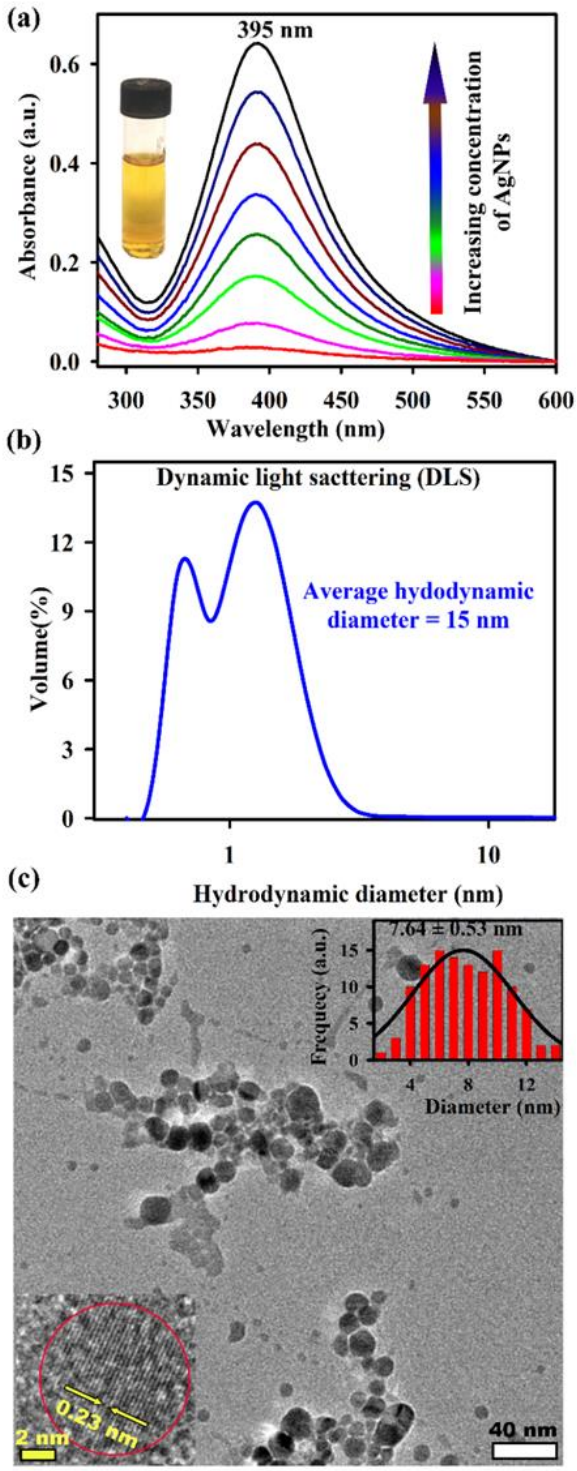

Figure 4.1: *(a) UV–Vis absorbance spectra of citrate capped silver nanoparticle's (AgNPs) colloidal solution with varying concentrations of AgNPs. The Inset shows the image of the colloidal solution. (b) Volume distribution of hydrodynamic diameter (axis in common logarithm) of AgNPs measured using Dynamic Light Scattering. (c) TEM image of the AgNPs. Upper inset shows the size distribution of the AgNPs and lower inset shows a HRTEM image of the NP.*

The average diameter of the AgNP has been calculated and is found ~8 nm (upper inset of Figure 4.1c). The LSPR peak of prepared AgNPs is found to be around 395 nm and is due to the presence of non-aggregated single NPs which has been used for further studies. We have now studied the aggregation of AgNPs in the presence of Pb^{2+} ions by analysing the LSPR spectra of AgNPs in the presence of Pb^{2+}.

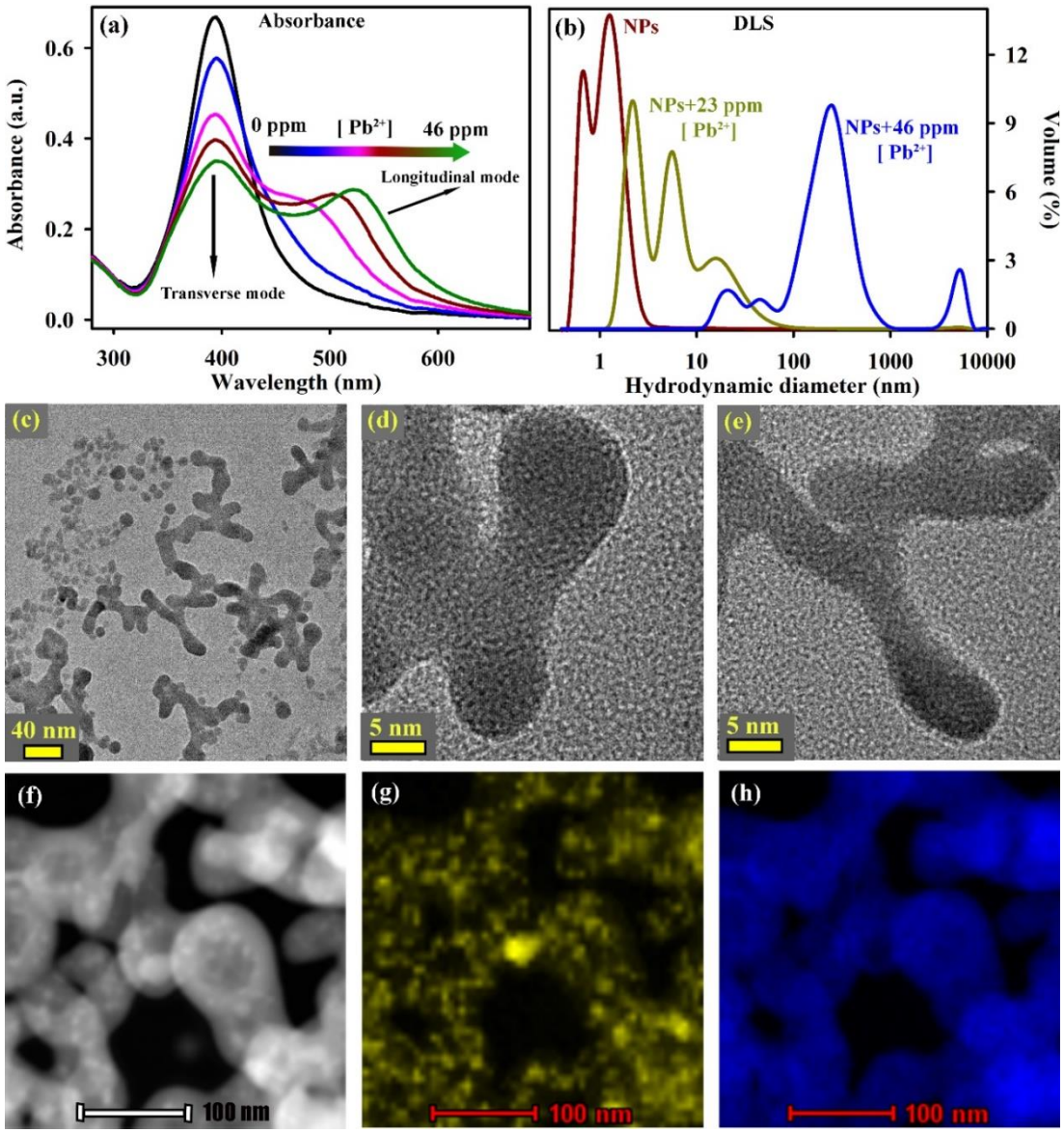

Figure 4.2: *(a) UV-Vis absorbance spectra of AgNPs after interaction with Pb^{2+} in increasing order of concentration of Pb^{2+}. (b) Volume distribution of hydrodynamic diameter of AgNPs (in Black) before and after interaction with two different concentrations of Pb^{2+} (in Green 23 ppm and Blue 46 ppm). (c) TEM image of the AgNPs after interaction with Pb^{2+}. (d, e) HRTEM images the AgNPs after the interaction with Pb^{2+}, showing chain like geometry of the NPs of varying chain length. (f) Drift corrected spectrum image scanning display of lead added NP aggregates and its energy-filtered compositional analysis are shown in panel (g, h). (g, h) Yellow and Blue represents the presence of silver and lead respectively.*

In the presence of Pb^{2+} ions, AgNPs have started to form non-spherical aggregates. The interaction mechanism is governed by the physiochemical changes in terms of the rise of new LSPR bands of AgNPs due to the formation of aggregated structure upon interaction with Pb^{2+}. A new absorption band at ~470-520 nm (Figure 4.2a) along with the existing one is found to be observed after the addition of Pb^{2+} in the AgNPs solution. At the same time, the intensity of the LSPR peak at ~395 nm reduces as an effect of Pb^{2+} addition. The simultaneous existence of two peaks can be attributed to the presence of Pb^{2+} in the system. The appearance of a new red-shifted peak at around 470-520 nm is due to the formation of larger self-assembled aggregates of AgNPs. It is observed from Figure 4.2a that the band centre at around 470-520 nm undergoes a gradual red shift and concurrently the O.D. of the peak also increases with the increment of Pb^{2+} ion. The appearance of two LSPR peaks at 395 nm (denoted as peak 1) and around 470-520 nm (denoted as peak 2) is due to the non-spherical arrangement of the NPs. Overall, these spectroscopic findings indicate that the formed aggregated geometry is similar to that of due to the self-assembly of NPs into one-dimensional linear chains [45]. Here, the two peaks can be ascribed to the existence of two simultaneous modes, one longitudinal and another transverse, which is associated with the surface plasmon oscillation of electron cloud along and perpendicular to the axis of one-dimensional self-assembled chain like architecture of the NPs [56]. With variation in chain length the charge distribution along the longitudinal axis, consequently, the resonance condition varies and hence the corresponding absorption peak. The observed gradual red shift of peak 2 upon gradual increment in lead concentration can be hypothesized due to the growth in chain length. Inspired from this spectroscopic result we performed DLS and TEM measurements to know the exact aggregate type. It is evident from Figure 4.2b that the average hydrodynamic diameter of the system (calculated using DLS) increases with the increment on Pb^{2+} in the system which is an indication of formation of larger aggregates. TEM analysis has proven to be a more confirmatory tool for the hypothesis of self-assembled

chain like geometry of AgNPs. TEM image of the Pb^{2+} added AgNPs system shown in Figure 4.2c reveal that due to the presence of Pb^{2+}, AgNPs come closer to each other forming NPs chains such that Pb^{2+} matrix would have acted to couple the AgNPs together. It is also apparent from HRTEM images shown in Figure 4.2d,e that the formed NP chain aggregates are made of various length. However, it is observed that some of the NPs remain intact (i.e. do not form aggregates). The increment of peak 2 and decrement of peak 1 upon lead (Pb) addition indicates a diminishing number of free nanoparticles with the concurrent increase in a number of self-assembled NPs. Further, to understand the compositional analysis of lead added AgNPs system, we have performed energy-filtered transmission electron microscopy (EFTEM). It can be elucidated from the EFTEM map shown in Figure 4.2g,h that NP-assemblies are embedded by the lead matrix. The mechanism could be explained such as the charged NPs might have come closer to each other via electrostatic attraction with the oppositely charged divalent lead ions in such a way that it surrounds the nearby matrix of the chain like geometry of NPs. It is also noticeable that lead has a high interaction affinity with citrate [57]. The citrates molecules which are adsorbed on the AgNPs surface contains free carboxylate group [58] and therefore are favourable for interaction with Pb^{2+}. Throughout this discussion, UV-Vis and TEM result both supports the argument that in presence of Pb^{2+} NPs form 1D chain like geometry which is responsible for the generation of new LSPR mode along with the existing one.

Here, by the help of basic theoretical understanding, we developed some analytical equations based nanoparticles and nanoparticle aggregates which is going to boost our experimental results. In this current work, the plasmon absorption cross-section of single nanoparticles and nanoparticle pair cluster systems have been calculated analytically using the basic electrostatic results in the quasi-static regime. The optical absorption cross-section have been calculated by using the quasi-static response ($R \ll \lambda$, i.e. the particle size is much smaller than the wavelength of light) of a metal sphere in an electric field [59]. The interaction of light with these metal nanoparticles induces a dipole on the

surface of the nanoparticles and thereafter the curved surface of the NP applies a restoring force on the free electron cloud (plasmon), resulting in their back-and-forth movement hence possess a natural frequency of oscillation. Our study is focused in the visible region of the electromagnetic spectrum since for silver, the natural frequency of dipole oscillation thereby the polarizability α(ω) concomitant a resonance enhancement in visible region, and this resonance is named as 'Localized surface plasmon resonance [24, 60]. Metals possess a complex dielectric function and, therefore, the real and imaginary parts of the dielectric function have been separately calculated based on the experimental finding of Johnson and Christy for silver (Ag) [61].

$$\varepsilon_1 = A_1 \exp(-A_2\lambda) + A_3 \quad 4.1$$

$$\varepsilon_2 = 2C_1 \left\{ B_1 + \left(\frac{B_2\lambda^2}{{B_3}^2+\lambda^2} \right) \right\} \quad 4.2$$

The equations 4.1, and 4.2 follow the fitted curve respectively for the real and imaginary part of dielectric function with the appropriate real valued constants A_1, A_2, A_3, B_1, B_2, B_3, C_1. The wavelength dependency of the absorption cross-section equations has been incorporated through the expressions of the dielectric constant. The growth of NPs to NP chains and their corresponding plasmon evaluation have been well understood by the fitting of the experimentally obtained results with absorption cross-section equations of appropriate NPs geometries. To explain the effect of Pb^{2+} on AgNPs aggregation and plasmon modification, the absorption cross-section equations and, the resonance conditions have been investigated both before and after the addition of Pb^{2+}. It is appropriate now to discuss the absorption cross-section calculations for NP aggregates especially the 1D chains. Here, we have limited our discussion to the NP pair systems. This resonance enhancement appears as an absorption peak [24] in UV-Vis absorbance spectroscopy. The optical absorption cross-section is directly proportional to the imaginary part of polarizability and is given by the below equation as [62],

$$\sigma_{abs} = \frac{K}{\varepsilon_0} \mathrm{Im}\,[\alpha(\omega)] \quad 4.3$$

where K is the wave vector of incident light, ε_0 is vacuum permittivity and speed of light is taken 1. For an isolated metallic sphere of radius R in an external electric field of wavelength λ, the polarizability is given as [59]

$$\alpha(\omega) = 4\pi R^3 \varepsilon_0 \left(\frac{\varepsilon(\omega)-\varepsilon_m}{\varepsilon(\omega)+2\varepsilon_m}\right) \quad 4.4$$

The dielectric constant (ε_m) of the medium i.e., aqueous colloidal silver nanoparticles solution was taken to be 1.768. We choose the dielectric function ε(ω) (frequency of electromagnetic radiation ω) which fits the experimental data given by Johnson and Christy for sliver in visible region [61]. The dielectric function of metals is complex and hence putting $\varepsilon(\omega)=\varepsilon_1+i\varepsilon_2$, solving for the imaginary part we have of polarizability,

$$\mathrm{Im}[\alpha] = \frac{3\varepsilon_m\varepsilon_2}{(\varepsilon_1+2\varepsilon_m)^2+{\varepsilon_2}^2} \quad 4.5$$

Putting this value in equation 4.1,

$$\sigma_{abs(1)} = \frac{8\pi^2 R^3}{\lambda}\left(\frac{3\varepsilon_m\varepsilon_2}{(\varepsilon_1+2\varepsilon_m)^2+{\varepsilon_2}^2}\right) \quad 4.6$$

Where, ε_1 and ε_2 separately follows the experimental values given by Johnson and Christy. After interaction with Pb^{2+} ions, NPs were aggregated mostly to form chain-like structures made of various numbers of NP. The sizes of the formed nanoparticle aggregates were assumed to be small concerning the wavelength of incident light (λ) such that quasi-static approximation remains valid. If two or more nanoparticles come closer to each other in such a way that there is a significant overlapping of their dipolar electromagnetic fields, the localized plasmon resonance of individual particles coupled to each other to give new resonance modes [27, 59]. The resultant polarizability for two in-phase modes of the nanoparticle-pair system was taken using the assumption that the two particles have the same radius (R) and given by the following equation [59],

$$\alpha(\omega) = 4\pi R^3 \varepsilon_0 \frac{\eta}{3}\left(\frac{1}{1-2\eta\left(\frac{R}{D}\right)^3}+\frac{2}{1+\eta\left(\frac{R}{D}\right)^3}\right) \quad 4.7$$

Where, $\eta = \left(\frac{\varepsilon(\omega)-\varepsilon_m}{\varepsilon(\omega)+2\varepsilon_m}\right)$ and D is the centre to centre distance of the two particles.

Solving for the imaginary part of equation 4.5, we got the absorption cross-section for the pair system as,

$$\sigma_{abs}(2) = \frac{8\pi^2 R^3}{\lambda}\left\{\frac{1}{3}\left(\frac{\varepsilon_m \varepsilon_2 (2m+l)}{(\varepsilon_1 l + 2\varepsilon_m m)^2 + \varepsilon_2{}^2 l^2}\right) + \frac{2}{3}\left(\frac{\varepsilon_2 \varepsilon_m (n+o)}{(\varepsilon_1 n + \varepsilon_m o)^2 + \varepsilon_2{}^2 n^2}\right)\right\} \quad 4.8$$

Where $m = 1 + \left(\frac{R}{D}\right)^3$, $l = 1 - 2\left(\frac{R}{D}\right)^3$, $n = 1 + \left(\frac{R}{D}\right)^3$ $o = 2 - \left(\frac{R}{D}\right)^3$. Here, we have taken D = 2R for calculation purposes. $\sigma_{abs}(1), \sigma_{abs}(2)$ represent the absorption cross-section equations for single NP and NP-pair system respectively and would be used to develop model equations for the fitting of the observed experimental LSPR band. To fit the experimentally obtained absorbance peaks, the obtained absorption cross-section equations were first normalized by their magnitude at found LSPR peak values. The LSPR spectra of the AgNPs before and after the addition of Pb^{2+} are shown in Figure 4.3a and are named as spectrum 1 (without Pb^{2+}), spectrum 2 (16 ppm Pb^{2+}), spectrum 3 (23 ppm Pb^{2+}). The resonance enhancement condition for single NP systems (i.e. when ε_1=-2ε_m) satisfied by equation 4.4, for a particle of 10 nm diameter, is found to be near 395 nm which is equal to the experimentally observed spectral peak of the AgNPs. Hence, this theoretically obtained absorbance cross-section expression of a single NP normalized at 395 nm taking wavelength of incident light (λ) to be an independent variable has found to best fit the observed normalized LSPR spectrum 1 (shown in Figure 4.3b). Earlier in our discussion, we have predicted that AgNPs form 1D chain like geometry in presence of Pb^{2+}. The absorption cross-section for a NP pair system has been calculated by the previously mentioned procedure and given by equation 4.6. The resonance enhancement in this case (particles of diameter 10 nm) has been found to get satisfied twice giving two in-phase modes, one transverse mode (~395 nm) which is perpendicular to the electric field and the other longitudinal mode (~470 nm, along the chain axis) which is parallel to the field, however, there also exist two opposite phase modes but, only the in-phase modes are dominant for optical excitation when considering for quasi-static approximation i.e., for small NPs [59]. As we investigated earlier not all NPs form aggregates upon interaction

with lead, the normalized LSPR spectrum 2 and spectrum 3 have been fitted by taking contribution from both i.e., single NP (equation 4.4) and NP pair system (equation 4.6) depending on the lead ion concentration. With an increment in lead concentration the tendency of NPs to form longer aggregates increases and therefore we have taken a higher contribution from NP pair system for spectrum 3 compared spectrum 2 for fitting purpose. The equations which have been found to be the best fit the normalized spectrum 2 and spectrum 3 are given by equations 4.9 and 4.10 as follows:

$$\sigma_{abs} = \frac{8\pi^2 R^3}{\lambda}\{5(\sigma_{abs}(1)) + 2(\sigma_{abs}(2))\} \quad 4.9$$

$$\sigma_{abs} = \frac{8\pi^2 R^3}{\lambda}\{5(\sigma_{abs}(1)) + 9(\sigma_{abs}(2))\} \quad 4.10$$

It is evident from both the equations that the contribution of single NPs to NP pairs has increased from 5:2 to 5:9 as lead concentration increased. The fitted curves along with their experimentally observed normalized absorption spectra are shown in Figure 4.3c,d and found to be in good agreement with each other. The fitting parameters, appeared via ε_1 and ε_2, for the three spectra namely 1,2,3 have tabulated in Table 4.1. The spectroscopic results for much higher Pb^{2+} concentrations as observed (Figure 4.2a) are also in accordant with many previously reported theoretical studies that have been done for silver nanoparticle linear chains. These studies confirm the fact that the absorbance corresponding to longitudinal mode undergoes a red shift when more NPs couple to form longer chains [59, 63].

Table 4.1: *List of parameters for ε_1 and ε_2 which best fit the equations 4.4, 4.9 and 4.10*

Parameters	**Spectrum 1 (eq. 4.4)**	**Spectrum 2 (eq. 4.9)**	**Spectrum 3 (eq. 4.10)**
A_1	-22.70±0.25	-23.86±0.86	-23.07±0.20
A_2	-725.33±8.80	-732.18±23.43	-1049.88±9.06
A_3	35.74±0.20	37.86±0.78	30.48±0.20
B_1	-0.18±1.05	-2.13±1.67	-0.84±0.46
B_2	8.02±5.74	15.75±7.92	7.75±1.51
B_3	656.32±546.24	640.65±396.82	620.06±172.34
C_1	0.41±0.00	0.41±0.00	0.41±0.00

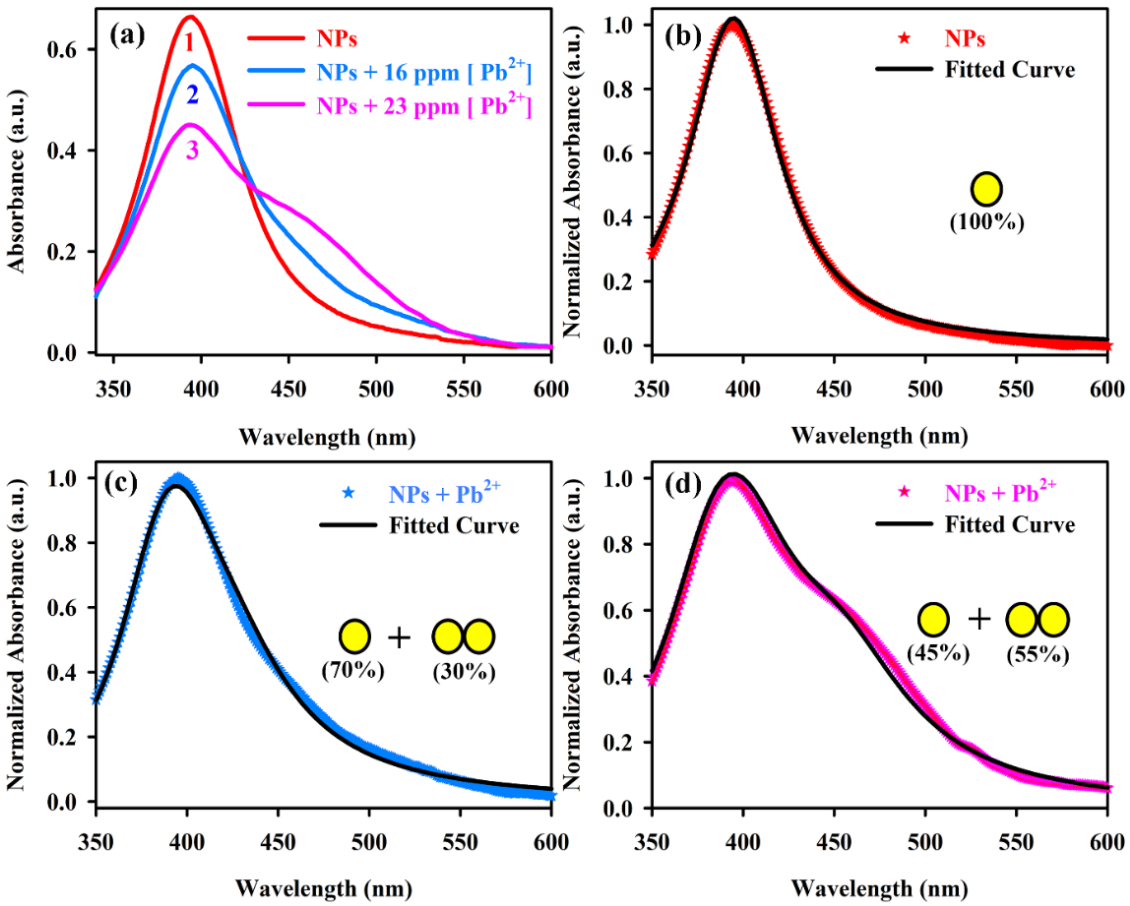

Figure 4.3: *(a) UV-Vis absorbance spectra of AgNPs before (red) and after interaction with 16 ppm (Blue), 23 ppm (Pink) of Pb^{2+}. The normalized UV-Vis absorbance spectra (as numbered in (a)) and the fitted curve (in Black) based on their corresponding equation for absorption cross-section equations are represented in panels from (b-d). The normalized UV-Vis absorbance spectra of (b) AgNPs before interaction with Pb^{2+} and its fitted curve following equation 4.6 for absorption cross-section of nanoparticle, (c) AgNPs after the interaction with Pb^{2+} (16 ppm) and its fitted curve following equation 4.9 for absorption cross-section of nanoparticle and nanoparticle pair mixed system in ratio of 5:2, (d) AgNPs after the interaction with Pb^{2+} (23 ppm) and its fitted curve following equation 4.10 for absorption cross-section of nanoparticle and nanoparticle pair mixed system in ratio of 5:9.*

It justifies and supports our interpretation that with an increment in Pb^{2+} concentration, more AgNPs assembled to form longer chains which lead to much red-shifted LSPR peaks. Although we have established mechanism for the change of plasmonic properties in AgNPs in the presence of Pb^{2+} ion, it is highly desirable to utilize this fact for practical application purposes. One of the main sources of lead pollution is from industrial waste-water which contains a very high concentration upto 500 mg/L of Pb^{2+} [21]. So, it is very important to detect Pb^{2+} ions from industry waste-water. The direct resemblance of variation in AgNPs LSPR spectra with Pb^{2+} concentration can be very beneficial when

utilized as a lead detecting nanosensor. There are many parameters which affect the interaction affinity of the AgNPs towards the Pb^{2+}. Of them, particle size, nanoparticle concentration and probing time plays a very crucial role in order to increase the limit of detection (LOD) of the AgNP sensor [64]. In the present section, we have systematically varied different parameter to improve the LOD of the nanosensor for Pb^{2+} detection. As the LSPR band highly depends on the size of the NP, it is expected that smaller size AgNPs have a higher affinity towards heavy metal ions than larger ones due to their higher surface to volume ratio [65].

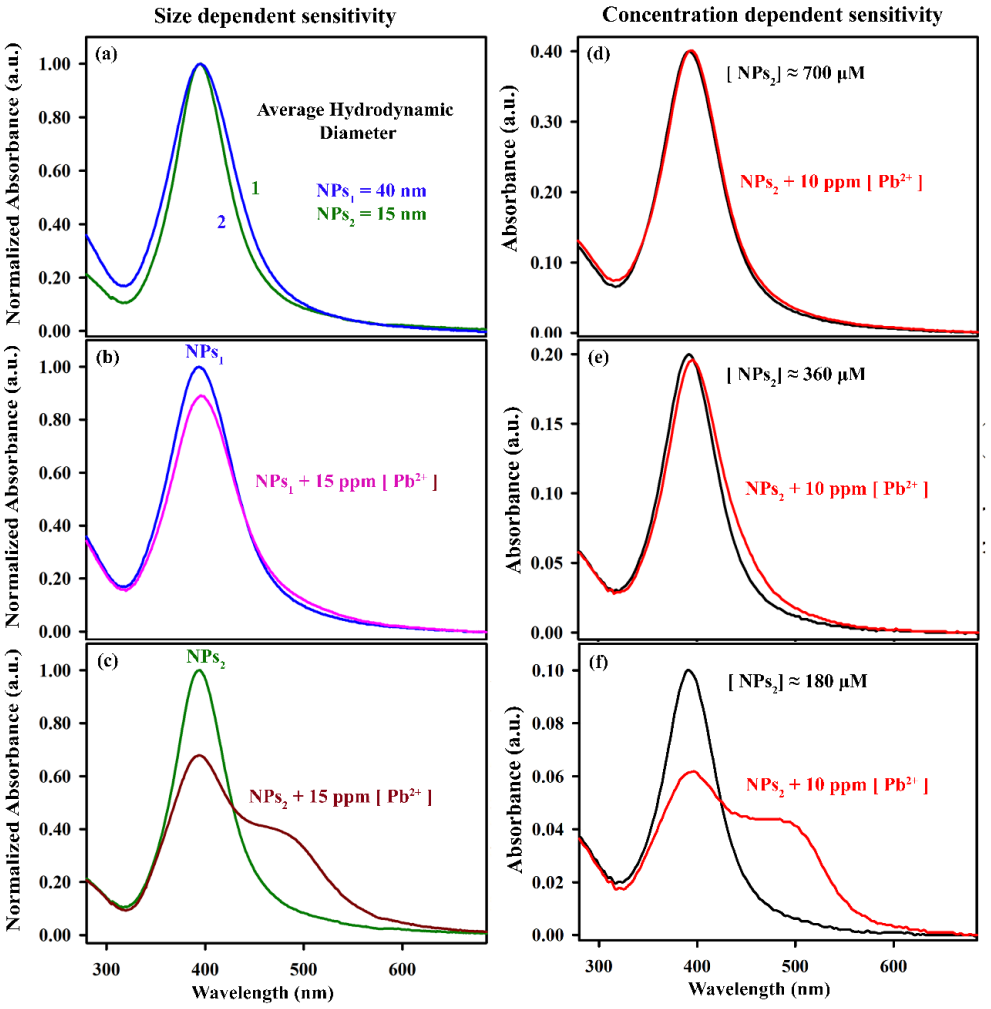

Figure 4.4: *(a) Normalized UV-Vis absorbance spectra of two sets of AgNPs, namely NPs_1 (Blue) and NPs_2 (Green) having a hydrodynamic diameter equal to 40 nm and 15 nm respectively. (b, c) Normalized UV-Vis absorbance spectra of the two AgNPs and their response i.e. NPs_1 (Pink) and NPs_2 (Dark Red) with 15 ppm of Pb^{2+}. (d-f)The UV-Vis absorbance spectra of AgNPs (having three different concentrations) in the absence (Black) and presence (Red) of Pb^{2+} (10 ppm) are shown in the panels; of 700 µM, 360 µM and 180 µM concentrations of NPs_2 at 10 ppm of Pb^{2+} respectively.*

The synthesis procedure of silver NPs plays a critical role in the production of smaller and monodispersed silver NPs, which affects the aggregation response very much. We have synthesized two sets of AgNPs namely NPs_1 and NPs_2 having an average hydrodynamic diameter equal to 40 nm and 15 nm respectively. The UV-Vis absorbance spectra as shown in Figure 4.4a, clearly delineate that NPs_1 have broadened LSPR band than NPs_2 due to its larger and nonuniform size distribution. The sensitivity of both the NPs (at the same concentration) towards Pb^{2+} has been observed. It is noticed from Figure 4.4 b,c that, in case of NPs_2 a dominant LSPR band has been generated at ~500 nm whereas for same lead concentration there is no such significant band appeared with NPs_1. From this observation, we can conclude that the probability of AgNPs to couple to form NP chains is much higher in smaller sized NPs (15 nm) than larger one (40 nm) hence shows higher response with NPs_2. Thereby we have used NPs_2 now onwards for further parameter dependency investigations. The concentration of nanoparticle in the solution plays another pivotal role to increase lead ion interaction sensitivity in terms of LSPR modes. The accurate estimation of the AgNPs concentration is quite difficult to calculate since each batch of NPs varies in size and shape. However, we need to have an approximate idea of the AgNPs concentration which have been calculated using previously reported theoretical results taking the molar extinction coefficient of citrate capped silver nanoparticle of diameter 10 nm equal to 5.56×10^8 M^{-1} cm^{-1} [66]. The molar concentration of the AgNPs has been calculated using Beer-Lambert law. Here, we have taken three different concentrations (in increasing order) of NPs_2 and investigated the effect of concentration on interaction affinity. Figure 4.4d-f illustrate the UV-Vis spectral response of three different concentrations i.e. 0.4 a.u (~700 µM), 0.2 a.u. (~360 µM) and 0.1 a.u (~180 µM) of AgNPs sensor respectively in presence of same lead ions. It is found that spectral changes increase with the decrement of sensor concentration. Hence, for prepared AgNPs to be used as a lead sensor we must need to use minimal possible AgNPs concentration for better sensitivity. It may be due to the fact that the contribution from excess unreacted AgNPs subdue the contribution from aggregated ones.

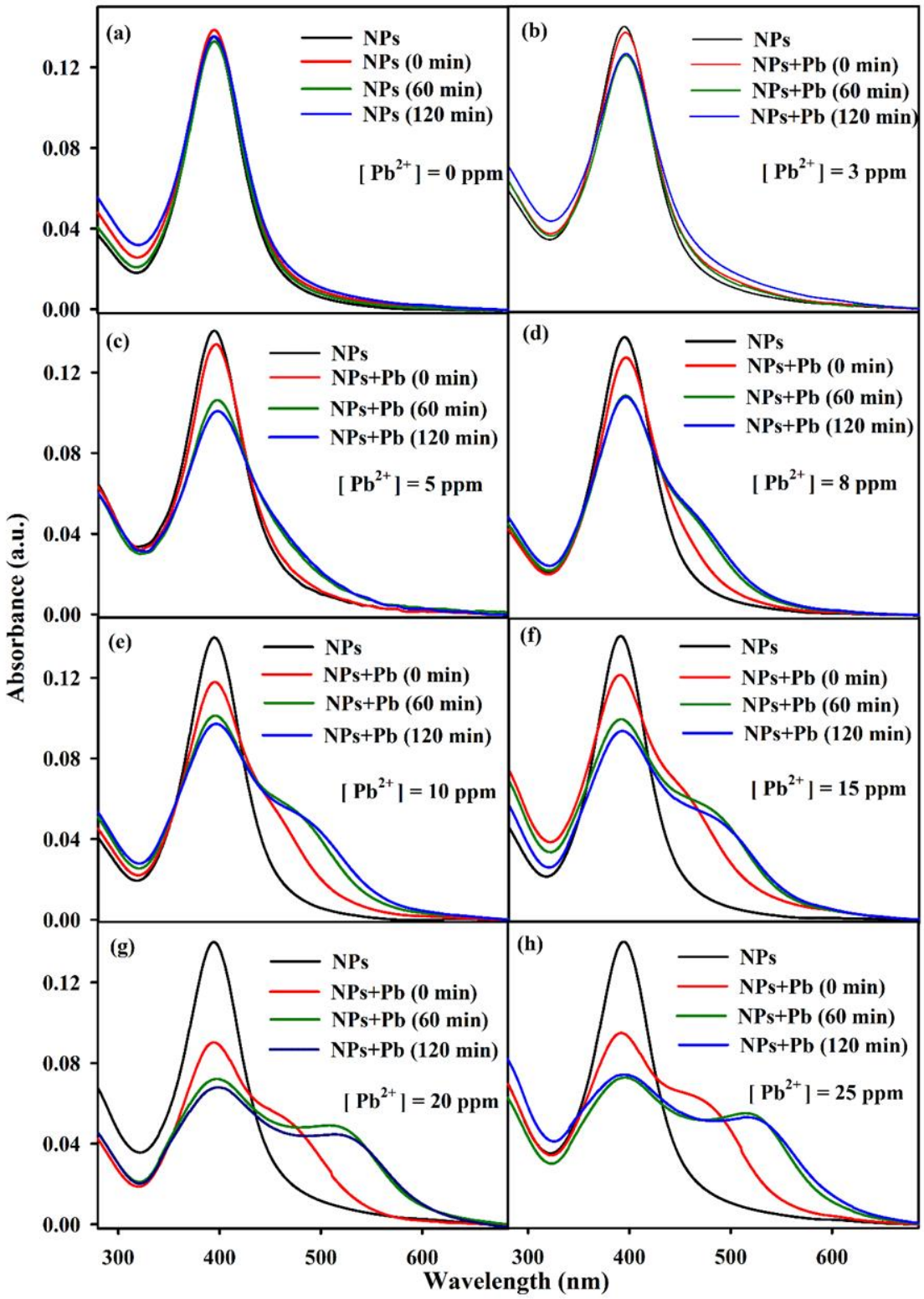

Figure 4.5: *(a) Shows the variation of SPR in longer time window at [Pb^{2+}] = 0 ppm. (b-h) Time-dependent absorbance spectra of AgNPs colloidal solution at different concentrations of Pb^{2+} are shown in panels*

We have also investigated how the interaction affinity of AgNPs towards Pb^{2+} detection changes with respect to time. Significant spectral changes have been

noticed up to 60 minutes of incubation time. The temporal variation of the AgNPs for 0 to 25 ppm of Pb^{2+} shown in Figure 4.5, where 0 ppm is the control spectral response of the AgNPs without lead. It is observed that, the LSPR peak height of AgNPs decreases with time, additionally second peak (~500 nm) height increases simultaneously. This result suggests that the interaction affinity of AgNPs increases with longer incubation time. Moreover, there is a significant red shift of the second peak with respect to time for all cases. Here, 60 min of reaction time could be considered as enough for Pb^{2+} detection, beyond which insignificant changes have been observed. The sensitivity of AgNPs increases with higher incubation time.

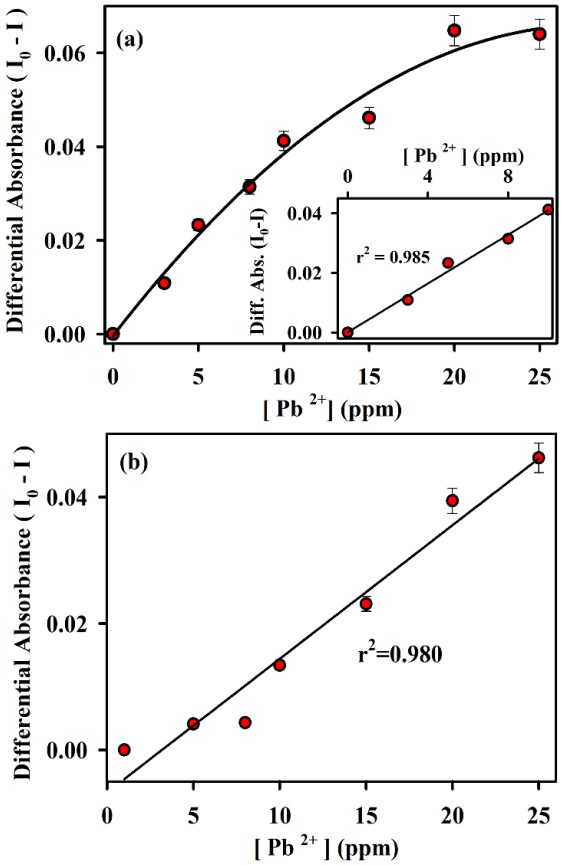

Figure 4.6: *(a) The differential absorbance spectra of the AgNPs solution at 395 nm with varying Pb^{2+} concentrations. Inset shows the linear response of the curve with [Pb^{2+}] ranging from 0 to 10 ppm. (b) Shows the plot of differential absorbance of the AgNPs solution at 520 nm with varying Pb^{2+} concentration.*

To get insights of the nature of sensor response towards Pb^{2+} the relative difference of the two absorption peak heights (I_0-I) before and upon interaction with varying Pb^{2+} concentration has been plotted and shown in Figure 4.6a,b. I_0

is the absorbance of the AgNPs before interaction with Pb^{2+} at peak positions 395 and 520 nm, whereas I represent the absorbance measured after 60 min of incubation with Pb^{2+} at same peak positions. Figure 4.6a demonstrates the differential absorbance (I_0-I) for all concentrations from 0 ppm- 25 ppm at 395 nm which follows non-linearity given by equation $Y = 0.08 - 0.09\exp(-X/16.04)$, where Y is the differential absorbance and X represent the Pb^{2+} ion concentration. However, the region between 0 ppm-10 ppm exhibits a good linear correlation (correlation coefficient r^2 = 0.98) and shown in the inset of Figure 4.6a. Similarly, at 520 nm there is a complete linear response of the sensor with Pb^{2+} having a correlation coefficient equal to 0.98 (Figure 4.6b). Here, 60 min of reaction time could be considered as enough for Pb^{2+} detection, beyond which insignificant changes have been observed. The limit of detection is ~1.5 ppm, which has been obtained from the linear region (0 -10 ppm) corresponding to peak 1 [67]. Thus, the present discussion demonstrates that by varying the size, concentrations of AgNPs and allowing for enough reaction time, better sensitivity has been achieved. Further, we have checked out the LSPR response of AgNPs with various other metal ions present in the environment.

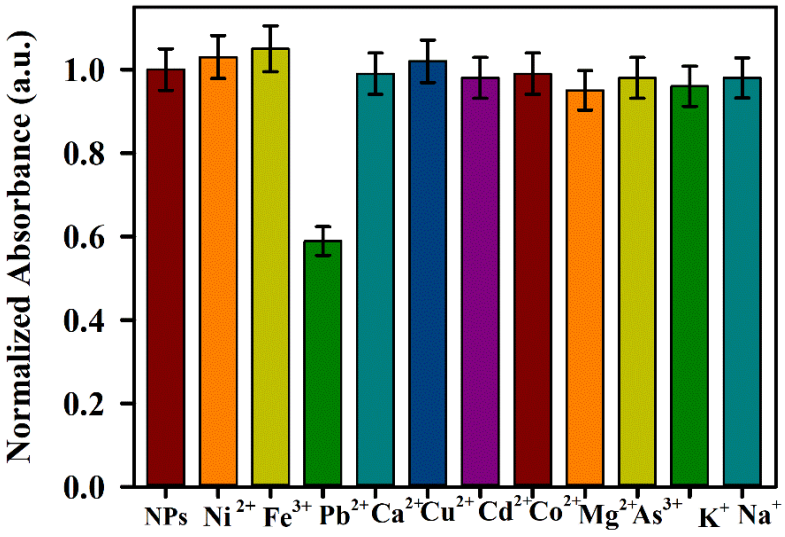

Figure 4.7: *Normalized UV-Vis absorbance spectra of the AgNPs colloidal solution monitored at 395 nm in the presence of various metal ions.*

We have investigated the spectral response AgNPs towards other relevant metal ions such as Hg^{2+}, Ni^{2+}, Fe^{3+}, Ca^{2+}, Co^{2+}, Cu^{2+}, Cd^{2+}, Mg^{2+}, As^{3+}, K^{+}, Na^{+} under the same experimental conditions. The study shows (Figure 4.7) that other than

Pb^{2+} above-mentioned metal ions do not show any significant spectral changes upon interaction with the prepared AgNPs (spectra not shown). Although, for Hg^{2+} a blue shift is observed in the LSPR spectra of AgNPs however it is followed completely different aggregation/agglomeration mechanism since no new LSPR modes have observed. Hence our citrate-based silver NPs proved to be highly selective Pb^{2+} sensor.

4.2.2. Paper-based Plasmonic Nanosensor Monitors Environmental Lead Pollution in Real Field [68]: The aqueous colloidal solution of the as prepared citrate functionalized silver nanoparticle's (AgNPs) has been characterized by UV-Vis spectrophotometry. Figure 4.8a represents the UV-Vis absorbance spectra of the yellow coloured aqueous AgNPs solution and a reddish coloured solution after addition of Pb^{2+} into it. The characteristic LSPR spectra of the prepared AgNPs has single absorbance maxima at around 395 nm however when Pb^{2+} have been added to the system, there is a generation of an additional peak at around 520 nm (Figure 4.8a). At the same time, the intensity of the LSPR band of AgNPs (at ~395 nm) reduces as an effect of Pb^{2+} addition. The sensing mechanism is based on the simultaneous existence of two peaks of AgNPs due to the formation of aggregated structure upon interaction with Pb^{2+}. In one of our earlier publications [55], we have explained the aggregation mechanism in detail that the AgNPs in the presence of Pb^{2+} formed a chain-like assembly due to which there is a coupling of nearby plasmon modes. The two peaks thus correspond to the transverse and the longitudinal mode of vibration associated with the plasmon oscillation of electron cloud along and perpendicular to the axis of one-dimensional self-assembled chain AgNPs. However, mostly oxide forms of Pb are present as suspended air particulates. As a real-world sample, we have taken lead dioxide, which is one of the naturally present oxides forms of Pb in the atmosphere [69]. Being insoluble in aqueous media, acid digestion methods (mentioned in the materials and methods section) have been used for the conversion of oxide forms into water-soluble forms. A whitish precipitate is obtained by the acid digestion of PbO_2, this precipitate has been dissolved in water and is described as Pb extract.

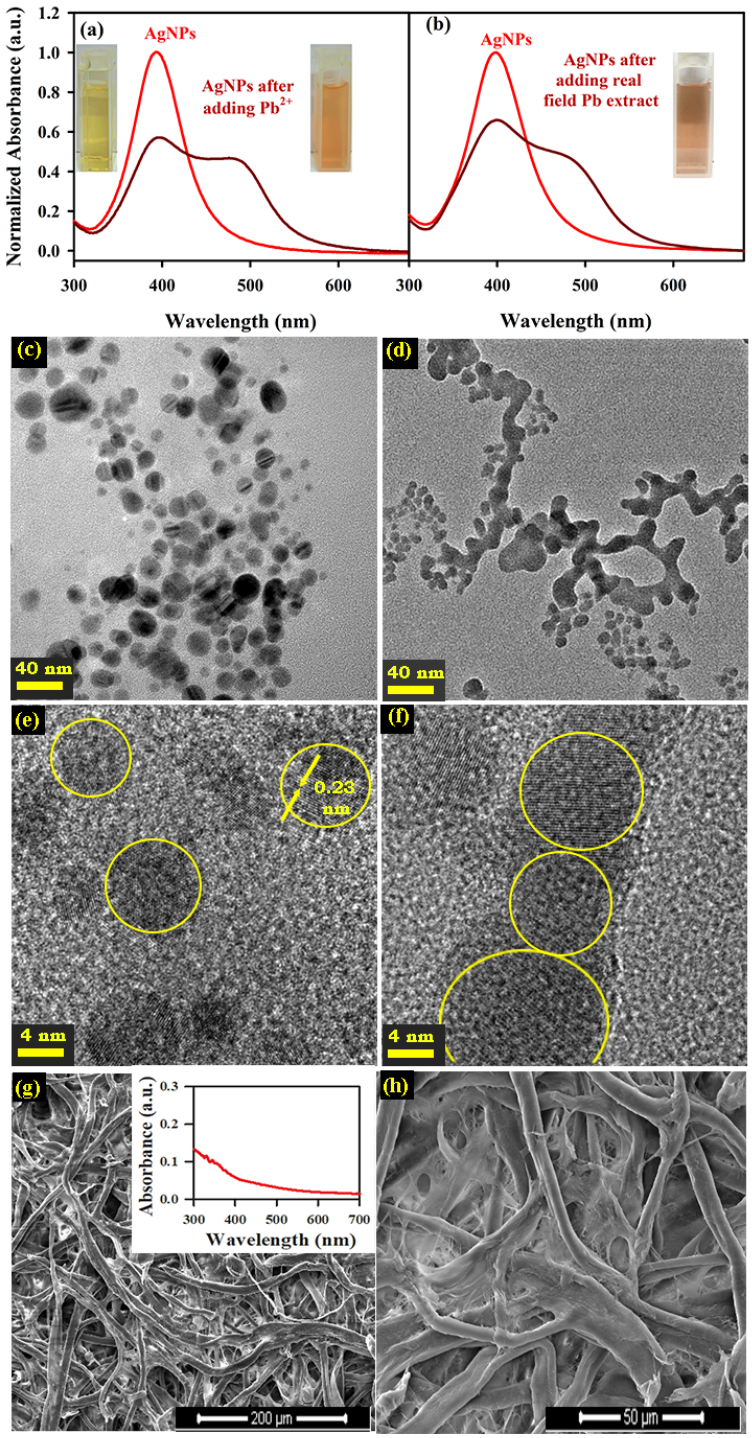

Figure 4.8: *(a) UV-Vis absorbance spectra of the as prepared colloidal AgNPs solution before and after addition of [Pb^{2+}]. (b) UV-Vis absorbance spectra of AgNPs and AgNPs with real field acid digested Pb extract. TEM images of the AgNPs (c) before and (d) after addition of Pb extract. The corresponding HRTEM images of the AgNPs (e) before and (f) after addition of Pb extract. (g, h) FESEM image of the paper substrate at two different magnifications, inset of (g) shows the UV-Vis spectra of paper substrate.*

It can be ascribed from these findings that the acid treated product of the PbO_2 is converted to ionic form when dissolves in water and its presence can be

detected with the help of the AgNPs nanosensor using spectroscopic tools. Also, the inset of Figure 4.8b shows the colorimetric change of the nanosensor upon addition of Pb extract into it which gives similar sensing mechanism as in Figure 4.8a i.e., the yellow-coloured colloidal solution of AgNPs has been shown to become reddish when Pb extract has been added to it. Now we have performed TEM imaging for microscopic analysis of the self-assembled arrangement of the Pb extract added AgNPs system. From Figure 4.8c the almost spherical shape and a uniform size distribution of the NPs have been confirmed. The high-resolution transmission electron microscopy (HRTEM) analysis gives the crystalline nature of the NPs having unidirectional fringe growth and spacing of ~0.23 nm. We have now analysed the TEM images of the Pb extract added AgNPs systems, as observed from Figure 4.8d, aa shown from Figure 4.8e,f, chain like self-assembled geometrical arrangement have been observed which is in accordance with our previously reported work. The HRTEM images of the Pb extract added systems clearly shows the crystalline nature of the assembled AgNPs. Thus, both spectroscopically and microscopically we have found that the Pb in the form of oxides (as an air suspended particulate) when converted to the ionic form through acid treatment is also highly sensitive to AgNPs to be used as a nanosensor for real field Pb detection. A clear cellulose fibre mesh is visible from the FESEM image of the paper substrate (Figure 4.8g,h) which shows the hierarchical fibrous morphology of the filter paper. The paper-substrate largely made of microscale cellulose fibrous strands and are interwoven with the ones of smaller strands, indicate that the paper has a large active surface area. Also, from the UV-Vis spectra (diffuse reflectance mode) of paper substrate as shown in inset of Figure 4.8g, it is observed that paper substrate itself have no significant absorbance in the region of interest. Herein, we have developed a paper based plasmonic nanosensor for real field Pb detection in a sensitive and cost effective way. In this regard cellulose paper proves to be very cost effective and also totally unreactive to our developed nanosensor. The use of Whatman grade 4 filter paper is 201 advantageous in many respects when considering for colorimetric sensing. Due to its improved,

homogenous and fast flow rate, embedment of the AgNPs sensor is preferable in these paper [1, 70]. Choice of the filter paper substrate is based on the fact that it is consisting mainly of α-cellulose (~98%) and hence ensures minimal interference from other components (trace pollutants, coatings, etc.) [71].

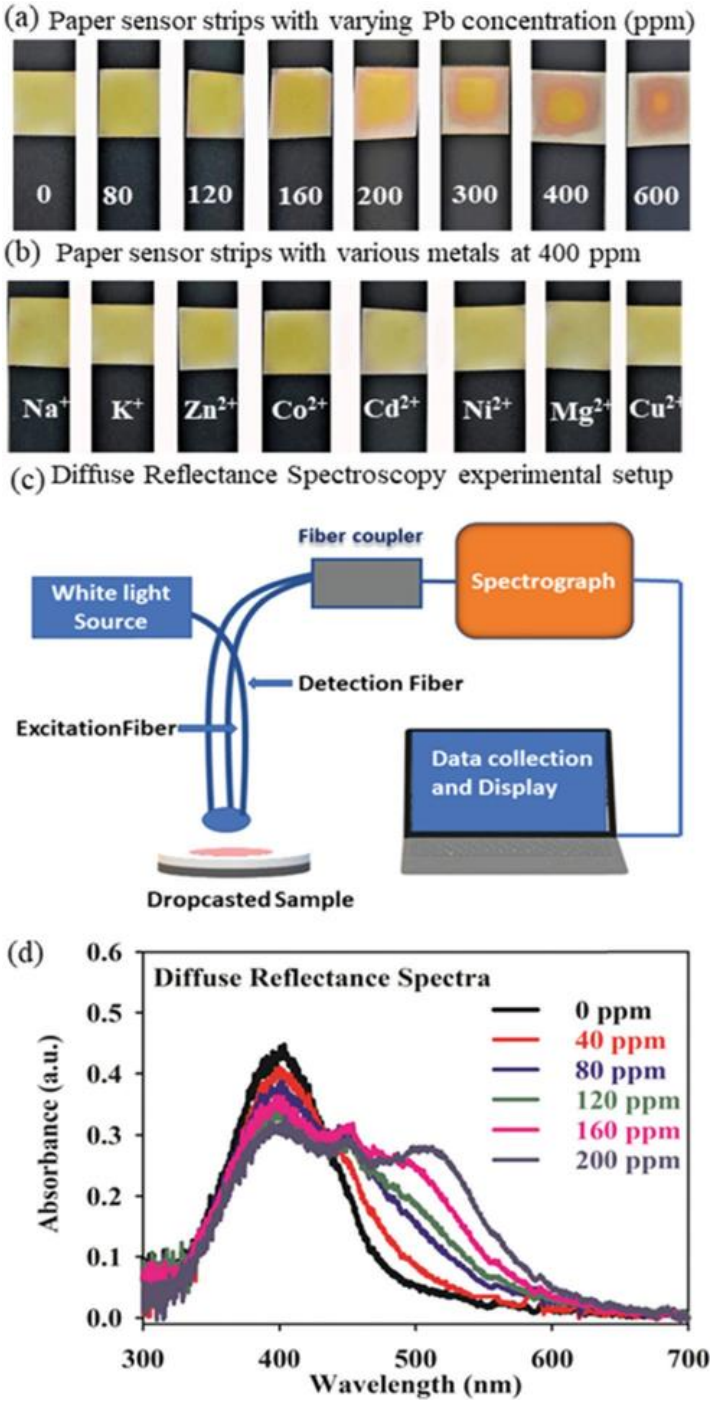

Figure 4.9: *(a) Paper-based AgNPs sensor strips in the presence of different concentrations of Pb extract. (b) Ion selectivity test of the paper sensor strips in the presence of various metal ions at 400 ppm. (c) Experimental setup for absorbance measurement of paper-based samples through the diffuse reflectance mode. (d) The corresponding diffuse reflectance absorbance spectra of the paper-based samples having different concentrations of Pb extract.*

As mentioned earlier, we developed RPPs as base where we can dropcast the sample. At first, the sensor i.e only AgNPs have been dropcasted on RPPs as a control experiment, no significant colorimetric as well as changes in LSPR properties of the sensor have been observed. Now to sense the Pb content present in the sample, first we have dropcasted the varied concentration of Pb extract on the RPPs and then dropcasted the AgNPs sensor over it. As we have discussed earlier, a colorimetric change in a cuvette based system has been observed in the sensor upon addition of Pb extract to it. We have now tried to implement those colorimetric changes to the cellulose paper based system. From Figure 4.9a it is clear that there is gradual change in the colour of the dropcasted Pb extract upon addition of AgNPs nanosensor into it. These colour change signifies the formation of larger aggregates. For further confirmation of the aggregate formation mechanism on the RPPs, we have used diffuse reflectance spectroscopy (DRS) to find the spectroscopic changes. The schematic of the DRS setup has been shown in Figure 4.9c and the setup details has been mentioned earlier. The DRS of the RPPs of varying Pb extract concentration have been shown in Figure 4.9d. Similar spectroscopic changes in RPPs have been observed as in cuvette based systems i.e. here also a simultaneous existence of second peak at around 520 nm along with the first peak at 395 nm is observed. The appearance of the second peak at 520 nm along with first at 395 nm is indicating the formation of 1D chain aggregates as suggested by TEM images (Figure 4.9f). These DRS results implies that AgNPs are forming similar chain like aggregation even on RPPs, so that we are getting the transverse and longitudinal mode of vibration corresponding to the formed chain aggregates. Also, it is evident from the DRS that there is a gradual red shift in the second (520 nm) peak with simultaneous decrease in the first peak (395 nm) which confirms the formation of longer chain aggregates [55] with increment in Pb extract concentration. Formation of longer chain aggregates with increment in Pb concentration is also the cause of increment of red content (visually) of the RPPs. Thus, the chosen Whatman cellulose filter paper (grade 4) is non-reactive efficient substrate for paper based sensing. Furthermore, the paper strips dropcasted with AgNPs has

been tested for several other metal ions such as Ni^{2+}, Co^{2+}, Cd^{2+}, Cu^{2+}, Na^{+}, K^{+}, Mg^{+}, and Zn^{2+}. The paper sensor response with these metal ions has been shown in Figure 4.9b. The unique red colour response has only been observed with Pb than other relevant heavy metal ions. As shown in Figure 4.9a, the significant colour change of the RPPs with varying Pb extract concentration have been observed, which can be utilized as an efficient cost effective Pb sensing tool on paper substrate. Here, we have developed an electro-optic prototype arrangement for the direct and instant measurement of the different colour content present in the RPPs without going to the laborious analysis of captured or scanned images. The developed prototype arrangement is based on the basic principle of retro reflection of light by a material. In such methods, the visible spectrum of the electromagnetic radiation carries information from the surface of the material which defines the colour of the product [72]. To gather the instantaneous colorimetric information of the retro reflected visible spectrum from the paper substrate we have placed an electronic colour sensor perpendicularly top of the paper substrate slot in the device. The schematic of the prototype arrangement is shown in Figure 4.10a, shows the top & side view as well as the internal arrangement of the components inside the prototype. The prototype arrangement is consisted of a customized sample holder (tray) of 40 mm by 10 mm dimension. The colour sensor (TCS34725) arrangement is such that the white light LED source (colour temperature 5700K) is assembled side by the colour sensor and set perpendicularly top of the sample holder so that white light from LED fall on the paper substrate and simultaneously the retro reflected information is collected by the colour sensor. Later raw data from the colour sensor have been collected through a microcontroller arrangement for further processing. The entire arrangement is controlled by our indigenously developed software in Arduino platform. The microcontroller and the relay arrangements have been mounted side by the sample holder inside the device. The device casing has outer dimensions of 127 nm × 35.5 nm × 62 nm with all optical and electronic components and is covered from all the directions so that no extra unwanted ambient optical information should be captured by the sensor. The

entire setup is attached to rechargeable power supply of 5 Volt and a display screen governed by the Arduino software. The flow chart of the working principle of the device is shown in Figure 4.10b.

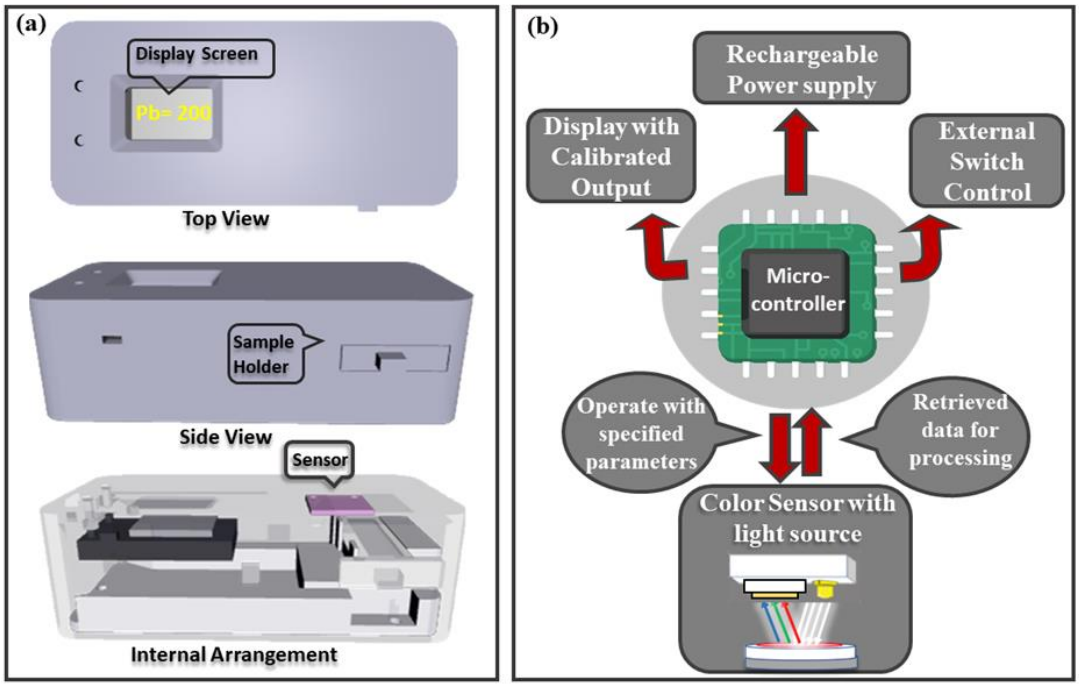

Figure 4.10: *(a) Schematic of the developed paper based prototype device for environmental Pb detection. (b) Flow chart of the working principle of the developed prototype device.*

Furthermore, the device is IoT enabled to transfer the data from remote areas to enable immediate remedial actions for avoiding environmental or health hazards. Prior to the calibration of the device, we have optimized the minimum required sample for the best possible colorimetric response of the sensor strips. The nanosensor response to the Pb also depend on its size shape and concentration. The calculated size, hydrodynamic diameter concentration of the used AgNPs is similar to our earlier reported literature i.e. average diameter is 8 nm [55]. We have found that 50 mL volume of sample, which include 30 mL of Pb extract and 20 mL of the AgNPs sensor, is need for the best colorimetric response. We have analyzed the effect of pH, temperature and time dependence on the performance of the sensor. We have found that at pH ~6.5, the nanoparticle gives maximum sensing response in comparison to when in acidic and basic medium i.e., the prepared nanoparticles are very stable and have high interaction affinity with Pb under neutral pH. Also, the prepared nanoparticles

are found to be stable in temperature range 4^0C to 40^0C. However, when checked the sensing response in the temperature range 20^0C to 40^0C (the range of our interest), no significant change has been observed. The detection time plays one of the key roles in sensing response. We have also investigated that the interaction affinity of AgNPs towards Pb detection increases with respect to time [55]. For paper based sensor strips we found similar nature and concluded that a time duration of 15 minutes is required for the optimum response of the sensor.

Table 4.2: *Colour content present with varying Pb concentrations*

Pb (ppm)	% Red Content	% Green Content	% Blue Content
0.00	29.45	37.27	33.17
80.00	30.62	37.38	32.40
120.00	30.48	37.10	32.19
160.00	31.63	36.75	31.73
200.00	31.05	36.67	32.25
300.00	31.55	36.11	31.77
400.00	32.68	36.73	30.49
600.00	33.27	36.22	30.09

However, for instantaneous measurement the waiting time of 15 minutes is acceptable with respect to time lapse for bringing the sample to the specified laboratories for measurement. The percentage of colour content present in the RPPs with varying Pb concentrations (0 to 600 ppm) are tabulated in Table 4.2. The percentage values are repeatable within error range, three sets of data have been taken and a slandered error of 0.15% (error range) have been calculated (see supporting information). The corresponding values of red (%), green (%), blue (%) have also been plotted and shown in Figure 4.11. Here we found that the percentage of red content is increasing linearly while the blue is decreasing linearly with Pb concentration. However, the green content is almost remains same for all the concentrations. From the colorimetric assays as represented in Figure 4.9a, we have observed that there is a gradual increase in the red content

of the sensor strips with an increment of Pb concentration which is also consistent with the finding of the device.

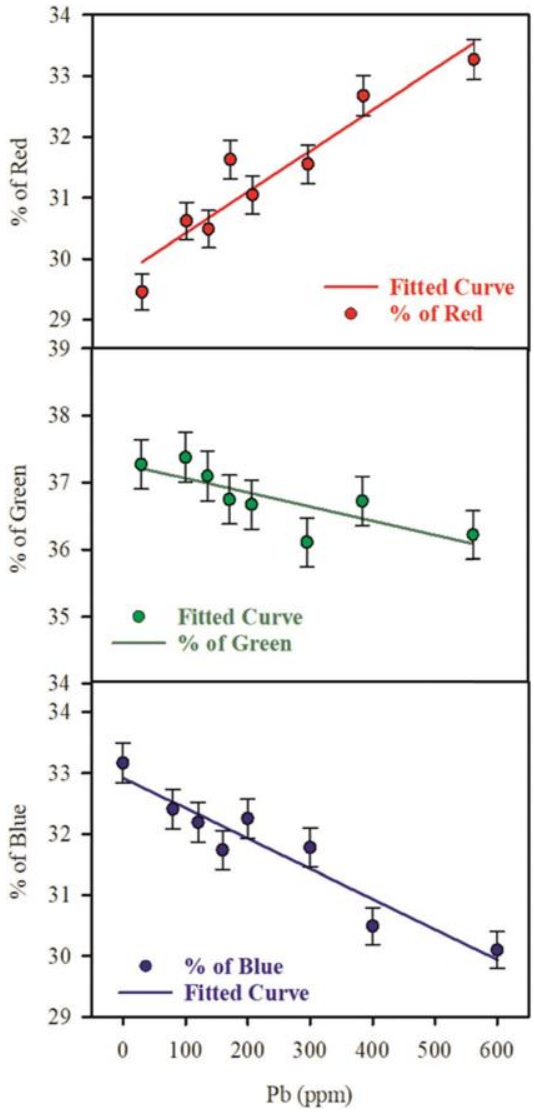

Figure 4.11: *(a) Percentage of red (red curve), blue (blue curve) and green (green curve) content present in the paper-based strips for different concentra- tions of Pb extract. Calibration curve for (a) red, (b) green and (c) blue content present in the paper-based sensor in the presence of different concentrations of Pb extract.*

All these curves i.e. % red, % blue and % green content (shown in Figure 4.11, with 0.15% slandered deviation) have been fitted with straight line (equation y = A + B x), where the values of A, B are tabulated in Table 4.3. The device has been calibrated with the linear response that we have found for red content i.e. the linear calibration is equation y = 29.5 + 0.0067 x. According to the given calibration equation the device shows the value of Pb in ppm within 2 min. Additionally, we have calculated the limit of detection (LOD) to be 50 ppm by

taking 95% of confidence interval (probability of being larger than the blank) [73]. The device response has also been revalidated with samples of various Pb concentrations after the calibration.

Table 4.3: *Fitting parameters.*

% Content	A	B
Red	29.9±0.24	0.0067±0.00117
Green	37.3±0.16	-0.0024±0.00081
Blue	32.9±0.23	-0.005±0.001

The overall working mechanism citrate functtionalized AgNPs towards Pb detectecion has been shown in scheme 4.1.

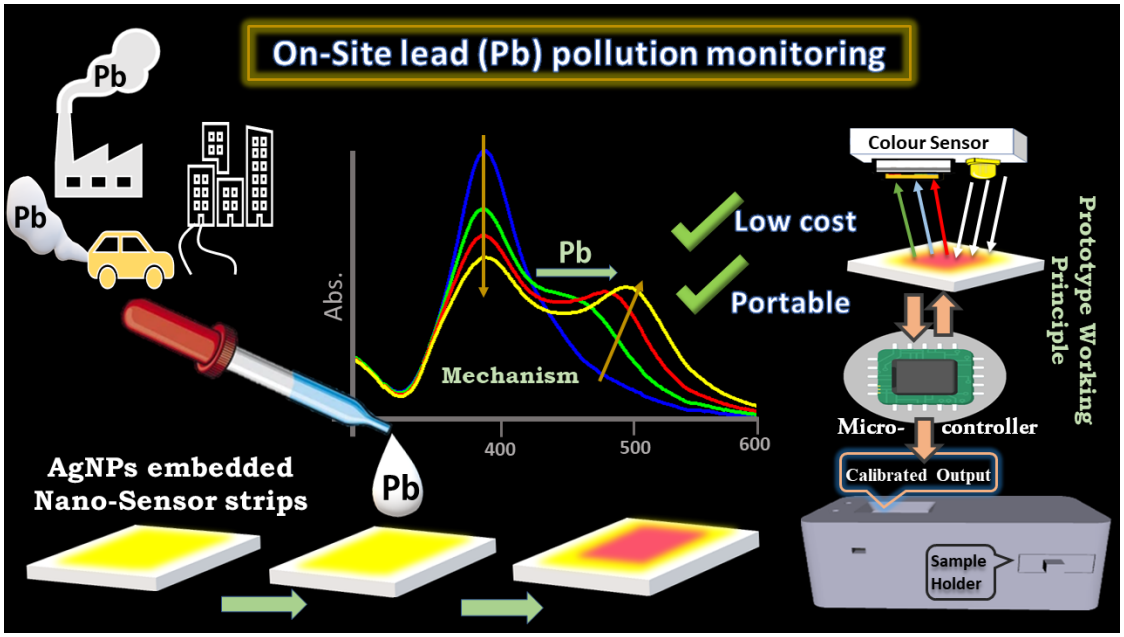

Scheme 4.1: *The overall working mechanism of the citrate functtionalized AgNPs as a lead sensor.*

4.2.3. A Nanosensor-based Prototype Development for Heavy Metal Detection: A Combined Spectroscopic and Theoretical Study [74]: Here, we used Au nanoparticles functionalized with citrate, for potential use in sensing lead, a well-known agent for environmental pollution. The citrate adlayer formed of interacting citrate molecules acts as a stabilizing agent on the surface of bare AuNPs. The citrate functionalized AuNPs are highly stable at pH 6.5 and

have a three to four months shelf-life [58]. The TEM micrograph (Figure 4.12a) shows the spherical shape of the citrate functionalized gold nanoparticles (AuNPs). The average diameter from TEM and the hydrodynamic diameter from DLS of the AuNPs is 9.99±0.03 nm and 37.8 nm with a surface zeta potential of -29.2 mV.

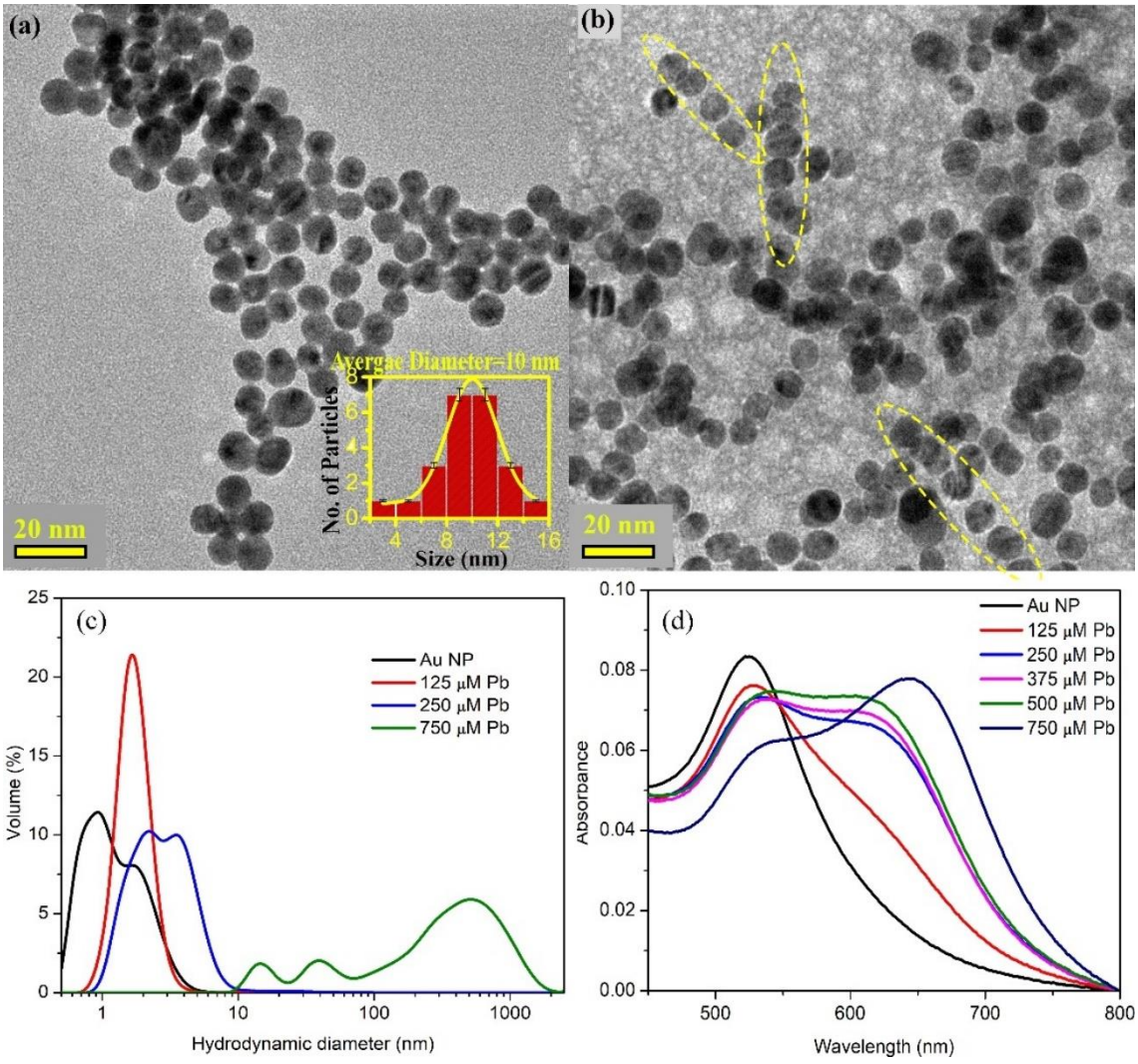

Figure 4.12: *(a) TEM image of the AuNPs. Inset of Figure shows the size distribution of the AuNPs. (b) TEM image of the AuNPs after interaction with Pb^{2+}. (c) Volume distribution of hydrodynamic diameter of AuNPs (in black) before and after interaction with different concentrations of Pb^{2+}. (d) UV–Vis absorbance spectra of AuNPs after interaction with Pb^{2+}.*

The TEM micrograph (Figure 4.12b) corresponding to 250 µM of Pb^{2+} reveals that, due to the presence of Pb, AuNPs come closer to each other, forming a rod consisting of NPs such that the Pb^{2+} matrix would have acted to couple the AuNPs together. Furthermore, longitudinal size is due to the aggregation of NPs in rod geometry. It is evident from Figure 4.12c that the average hydrodynamic

diameter of the AuNPs increases with the increment in Pb^{2+} ions. The surface zeta potential of the AuNPs tends to be more positive (Table 4.4) with the addition of Pb^{2+} ions in the system.

Table 4.4: *Size and surface charge characteristics upon interaction with Pb^{2+}.*

System	Hydrodynamic Diameter (nm)	Zeta Potential (mV)
Au NP	37.8	-29.200
Au NP +125 µM Pb^{2+}	68.1	-12.800
Au NP +250 µM Pb^{2+}	91.3	-16.500
Au NP +500 µM Pb^{2+}	295.0	-15.000
Au NP +750 µM Pb^{2+}	396.0	0.008

The characteristic LSPR absorbance band of Au NP is found to be around 520 nm (Figure 4.12d) consistent with the previously reported literature [37]. This peak corresponds to the LSPR of a non-aggregated single NP. To evaluate the aggregation behaviour of the AuNPs upon interaction with Pb^{2+} ions, we monitored the change in the absorbance of the LSPR band of the AuNPs (~520 nm). Procedure for Pb^{2+} sensing experiments are mentioned in details in the materials and method section under subsection 'd' of SI. Upon interaction of Pb^{2+} ions, the AuNPs form non-spherical aggregates which give rise to a new LSPR band at around ~650-670 nm and consequently, the peak intensity at ~520 nm decreases (Figure 4.12d). This simultaneous existence of two peaks may be attributed to the existence of two types of species: the larger self-assembled aggregates of AuNPs with Pb^{2+} along with single AuNPs. The gradual red shift of the new peak at ~650-670 nm with increasing lead concentration, may be due to the non-spherical arrangement of the nanoparticles within the system. The AuNPs here present within the system in two simultaneous modes (longitudinal and transverse) associated with the surface plasmon oscillation of electron cloud along and perpendicular to the axis of the one-dimensional self-assembled rods-like architecture of the NPs [45]. The absorption maxima of the longitudinal mode consequently shift towards red whereas the peak at around 520 nm remains in the same position. This clearly implies the formation of a pseudo

nanorod, having a fixed transverse width but increasing longitudinal length which only corresponds to the formation of nanorod [75]. The LSPR spectra of the NPs for other geometrical aggregates do not follow such pattern. Thus, these findings indicate the formation of an aggregated geometry which is similar to the linear, one-dimensional rod like self-assembly of the nanoparticles [55]. The DLS and the TEM studies of the AuNPs on addition of Pb^{2+} ions also corroborate with the formation of larger self-aggregated species. This further corroborates the attachment of the Pb^{2+} ions with the citrate moiety of the AuNPs rending an increase in the hydrodynamic diameter of the aggregated species and a more positive zeta potential value. Although, the simultaneous increase in the aggregated peak (~650-670 nm) and the decrease of the LSPR peak of Au NP upon increasing lead concentration indicates a gradual decrease in the number of free nanoparticles accompanied by an increase in the number of self-assembled NPs, it is to be noted that not all the NPs are engaged in aggregation upon Pb^{2+} interaction, some of them remain intact as single NPs. The mechanism of interaction of the AuNPs with Pb^{2+} ions could be explained by the electrostatic interaction between the negatively charged citrate capped AuNPs (-29.2 mV, Table 4.4) with the positively charged divalent Pb^{2+} ions, in such a way that it encloses the nearby matrix of the rod like geometry of the NPs. The high affinity of the citrate moiety adsorbed on the NP surface towards lead also makes it favourable towards its interaction with Pb^{2+} ions [57, 58]. Additionally, citrate possesses a very high interaction affinity with Pb^{2+}. The involvement of citrate in hydrogen bonds with water molecules and abutting Pb–citrate moieties lead to a stable structure. The change in LSPR spectra of AuNPs upon addition of Pb is also a time-dependent phenomenon. The spectroscopic changes are observed with time and it has been found that in 20 minutes time duration, the response of the AuNP nanosensor reaches maximum (Figure 4.13a-e). The limit of detection (LOD) and sensitivity of the sensor has been calculated at both 0 and 20 min, and it is found that the LOD of the sensor at time t=0 is 73 μM and at t=20min is 56 μM. (Figure 4.13f, g). In order to evaluate the temporal dependency of AuNPs towards Pb^{2+}, we allowed the NPs to interact with the Pb^{2+} ions for up

to 20 minutes of incubation time, beyond which no significant spectral changes have been observed. The temporal variation of the AuNPs for after interaction with 0 to 625 μM of Pb^{2+} is shown in Figure 4.13a-f.

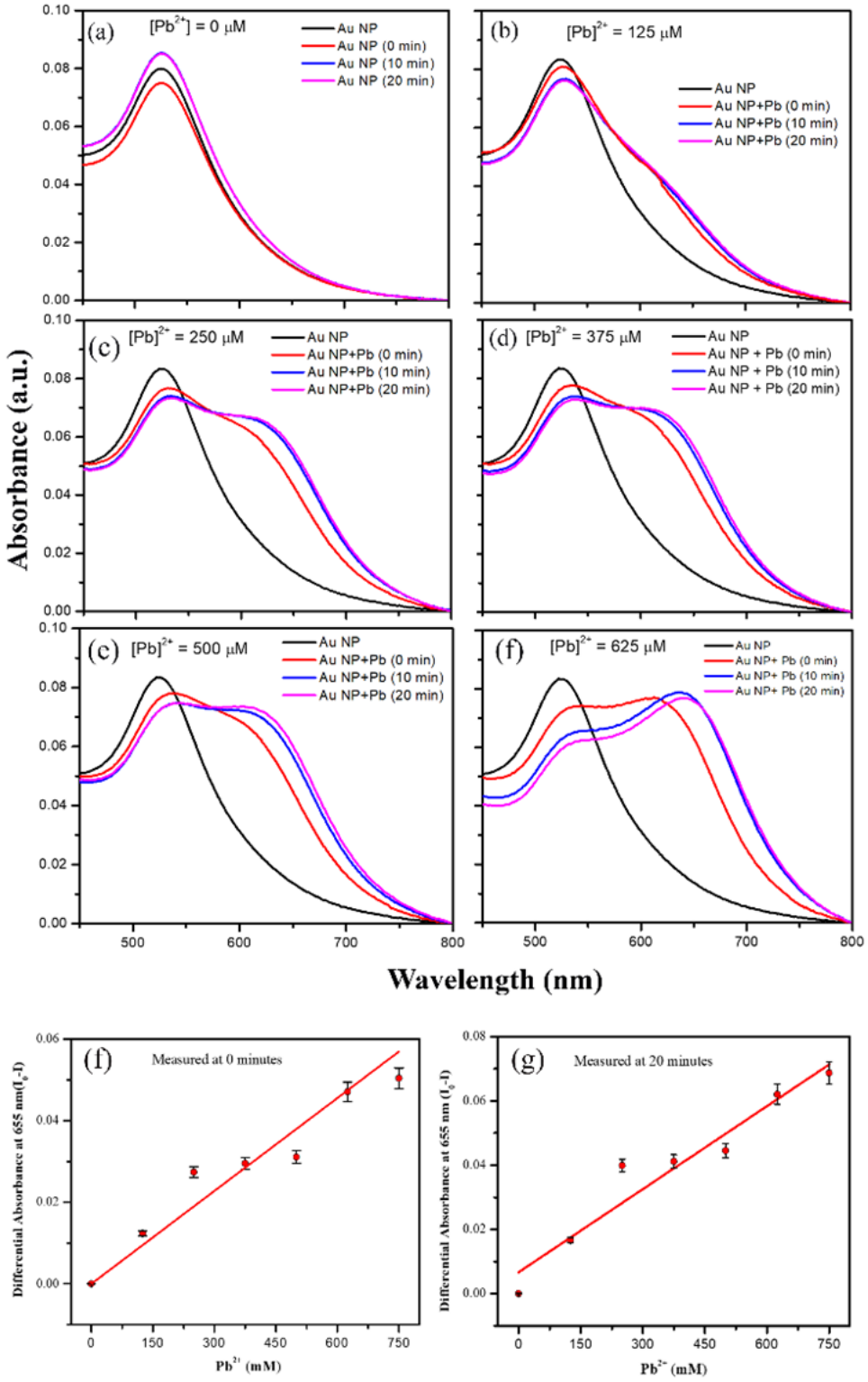

Figure 4.13: *(a-e) Temporal dependency of Au NP on different concentration of lead at different time points. (f) and (g) The linear response of the sensor at 655 nm at 0 minutes and 20 minutes respectively.*

It has been observed that with the passage of time the intensity of the LSPR peak of AuNPs (~520 nm) decreases and consequently, the intensity of the second peak (~ 670 nm) increases. This result suggests that the affinity of the interaction of the AuNPs with the Pb^{2+} ions increases with a longer incubation time. Moreover, the increase in the spectral shift towards a longer wavelength with respect to time for a specific concentration of Pb^{2+} is also indicative of the formation of larger self-assembled aggregates. In order to evaluate the response of the sensor at different time points, we evaluated the sensitivity and the LOD of the sensor at 0 min and 20 minutes (Figure 4.13f,g). It follows a linear relationship for both the cases and is governed by the equations $Y = 7.59 \times 10^{-5} X - 2.59 \times 10^{-6}$ and $Y = 8.61 \times 10^{-5} X - 0.00668$ respectively for 0 min and 20 min, where Y is the differential absorbance and X represents the Pb^{2+} ion concentration. The LOD of the sensor at time t=0 is 73 μM and at t=20 min 56 μM has been calculated. As clearly observed, we can to much lower limit of detection with increase in reaction time.

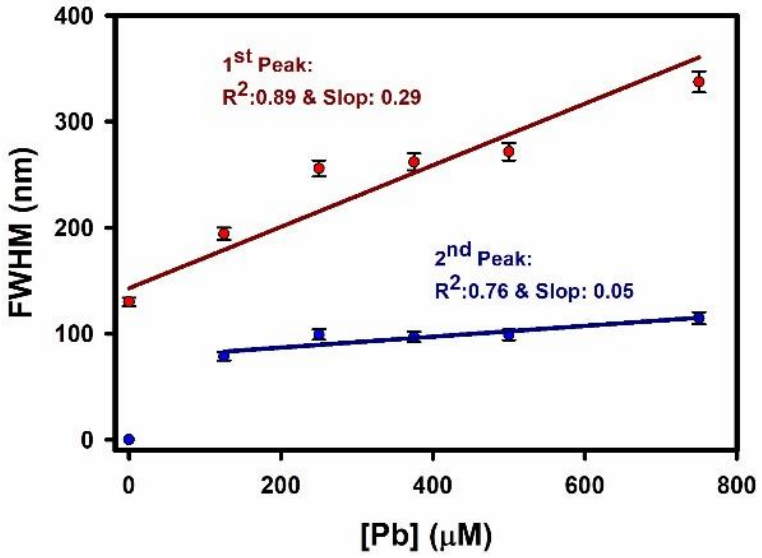

Figure 4.14: *FWHM variation of absorption maxima at 520 nm and 650 nm with increase in Pb concentration.*

Also, the sensitivity of the sensor increased from 7.59 x 10-5 at t=0 minute to 8.62 x 10^{-5} at t = 20 minute, due to more interaction and complexation of the Pb^{2+} ions with the AuNPs. As we have observed from the LSPR spectra with varying concentration Pb concentrations, the FWHM of the peak corresponding to 520

nm and 650 nm varies significantly. It could have also been a good parameter for Pb sensing (Figure 4.14). However, the developed prototype is based on the principle of measurement of change in intensity of the red end of the EM spectrum, these changes in intensity are inherently included through the changes in LSPR peaks i.e. the generation of the second peak and redshift. Hence, we have limited our study to the changes in LSPR peaks in this context.

Similarly as in the case of AgNPs, for further confirmation of the geometrical arrangement of the aggregated AuNPs, and to find out the percentage of the aggregates, we have fitted the LSPR spectra of the Pb added system with model absorption cross-section equations of single NP $\sigma_{abs(1)}$ (equation 4.4) and NP dimer $\sigma_{abs(2)}$ (equation 4.6). Here, we have introduced the wavelength dependency of the dielectric constant of the NP material through the best-fitted equations based on available calculated data for gold [61]. The real (ε_1) and imaginary part (ε_2) of ε for gold have been fitted separately and the fitted equations are given as

$$\varepsilon_1 = A_1 + A_3 \qquad 4.11$$

$$\varepsilon_1 = \exp(B_1 + B_2\lambda + B_3\lambda^2) \qquad 4.12$$

Here A_1, A_2, B_1, B_2, and B_3 are the appropriated real-valued fitting parameters. The LSPR spectra of the AuNPs before and after the addition of Pb^{2+} are shown in Figure 4.15a, Au NP (black), AuNP + 125 mM Pb (red), AuNP + 250 mM Pb (blue). The spectrum of Au NP has been fitted solely with the absorption cross-section of single NPs $\sigma_{abs(1)}$ whereas to fit the red and blue spectra absorption cross-section of single NPs as well as NPs aggregates, i.e., NPs dimer $\sigma_{abs(2)}$ have been used. We have put R=4.5 nm based on our experimental finding to fit the black spectrum. As distinctively appeared from the fitted curve, the resonance enhancement (i.e. when $\varepsilon_1=-2\varepsilon_m$) occurred for wavelength near 520 nm which exactly resembles our experimentally obtained LSPR peak (Figure 4.15b). Thereafter, red and blue spectra have been fitted with suitable combination of $\sigma_{abs(1)}$ and $\sigma_{abs(2)}$ the model equations which found to best fit two spectra are

$$\sigma_{abs} = \frac{8\pi^2 R^3}{\lambda}\{(\sigma_{abs}(1)) + 2(\sigma_{abs}(2))\} \quad 4.13.$$

$$\sigma_{abs} = \frac{8\pi^2 R^3}{\lambda}\{(\sigma_{abs}(1)) + 4(\sigma_{abs}(2))\} \quad 4.14$$

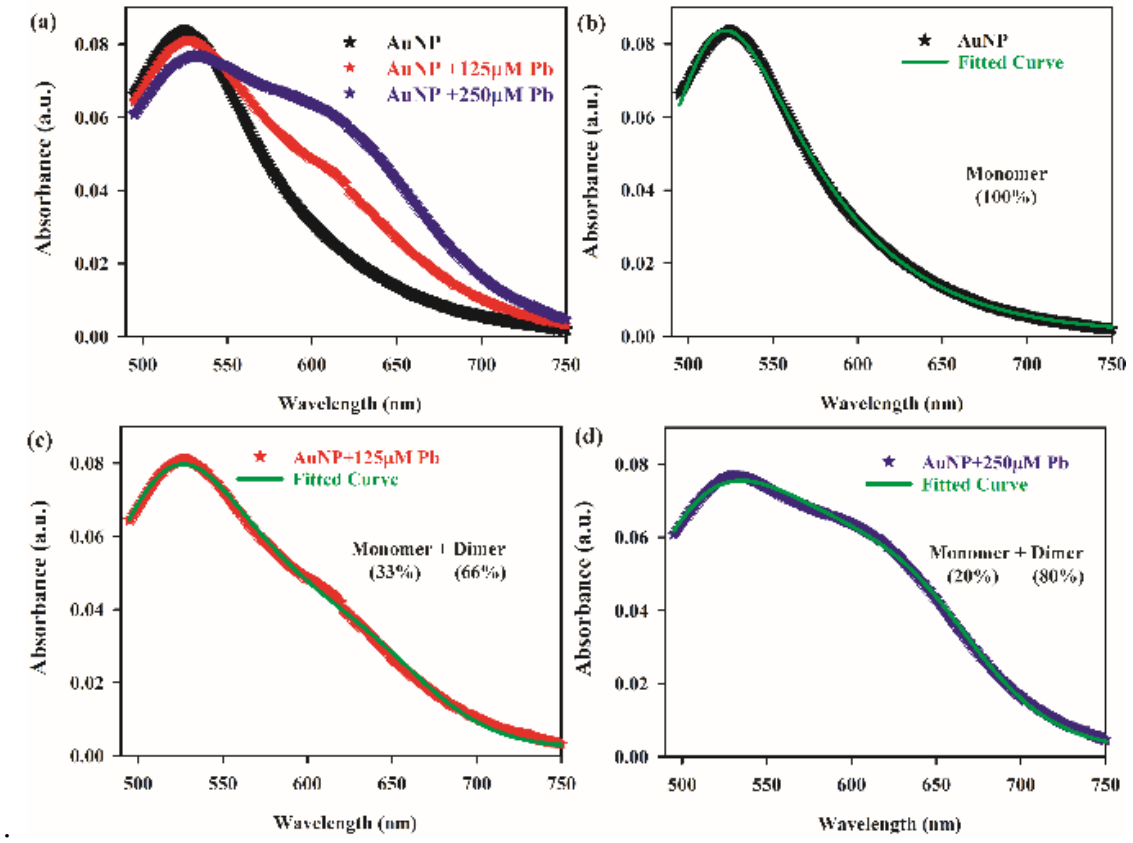

Figure 4.15: *(a) The UV–Vis absorbance spectra of AuNPs before (black) and after interaction with 125 mM (red) and 250 mM (blue) of Pb^{2+}. (b) AuNPs its fitted curve following equation for absorption cross-section of single NPs $\sigma_{abs(1)}$, (c) AuNPs +125 mM Pb^{2+} and its fitted curve following cross-section of single NPs and NPs dimer mixed system in ratio of 1:2, and (d) AuNPs +250 mM Pb^{2+} and its fitted curve following absorption cross-section of single NPs and NPs dimer mixed system in ratio of 1:4.*

The fitting results resemble that in case of 125 mM Pb. The ratio of $\sigma_{abs(1)}$ and $\sigma_{abs(2)}$ is 1:2 (Figure 4.15c) whereas for 250 mM Pb this ratio has increased to 1:4 (Figure 4.15d) indicating the tendency to form pseudo rod-shaped geometry in presence of Pb. The fitting parameters have been tabulated in Table 4.5. The appearance of red-shifted peak is appropriately justified by the longitudinal mode of the NP dimer absorption cross-section equation. It supports our elucidation that with an increase in Pb^{2+} concentration, more AuNPs are assembled to form longer aggregates, resulting in more redshifts in LSPR peaks.

Table 4.5: *List of parameters for ε_1 and ε_2 which best fit the equations (4.4), (4.12) and (4.14).*

Parameters	Au NP	Au NP + 125 µM Pb^{2+}	Au NP + 250 µM Pb^{2}
A_1	40.2673	17.13586	2.52149
A_2	-0.08216	-0.03703	-0.00952
B_1	11.00	10.85975	20.35133
B_2	-0.04398	-0.0414	-0.07018
B_3	4.84284E-5	4.26785E-5	6.31039E-5

In addition, we investigated the response of AuNPs to other relevant metal ions present in the environment such as Ni^{2+}, Co^{2+}, Zn^{2+}, Mg^{2+}, Cd^{2+}, Na^{+}, $K^{+,}$ and Cu^{2+} (Figure 4.16a,b) at both 650 nm and 525 nm. The study shows that the AuNPs show high selectivity towards Pb^{2+} ions and don't have any significant spectral changes in response to the other metal ions mentioned above. Herein, we developed a prototype device that utilizes the spectroscopic results we have obtained after the addition of Pb^{2+}. As the concentration of Pb increases, the absorbance at 650 nm also increases and this change has been utilized as a Pb detection marker. The measurements were taken from the indigenously developed device through the sample, dropcasted on a cellulose paper substrate. We have used Whatman grade 4 filter paper as a paper substrate for performing sensing measurements through the prototype. The Choice of the cellulose filter paper as a substrate for the sensing experiment is based on the fact that it mainly consists of α-cellulose (~98%) and hence ensures minimal interference from other relevant components (trace pollutants, coatings, etc.) . The cellulose paper substrate is largely composed of microscale cellulose fibrous strands which are interwoven with the other smaller strands, providing a large active surface area. The use of Whatman grade 4 filter paper is advantageous in many respects while considering the homogeneous dispersion of the sensor. Due to its improved, homogenous and fast flow rate, embedment of the AuNPs sensor is preferable in these cellulose materials [70]. All the information from the paper substrate were collected in transmission geometry. For that, every time 20µL of the prepared ion (heavy metal) solution and 50µL ~180nM of AuNPs were mixed

priorly and then 5 µL of solution was dropcasted on the paper substrate for measurement. Figure 4.16c depicts the schematic of the indigenously developed prototype for the detection of Pb^{2+} ions for the potential quantification of lead within the environment. The device was calibrated with the absorbance values at the red end of the spectrum (~650 nm).

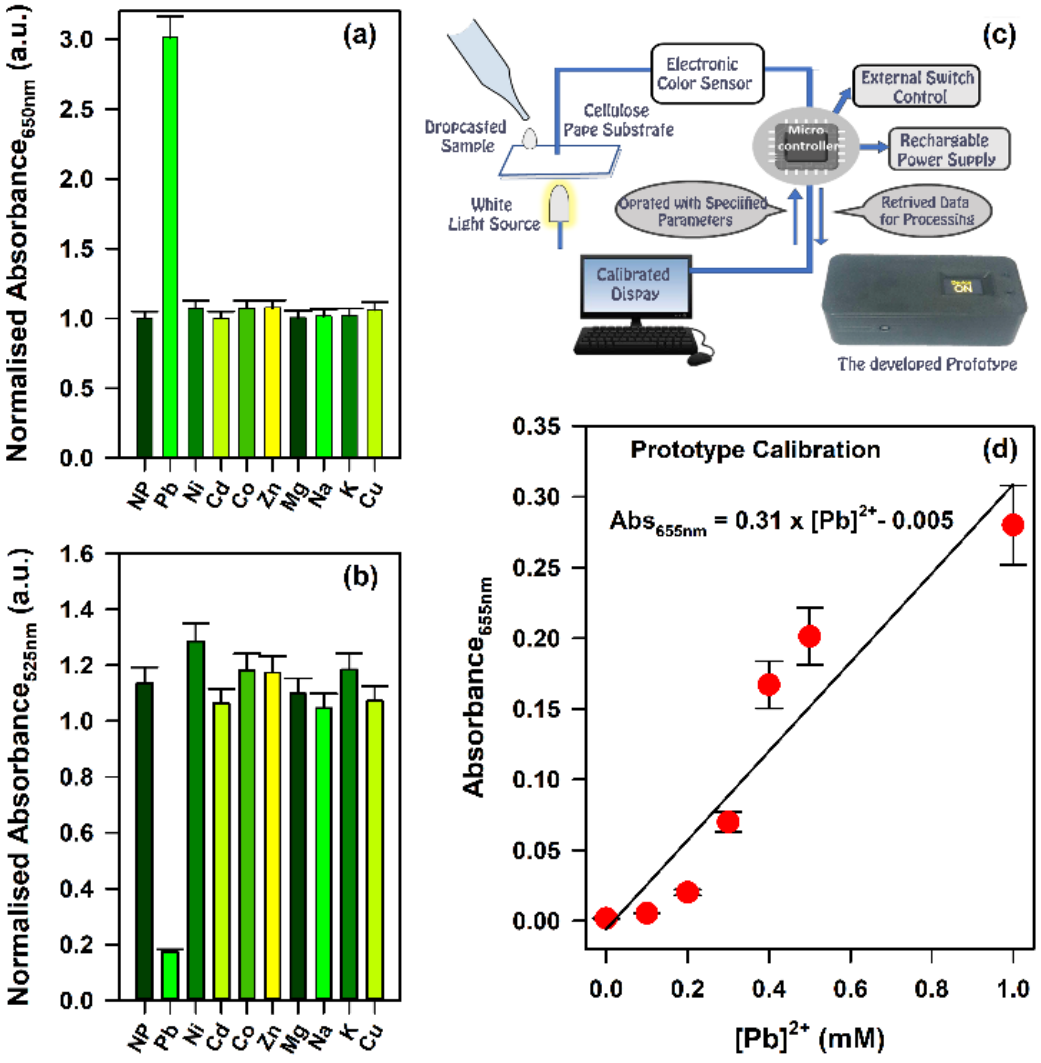

Figure 4.16: *The sensor response in presence of other metal ions measured at (a) 650 nm and (b) 525 nm. (c) Schematic of the experimental setup for absorbance measurement of the samples on paper-substrates in transmittance mode, below inset shows the design of the prototype. (d) The calibration curve for the developed prototype using Au NP sensor with varying Pb^{2+}concentrations at 650 nm.*

The absorption maxima $\log(I_0/I)$ at 650nm before and after incubation with varying Pb^{2+} concentration has been plotted and shown in Figure 4.16d. The developed prototype works on the basic principle of spectrophotometry, where the white LED light source and the detector are at an angle of 180˚ to each other.

The raw data from the detector in the form of intensity was collected through an electronic color sensor, and the signal corresponding to the red channel was processed through a microcontroller operated by an indigenously developed software in the Arduino platform for further processing. The I_0 is the absorbance at 650 nm in the absence of Au NP, and I represent the absorbance of AuNPs at the same peak position after complexation with Pb^{2+} ions. The absorbance $\log(I_0/I)$ for all concentrations from 0 to 1mM at 655 nm follows a linear relationship and can be represented by the equation Y = 0.31 X - 0.005, where Y is the differential absorbance and X represents the Pb^{2+} ion concentration.

4.3. Conclusion:

In summary, we have investigated the role of Pb^{2+} towards definite one-dimensional chain like self-aggregation of citrate capped silver and gold nanoparticle using UV-Vis, DLS and TEM measurement supported with analytically calculated absorption cross-section equations for NPs and NP-pair system based on quasi-static approximation. Self-assembled anisotropic geometry of formed 1D NPs chain leads to the coupling nearby LSPR modes of NPs thereby new modes at a higher wavelength (~520 nm) have generated along with existing LSPR band (~395 nm). TEM and HRTEM images of the lead added Ag/AuNPs systems confirms the formation of 1D self-assembled geometry of NPs. The fact that increment in Pb^{2+} concentration leads to the formation of longer NP chains is verified by the fitting of analytically calculated NP and NP-pair equations in an appropriate ratio. Eventually we optimize several other NP parameters such as size, concentration and interaction time towards Ag/ AuNPs to be utilized as an efficient Pb^{2+} sensor. Presence of other relevant metal ions is also been studied which suggests that only Pb^{2+} is capable of generation of 1D chain like geometry of the NPs. This spectroscopic and microscopic results incite the detailed 1D self-assembly of Ag/ AuNPs in the presence of Pb^{2+} and both Ag/AuNPs have been proven to be used as highly selective, favourably sensitive tools to detect lead for potential application in industrial wastewater pollution as well as air pollution monitoring. Finally, we extended the studies for both

silver and gold toward the development of the colorimetric paper-based prototype. Herein, we report a highly selective, portable, low-cost device with the improved technique of retroreflection, which towards Pb. Our developed prototype is superior to conventional techniques for Pb detection in air due to its portability and infield measurement facility. Also, our developed device has been IoT enabled for almost instant transfer of data, especially from remote areas. Thus, the outcomes from this study provide a future platform for the development of such low-cost, field-deployable techniques for heavy metal detection. Overall, this study gives insights for the development of a highly selective low-cost prototype for the detection and quantification of lead present in the environment, whose application may further be extended to analyze industrial wastes.

References

[1] J. Wu, M. Li, H. Tang, J. Su, M. He, G. Chen, L. Guan, J. Tian, Portable paper sensors for the detection of heavy metals based on light transmission-improved quantification of colorimetric assays, *Analyst* 144 (2019) 6382.

[2] D. A. Thai, N. Y. Lee, A paper-based colorimetric chemosensor for rapid and highly sensitive detection of sulfide for environmental monitoring, *Anal. Methods.* 13 (2021) 1332.

[3] P. K. Jain, X. Huang, I. H. El-Sayed, M. A. El-Sayed, Review of some interesting surface plasmon resonance-enhanced properties of noble metal nanoparticles and their applications to biosystems, *Plasmonics* 2 (2007) 107.

[4] N. Wu, Plasmonic metal–semiconductor photocatalysts and photoelectrochemical cells: A review, *Nanoscale* 10 (2018) 2679.

[5] D. O'Connor, A. V. Zayats, The third plasmonic revolution, *Nat. Nanotech.* 5 (2010) 482.

[6] S. K. Gray, Surface plasmon-enhanced spectroscopy and photochemistry, *Plasmonics* 2 (2007) 143.

[7] K. L. Kelly, E. Coronado, L. L. Zhao, G. C. Schatz, The optical properties of metal nanoparticles: The influence of size, shape, and dielectric environment, *J. Phys. Chem. B* 107 (2003) 668.

[8] J. Homola, M. Piliarik, Surface plasmon resonance (SPR) sensors in Surface plasmon resonance based sensors, *Springer*, Berlin & Heidelberg, 2006.

[9] M. R. Knecht, M. Sethi, Bio-inspired colorimetric detection of Hg^{2+} and Pb^{2+} heavy metal ions using Au nanoparticles, *Anal. Bioanal. Chem.* 394 (2009) 33.

[10] Y. Wu, H. Pang, Y. Liu, X. Wang, S. Yu, D. Fu, J. Chen, X. Wang, Environmental remediation of heavy metal ions by novel-nanomaterials: A review, *Environ. Pollut.* 246 (2019) 608.

[11] R. M. Harrison, D. Laxen, Lead pollution: Causes and control, *Chapman and Hall Ltd.*, London & New York, 1981.

[12] B. Gao, L. Chi, R. Mahbub, X. Bian, P. Tu, H. Ru, K. Lu, Multi-omics reveals that lead exposure disturbs gut microbiome development, key metabolites, and metabolic pathways, *Chem. Res. Toxicol.* 30 (2017) 996.

[13] J. Wieczorek, A. Baran, K. Urbański, R. Mazurek, A. Klimowicz-Pawlas, Assessment of the pollution and ecological risk of lead and cadmium in soils, *Environ. Geochem. Health* 40 (2018) 2325.

[14] J. Tulinska, Z. Krivošíková, A. Liskova, M. L. Mikusova, V. Masanova, E. Rollerova, K. Stefikova, L. Wsolova, A. Babelova, Ľ. Tóthová, Six-week inhalation of lead oxide nanoparticles in mice affects antioxidant defense, immune response, kidneys, intestine and bones, *Environ. Sci. Nano* 9 (2022) 751.

[15] Y. Erel, R. Pinhasi, A. Coppa, A. Ticher, O. Tirosh, L. Carmel, Lead in archeological human bones reflecting historical changes in lead production, *Environ. Sci. Technol.* 55 (2021) 14407.

[16] H. Bode, Lead-acid batteries, *John Wiley & Sons*, New York, 1977.

[17] G. Macchi, M. Pagano, M. Santori, G. Tiravanti, Battery industry wastewater: Pb removal and produced sludge, *Water Res.* 27 (1993) 1511.

[18] A. C. V. dos Santos, J. C. Masini, Evaluating the removal of Cd (II), Pb (II) and Cu (II) from a waste water sample of a coating industry by adsorption onto vermiculite, *Appl. Clay Sci.* 37 (2007) 167.

[19] U. Aleksander-Kwaterczak, E. Helios-Rybicka, Contaminated sediments as a potential source of Zn, Pb, and Cd for a river system in the historical metalliferous ore mining and smelting industry area of South Poland, *J. Soils Sediments* 9 (2009) 13.

[20] V. K. Gupta, I. Ali, Removal of lead and chromium from wastewater using bagasse fly ash: A sugar industry waste, *J. Colloid. Interface Sci.* 271 (2004) 321.

[21] M. Arbabi, S. Hemati, M. Amiri, Removal of lead ions from industrial wastewater: A review of removal methods, *Int. J. Epidemiol. Res.* 2 (2015) 105.

[22] L. Xiaolin, Y. Zhang, T. Mingguang, L. Jiangfeng, B. Liangman, G. Zhang, L. Yan, I. Atsuo, Atmospheric lead pollution in fine particulate matter in Shanghai, China, *Res. J. Environ. Sci.* 21 (2009) 1118.

[23] P. Hien, N. Binh, N. Ngo, V. Ha, Y. Truong, N. An, Monitoring lead in suspended air particulate matter in Ho Chi Minh City, *Atmos. Environ.* 31 (1997) 1073.

[24] S. A. Maier, Plasmonics: Fundamentals and applications, *Springer*, New York, 2007.

[25] K. Khurana, N. Jaggi, Localized surface plasmonic properties of Au and Ag nanoparticles for sensors: A review, *Plasmonics* (2021).

[26] Y. Guo, Z. Wang, H. Shao, X. Jiang, Stable fluorescent gold nanoparticles for detection of Cu^{2+} with good sensitivity and selectivity, *Analyst* 137 (2012) 301.

[27] H. Zhang, K. H. Fung, J. r. Hartmann, C. T. Chan, D. Wang, Controlled chainlike agglomeration of charged gold nanoparticles via a deliberate interaction balance, *J. Phys. Chem. C* 112 (2008) 16830.

[28] H. Zhang, D. Wang, Controlling the growth of charged-nanoparticle chains through interparticle electrostatic repulsion, *Angew. Chem.* 120 (2008) 4048.

[29] Y. W. Lin, C. C. Huang, H. T. Chang, Gold nanoparticle probes for the detection of mercury, lead and copper ions, *Analyst* 136 (2011) 863.

[30] D. Vilela, M. C. González, A. Escarpa, Sensing colorimetric approaches based on gold and silver nanoparticles aggregation: Chemical creativity behind the assay, *Anal. Chim. Acta.* 751 (2012) 24.

[31] M. Guo, W. C. Law, X. Liu, H. Cai, L. Liu, M. T. Swihart, X. Zhang, P. N. Prasad, Plasmonic semiconductor nanocrystals as chemical sensors: Pb^{2+} quantitation via aggregation-induced plasmon resonance shift, *Plasmonics* 9 (2014) 893.

[32] P. K. Sarkar, A. Halder, N. Polley, S. K. Pal, Development of highly selective and efficient prototype sensor for potential application in environmental mercury pollution monitoring, *Water Air Soil Pollut.* 228 (2017) 314.

[33] A. Alizadeh, M. Khodaei, C. Karami, M. Workentin, M. Shamsipur, M. Sadeghi, Rapid and selective lead (II) colorimetric sensor based on azacrown ether-functionalized gold nanoparticles, *Nanotechnology* 21 (2010) 315503.

[34] S. Di Stasio, Electron microscopy evidence of aggregation under three different size scales for soot nanoparticles in flame, *Carbon* 39 (2001) 109.

[35] Y. Soda, E. Bakker, Quantification of colorimetric data for paper-based analytical devices, *ACS Sens.* 4 (2019) 3093.

[36] L. Beqa, A. K. Singh, S. A. Khan, D. Senapati, S. R. Arumugam, P. C. Ray, Gold nanoparticle-based simple colorimetric and ultrasensitive dynamic light scattering assay for the selective detection of Pb (II) from paints, plastics, and water samples, *ACS Appl. Mater. Interfaces* 3 (2011) 668.

[37] A. D'Agostino, A. Taglietti, B. Bassi, A. Donà, P. Pallavicini, A naked eye aggregation assay for Pb^{2+} detection based on glutathione-coated gold nanostars, *J. Nanoparticle Res.* 16 (2014) 2683.

[38] J. P. Devadhasan, J. Kim, A chemically functionalized paper-based microfluidic platform for multiplex heavy metal detection, *Sens. Actuators B: Chem.* 273 (2018) 18.

[39] V. Veeramani, Y. H. Chen, H. C. Wang, T. F. Hung, W. S. Chang, D. H. Wei, S. F. Hu, R. S. Liu, CdSe/ZnS QD@CNT nanocomposite photocathode for improvement on charge overpotential in photoelectrochemical Li-O_2 batteries, *Chem. Eng. J.* 349 (2018) 235.

[40] Q. Liu, Y. Lin, J. Xiong, L. Wu, X. Hou, K. Xu, C. Zheng, Disposable paper-based analytical device for visual speciation analysis of Ag (I) and silver nanoparticles (AgNPs), *Anal. Chem.* 91 (2019) 3359.

[41] Z. Xia, D. Li, W. Deng, Identification and detection of volatile aldehydes as lung cancer biomarkers by vapor generation combined with paper-based thin-film microextraction, *Anal. Chem.* 93 (2021) 4924.

[42] L. Qi, Y. Shang, F. Wu, Colorimetric detection of lead (II) based on silver nanoparticles capped with iminodiacetic acid, *Microchim. Acta* 178 (2012) 221.

[43] H. Cao, M. Wei, Z. Chen, Y. Huang, Dithiocarbamate-capped silver nanoparticles as a resonance light scattering probe for simultaneous detection of lead (II) ions and cysteine, *Analyst* 138 (2013) 2420.

[44] Z. A. Tagar, N. Memon, M. H. Agheem, Y. Junejo, S. S. Hassan, N. H. Kalwar, M. I. Khattak, Selective, simple and economical lead sensor based on ibuprofen derived silver nanoparticles, *Sens. Actuators B Chem.* 157 (2011) 430.

[45] C. Xi, P. F. Marina, H. Xia, D. Wang, Directed self-assembly of gold nanoparticles into plasmonic chains, *Soft Matter* 11 (2015) 4562.

[46] E. Hao, G. C. Schatz, Electromagnetic fields around silver nanoparticles and dimers, *J. Chem. Phys.* 120 (2004) 357.

[47] J. Zuloaga, E. Prodan, P. Nordlander, Quantum description of the plasmon resonances of a nanoparticle dimer, *Nano Lett.* 9 (2009) 887.

[48] A. Szalai, Á. Sipos, E. Csapó, L. Tóth, M. Csete, I. Dékány, Comparative study of plasmonic properties of cysteine-functionalized gold and silver nanoparticle aggregates, *Plasmonics* 8 (2013) 53.

[49] T. K. Maji, D. Bagchi, N. Pan, A. Sayqal, M. Morad, S. A. Ahmed, D. Karmakar, S. K. Pal, A combined spectroscopic and ab initio study of the transmetalation of a polyphenol as a potential purification strategy for food additives, *RSC Adv.* 10 (2020) 5636.

[50] R. García, A. Báez, Atomic absorption spectrometry (AAS), *IntechOpen*, Rijeka, 2012.

[51] M. Ochsenkühn-Petropoulou, K. M. Ochsenkühn, Comparison of inductively coupled plasma–atomic emission spectrometry, anodic stripping voltammetry and instrumental neutron-activation analysis for the determination of heavy metals in airborne particulate matter, *Fresenius J. Anal. Chem.* 369 (2001) 629.

[52] J. Su, Portable and sensitive air pollution monitoring, *Light Sci. Appl.* 7 (2018) 3.

[53] Air pollution monitoring in, *United State Enviornmental Protection Agency*, 2022.

[54] National air quality standards, in, *Central pollution control board, goverrntment of India*, 2022.

[55] N. Pan, T. K. Maji, S. Bandyopadhyay, P. Biswas, A. Chatterjee, M. Mitra, A. Chatterjee, S. K. Pal, A combined spectroscopic and theoretical analysis of plasmonic silver nanoparticle sensor towards detailed microscopic understanding of heavy metal detection, *Plasmonics* 17 (2022) 223.

[56] H. Xia, G. Su, D. Wang, Size-dependent electrostatic chain growth of pH-sensitive hairy nanoparticles, *Angew. Chem.* 125 (2013) 3814.

[57] M. Kourgiantakis, M. Matzapetakis, C. Raptopoulou, A. Terzis, A. Salifoglou, Lead–citrate chemistry. Synthesis, spectroscopic and structural studies of a novel lead (II)–citrate aqueous complex, *Inorganica Chim. Acta* 297 (2000) 134.

[58] J. W. Park, J. S. Shumaker-Parry, Structural study of citrate layers on gold nanoparticles: Role of intermolecular interactions in stabilizing nanoparticles, *J. Am. Chem. Soc.* 136 (2014) 1907.

[59] U. Kreibig, M. Vollmer, Theoretical considerations in Optical properties of metal clusters, *Springer*, Berlin & Heidelberg, 1995.

[60] E. Hutter, J. H. Fendler, Exploitation of localized surface plasmon resonance, *Adv. Mater.* 16 (2004) 1685.

[61] P. B. Johnson, R. W. Christy, Optical constants of the noble metals, *Phys. Rev. B* 6 (1972) 4370.

[62] U. Kreibig, Optical properties of small particles in insulating matrices in Contribution of clusters physics to materials science and technology, *Martinus Nijhoff Publishers*, Dordrecht, Boston & Lancaster 1986.

[63] G. Pellegrini, G. Mattei, V. Bello, P. Mazzoldi, Interacting metal nanoparticles: Optical properties from nanoparticle dimers to core-satellite systems, *Mater. Sci. Eng. C.* 27 (2007) 1347.

[64] C. Caucheteur, T. Guo, J. Albert, Review of plasmonic fiber optic biochemical sensors: Improving the limit of detection, *Anal. Bioanal. Chem.* 407 (2015) 3883.

[65] B. Mehrdel, N. Othman, A. A. Aziz, P. M. Khaniabadi, M. S. Jameel, M. A. Dheyab, I. Amiri, Identifying metal nanoparticle size effect on sensing common human plasma protein by counting the sensitivity of optical absorption spectra damping, *Plasmonics* 15 (2020) 123.

[66] D. Paramelle, A. Sadovoy, S. Gorelik, P. Free, J. Hobley, D. G. Fernig, A rapid method to estimate the concentration of citrate capped silver nanoparticles from UV-visible light spectra, *Analyst* 139 (2014) 4855.

[67] B. Khadro, C. Sanglar, A. Bonhomme, A. Errachid, N. Jaffrezic-Renault, Molecularly imprinted polymers (MIP) based electrochemical sensor for detection of urea and creatinine, *Procedia Eng.* 5 (2010) 371.

[68] N. Pan, N. Bhattacharyya, A. Banerjee, P. Biswas, L. Roy, A. Chatterjee, R. Bhattacharjee, S. Singh, S. A. Ahmed, A. Chattopadhyay, M. Mitra, S. K. Pal, Paper-based plasmonic nanosensor monitors environmental lead pollution in real field, *New J. Chem.* 46 (2022) 8177.

[69] J. E. Taggart, E. E. Foord, A. Rosenzweig, T. Hanson, Scrutinyite, natural occurrences of alpha PbO_2 from Bingham, New Mexico, USA, and Mapimi, Mexico, *Can. Mineral.* 26 (1988) 905.

[70] R. Frimpong, W. Jang, J. H. Kim, J. D. Driskell, Rapid vertical flow immunoassay on AuNP plasmonic paper for SERS-based point of need diagnostics, *Talanta* 223 (2021) 121739.

[71] C. H. Lee, M. E. Hankus, L. Tian, P. M. Pellegrino, S. Singamaneni, Highly sensitive surface enhanced Raman scattering substrates based on filter paper loaded with plasmonic nanostructures, *Anal. Chem.* 83 (2011) 8953.

[72] P. K. Sarkar, S. Pal, N. Polley, R. Aich, A. Adhikari, A. Halder, S. Chakrabarti, P. Chakrabarti, S. K. Pal, Development and validation of a noncontact spectroscopic device for hemoglobin estimation at point-of-care, *J. Biomed. Opt.* 22 (2017) 055006.

[73] H. P. Loock, P. D. Wentzell, Detection limits of chemical sensors: Applications and misapplications, *Sens. Actuators B: Chem.* 173 (2012) 157.

[74] N. Pan, R. Ghosh, D. Mukherjee, N. Bhattacharyya, L. Roy, A. Banerjee, S. Singh, R. T. Goswami, M. Mitra, A. Chattopadhyay, S. K. Pal, A nanosensor-based prototype development for heavy metal detection: A combined spectroscopic and theoretical Study, *IEEE Sens. Lett.* 7 (2023) 1.

[75] S. Link, M. A. El-Sayed, Spectral properties and relaxation dynamics of surface plasmon electronic oscillations in gold and silver nanodots and nanorods, *J. Phys. Chem. B* 103 (1999) 8410.

CHAPTER 5

Spectroscopic Studies on Broadband Light Harvesting using Organic Sensitizer-based Micellar Self-assemblies for Environmental Remediation Applications

5.1. Introduction:

The conversion of solar energy has the ability to solve the energy crisis that the earth is facing today due to the shortage of conventional energy resources [1, 2]. In addition to the energy crisis, conversion of solar energy into chemical is a happening approach to combat the alarming environmental pollution also which is the greatest threat of the era [3]. One of the widely reported examples of solar to chemical energy conversion is the generation of reactive oxygen species (ROS) from water molecules or the dissolved oxygen in water, using some potential light-absorbing materials [4, 5]. The ROS eventually takes part in antimicrobial activities [6-8] and degradation of organic-inorganic pollutants [9, 10] present in the water. There are a number of very recent studies where ROS has been recognized as a weapon to solve the water toxicity issue [11]. ROS can also act as a biological antioxidant in order to play an important role in the mechanism of the medicinal activities of important diseases such as cancer, neurological imbalances and immune system disorders [12]. Wide absorption band, less toxicity and stability in water are a few essential properties that a ROS generating material is supposed to have [13, 14]. Other than semiconductor nanostructures, the most commonly used light absorbers in designing these materials are organic photosensitizers [15]. The advantages of using organic photosensitizers are their high molar extinction coefficient and lower toxicity which makes them suitable for biological applications and water cleaning as well [16-18]. However, the narrow absorption band of the organic photosensitizer is one of the limitations in designing light energy converting materials [16]. There are a plethora of earlier reports where visible absorbing sensitizers such as

porphyrin has been used as a ROS generating material in conjugation with other host materials [19-21]. However, the efficiency of ROS generation is largely limited by the poor photon conversion in the near-infrared (NIR) spectral region [22]. The need for dual sensitizers arises to address this particular issue of converting the entire solar spectra as much as possible. Nevertheless, whenever multiple sensitizers are being used to absorb different parts of the solar spectra, the photophysical behaviour and interaction between the sensitizers play a significant role in determining the ultimate efficiency of the material [23]. Choosing the proper host material is also very important in determining the photophysical interactions between the sensitizers [24]. Self-assembled surfactant media such as micelles and vesicles are potential hosts which are able to solubilize the hydrophobic sensitizers and at the same time can provide the restricted environment suitable for the preferred interactions such as Förster resonance energy transfer (FRET) [25]. The use of two different dye mixtures in close proximity of each other in restricted environment can be termed as dual sensitization [26]. In earlier publications of our group, the use of two sensitizers has been found to be beneficial in case of dye sensitized solar cells (DSSC) [27] and in photocatalysis [28] as well. However, to the best of our knowledge, the use of dual sensitizers under restricted environment of micelles to generate ROS in aqueous media has yet not reported.

In the present work, we have used dye mixtures as dual sensitizers in a self-assembled CTAB surfactant environment with PPIX (visible absorbing sensitizer) and SQ2 (NIR absorbing sensitizer) for a broad range of light-harvesting application. The donor PPIX and acceptor SQ2 are found to behave as a FRET pair under the restricted environment of cationic micelles and this process of energy transfer is advantageous for enhanced ROS generation under white light irradiation. Steady-state and time-resolved fluorescence studies have been performed to confirm the FRET from PPIX to SQ2. Choice of suitable micellar medium is also investigated for proper position of sensitizer attachment in cationic, anionic and non-ionic micelles with the help of picosecond resolved fluorescence spectroscopy [12]. Enhanced ROS generation under white light

irradiation is also confirmed based on several control experiments with and without dual sensitization under the same conditions. It may have potential photo remediation applications; some possibilities have been explored towards anionic pollutant. Protoporphyrin and squarine are well known photosensitizers and have widely been reported earlier in case of photocatalysis or antimicrobial activities [29, 30]. However, to the best of our knowledge, the ROS generation using these sensitizers has mostly been reported in conjugation with some semiconductor in order to separate the charge efficiently [28, 31]. In the present study, we have done a dual photosensitizer based FRET enhanced ROS generation in a restricted environment of self-assembled surfactant systems. The confined media or the host micelle plays a key role in controlling the photophysics depending on the local environment of the sensitizer which is one of the new findings of this present study. Thus, it is itself an interesting photophysical study to monitor whether the generated ROS is local to the restricted surfactant system or sufficiently in contact with the external medium (say water). Overall this photophysical study is focused to understand the FRET enhanced ROS generation phenomenon based on proper choice of micellar system, processes important outcomes which may help to design new light-harvesting materials in future. Additionally, there is a possibility of charge specific photo remediation applications towards selective anionic pollutants due to the charge specification of the host micelle which is sparse in the existing literature. A mechanistic explanation of FRET induced enhanced ROS generation has been proposed. Our study reveals the detailed photophysical understanding of dual sensitization leading to enhanced ROS generation which could be beneficial to manifold potential applications.

5.2. Results and Discussion:

5.2.1. Broad Light Harvesting Under Restricted Environment: Photophysical Understanding Leading to Enhanced Reactive Oxygen Species Generation [32]: In the present study, we have chosen protoporphyrin (PPIX) and squaraine (SQ2) mixture as dual sensitizers. Being hydrophobic in nature, a suitable

environment is needed for the solubilisation of the sensitizers in water. In order to solubilize both the sensitizers in water, micellar host system has been chosen because of the probable affinity of the sensitizers towards the charged Stern layer or hydrophobic core of the micelles [33]. A cationic micellar solution CTAB has been used as a host for these two dyes to solubilise them in water and to provide proximity between the sensitizers confined within the restricted environment. The absorption spectrum of SQ2 entrapped CTAB solution (Figure 5.1a) shows an intense peak at 656 nm (NIR region), also it has a significant overlap with the

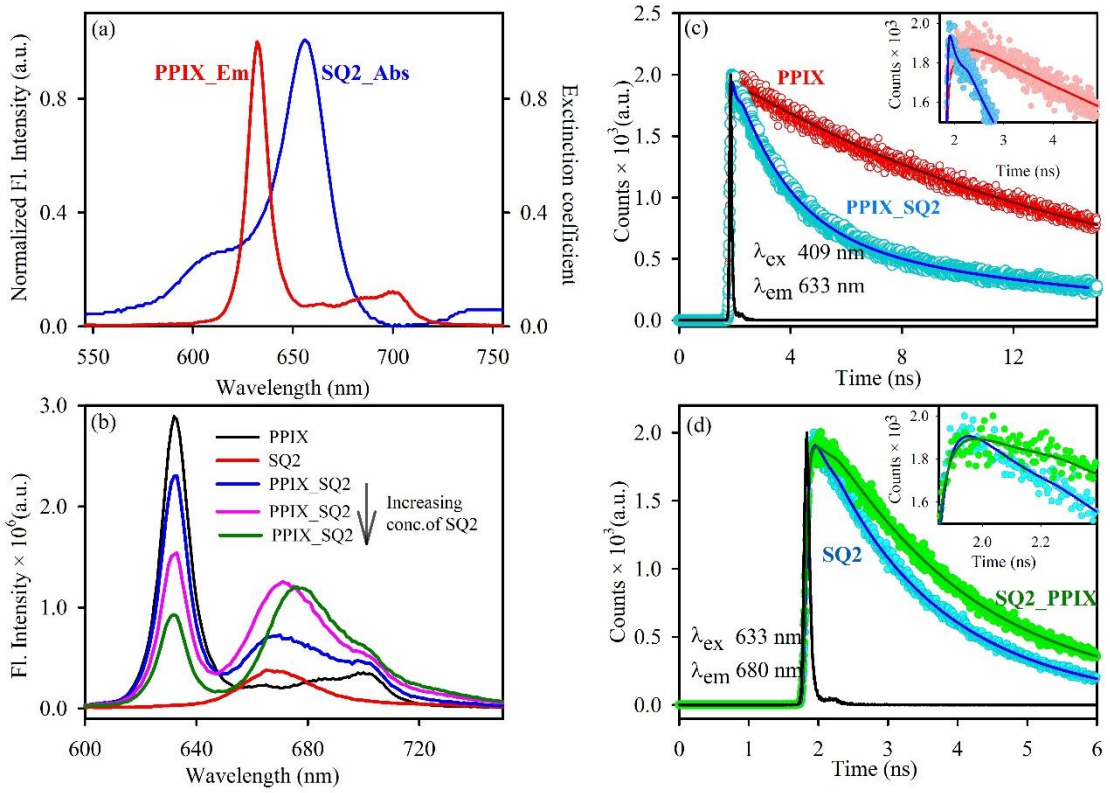

Figure 5.1: *(a) The spectral overlap between the normalized steady-state fluorescence emission spectra of PPIX and normalized absorption of SQ2 in CTAB micellar media. (b) Steady-state emission spectra of PPIX (black), SQ2 (red) and PPIX_SQ2 with increasing concentration of SQ2 (blue, pink and dark green). The picosecond resolved fluorescence decays of PPIX (c) in absence (red) and in presence of SQ2 (blue). The inset shows the magnified view of the respective decay transients. (d) SQ2 (blue) and SQ2 in presence of PPIX (green) in CTAB micellar media. The inset shows the magnified view of the respective decay transients.*

emission spectra of the visible absorbing sensitizer PPIX entrapped (633 nm), in CTAB micellar solution. micellar surface. It indicates that the sensitizer PPIX and SQ2 may behave as a donor-acceptor pair to take part in intermolecular dipole-dipole (FRET) coupling in close proximity of each other upon attachment with

the CTAB Figure 5.1b represents quenching in the steady-state emission intensity of the donor PPIX after the addition of SQ2 and this quenching increases gradually as the amount of SQ2 increases. Simultaneously, a gradual increase in the fluorescence intensity at the emission maxima of the acceptor SQ2 (~670 nm) is observed. This process of simultaneous quenching in donor intensity and increase in acceptor fluorescence intensity provides additional evidence of the occurrence of FRET [34]. For further confirmation of FRET, time-resolved studies have been done using CTAB micellar solutions. The fluorescence transient of donor PPIX in cationic micelle (CTAB) solution decays single exponentially with an excited-state life-time of around 14 ns upon excitation with 409 nm. From Figure 5.1c, it is clear that the donor life-time is quenched significantly upon the addition of acceptor SQ2 to this solution. Similarly, in Figure 5.1d, the rise in the acceptor's decay pattern upon adding the donor PPIX further validates the possibility of FRET between PPIX and SQ2. The average life-time of the donor has decreased from 14.2 ns to 9.5 ns due to FRET from PPIX to SQ2.

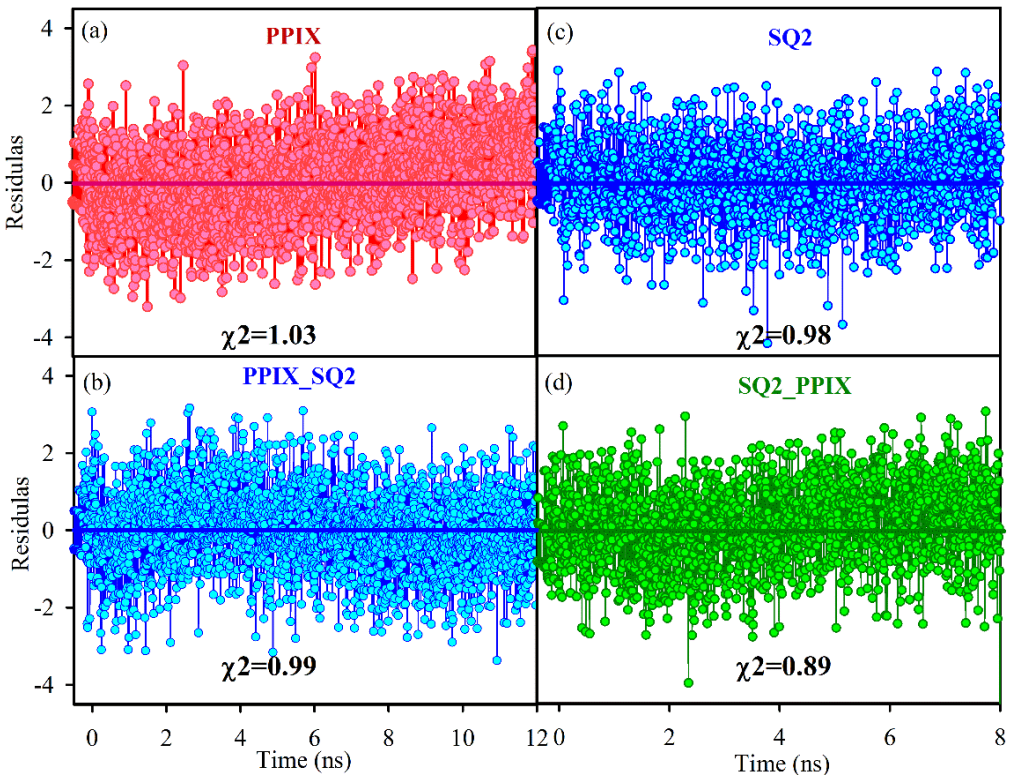

Figure 5.2: *Residual and Chi-square values of fitted Picosecond resolved fluorescence decay of (a) PPIX (b) PPIX_SQ2 (c) SQ2 (d) SQ2_PPIX.*

Table 5.1: *Excited state life-time of the donor PPIX in presence and absence of the acceptor SQ2 and the excited state life-time of the acceptor SQ2 presence and absence of the donor PPIX in CTAB micellar environment.* [a]

Sample	Excitation wavelength (nm)	Emission wavelength (nm)	τ_1 (ns)	τ_2 (ns)	τ_3 (ns)	τ_{avg} (ns)
PPIX	409	633	14.2 (100%)			14.2
PPIX_SQ2	409	633	1.6 (38%)	14.4 (61%)		9.4
SQ2	633	670	0.4 (12%)	1.8 (88%)		1.6
SQ2_PPIX	633	670	0.8 (-61%)	0.9 (82%)	2.5 (79%)	1.6

[a]*Numbers in the parenthesis indicate the relative weightages.*

All the decay components and their relative weights have been summarized in Table 5.1. The residual plots along with the $\chi 2$ values have also been shown in the Figure 5.2. This steady-state and picosecond time-resolved fluorescence decay results of the donor and acceptor molecules confirm the FRET between these two sensitizers under the restricted environment of the cationic CTAB micelle. 34% FRET efficiency and a donor-acceptor distance of 4.2 nm have been calculated using the conventional methodology as discussed in section 2.3. FRET parameters are summarized in detail in Table 5.2.

Table 5.2*: FRET parameters.*

System	J(λ)	R_0 (nm)	E (%)	R_{DA}(nm)
SQ2_PPIX	1.8 x10^{16}	4.5	34	4.2

However, donor-acceptor concentration plays an important role in FRET efficiency [35]. Additionally, we want to mention that we have got a FRET efficiency upto 80% for higher acceptor concentration. The FRET efficiencies and the related time-resolved components with different acceptor concentration have been shown in Figure 5.3 and Table 5.3. The FRET between the visible absorbing donor and NIR absorbing acceptor pair can be advantageous in terms of ROS generation and potentially lead to broad light harvesting. DCFH has been

used as a marker to investigate the ROS generation in sensitizer encapsulated micellar systems [36].

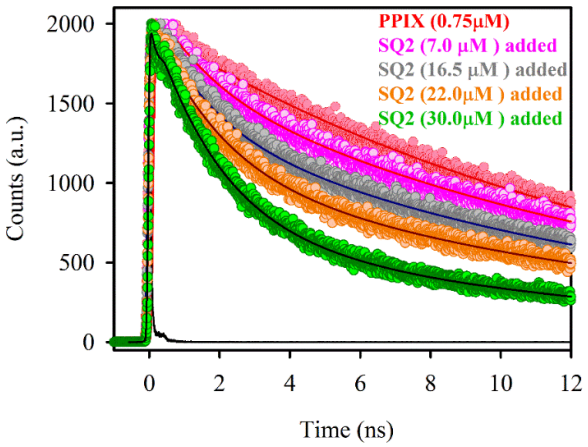

Figure 5.3: *The picosecond resolved fluorescence decays of PPIX (0.75 mM) in absence (red) and in presence of SQ2: 7.0 mM (Pink), 16.5 mM (Gray), 22.0 mM (Orange), 30.0 mM (Green).*

All the ROS generation studies have been performed in CTAB micellar solution since a higher amount of ROS generation is found in presence of cationic surfactant other than anionic or non-ionic systems. The ROS generation study has been done with three sensitizer-surfactant systems namely PPIX_CTAB, SQ2_CTAB, PPIX-SQ2_CTAB under blue light, red light and white light irradiation accordingly.

Table 5.3. *Excited state life-time of the donor PPIX in the presence and absence of the different acceptor concentrations of SQ2 in CTAB micellar environment, at an excitation wavelength of 409 nm and emission collected at 633 nm.*

Sample	τ_1 (ns)	τ_2 (ns)	τ_3 (ns)	τ_{avg} (ns)	FRET Efficiency
PPIX (0.75mM)	14.2 (100%)			14.2	
PPIX (0.75mM)_SQ2 (7.0mM)	1.5 (22%)	15.0 (78%)		12.0	15%
PPIX (0.75mM)_SQ2 (16.5mM)	1.6 (38%)	14.4 (61%)		9.4	34%
PPIX (0.75mM)_SQ2 (22.0mM)	0.6 (25%)	1.9 (35%)	15.1 (40%)	6.6	54%
PPIX (0.75mM)_SQ2 (30.0mM)	0.5 (23%)	1.9 (64%)	12.8 (13%)	2.8	80%

Simultaneously, the effect of FRET in dual-sensitized micellar system has been studied under white light irradiation, which reveals the enhanced ROS generation in the PPIX_SQ2_CTAB media.

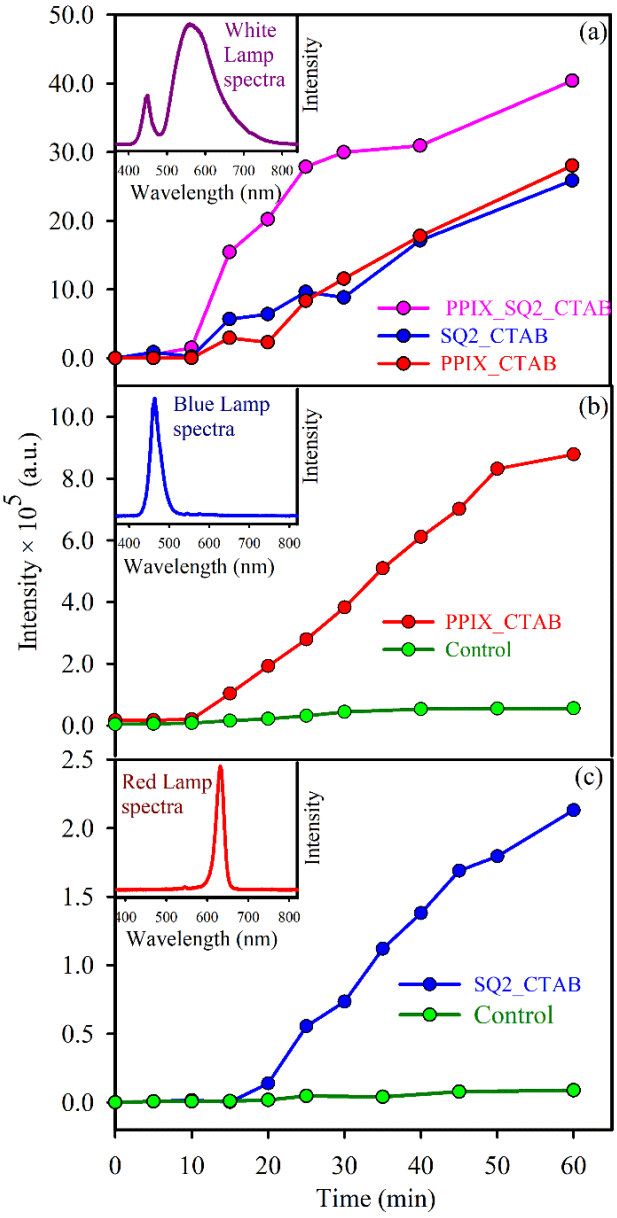

Figure 5.4: *Time-dependent oxidation of DCFH in water monitored at 520 nm under the irradiation of (a) white light, (b) blue light, and (c) red light. Inset of each figure shows the respective lamp spectra that have been used for irradiation.*

Figure 5.4a shows the higher ROS generation in the dual sensitizer system (PPIX-SQ2_CTAB) compared to the sensitizers alone (i.e. PPIX_CTAB and SQ2_CTAB) under irradiation with a white light source. Results of ROS generation under blue light irradiation by PPIX_CTAB and SQ2_CTAB systems under red light

irradiation are shown in Figure 5.4b and 5.4c respectively. The insets of Figures 5.4a, 5.4b, and 5.4c show the spectra of different lamps used in the experiment. The control experiments have also been done in DCFH assay only in presence of CTAB micelle where no significant ROS generation is found. The order of magnitude increase in DCFH oxidation by the micelle entrapped sensitizer systems than the controls, signifies the higher ROS generation by the sensitizer-surfactant assemblies under the irradiation of their respective absorption window. Additionally, the higher ROS generation by the dual sensitizer system than the single sensitizer system under white light irradiation further proves the scope of wide-range light harvesting and the advantage of FRET in the conversion of energy. To get more insight into the type of ROS generated, further ROS-specific experiments can be performed. In our earlier publications [28] similar photosensitizer systems have been shown to generate the electron-mediated ROS preferentially. The addition of electron and hole scavengers to the system could affect the generation of specific ROS and could behave like an identifier of the specific radicle. Being a similar sensitizer combination here, we can predict that a similar type of ROS, i.e., superoxide anion radicals, have a significantly higher contribution.

Nevertheless, to understand the spin state of the generated reactive oxygen species, a ROS-specific assay like SOSGR [37] would be helpful. Electron spin resonance (ESR) or electron paramagnetic resonance (EPR) spectroscopy could also be performed to better understand the spin specificity of the ROS radicals generated. However, considering the energy band gap values of the sensitizers could be a probable explanation for the generation of singlet oxygen if the energy gap is sufficient to reverse one of the spins of the unpaired electrons of molecular triplet oxygen [38]. The energy bandgap between singlet and triplet molecular oxygen states are 0.98 eV (^1D_g) and 1.63 eV (^1S_g) [39], whereas for PPIX and SQ2, the LUMO HOMO band gaps are 2.0 eV [40], 2.2 eV [41] respectively. According to the earlier literature, these energy values are feasible for triplet oxygen to singlet oxygen conversion [42]. Thus, having the possibility of both superoxide

radical and singlet molecular oxygen as ROS, spin-specific experiments could be done for more confirmatory conclusion. The step by step mechanistic pathways are represented by the scheme 5.1 and probable mechanism of ROS generation under white light irradiation has been shown in scheme 5.2. We have done further experiments to justify the choice of cationic CTAB micellar solution as a suitable restricted media by providing close proximity for the two sensitizers on the basis of proper attachment position.

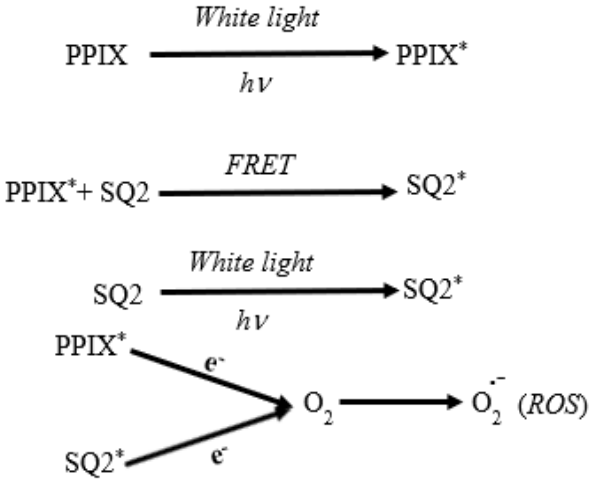

Scheme 5.1: *The step-by-step mechanistic pathways of ROS generation.*

These sensitizers contain a carboxylic acid attaching group (-COOH) which dissociates in aqueous media and maintains ionization equilibrium between the two states [43]. There is a possibility that porphyrin and squaraine are attached to the CTAB micelles by the anionic carboxylic acid groups via electrostatic interactions with their positive head groups. On the other hand, for an anionic SDS micellar system, the attachment is not possible due to the electrostatic repulsion between the host and the sensitizer. In the case of a non-ionic micellar system (Triton X-100), the possible attachment position may be the hydrophobic core of the micelle. In order to further prove the probable attachment positions, picosecond time-resolved fluorescence studies have been performed by solubilizing the dyes in solvents of different polarities. A sensitizer in a micelle can be entrapped in three different locations such as (a) the hydrophobic core, (b) towards the polar media and (c) the stern layer [44]. It is well reported that

the solvation dynamics of a dye becomes significantly slower when it gets into the hydrophobic core of the micelle [45], whereas it exhibits faster dynamics in the relatively polar medium. Whenever there is a single decay component in the excited state fluorescence transient, it can be assumed that all the sensitizers are in a unique local environment.

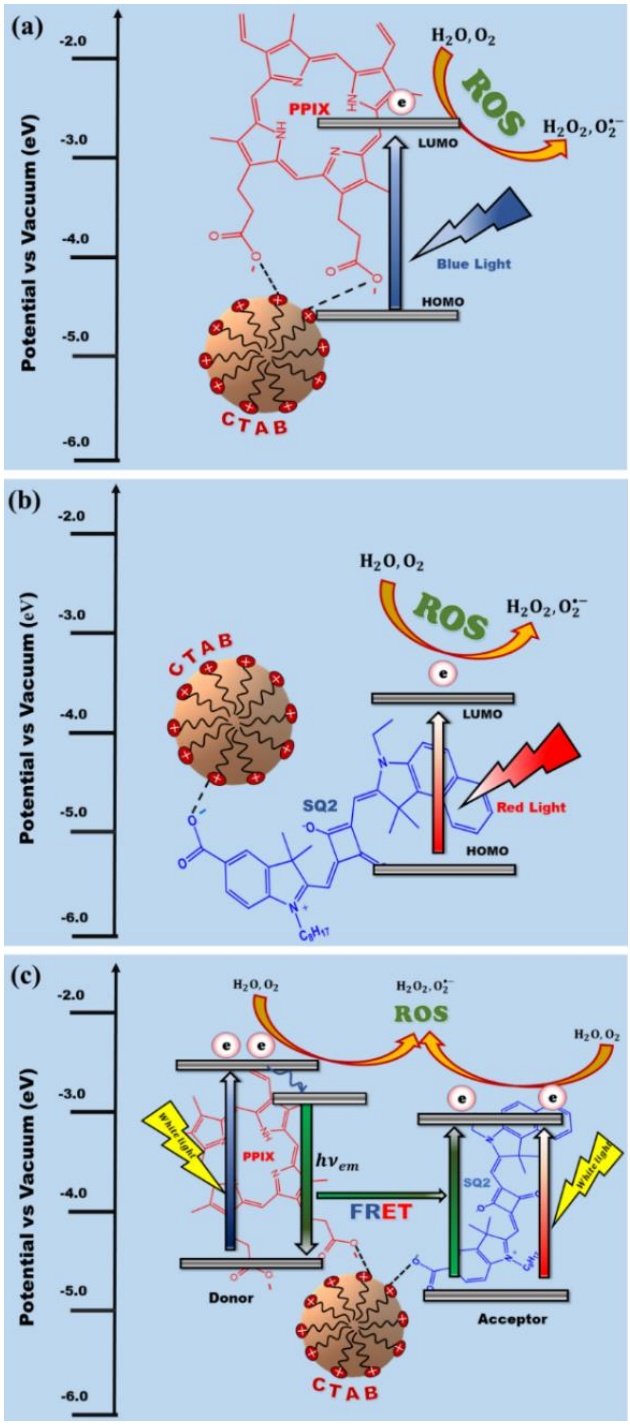

Scheme 5.2: *Energy levels of the sensitizers and the mechanism of generating ROS under (a) blue light, (b) red light, (c) white light irradiation.*

However, there are systems where two decay components were present which leads to a probability of two immediate local environments. In such systems, a portion of the sensitizer's population might be entrapped in the core contributing to the longer decay component, and some of the population is towards the polar media, which contributes to the faster decay component. Figure 5.5a shows the decay profiles of PPIX in three micellar systems namely the cationic CTAB, anionic SDS and non-ionic Triton X-100 systems. We have compared the attachment of PPIX on the micellar systems by taking DMSO and DMSO water mixture (1:2) as solvents in the order of their increasing polarity. The decay patterns of PPIX in these solvents (Figure 5.5b) clearly represent that with the increase in polarity of solvent, the time-resolved fluorescence life-times become faster.

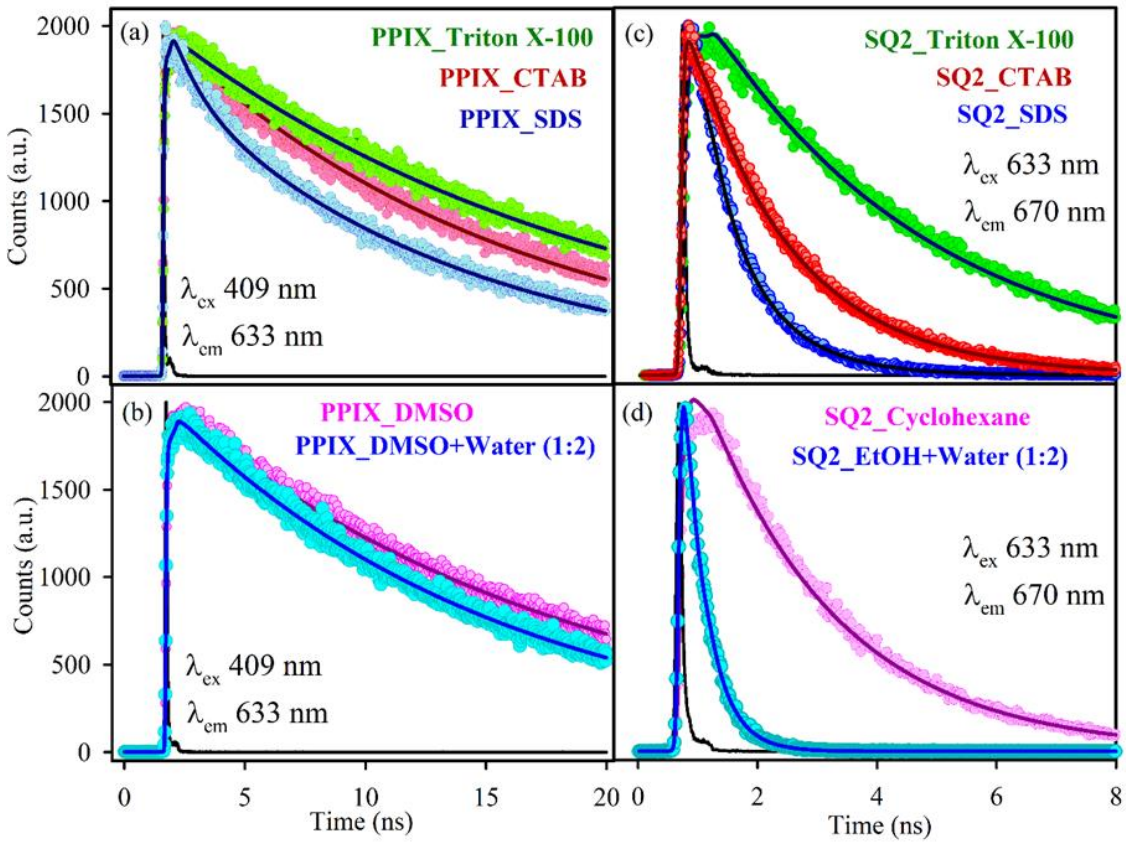

Figure 5.5: *Picosecond resolved fluorescence decays of PRIX in (a) three different micellar media Triton X-100 (green), CTAB (pink) and SDS (dark blue), (b) in solvents of different polarity as DMSO (magenta) and DMSO water mixture (blue). Fluorescence transients of sensitizer SQ2 (a) in three different micellar media Triton X-100 (green), CTAB (red) and SDS (dark blue), (b) in solvents of varying polarity as cyclohexane (magenta) and ethanol water mixture (blue).*

The picosecond resolved decays of PPIX in DMSO is ~17 ns and it becomes faster ~14 ns in a relatively more polar solvent (DMSO water mixture). Similarly, we have found that the time-resolved decays of PPIX in Triton X-100 is comparatively slower ~18 ns than in CTAB ~14 ns. The trends reveal that in Triton X-100 the decay got significantly slower may be due to a hydrophobic environment than CTAB, where a relatively polar environment is present. We can infer from this observation that the preferential position of PPIX is the hydrophobic core in non-ionic micelles. The DMSO-water mixture gives an equivalent environment as that of the Stern layer of the micelle and PPIX_CTAB, shows a similar decay timescale as in PPIX_DMSO+water.

Table 5.4: *Dynamics of picosecond resolved fluorescence decays of the sensitizer PPIX and SQ2 in different micellar environment and in solvents of different polarity.*

Sample	Excitation wavelength (nm)	Emission wavelength (nm)	τ_1 (ns)	τ_2 (ns)	τ_{avg} (ns)	χ^2
PPIX_CTAB	409	633	14.5 (100%)		14.5	1.20
PPIX_TritonX	409	633	18.4 (100%)		18.4	0.95
PPIX_SDS	409	633	1.2 (20%)	12.1 (80%)	9.9	1.20
PPIX_DMSO	409	633	16.7 (100%)		16.7	0.97
PPIX_DMSO+ Ethanol (1:2)	409	633	13.9 (100%)		13.9	0.89
SQ2_CTAB	633	670	0.4 (12%)	1.8 (88%)	1.6	0.93
SQ2_TritonX	633	670	3.8 (100%)		3.8	1.20
SQ2_SDS	633	670	0.3 (40%)	0.9 (60%)	0.7	1.14
SQ2_Cyclohex -ane	633	670	2.2 (100%)		2.2	1.31
SQ2_Ehtanol+ water (1:2)	633	670	0.2 (39%)	0.4 (61%)	0.3	1.04

We can infer from here that in cationic CTAB micelle, the sensitizer PPIX is attached in such a position that it is in contact with the polar and non-polar

media both i.e. on its Stern layer. The excited-state life-time is faster in SDS micelle than that of both CTAB and Triton X-100 and the solubility of PPIX is very low in this anionic micellar system as well. In SDS media, the fluorescence life-time of PPIX becomes even faster ~10 ns, having fitted with 20% and 80% contribution from 1.2 ns and 12 ns respectively. Here, the appearance of biexponential nature indicates that two different local environments are present. Thus, we can infer that in SDS micelle 20% of the sensitizer's population is completely exposed to the bulk water and 80% of it lies in a relatively more polar medium than CTAB. Similar trends have been found with the other sensitizer SQ2 in each of the three micellar media. Here we have used cyclohexane and ethanol-water mixture as a representative of hydrophobic (non-polar) and polar environments. In SQ2_cyclohexane, we got a ~2.2 ns decay time scale whereas in the ethanol-water mixture we got a very fast life-time of ~0.3 ns having 40% contribution from 0.3 ns and 60% from 0.4 ns respectively. Accordingly, with Triton X-100 the sensitizer SQ2 has a ~3.8 (100%) ns excited state life-time which is comparatively slower than CTAB (1.6 ns). In CTAB medium (1.6 ns) biexponential excited sate life-time has been fitted with 12% and 88% contributions from 0.4 ns and 1.8 ns respectively. Thus, almost 90% population lies on the Stern layer due to the presence of a 1.8 ns component which is even faster than 3.8 ns (TritonX) and 10% is completely exposed to the bulk water. As found earlier with PPIX_SDS system, SQ2_SDS system the excited state life-time is also quite fast ~0.7 ns which contains 40% and 60% contribution from 0.3 ns and 0.9 ns respectively. In anionic media such a faster life-time indicates that 40% of the sensitizer's population remains in the polar region i.e. does not even get attached to the micelle. All the life-time decay timescales along with their $\chi 2$ values have been shown in Table 5.4. Thus, the trends indicate that in the non-ionic Triton Xmicellar system SQ2 and PPIX go to the core and in the case of cationic CTAB surfactant media, it stays on the Stren layer of it. For anionic media due to charge repulsion, most of the PPIX and SQ2 population lies in bulk water. Scheme 5.3 represents the probable sensitizer attachment position in all three micellar systems in aqueous media. As represented in Scheme 5.3, among

the three possible surfactant assemblies, only in the cationic one i.e. in CTAB the sensitizer is solubilized very well and have a chance of exposure to the water as well. Thus, only in CTAB the sensitizer is getting access to interact with the dissolved oxygen in the water and can eventually lead to a higher ROS generation activity. ROS generation by the cationic micelle entrapped photosensitizers could be beneficial towards the selective photo remediation application of charged pollutants.

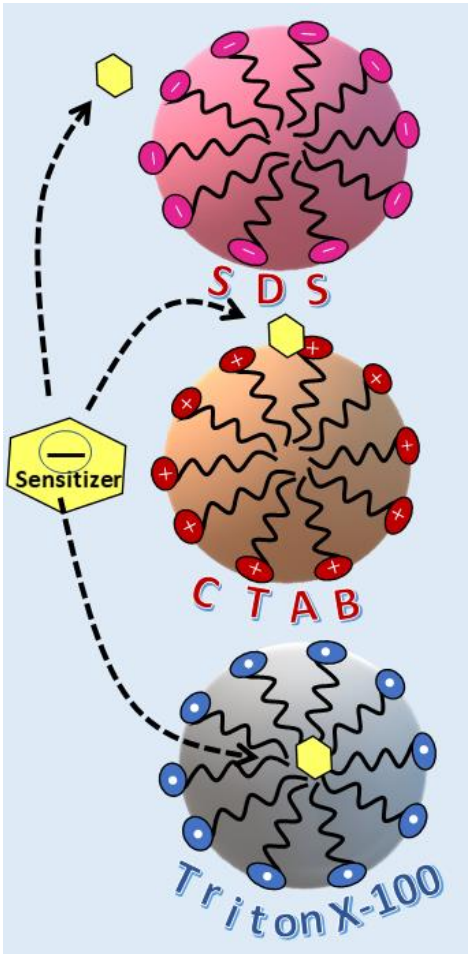

Scheme 5.3: *Possible location of the anionic photosensitizers at three different micellar environments.*

Anionic organic dyes can be taken as a model pollutant to be treated by a dual sensitized cationic micellar system because the surface charge of the host micelle can attract the oppositely charged pollutant towards the sensitizer, facilitating the degradation process. For the present study, the photocatalytic degradation of phenol red is shown as proof of the concept of using the CTAB micelle

encapsulated system for potential photo-remediation application. However, the degradation results are very preliminary and need further optimization for the sensitizer's concentration to be prepared as a sustainable photocatalyst.

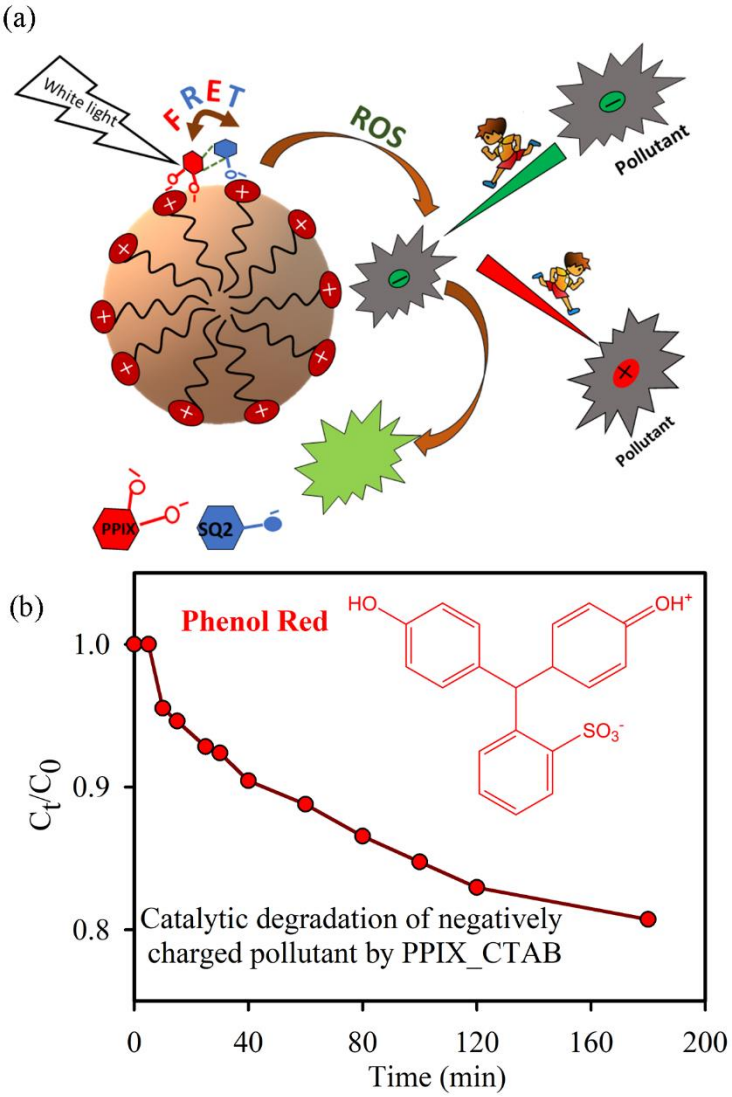

Figure 5.6: *(a) Schematic representation of selective degradation of anionic pollutants by the model catalyst and (b) Photocatalytic degradation of negatively charged phenol red by the model catalyst PPIX_CTAB.*

The photodegradation schematic has been presented in Figure 5.6a and the primary degradation results have been shown in Figure 5.6b. We have also performed recyclability studies. The systems showed reduced efficiency in consecutive cycles because of the degradation of the sensitizers caused by locally generated ROS. Thus, there is a scope for optimization in order to achieve a perfectly reusable photocatalyst out of the present concept which we would like to explore in our next study focusing on the application part of these materials.

Another important point to be addressed is the removal of host micelle and the photodegraded by-products According to the many reported kinds of literature, the superoxide radical present in the medium mostly reacts with the proton of phenol part present in the dye and thereby forming an intermediate compound [45]. This intermediate compound further degrades to simpler products. In this process, the radicals dimerise to give hydrogen peroxide, which degrades ultimately to water and oxygen. Finally, Phenol red is decomposed by radicals into most simpler ions/molecules, such as ammonium and sulphate ions, carbon dioxide, water, etc after photo-degradation [46]. Thus, the dye degrades to non-toxic or less toxic products upon ROS interaction, hence the removal of such products is of less concern field. There is much scope regarding the removal of the host micelle in the system if required. In this work, we have used mainly CTAB as a host micelle which has some toxic effects if not completely removed or used in excess amount. To deal with this issue we can use non-toxic surfactant systems such as Pluronic micelles. There is a possibility of surface charged modification of such micellar systems which will open up new photo remediation pathways for these types of charged surfactant encapsulated dual sensitizers based on enhanced ROS generation systems [47]. Again, there is huge scope in this direction which we would like to explore in detail in our future projects focusing on the application part of the generated ROS.

5.3. Conclusion:

In summary, a dual sensitization technique in restricted micellar solution has been explored to achieve an efficient reactive oxygen species generation (ROS) under white light irradiation. The simultaneous use of visible absorbing photosensitizer PPIX and the NIR absorbing SQ2 has been found to enhance the absorption window and their photophysical behaviour under the restricted environment and has been explored in detail. PPIX is found to behave as a donor and SQ2 as an acceptor in close proximity on the surface of cationic CTAB micelle for FRET. FRET plays an important role in enhanced reactive oxygen species generation and has been confirmed here with the help of steady-state and time-

resolved fluorescence experiments. The choice of CTAB micellar media as a restricted environment has been justified on the basis of electrostatic interaction between the oppositely charged surfactant and hydrophobic organic sensitizers in comparison with other anionic and non-ionic micellar media. The proper dye attachment position has also been investigated in the three micellar environments. The probable position in the case of CTAB is found to be on its surface rather with Triton X-100 in its hydrophobic core. Thus, a unique ultrafast dynamical study is presented to understand the dual sensitization in presence of micellar media leading to FRET induced efficient light-harvesting via enhanced ROS generation.

References

[1] R. Foster, M. Ghassemi, A. Cota, Solar energy: Renewable energy and the environment, *CRC Press*, Boca Raton, 2009.

[2] W. Dunwei, C. Guozhong, Nanomaterials for energy conversion and storage, *World Scientific*, London, 2017.

[3] Z. Şen, Solar energy fundamentals and modeling techniques: Atmosphere, environment, climate change and renewable energy, *Springer*, Istanbul, 2008.

[4] A. Lipovsky, Z. Tzitrinovich, H. Friedmann, G. Applerot, A. Gedanken, R. Lubart, EPR study of visible light-induced ROS generation by nanoparticles of ZnO, *J. Phys. Chem. C* 113 (2009) 15997.

[5] Y. Nosaka, A. Y. Nosaka, Generation and detection of reactive oxygen species in photocatalysis, *Chem. Rev.* 117 (2017) 11302.

[6] M. N. Karim, M. Singh, P. Weerathunge, P. Bian, R. Zheng, C. Dekiwadia, T. Ahmed, S. Walia, E. Della Gaspera, S. Singh, Visible-light-triggered reactive-oxygen-species-mediated antibacterial activity of peroxidase-mimic CuO nanorods, *ACS Appl. Nano Mater.* 1 (2018) 1694.

[7] F. Vatansever, W. C. de Melo, P. Avci, D. Vecchio, M. Sadasivam, A. Gupta, R. Chandran, M. Karimi, N. A. Parizotto, R. Yin, Antimicrobial strategies centered around reactive oxygen species–bactericidal antibiotics, photodynamic therapy, and beyond, *FEMS Microbiol. Rev.* 37 (2013) 955.

[8] Y. Min, X. F. Qi, Q. Xu, Y. Chen, Enhanced reactive oxygen species on a phosphate modified C_3N_4 /graphene photocatalyst for pollutant degradation, *CrystEngComm* 16 (2014) 1287.

[9] P. Dunlop, J. Byrne, N. Manga, B. Eggins, The photocatalytic removal of bacterial pollutants from drinking water, *J. Photochem. Photobiol. A: Chem.* 148 (2002) 355.

[10] X. Yang, J. Qin, Y. Jiang, K. Chen, X. Yan, D. Zhang, R. Li, H. Tang, Fabrication of P25/Ag_3PO_4/graphene oxide heterostructures for enhanced solar photocatalytic degradation of organic pollutants and bacteria, *Appl. Catal. B.* 166 (2015) 231.

[11] D. Chatterjee, S. Dasgupta, Visible light induced photocatalytic degradation of organic pollutants, *J. Photochem. Photobiol. C* 6 (2005) 186.

[12] O. A. Chat, M. H. Najar, M. A. Mir, G. M. Rather, A. A. Dar, Effects of surfactant micelles on solubilization and DPPH radical scavenging activity of Rutin, *J. Colloid Interface Sci.* 355 (2011) 140.

[13] L. M. Gonçalves, V. de Zea Bermudez, H. A. Ribeiro, A. M. Mendes, Dye-sensitized solar cells: A safe bet for the future, *Energy Environ. Sci.* 1 (2008) 655.

[14] R. Y. Y. Lin, Y. S. Yen, Y. T. Cheng, C. P. Lee, Y. C. Hsu, H. H. Chou, C. Y. Hsu, Y. C. Chen, J. T. Lin, K. C. Ho, Dihydrophenanthrene-based metal-free dyes for highly efficient cosensitized solar cells, *Org. Lett.* 14 (2012) 3612.

[15] S. J. Moon, J. H. Yum, R. Humphry-Baker, K. M. Karlsson, D. P. Hagberg, T. Marinado, A. Hagfeldt, L. Sun, M. Grätzel, M. K. Nazeeruddin, Highly efficient organic sensitizers for solid-state dye-sensitized solar cells, *J. Phys. Chem. C* 113 (2009) 16816.

[16] U. Resch-Genger, M. Grabolle, S. Cavaliere-Jaricot, R. Nitschke, T. Nann, Quantum dots versus organic dyes as fluorescent labels, *Nat. Mater.* 5 (2008) 763.

[17] W. H. Howie, F. Claeyssens, H. Miura, L. M. Peter, Characterization of solid-state dye-sensitized solar cells utilizing high absorption coefficient metal-free organic dyes, *J. Am. Chem. Soc.* 130 (2008) 1367.

[18] R. Li, X. Chen, S. Wei, K. Sun, L. Fan, Y. Liu, L. Qu, Y. Zhao, B. Yu, A visible-light-promoted metal-free strategy towards arylphosphonates: Organic-dye-catalyzed phosphorylation of arylhydrazines with trialkylphosphites, *Adv. Synth. Catal.* 360 (2018) 4807.

[19] B. Guo, G. Feng, P. N. Manghnani, X. Cai, J. Liu, W. Wu, S. Xu, X. Cheng, C. Teh, B. Liu, A porphyrin-based conjugated polymer for highly efficient in vitro and in vivo photothermal therapy, *Small* 12 (2016) 6243.

[20] F. Giuntini, F. Foglietta, A. M. Marucco, A. Troia, N. V. Dezhkunov, A. Pozzoli, G. Durando, I. Fenoglio, L. Serpe, R. Canaparo, Insight into ultrasound-mediated reactive oxygen species generation by various metal-porphyrin complexes, *Free Radic. Biol. Med.* 121 (2018) 190.

[21] U. Giri, M. Iqbal, M. Athar, Porphyrin-mediated photosensitization has a weak tumor promoting activity in mouse skin: Possible role of in situ-generated reactive oxygen species, *Carcinogenesis* 17 (1996) 2023.

[22] A. Zitzler-Kunkel, M. R. Lenze, N. M. Kronenberg, A. M. Krause, M. Stolte, K. Meerholz, F. Würthner, NIR-absorbing merocyanine dyes for BHJ solar cells, *Chem. Mater.* 26 (2014) 4856.

[23] P. Pallavi, B. Sk, P. Ahir, A. Patra, Tuning the förster resonance energy transfer through self-assembly approach for efficient white-light emission in aqueous medium, *Chem. Eur. J.* 24 (2017) 1151.

[24] S. Chatterjee, S. Nandi, S. C. Bhattacharya, Fluorescence resonance energy transfer from fluorescein to safranine T in solutions and in micellar medium, *J. Photochem. Photobiol. A: Chem.* 173 (2005) 221.

[25] S. Biswas, S. C. Bhattacharya, P. K. Sen, S. P. Moulik, Absorption and emission spectroscopic studies of fluorescein dye in alkanol, micellar and microemulsion media, *J. Photochem. Photobiol. A* 123 (1999) 121.

[26] A. A. Dar, O. A. Chat, Cosolubilization of coumarin30 and warfarin in cationic, anionic, and nonionic micelles: A micelle–water interfacial charge dependent FRET, *J. Phys. Chem. B* 119 (2015) 11632.

[27] J. Patwari, S. Sardar, B. Liu, P. Lemmens, S. K. Pal, Three-in-one approach towards efficient organic dye-sensitized solar cells: Aggregation suppression, panchromatic absorption and resonance energy transfer, *Beilstein J. Nanotechnol* 8 (2017) 1705.

[28] J. Patwari, A. Chatterjee, S. Sardar, P. Lemmens, S. K. Pal, Ultrafast dynamics in co-sensitized photocatalysts under visible and NIR light irradiation, *Phys. Chem. Chem. Phys.* 20 (2018) 10418.

[29] Y. Chen, A. Li, Z. H. Huang, L. N. Wang, F. Kang, Porphyrin-based nanostructures for photocatalytic applications, *Nanomaterials* 6 (2016) 51.

[30] D. Bagchi, A. Halder, S. Debnath, P. Saha, S. K. Pal, Exploration of interfacial dynamics in squaraine based nanohybrids for potential photodynamic action, *J. Photochem. Photobiol. A* 380 (2019) 111842.

[31] D. Bagchi, V. S. Rathnam, P. Lemmens, I. Banerjee, S. K. Pal, NIR-light-active ZnO-based nanohybrids for bacterial biofilm treatment, *ACS omega* 3 (2018) 10877.

[32] S. A. Ahmed, N. Pan, H. M. Altass, J. Patwari, R. J. Obaid, H. Alessa, R. S. Jassas, S. K. Pal, Broad light harvesting under restricted environment: Photophysical understanding leading to enhanced reactive oxygen species generation, *J. Photochem. Photobiol. A: Chem.* 418 (2021) 113422.

[33] M. D. Garcia, A. Sanz-Medel, Dye-surfactant interactions: A review, *Talanta* 33 (1986) 255.

[34] J. R. Lakowicz, Principles of fluorescence spectroscopy, *Springer Science & Business Media*, New York, 2013.

[35] L. Gartzia-Rivero, L. Cerdán, J. Bañuelos, E. Enciso, I. Lopez Arbeloa, A. n. Costela, I. García-Moreno, Förster resonance energy transfer and laser efficiency in colloidal suspensions of dye-doped nanoparticles: concentration effects, *J. Phys. Chem. C* 118 (2014) 13107.

[36] J. Patwari, H. Joshi, H. Mandal, L. Roy, C. Bhattacharya, P. Lemmens, S. K. Pal, Exciton dissociation in an NIR-active triohybrid nanocrystal leading to efficient generation of reactive oxygen species, *Phys. Chem. Chem. Phys.* 21 (2019) 10667.

[37] A. Bera, D. Bagchi, S. K. Pal, Improvement of photostability and NIR activity of cyanine dye through nanohybrid formation: Key information from ultrafast dynamical studies, *J. Phys. Chem. A* 123 (2019) 7550.

[38] C. C. Winterbourn, Biological chemistry of superoxide radicals, *ChemTexts* 6 (2020) 1.

[39] K. Hirakawa, Computational chemistry for photosensitizer design and investigation of DNA damage, *Front. comput. chem.* 2 (2016) 27.

[40] S. Sarkar, A. Makhal, T. Bora, K. Lakhsman, A. Singha, J. Dutta, S. K. Pal, Hematoporphyrin–ZnO nanohybrids: Twin applications in efficient visible-light photocatalysis and dye-sensitized solar cells, *ACS Appl. Mater. Interfaces.* 4 (2012) 7027.

[41] S. A. Al-horaibi, M. T. Alghamdi, S. Gaikwad, A. S. Rajbhoj, Comparison and determine characteristics potentials of HOMO/LUMO and relationship between Ea and Ip for squaraine dyes (SQ1, SQ2) by using cyclic voltammetry and DFT/TD-DFT, *Mor. J. Chem.* 6 (2018) 6.

[42] A. Molnár, R. Dědic, M. Kořínek, A. Svoboda, J. Hála, Protoporphyrin IX and hematoporphyrin derivatives interactions with oxygen studied by time and spectral resolved phosphorescence, *J. Mol. Struct.* 744 (2005) 723.

[43] A. R. Tehrani-Bagha, K. Holmberg, Solubilization of hydrophobic dyes in surfactant solutions, *Materials* 6 (2013) 580.

[44] N. Sarkar, A. Datta, S. Das, K. Bhattacharyya, Solvation dynamics of coumarin 480 in micelles, *J. Phys. Chem.* 100 (1996) 15483.

[45] P. Chowdhury, S. Nag, A. K. Ray, Degradation of phenolic compounds through UV and visible-light-driven photocatalysis: Technical and economic aspects in Phenolic compounds - natural sources, Iimportance and applications, *IntechOpen*, Croatia, 2017.

[46] S. Lodha, D. Vaya, R. Ameta, P. B. Punjabi, Photocatalytic degradation of phenol red using complexes of some transition metals and hydrogen peroxide, *J. Serbian Chem. Soc.* 73 (2008) 631.

[47] A. Parmar, S. Chavda, P. Bahadur, Pluronic–cationic surfactant mixed micelles: Solubilization and release of the drug hydrochlorothiazide, *Colloids Surf. A Physicochem. Eng. Asp.* 441 (2014) 389.

CHAPTER 6

Spectroscopic Studies on Photoinduced Charge Separation, Excitonic Behaviour at the Interfaces of the Hybrid Nanomaterials

6.1. Introduction:

The 21st century has witnessed significant challenges arising from the growing demand for energy and the resulting environmental impacts [1-3]. Solar radiation is deemed the primary green and renewable energy source among others, owing to its consistent and abundant existence on the earth's surface [4, 5]. The efficient harvesting of solar energy into chemical and electrical energy can solve the energy crisis as well as the alarming environmental pollution the earth is facing today [6, 7]. To combat the current situation, a plethora of research is going around the world for the advancement in technologies akin to photosynthesis, DSSCs [8, 9] and DSPECs [10], are among the most efficient emerging renewable energy sources. In the near future, water splitting will be considered one of the most environmentally sound methods for solar energy conversion through hydrogen generation [11, 12]. Other than DSSCs and DSPECs, photocatalysis is a well-known technique that utilizes the ROS generated from recyclable nanomaterials and degrades organic pollutants by producing oxidizing free radicals [13]. Numerous studies have reported the generation of reactive oxygen species (ROS) [14] from the water molecules or from the dissolved oxygen in water via various nanohybrids on the absorption of light as a technique for conversion of solar energy to chemical energy [15, 16]. The generated ROS has the potential to exert antimicrobial action and can degrade both organic and inorganic pollutants present in water [17-19].

As a result, the development of novel nanomaterials with efficient photocatalytic activity, high stability, and a significantly good absorption window in the solar spectrum has been regarded as a critical prerequisite for combating energy crisis and environmental pollution via solar energy conversion [20]. Among many,

TiO_2 can be called the best semiconductor photocatalyst due to its unique features. To improve its photocatalytic properties, TiO_2 can be conjugated into a range of materials, including metals, nonmetals, and other photocatalysts, to form different types of hybrids. The photoresponse can be improved in the visible region by sensitizing mesoporous wide-bandgap semiconductor photocatalysts (TiO_2 and ZnO) with sensitizers and tuning the absorption window accordingly. This method captures attention because of its promising response towards cheaper and more environmentally friendly approaches, where the choice of sensitizers has become equally important. However, the poor photocatalytic efficiency, dye leaching, and degradation under solar irradiation remain concerns. Thus, the choice of the sensitizer material and its constructional arrangement play a crucial role.

In contrast to conventional silicon based solar light-harvesting technologies, photons harvested by chromophore adsorbed on surface of mesoporous wide band gap semiconducting materials such as TiO_2 are attracting attention because of their promising response towards cheaper and environment friendly approach [21]. In this direction, the choice of the chromophore is equally important [22]. Traditional ruthenium-based metal sensitizers are always the first choice for many years due to their high-power conversion efficiency in spite of their toxic effects on the environment [23]. Recently many efforts have been given to the development of new structurally improved efficient metal free sensitizers that could be helpful to improve device performances [24]. Also, the sensitizer's constructional arrangement has been found to control pivotal exciton transfer phenomenon at the TiO_2/sensitizer/electrolyte interfaces. Nowadays, organic molecules having an electron donor and acceptor group structured in a bridge framework (D-A) structure are extensively studied providing high molar extinction coefficient, stability and higher electron injection efficiency as well due to their easy synthesis and tunable optical properties [25, 26]. Besides the general use of such organic molecules, a distinctive charge transfer character is found in predominant use as a chromophore in advanced light harvesting materials. Here, we have used RK1 [8, 27, 28], which is a commercially available

triphenylamine-based sensitizer with a D-π-A structure, RK1 is a highly stable chromophore under solar light irradiation, The recently reported push-pull organic sensitizer RK1 exhibits high power conversion efficiency and stability in DSSCs even higher than ruthenium dye [8]. However, unwanted exciton recombination and narrow absorption window are some of the major issues that have to be dealt with [29]. There are ways by which recombination can be reduced i.e., lowering the thickness of the layer but in the cost of dye loading. Among others, the use of metal semiconductor hybrid nanomaterial is advantageous in many aspects [30, 31]. The specific role of noble metallic nanoparticles (eg. Ag, Pd, Pt, Au) has raised significant attention due to their plasmonic response [32-34]. Photosynthesis in an artificial way is to concentrate and harvest the solar light in molecular sized regions [11]. Plasmonic nanoparticles are one of the promising candidates in this direction, due to its tunable surface plasmon absorption and excellent ability to convert electromagnetic radiation in molecular sized regions. Plasmonically excited metal nanoparticles provide additional charge transfer to the semiconductor which has been proven to be beneficial for increasing the photovoltaic performance. Metal semiconductor hybrid junction leads to the formation of the Schottky barrier which provides a route to lower the charge recombination process [30]. Gold is a noble metal that is very stable during photoreaction; also, gold nanoparticles process an extraordinary light trapping ability due to the presence of a strong LSPR band at the red end of the visible spectrum [35]. Few studies have been reported related to the photosensitization of noble metal nanoparticles encapsulated TiO_2 hybrid with the suitable organic sensitizer, still, the poor photovoltaic efficiency remains a concern [36, 37]. Nevertheless, the detailed photophysical excited state charge/energy transfer dynamical investigation is still lacks in the contemporary literature in case of DSSCs as well as DSPECs [38-41]. The structurally improved D-A type of organic sensitizer having significant spectral overlap with the LSPR band of the metal nanoparticle encapsulated on TiO_2 surface leading to the additional possibilities of Förster Resonance Energy Transfer (FRET) could be explored in detail for considerably

good photovoltaic efficiency [42]. The lowering of the back electron hole recombination due to the formation of metal semiconductor junction [43] and simultaneous occurrence of plasmon coupled Forster resonance energy transfer [33] with the sensitizer can boost the photovoltaic performance of the DSSCs, especially it can significantly improve the performance of DPECs, which is still sparse in the literature [11].

In the first part of the work, we have investigated the photophysical behaviour of RK1 sensitized gold (Au) decorated TiO_2 (TiO_2_Au_RK1) photoanodes towards dual application in DSSCs and DSPECs. We have here extended our study towards photoelectrochemical water splitting the most occurring photovoltaic technique by implementing dye sensitization over gold decorated TiO_2 photoanodes. The choice of plasmonic material is such that the LSPR band of gold nanoparticles has significant overlap with the fluorescence of the sensitizer RK1, other than this there is a significant lowering of unwanted exciton recombination with metal semiconductor junction which has been confirmed by slower open circuit voltage decay profile of RK1_TiO_2_Au than that of RK1_TiO_2. The combination of these two factors enhances the overall efficiency of DSSCs, and also 3 times increases the performance of the DSPECs. The ultrafast fluorescent transient has been studied for in detailed understanding of Plasmonic induced electron-transfer (ET) across the hybrid junctions and FRET among fluorophore and plasmonic nanoparticles. Several other electrochemical techniques have been utilized to validate the enhanced PEC performance of the prepared cells.

Along with it, the time scale involved in electron transfer phenomena at the TiO_2/ D-π-A sensitizers interface have been found to play a key role in efficient light-harvesting materials. Here, ultrafast charge injection on the order of femtosecond time scales can play a predominant role [44] while utilizing D-π-A sensitizers as a light-harvesting material, which is still a less explored area. The widespread applications of organic photosensitizers have been explored across various branches of modern research, including solar light harvesting, due to

their femtosecond-resolved ultrafast response [44, 45]. In this direction, the dynamics of such D-π-A sensitizers are sometimes crucial to understand in their pure state and when attached to a semiconducting/insulating substrate. Additionally, because of the presence of ultrafast spectral/electronic relaxation, femtosecond-resolved ultrafast tools are required for their dynamic understanding. D-π-A structural photosensitizers having D-A interaction account for even more interesting optoelectronic behavior, such as the formation of new lower energy molecular orbitals (MO) termed intramolecular charge transfer states (ICT) [25]. ICT is responsible for the polar nature of such sensitizers.

Thereby in the next part of the work, we have observed such behaviors of RK1 in the polar solvent, mesoporous RK1-TiO_2 nanohybrid, and on RK1-Al_2O_3 nanohybrid using steady-state and femtosecond-resolved fluorescence spectroscopy-based tools. It was found that compared to pure solvent, the spectral and time-resolved responses of such photosensitizers when grafted on semiconducting nanosurfaces get completely changed, which is again responsible for ROS generation and their application in photocatalysis. Here we have shown that due to the presence of ultrafast electron transfer from RK1 TiO_2, besides the use of organic photosensitizer RK1 as a high-efficiency material in DSSCs, it is an important environment-friendly material as a photocatalyst as well.

6.2. Results and Discussion:

6.2.1. Plasmon-coupled Donor−acceptor Type Organic Sensitizer-Based Photoanodes for Enhanced Photovoltaic Activity: Key Information from Ultrafast Dynamical Study [46]: The phase structure characterization of the prepared nanohybrid has been determined by X-ray powder diffraction. Figure 6.1a demonstrates the diffraction patterns of TiO_2 (black) and synthesised Au-TiO_2 nanohybrid (purple). The characteristic diffraction peaks at around 25^o, 48^o and peaks at 27^o, 36^o, 55^o indicate the presence of mixed anatase and rutile phase

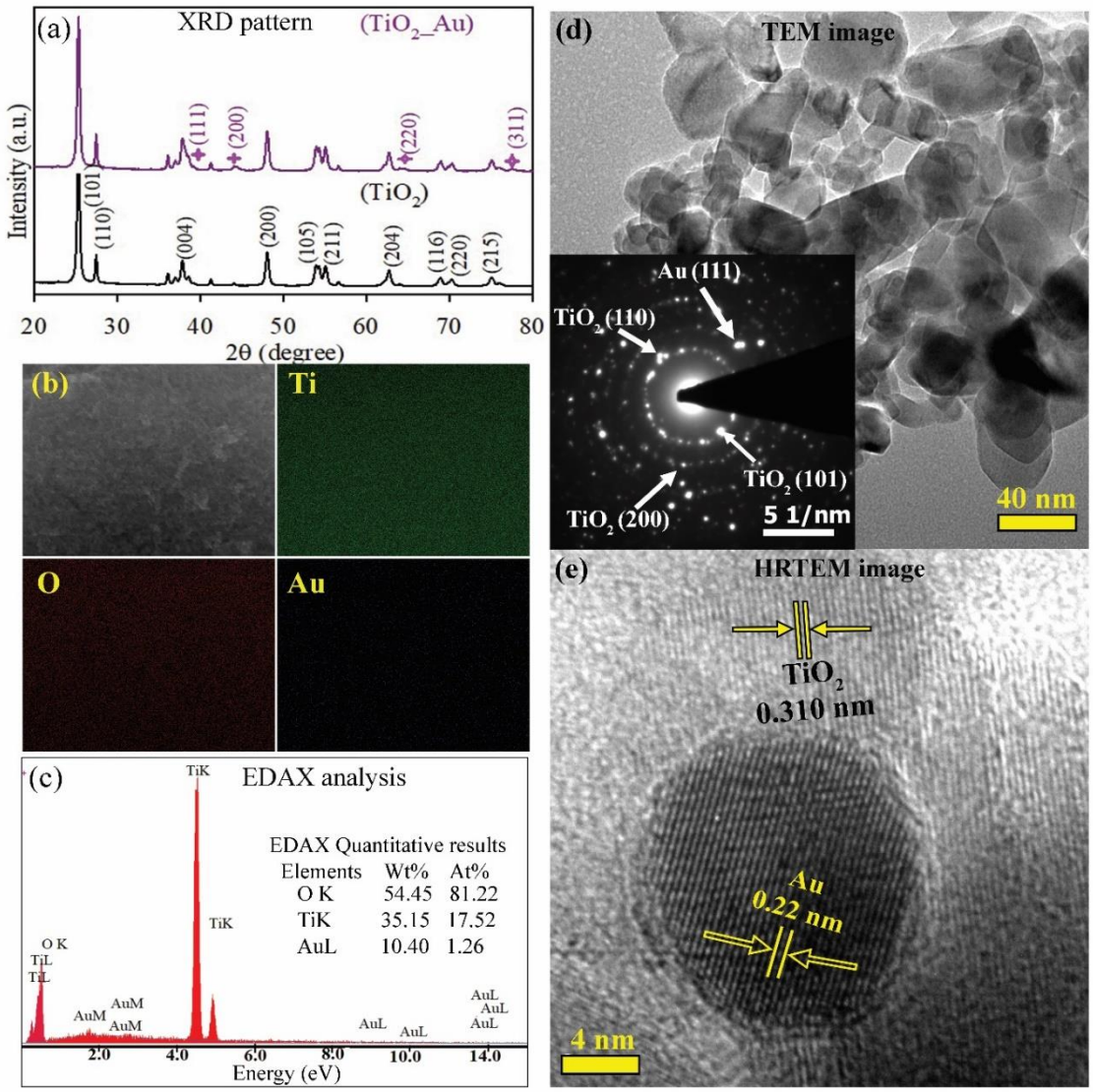

Figure 6.1: *(a) XRD pattern of the TiO_2_Au nanohybrid. (b) SEM image of TiO_2_Au nonhybrid and the elemental mapping of Ti, O, Au. (c) The corresponding EDAX spectrum of the nanohybrid. (d) The TEM image of the TiO_2_Au nanohybrid. Inset shows the SEAD pattern. (e) HRTEM image of the TiO_2_Au nanohybrid.*

of TiO_2 respectively [47]. Additionally, tiny characteristic peaks at around 38°, 44°, 64° and 77° confirm the presence of metallic gold in the Au-TiO_2 nanohybrid. The elemental distribution of the Au-TiO_2 is characterised by energy dispersive X-ray (EDAX) mapping. Figure 6.1b and 6.1c distinctly shows the homogeneous distribution of Au, O and Ti elements in Au-TiO_2 nanohybrid with presence of ~1.6% of Au in the nanohybrid respectively. The morphology of the nanohybrid has been analysed with TEM and high-resolution TEM (HRTEM). As shown in Figure 6.1d, the smaller darker regions on the TiO_2 surface clearly demonstrate the adsorption of spherical Au nanoparticles (Au NPs) on TiO_2 NPs. Inset of

Figure 6.1d shows the selected area (electron) diffraction (SEAD) pattern of the sample which proves the crystallinity of the sample having circular rings denoting to the planes of TiO_2 [Anatses; (101), (200) and Rutile; (110)] and Au [(111)]. The morphology and crystallinity of the sample have further been confirmed by HRTEM analysis shown in Figure 6.1e. Fringe width of ~0.310 corresponds to 110 plane [48] of TiO_2 and a spherical Au NPs is clearly visible having diameter of 15 nm, and fringe of 0.22 which is in accordance with the available literature [49]. The UV-Vis absorption and steady-state fluorescence emission spectra of the dye RK1 in toluene are illustrated in Figure 6.2a.

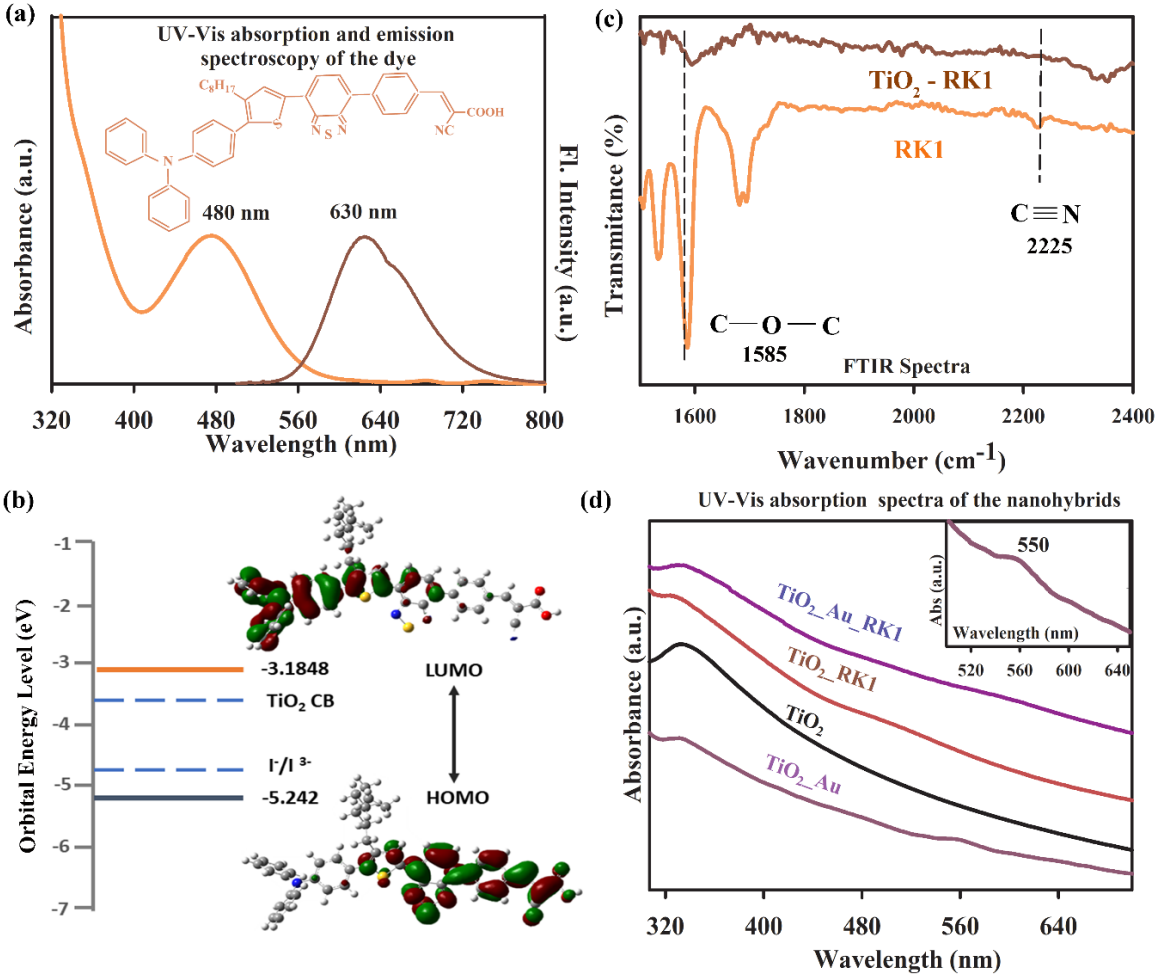

Figure 6.2: *(a) The UV-Vis absorbance and steady state fluorescence emission spectra of RK1 in toluene. Inset shows the structure of the sensitizer RK1, (b) HOMO and LUMO of RK1 calculated at the B3LYP/6-31++g (d, p) level of theory based on the optimized structure in toluene, (c) FTIR spectra of powdered RK1 and RK1-TiO2 nanohybrid, (d) The UV-Vis absorbance spectra of TiO_2, TiO_2_Au, TiO_2_RK1 and TiO_2_Au_RK1 nanohybrids. Inset shows the zoom view of TiO_2_Au absorption spectra, LSPR peak of Au nanoparticles on TiO_2 surafce is at 550 nm.*

An absorption at 480 nm band in visible region is observed which is assigned to the internal charge transfer (ICT) transition occurring between the electron-donating (triphenylamine group) and electron-withdrawing (cyanoacrylic acid) section of the molecule along with a band at 399 nm in the UV region which is assigned to π-π* transitions of the aromatic rings [8] whereas it has an emission maximum at 630 nm. The inset shows the structure of the RK1. The positions of the frontier molecular orbital have now been calculated using the B3LYP/6-31++g(d,p) level of theory based on the optimized structure in toluene and have been shown in Figure 6.2b. The dye is having directional electron distribution with electron delocalization of the highest occupied molecular orbital (HOMO) in the triphenylamine group and of the lowest unoccupied molecular orbitals (LUMO) in the benzothiadiazole and cyanoacrylic acid group. The calculated HOMO (-3.184 eV), and LUMO (-5.242) positions are favourable for electron injection into the conduction band (CB) of TiO_2 and also facilitate the reduction of oxidized dye by I^-/I^{3-}. Furthermore, for DSSC and DSPEC applications the attachment of RK1 with TiO_2 is investigated. FTIR spectra (shown in Figure 6.2c) of pure RK1 and RK1-TiO_2 hybrid (prepared in toluene solvent) revealed the attachment of the dye on TiO_2 surface through anchoring group (cyanoacrylic acid). A clear redshift of vibration mode (1573 cm^{-1}; C-O-C) of acrylic acid [50] in RK1 is observed to that of RK1-TiO_2, which give evidence of bridging bidentate binding [27] whereas the peak corresponding to 2225 cm^{-1} (C≡N) is almost suppressed in the hybrid system indicating the presence of COO/CN (A2) binding mode [27]. These spectral changes in FTIR spectra confirms the formation of the RK1_TiO_2 hybrid. The UV-Vis spectra of the hybrid systems are been shown in Figure 6.2d. TiO_2 has absorption band at ~340 nm. From the absorption spectra of TiO_2_Au nanohybrid, 550 nm peak (inset of Figure 6.2d) corresponding to LSPR band of Au nanoparticles is clearly observed. A distinct absorption band (~480 nm) is observed in the RK1_TiO_2 hybrid and in that of RK1_TiO_2_Au, two absorption bands (~480 nm and ~550 nm) are observed indicating the attachment of both plasmonic gold and dye. Interestingly there is a possibility of significant spectral overlap between the LSPR absorbance band

of gold (decorated on Al_2O_3 surface) and the emission band of chromophore RK1 attached on Al_2O_3 surface. This spectral overlap can facilitate the dipolar coupling that can lead to the mechanism of resonant energy transfer, between nanoparticle and chromophore.

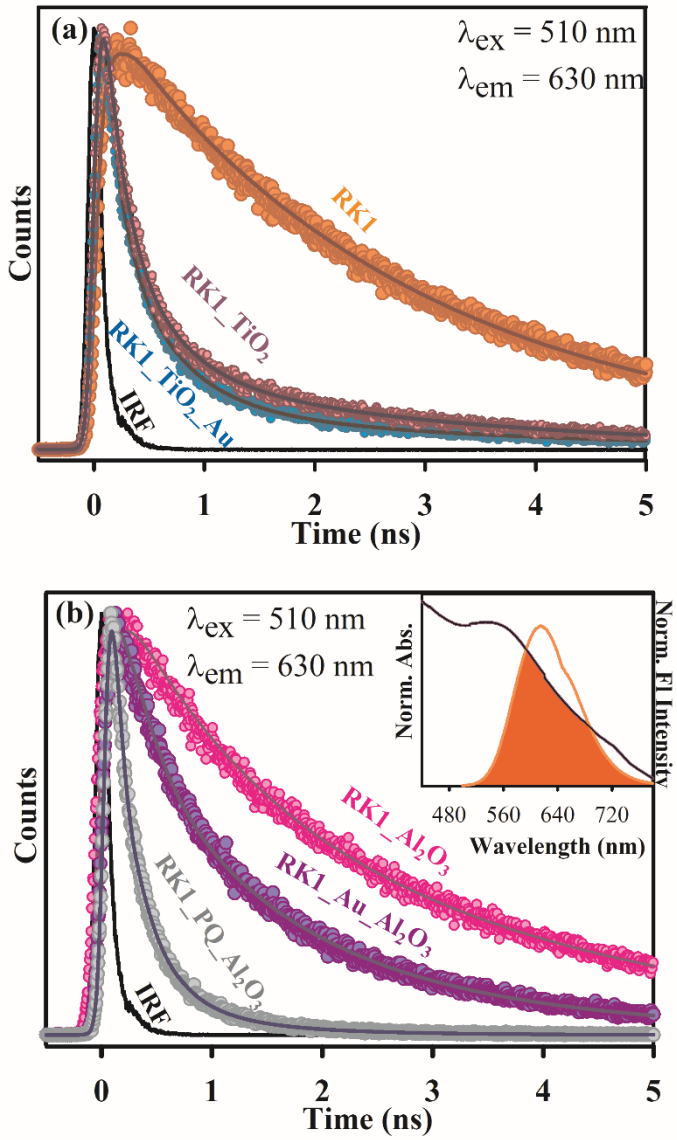

Figure 6.3: *(a) The fluorescence decay transients of RK1, RK1_TiO_2 and RK1_TiO_2_Au. (b) The fluorescence decay transients of RK1, RK1_Au and RK1_PQ attached on Al_2O_3 surface. Insets shows the overlap spectra between normalised absorption of gold NPs and RK1 normalised emission spectra both attached on Al_2O_3 surface.*

In order to study the energy and charge transfer process across the hybrid junctions, ultrafast time-resolved fluorescence transient experiments have been performed. The pico-second resolved decay depicts the faster component in fluorescence decay for both RK1_TiO_2 and RK1_TiO_2_Au nanohybrids,

compared to that of RK1 only in toluene (Figure 6.3a). These fluorescence decays were monitored at 630 nm with excitation of a 510 nm LASER source. The fluorescence transient of RK1 decays double exponentially with two-time constants 0.26 ns and a major contribution from 2.8 ns (90%) having an average lifetime of 2.6 ns. From the fluorescence transient of RK1_TiO_2, a significantly faster component of 0.12 ns having 67% of contribution is observed. The faster component of 0.12 ns is ascribed to the distinct excited state electron transfer from the LUMO of RK1 to the CB of TiO_2 nanoparticles [33]. In the case of RK1_TiO_2_Au nanohybrid, a further faster component of 0.08 ns is attributed to plasmon induced charge transfer [51]. Hence, the presence of Au NPs having an LSPR effect further enhances the injection of electrons from Au to TiO_2 due to the plasmon-induced charge transfer, where plasmon can decay via generating an electron in the CB of TiO_2 and hole in the metal [8] which is additionally advantageous for Photovoltaic performance. Whereas a time component of 0.35 ns could be an illustration of FRET from RK1 to Au [51],[33]. For confirmation of FRET between RK1 and Au, we have introduced nanohybrid formation with an insulator Al_2O_3. All the time-resolved dynamics with prepared nanohybrids on Al_2O_3 surface are shown in Figure 6.3b.

Table 6.1: *Lifetimes of picosecond time-resolved PL transients of RK1, RK1-Al_2O_3, RK1_Au-Al_2O_3, RK1_PQ_Al_2O_3, RK1_PQ_Al_2O_3, RK1_TiO_2 and RK1_Au_TiO_2 under excitation wavelength of 510 nm and emission monitored at 630 nm.*

Sample	τ_1 (ns)	τ_2 (ns)	τ_3 (ns)	τ_{avg} (ns)
RK1	0.26 (9%)	2.83 (91%)	0	2.6
RK1_Al_2O_3	0.29 (25%)	2.80 (75%)	0	2.44
RK1_Al_2O_3_Au	0.21 (40%)	1.23 (40%)	2.80 (20%)	1.14
RK1_PQ_Al_2O_3	0.05 (77%)	0.30 (19%)	0.94 (4%)	0.12
RK1_TiO_2	0.12 (57%)	0.50 (28%)	2.88 (15%)	0.49
RK1_TiO_2_Au	0.82 (72%)	0.35 (23%)	2.4 (5%)	0.35

The spectral overlap between the LSPR band of Au and the emission band of RK1 (both attached on Al_2O_3 surface) is very significant as shown in the inset of Figure 6.3b. As a controlled study, the time-resolved dynamics of RK1_Al_2O_3 have been performed and it is revealed that there is no such faster component corresponding to photoexcited electron transfer. Moreover, with a time component of 0.20 ns (40% contribution), the time-resolved decay of RK1_Al_2O_3_Au indicates the possibility of energy transfer from RK1 to Au. We have further attached a well-known electron quencher para-quinone to the RK_Al_2O_3 system and found that a much faster component 0.05 ns is responsible for excited state electron transfer hence the time component of 0.20 ns of RK1_Al_2O_3_Au is solely responsible for energy transfer. All the fitting parameters of time-resolved transients have been listed in Table 6.1. The overlap integral [J(λ)] and FRET efficiency are calculated to be 7.0×10^{17} M^{-1} cm^{-1} nm^4 and 53% respectively.

***Table 6.2**: FRET parameters.*

System	J(λ)	R_0 (nm)	E (%)	R_{DA}(nm)
RK1_Al_2O_3–Au_Al_2O_3	7 x 10^{17}	9.0	53	8.9

Now the distance between donor (RK1) and acceptor (surface of AuNPs) is calculated and it is 8.9 nm, which is within the FRET probing limit of 1-10 nm. All FRET parameters are summarized in Table 6.2. Figure 6.4a shows the photocurrent density-voltage (J-V) curves of the DSSCs based on RK1_TiO_2 and RK1_TiO_2_Au nanohybrid materials, and the corresponding parameters such as Jsc (short-circuit current density), Voc (open-circuit potential), PCE (power conversion efficiency) and FF (fill factor) are summarised in Table 6.3. PEC increased from 6.26% to 7.89% in the presence of gold nanoparticles reflecting the enhancement of photocurrent density from 13.28 to 17.14 mA cm^{-2}. The photocurrent vs wavelength study performed on cells is in good agreement with UV-vis absorbance maxima (~480 nm) of sensitizer RK1. In RK1_TiO_2_Au system higher photocurrent value is observed due to broadened absorption

window and the presence of LSPR (Figure 6.4b). The photocurrent vs wavelength spectra, also signify that the generation of photocurrent is due to the presence of sensitizers on photoanodes.

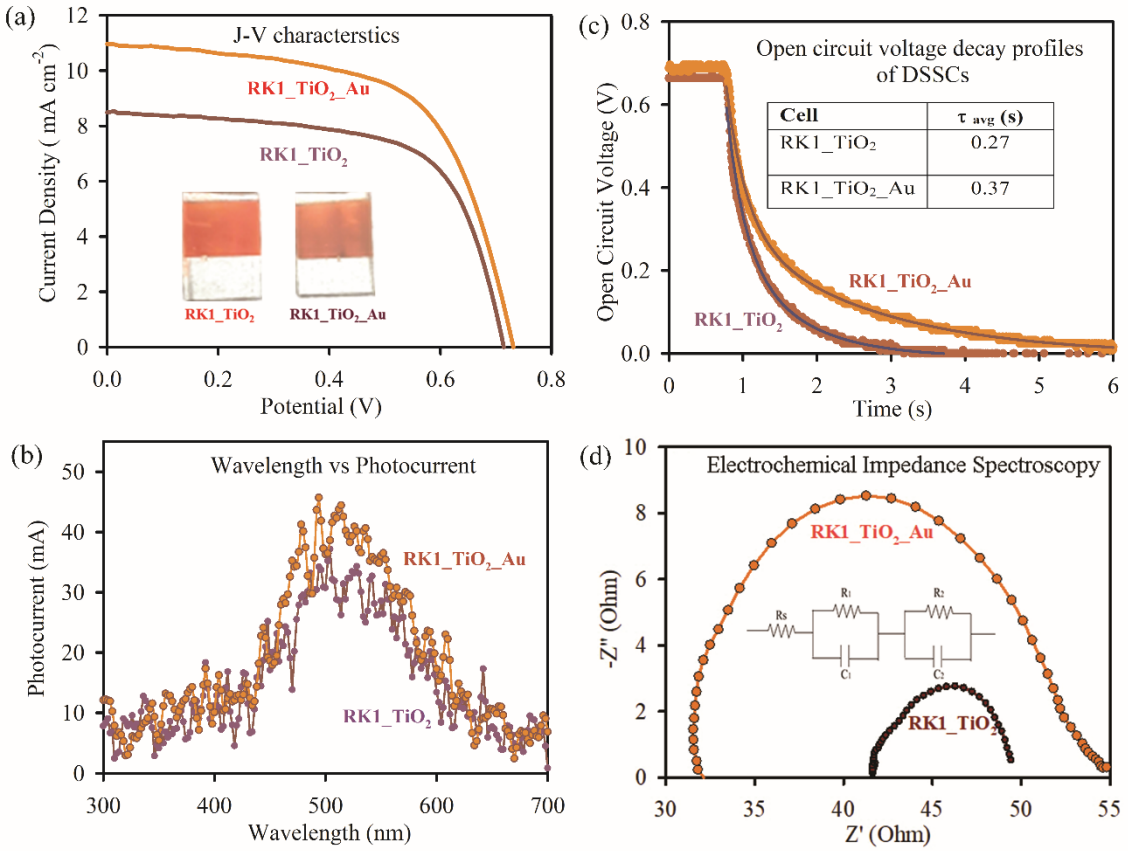

Figure 6.4: *(a) J-V characteristics (inset shows the photoanodes), (b) open circuit voltage decay profiles, (c) Wavelength versus photocurrent spectra and (d) Nyquist plots of the two DSSCs.*

The higher J_{sc} could be account for the relatively lower back electron-hole recombination and higher electron injection possibility to the conduction band of TiO_2. The charge carriers get traps due to the presence of the Schottky barrier in a semiconductor/metal interface and hereby prevents them from getting back to the metal. In order to investigate the charge accumulation at photoanode, open-circuit voltage decay profiles of the cells have been monitored in the dark following a short illumination of 1 sun solar radiation. Upon short light illumination, the photoexcited molecules of the dye, inject electrons into TiO_2 which in turn drives the Fermi level towards more negative potential. As light illumination stops, further electron injection gets terminated, and the discharging of charge carriers occurs through oxidized electrolytes.

Table 6.3: *Photovoltaic performance of DSSCs fabricated using two different active electrodes sensitized with RK1.*

Cell	J_{SC} (mA/cm²)	V_{OC} (V)	FF (%)	R_{rec} (Ohm)	Efficiency (%)
RK1_TiO_2	13.28	0.69	64	6	6.26
RK1_TiO_2_Au	17.14	0.73	62	20	7.89

As shown in Figure 6.4c, a slower decay rate is observed in the gold decorated TiO_2 system indicating band bending and higher accumulation of charge carriers. The fitted values of the decay components are represented in Table 6.4. Due to FRET from RK1 to Au, charge injection from Au to TiO_2 also boosted which further adds to the overall increase in device performance.

Table 6.4: *Dynamics of photovoltage transients of DSSCs fabricated using two different active electrodes. The values in parentheses represent the relative weight percentages of the time components.*

Cell	τ_1 (sec)	τ_2 (sec)	τ_{avg} (sec)
RK1_TiO_2	0.23 (92%)	0.83 (8%)	0.27
RK1_TiO_2_Au	0.26 (93%)	1.85 (7%)	0.37

The overall processes ionic and electronic processes occurring in DSSCs can be evaluated through electrochemical impedance spectroscopy (EIS). The ionic and electronic process involves charge transfer and transport property analysis across TiO_2 film, redox electrolyte, and platinum counter electrode [52]. Typically, Nyquist plots consist of two semicircles corresponding to intermediate (10-100 Hz) and high frequency (KHz) regions. A semi-circle within the higher frequency zone corresponds to the charge transfer process occurring at the platinum counter electrode whereas a semi-circle within the region of intermediate frequency is attributed to TiO_2 electron transport and the rearward reaction at the TiO_2 - electrolyte interface and hence corresponds to charge recombination resistance (R_{rec}). Here first semicircle (smaller) representing the charge transfer resistance (R1) at platinum counter electrode

whereas second semicircle (larger) signifying the back electron recombination resistance (R2). The second semicircle with large diameter signifying the increased recombination resistance. The equivalent circuit is shown inset of Figure 6.4d, R2 value constitute to R_{rec} at TiO_2 - electrolyte interface. The R_{rec} value is higher in the RK1_TiO_2_Au electrode (20 ohm) as compared with that of RK1_TiO_2 electrode (6 ohm) that can be ascribed to unfavourable charge recombination at the photoanode electrolyte interface in TiO_2_Au system (values tabulated in Table 6.3). These results are also consistent with the slower open circuit voltage decay profile of the TiO_2_Au photoanode.

DPECs provide a potent means of converting solar energy into stored chemical energy in chromophore molecules, for hydrogen generation via water splitting. Photoelectrochemical cells (PEC) comprised of a photoanode and a platinum cathode in the electrolyte solution. Here we have used RK1_TiO_2 and RK1_TiO_2_Au as photoanodes to carry out PEC measurements. Briefly, the electrochemical process consists of transfer of photoelectrons from photo-excited dye molecules to the CB of TiO_2. The electrons then move to the FTO, subsequently through the external circuit towards the counter electrode. The cathodic reaction (responsible for hydrogen gas production) occurs at the Pt electrode whereas the anodic (oxidation) reaction was carried out via holes at the valance band of semiconductor material. According to the above-mentioned process, several measurements such as LSV, Mott-Schottky and chronoamperometry measurements were carried out. As shown in Figure 6.5a, LSV measurements were being performed successive dark and light illumination (50s of on/off) at a scan rate of 10 mV/s for a potential range from -0.4 V to 1.2 V versus Ag/AgCl. From LSV measurements the UV-vis activity of gold decorated RK1_TiO_2 (J ~0.18 mA cm^{-2}) is found to be much higher (2.4 times) than that of RK1_TiO_2 (J ~0.074 mA cm^{-2}). The pure visible response of RK1_TiO_2_Au electrodes is ~ 0.080 mA cm^{-2} which is itself higher than the UV-Vis response of RK1_TiO_2. The sudden rise and fall of the current density under periodical light and dark states indicate that the change in photocurrent density

comes only from photochemical processes within the nanohybrid material (semiconductor) and is not caused due to thermal excitation. It can be ascribed from the results that plasmonic gold nanoparticles play a crucial role in PEC performance including enhancement of the visible response.

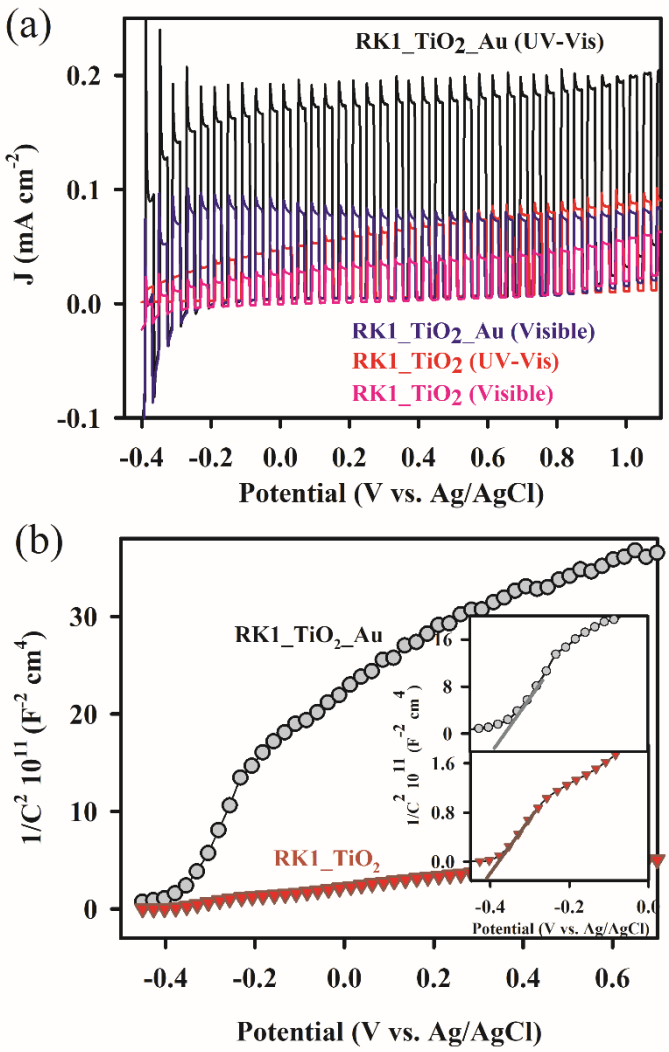

Figure 6.5: *(a) LSV plots of RK1_TiO₂_Au and RK1_TiO₂ active electrodes in 0.1 M Na_2SO_4, their comparative plots under UV-Vis and Visible illumination. (b) Mott-Schotty plots of RK1_TiO₂_Au and RK1_TiO₂ active electrodes at 1000 Hz frequency in 0.1 M Na_2SO_4 solution. Inset shows the magnified view of the two systems.*

As discussed earlier, plasmonic gold due to its dual action not only puts an impact on the charge carrier concentration at the junctions but also enhances the photovoltaic performance by the added phenomena of resonance energy transfer to the sensitizer itself.

Mott-Schottky (M-S) measurements were carried to find the charge accumulation nature of the gold decorated system to that of bare TiO_2. In addition, the charge density N_d can be calculated from the slope of the M–S equation. Further, the flat band potential of the two systems is calculated to be ~-0.4 V vs. Ag/AgCl which facilitates water oxidation process over their surface (shown in inset of Figure 6.5b). The positive slope of the $1/C^2$ vs. the potential plot confirms the n-type nature of the nanohybrid whereas its donor densities (N_d) are given by $2/e\varepsilon\varepsilon_0 N_d$, which is inversely proportional to the slope. As shown in Figure 6.5b, the flattened slope (5.494) of RK1_TiO_2 in $1/C^2$ vs. the potential plot represents lower carrier concentration at the hybrid junction than the much steeper slope (56.52) of the gold TiO_2 system. N_d as calculated are found to be of the order of 3.8×10^{18} and 3.9×10^{19} cm^{-3} for RK1_TiO2 & RK1_TiO_2_Au respectively.

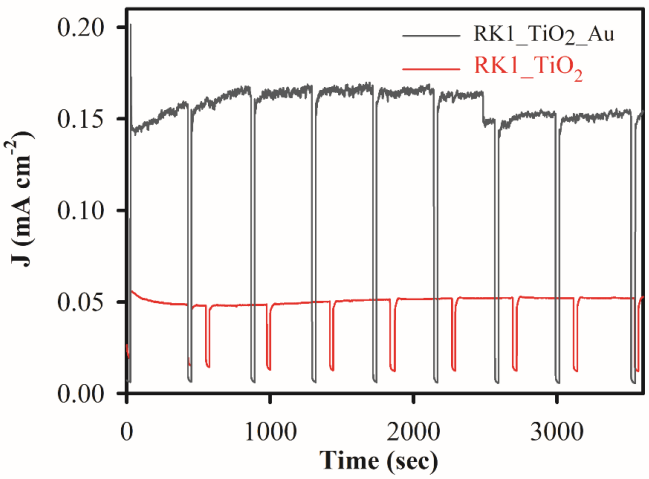

Figure 6.6: *Chronoamperometry stability plots of RK1_TiO_2_Au and RK1_TiO_2 active electrodes under constant illumination of 100 mW cm^{-2} for 3600 seconds.*

The flat band potential of the two systems is calculated to be ~-0.4 V (shown in inset of Figure 6.5b). An increase in the donor density indicates the improvement in photoelectrochemical performance of the RK1_Au-TiO_2 nanohybrid. The results favour our earlier explanation of lower back electron-hole recombination, and higher charge transfer at the photoanode in the presence of gold decorated system. The stability of the photoanode is one of the crucial parts governing PEC performance, here we found that RK1 shows excellent photostability under solar

light irradiation for a longer duration. Figure 6.6 represents chronoamperometry stability plots of the two systems up to 3600 seconds under the continuous illumination of 100 mW cm^{-2} and it is evident that only 3% loss in of photocurrent has been noticed in the system demonstrating i.e. the system is highly stable superior stability of the system. Overall, in visible region gold NPs generating hot electrons by absorbing resonant photons from LSPR excitation and injecting them in CB of TiO_2 has increased the activity of photocatalyst RK1_TiO_2_Au, and the electron and charges transfer pathway has been represented in Scheme 6.1. As a result, such hybrid combination of gold decorated push-pull organic sensitizer-based TiO_2 semiconductor provides promising scope for further advancement in low cost, effective PEC devices.

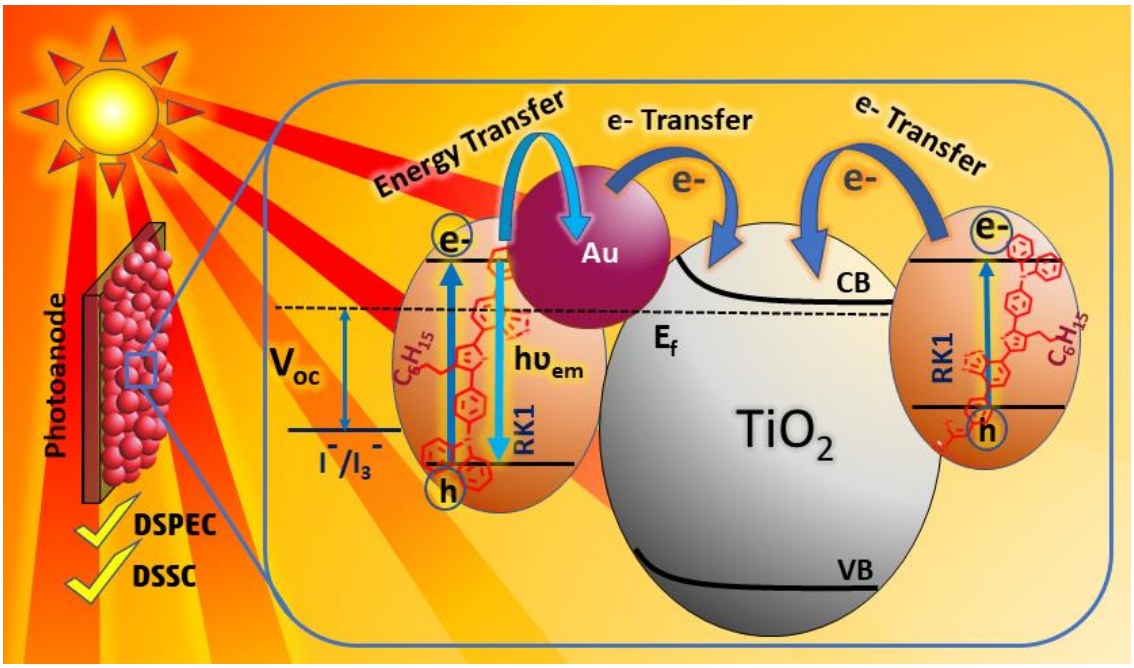

Scheme 6.1: *The electron and charge transfer pathway in RK1-TiO_2-Au nanohybrid and its potential application in DSSCs and DSPECs.*

6.2.2. Unraveling an Ultrafast Electron Transport Mechanism in a Photocatalytic "Micromachine" for Their Potential Light Harvesting Applications [53]: RK1 is is easily soluble in most polar solvents, such as ethanol, ACN, THF, etc., and in some of non-polar solvents. We have used ethanol as a solvent for the preparation of nanohybrids in our study. The optical absorption properties of the dye have been measured using UV-vis spectroscopy and are shown in Figure 6.7a. The interaction between the donor and acceptor groups,

known as the internal charge transfer (ICT) state, results in the absorption peaks of RK1 at 346 nm in the UV region and 470 nm in the visible region. The onset of Figure 6.7a shows the structure of RK1, which has a triphenylamine electron-donating group and cyanoacrylic acid as an electron-withdrawing group. Sensitization of the TiO_2 surface has been a widely accepted method for achieving a broader absorption window in applications where electron-hole pair separation under light irradiation is the basic phenomenon. Among them, photocatalysis is the most common technique to deal with environmental pollution monitoring [54]. The use of this dye was first reported in DSSSc [8] where it was used to sensitize the TiO_2 surface. In the present study, we have prepared the nanohybrid with RK1-sensitized TiO_2. The absorption of TiO_2 and RK1-TiO_2 has been shown in Figure 6.7b. The absorption of TiO_2 is in the UV region, with a peak maximum of 325 nm. For the RK1-TiO_2 nanohybrid, the attachment of RK1 is distinguishable from 400 to 700 nm. The difference between the two spectra has also been plotted and shown in the inset of Figure 6.7b, where a significant contribution of RK1 appears. Thermogravimetric analysis (TGA) has been performed to determine a material's thermal stability before and after RK1 loading on the surface of TiO_2. Figure 6.7c depicts the TGA profiles of TiO_2 (black) and TiO_2-RK1 nanohybrid (red). It shows that the nanohybrid is more stable than pristine TiO_2 nanoparticles due to the enfolding of RK1 in the pores of TiO_2 [55]. The dye loading capability is calculated from the TGA plot in temperature ranges from 180 °C to 450 °C, which was found to be 49%. Such efficient dye loading is beneficial for environmental applications. TEM and high-resolution TEM (HRTEM) have been used to examine the structural morphology of the nanohybrid. The nanoparticles of the hybrid have an average diameter of around 30 nm (Figure 6.7d), which is consistent with TiO_2 nanoparticles [46]. Inset shows the HRTEM image of the nanohybrid (inset of Figure 6.7d), where the fringe width of 0.32 nm corresponds to TiO_2 rutile 101 phases. Phase structural characterization of the TiO_2 and nanohybrid has been determined by powder X-ray diffraction. Figure 6.7e demonstrates the diffraction patterns of TiO_2 (black) and the synthesized RK1-TiO_2 nanohybrid (red).

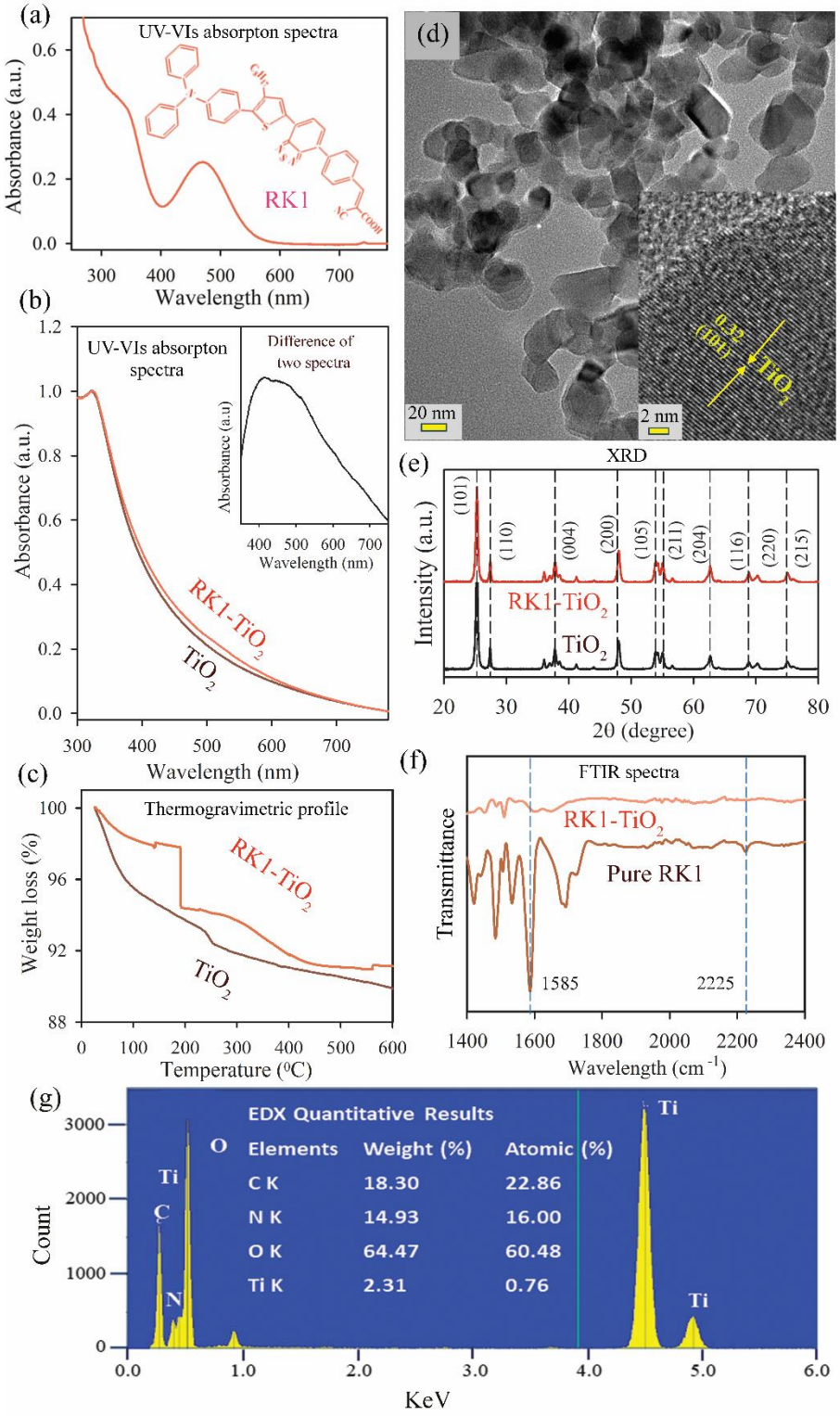

Figure 6.7: *(a) UV-Vis absorption spectrum of RK1 in ethanol solvent, inset shows the molecular structure of RK1. (b) Normalized UV-Vis absorbance spectra of TiO_2 (brown) and RK1-TiO_2 (red), inset shows the differential absorbance spectrum of TiO_2 and RK1-TiO_2. (c) Corresponding Thermogravimetric profile of TiO_2 (brown) and RK1-TiO_2 (red) monitored under N_2 flow. (d) TEM image of the RK1-TiO_2 nanohybrid, inset shows the HRTEM image of the RK1-TiO_2 nanohybrid (e) XRD patterns of TiO_2 (black) and RK1-TiO_2 (red) nanohybrid. (f) FTIR spectra of powdered pure RK1 (brown) and RK1-TiO_2 (red) nanohybrid. (g) The Energy dispersive X-ray spectrum of RK1-TiO_2 nanohybrid, and the corresponding elemental quantitative results.*

For two samples, the characteristic diffraction peaks at around 27°, 36°, 55°, and 25°, 48°, corresponding to planes (110), (004), (211), and (101), (200), respectively, refer to the presence of the mixed rutile and anatase phases of TiO_2 [47]. It has been shown from X-ray diffraction and TEM analysis that there is no change in morphology or phase composition after hybrid formation. Furthermore, the mode of attachment of RK1 to the TiO_2 surface has been investigated with the help of FTIR spectra. As shown in Figure 6.7f, the FTIR spectra of pure RK1 and RK1-TiO_2 hybrids (prepared in ethanol solvent) corroborate the attachment of the dye on the TiO_2 surface through the joining groups of cyanoacrylic acid, hydroxyl group, and cyano group. A clear decrement of peak intensity along with a shift of the vibrational modes, 1698 cm^{-1} C=O vibration of COOH [56] of the nanohybrid compared to RK1 in its pure state, is observed, giving evidence of bridged bidentate binding [27] whereas the peak corresponding to 1585 cm^{-1} of COO^- [56] and 2225 cm^{-1} of C≡N is almost suppressed in the hybrid system, indicating the presence of a COO/CN (A2) binding mode [27]. These changes in the peak positions in the anchoring groups further confirm that the attachment of RK1 on the TiO_2 surface is solvent independent. In addition to it, we have also performed energy dispersive X-ray (EDX) spectral analysis for elemental quantification in the prepared hybrid nanomaterial, as shown in Figure 6.7g. The presence of carbon (C), nitrogen (N), titanium (Ti), and oxygen (O) is due to the organic ligand RK1. For applications of such nanohybrids towards efficient photocatalysis, the steady state and the femtosecond resolved fluorescence transients of the sensitizer and its nanohybrid with TiO_2 were performed to understand the photoinduced chemical and physical phenomena associated with the processes of photon harvesting and exciton separation. As shown in Figure 6.8a, RK1 in ethanol has an emission maximum at 650 nm when excited at 500 nm, corresponding to its absorption maximum, whereas the excitation spectrum (inset of Figure 6.8a) resembles the absorption spectrum. Whereas, as shown in Figure 6.8b, RK1-TiO_2 nanohybrid, when dispersed in ethanol solvent, indicates a shift in emission spectrum to 550 nm with an increase in fluorescence intensity, with excitation spectra having a peak maximum at around 400 nm

(inset of Figure 6.8a). This blue shift in emission spectra suggests the formation of a higher energy intermediate state with an absorption maximum at around 400 nm, as confirmed by the excitation spectra. We have further grafted RK1 on the surface of an insulator so that a comparison could be made due to the electron/charge transfer possibility from the dye to the semiconductor. RK1, after forming a nanohybrid with Al_2O_3, shows similar behavior, i.e., the emission intensity has increased many times compared to the dye in pure solvent.

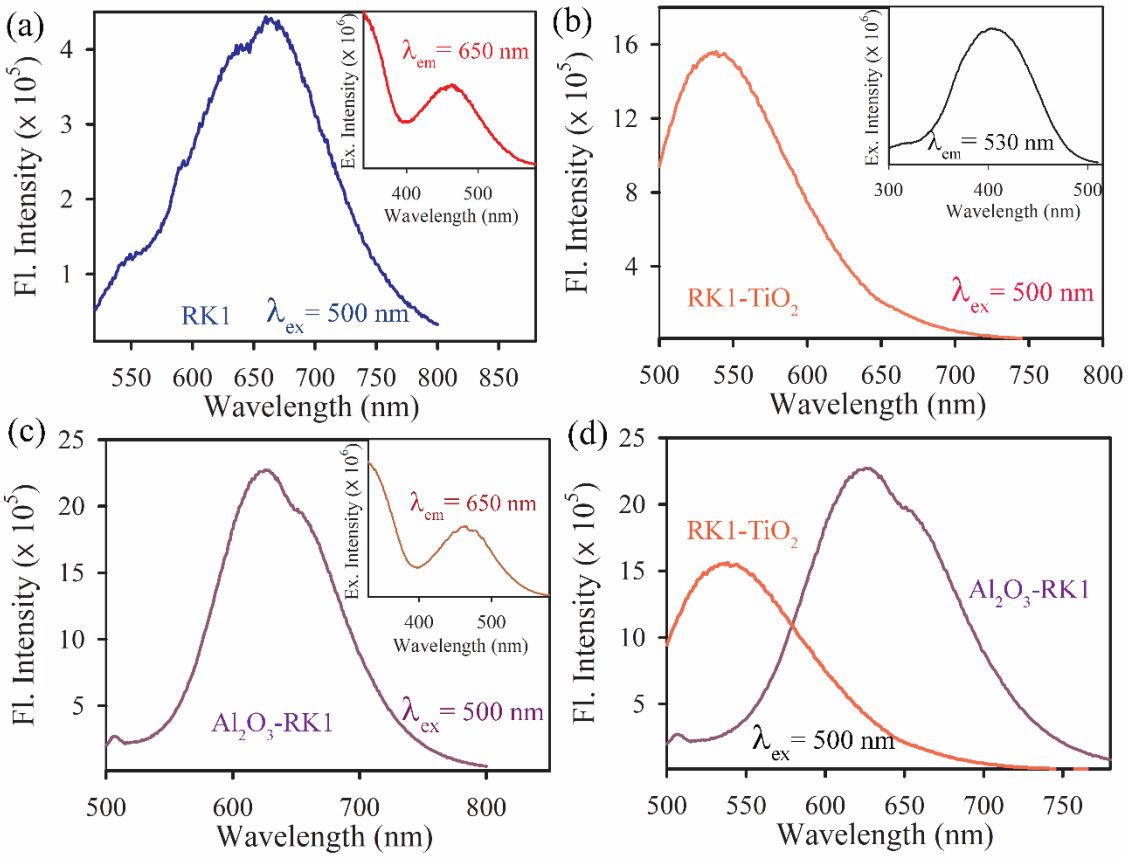

Figure 6.8: *The steady-state fluorescence emission spectra of (a) RK1, (b) RK1-TiO_2 nanohybrid, and (c) Al_2O_3-RK1 nanohybrid at an excitation wavelength of 500 nm. The insets of each show their respective excitation spectra. (d) Comparative emission spectra of RK1, Al_2O_3-RK1, and RK1-TiO_2 nanohybrids.*

However, no such shift in the emission maximum of Al_2O_3-RK1 has been found. As depicted in Figure 6.8c, the maximum of FL at around 650 nm and the absorption maximum at 480 nm resemble excitation spectra. The reduction in fluorescence intensity of RK1 in a polar solvent (ethanol) can be attributed to electronic relaxation from the initially excited Frank condom state (FC) toward an excited state with a more favorable charge transfer (CT) option. This state,

mainly formed in polar solvents, has been described in the literature [24] for push-pull dye and is less conjugated in nature, resulting in a decrease in fluorescence intensity. Additionally, the FL quenching in the presence of TiO_2 due to electron transfer from the dye to the semiconductor substrate compared to that of an insulator like Al_2O_3 has been shown in Figure 6.8d. Such push-pull dyes involve femtosecond-induced chemical and physical properties and have been analyzed through the customized streak camera setup. The photoexcited decays of charge carriers have been analyzed, and the fitted time parameters are summarized in Table 6.5.

Table 6.5. *Dynamics of femtosecond resolved fluorescence transients of RK1, Al_2O_3-RK1, and TiO_2-RK1.*

Sample	Excitation Wavelength (nm)	Emission Wavelength (nm)	τ_1 (ps)	τ_2 (ps)	τ_3 (ps)	τ_{avg} (ps)
RK1	440	650	7.24 (54%)	42.8 (46%)	_	23.56
Al_2O_3-RK1	440	650	28.32 (51%)	579.4 (49%)	_	297.76
TiO_2-RK1	440	550	10.00 (40%)	31.57 (45%)	523.26 (15%)	95.92

The 2D spectrum-time image of RK1 in ethanol is represented in Figure 6.9a when excited with the second harmonic (440 nm, 3.5 ps FWHM) of the femtosecond laser pulse, consisting of a femtosecond-resolved decay having maximum spread at around 650 nm. To get the component value information of transients' decay at FL peak maximum, a streak consisting of 5 nm width along the y-axis centered at 650 nm has been chosen, and the corresponding FL decay transient (Figure 6.9d) depicts two decay components of the order of 7.2 ps having a 54% contribution and 42.8 ps having a 46% contribution. The faster 7.2 ps component may be attributed to the electronic relaxation from the FC state to the CT state, and the later 42.8 ps resembles the ground state relaxation of the CT state. The dye, when attached to the Al_2O_3 surface, shows a completely different behavior. The 2D spectrum-time image (Figure 6.9b) of RK1-Al_2O_3 depicts two different transient decay components: one is of the order of tens of

pico-second while the other is of the order of hundreds of picoseconds. The decay components are 28 ps (51% contribution) and 580 ps (49% contribution) as shown in Figure 6.9e. The 28 ps component can be attributed to a possible injection from the dye excited state to the Al_2O_3 defect/trap states or spectral relaxation as an electronic transition mentioned above from the FC state to the more polar CT state. However, the relaxation here is not as fast (28 ps) as in the case of dye in solvent (7 ps) because of nanohybrid formation, and the ground

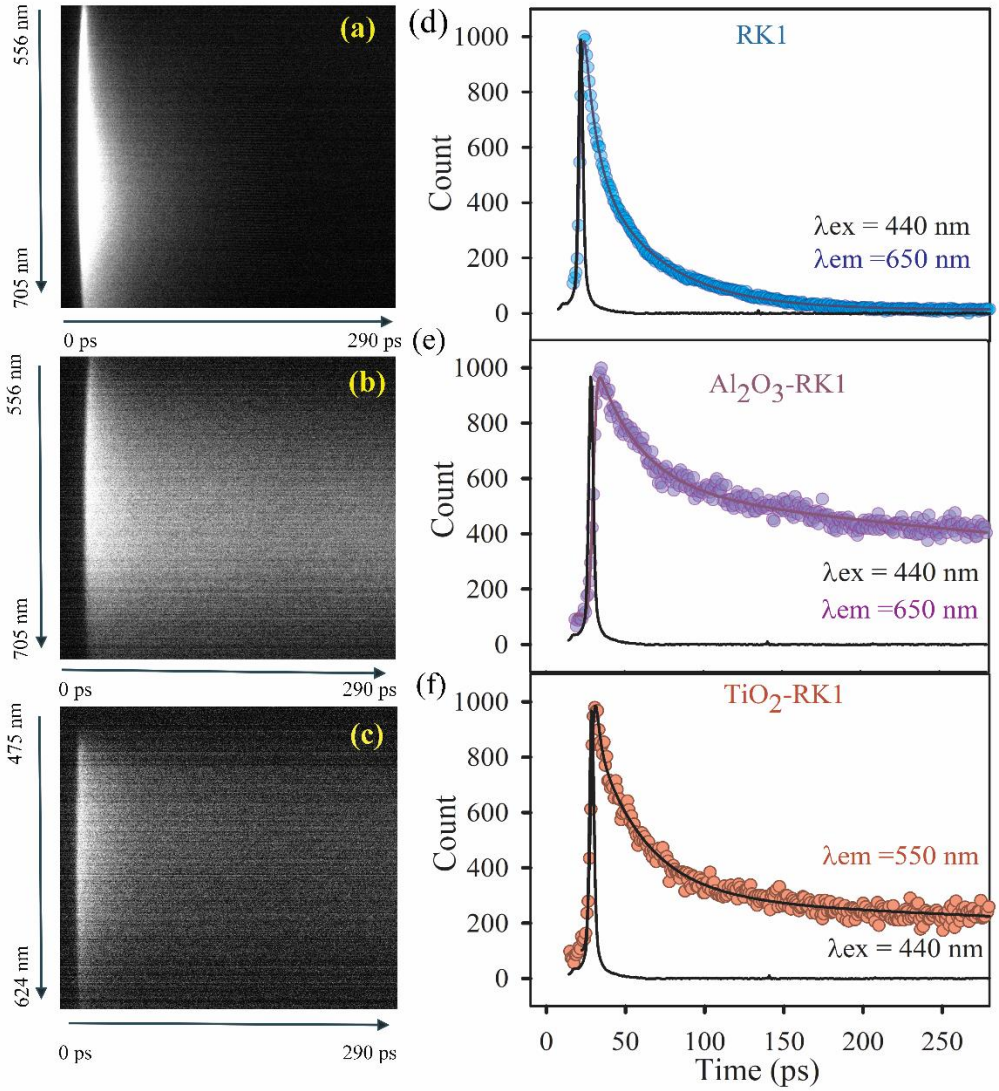

Figure 6.9: *Femtosecond resolved time-wavelength 2D fluorescence decay images of (a) RK1 at 650 nm, (b) Al_2O_3-RK1 nanohybrid at 650 nm, and (**c**) TiO_2 -RK1 nanohybrid, at 650 nm in ethanol solvent. The excitation laser was 440 nm (with a 4 ps pulse width). [Measurements were conducted in the 290 ns time window. The vertical and horizontal axes represent fluorescence emission wavelength, and time respectively.] Corresponding femtosecond resolved fluorescence decay transients of (d) RK1 at 650 nm, (e) Al_2O_3-RK1 nanohybrid at 650 nm, and (f) TiO_2 -RK1 nanohybrid at 650 nm.*

state relaxation from the CT state happens in the order of 580 ps. From the streak spectrum-time image (Figure 6.9c) of RK1-TiO_2, it has been observed that along with these components, a component of an even faster time scale, i.e., 10 ps with a 40% contribution exists (Figure 6.9f). This faster femtosecond timescale component is only due to the electron injection from the excited-state photosensitizer to the semiconducting TiO_2 substrate. The decay has been captured in this case at a 550 nm cantered streak window, which corresponds to its FL maximum.

In order to investigate the effect of such fast electron injection from the excited state of D-π-A visible absorbing chromophore to a wide band gap semiconductor, ROS generation and ROS-mediated photocatalysis towards pollutant degradation under white light irradiation have been monitored. The DCFH assay is a well-known technique to monitor ROS generation in water media. RK1-TiO_2 nanohybrid powder has been used for the photocatalytic measurements under study. From Figure 6.10a, it is evident that the increase in DCF emission at 520 nm upon oxidation of DCFH through ROS generation, which increases with photoexcitation of the nanohybrid under white light, Due to the sensitization of TiO_2 with RK1, a broader absorbance of RK1-TiO_2 has been observed, which thereby shows about three times higher ROS generation in water media compared to the control Al_2O_3-RK1. The higher ROS generation in the presence of TiO_2 compared to that of Al_2O_3 signifies the role of ultrafast electron transfer from the conduction band of RK1 to semiconductor TiO_2. Furthermore, this generation of reactive oxygen species, such as •OH and $O_2^{\bullet -}$, has been utilized for photocatalytic pollutant degradation. To explore the type of ROS generated, we have performed ROS generation experiments in the presence of excess radical scavengers, and the findings are shown in the inset of Figure 6.10a. In the presence of Cu^{2+}, a well-known electron scavenger, the ROS generation ability of RK1-TiO_2 is drastically reduced. It implies the presence of $O_2^{\bullet -}$ in the medium, and due to it, Cu^{2+} gets converted into Cu^{+} while accepting the electron from the medium. Whereas, in the presence of tertiary butyl alcohol

(TBA), which is a scavenger of •OH, no such change in ROS generation has been observed, which clearly indicates that among other reactive species, the negatively charged $O_2^{\bullet -}$ plays the most crucial role in ROS generation. We have here used AO as a model pollutant that would be degraded by recyclable TiO_2-RK1 nanohybrids.

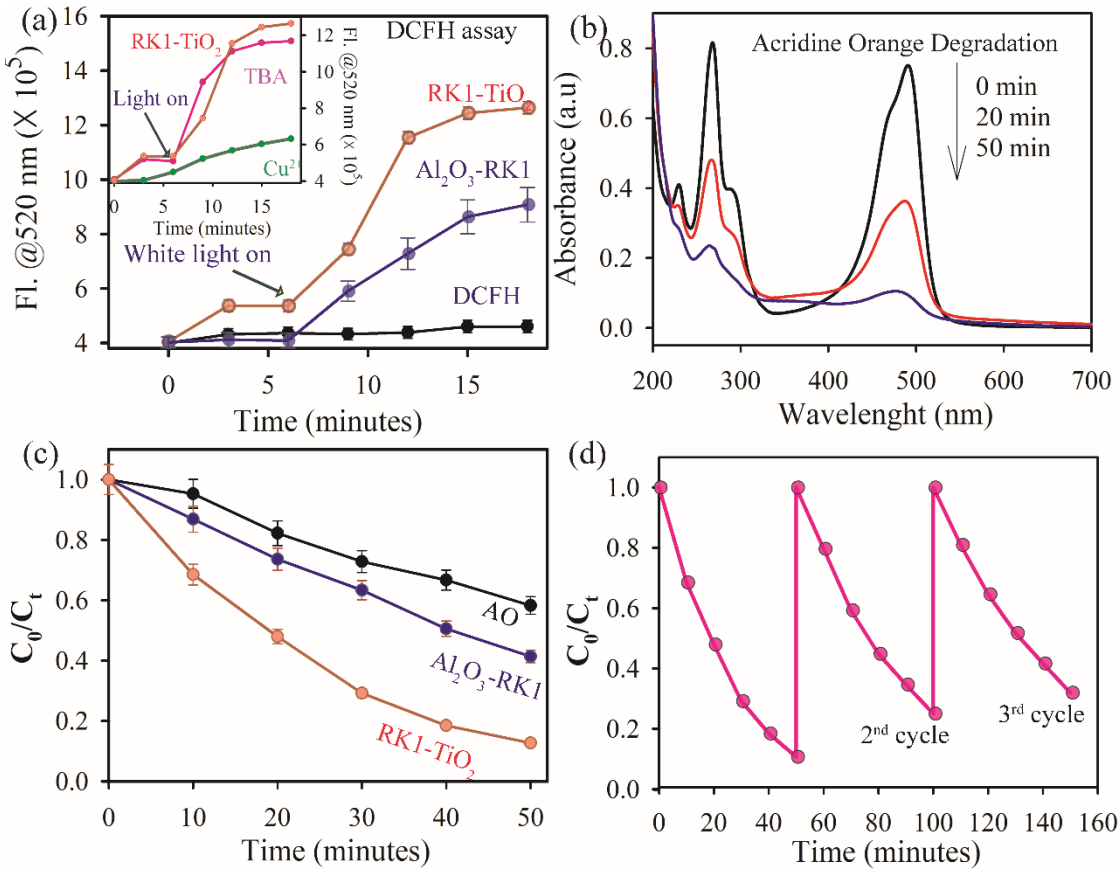

Figure 6.10: *(a) DCFH oxidation with respect to time with the addition of RK1-TiO_2 nanohybrid (brown) Al_2O_3-RK1 (Blue) and DCFH control (black) under white light irradiation monitored at 520 nm. Inset shows the RK1-TiO_2 ROS activity in the presence of radical scavengers; Cu^{2+} (green), and tert butyl alcohol (magenta), without any scavenger (red). (b) Photocatalytic degradation of acridine orange (AO) by RK1-TiO_2 nanohybrid. (c) Comparison of catalytic activity of RK1-TiO_2 with Al_2O_3-RK1 and AO itself at the absorption peak maximum of AO. (d) Recyclability of the catalyst RK1-TiO_2 nanohybrid.*

For the photocatalysis experiment, the nanohybrid and the AO solution were priorly shaken well and kept under dark conditions for 1 h so that they could attain equilibrium after limited adsorption of AO on the surface of the nanohybrid. The measure of photocatalysis is the amount of degradation of AO itself in the presence of a photocatalyst-nanohybrid with light irradiation. Figure 6.10b shows the photocatalytic degradation profile of AO under white light

irradiation; the discoloration of the AO solution and the absorption shift of AO indicates the formation of non-harmful proflavine [57]. To confirm the enhanced AO degradation due to the femtosecond timescale faster electron injection from photoexcited RK1 to TiO_2, control AO degradation experiments were performed with the RK1-Al_2O_3 nanohybrid and AO itself. From Figure 6.10c, RK1-TiO_2 shows maximal photocatalytic activity as observed for the duration of 50 min. Recyclability of the used photocatalyst is one of the important parameters in designing such materials; the intact nature of the FTIR vibrational mode indicates the integrity of the nanohybrid after light irradiation. We have found from Figure 6.10d that our photocatalyst is almost 40% active even after three cycles. The reason behind the decrease in photocatalytic activity after three cycles may be attributed to the agglomeration of reaction products on the surface of the photocatalytic material. These reaction products can block the active sites on the surface of the material, reducing the surface area available for reaction.

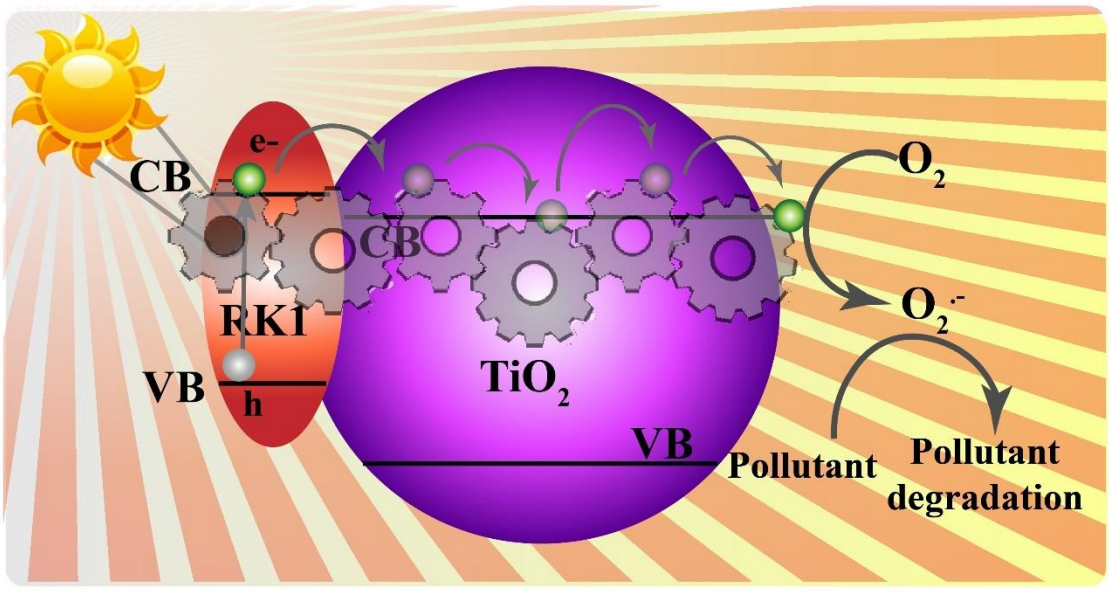

Scheme 6.2: *The RK1-TiO_2 is a photocatalytic micromachine for environmental remediation.*

In addition, the photocatalytic material may also experience surface damage over time due to repeated exposure to light and the generation of reactive species. It can be proven from here that electron injection from dye to the semiconductor surface plays a crucial role in ROS-mediated photocatalysis. A schematic representation (Scheme 6.2) has been shown for more clarification regarding electron transfer and ROS generation.

6.3. Conclusion:

Our present work on a model D-π-A sensitizer, RK1, gives insights into its excited state dynamical behavior for potential application in DSSCs and DPECs and in photocatalysis as a light-harvesting photosensitizer when attached to the surface of TiO_2 nanoparticles. Further addition of plasmonic gold to the overall RK1_TiO_2 system not only improves the DSSCs performance but also increases the PEC performance by almost 3 times. The attachment of Au on the TiO_2 surface was characterized by optical spectroscopic techniques such as X-ray diffraction, and microscopic and IR spectroscopic techniques. The decoration of gold over TiO_2 enhances the device performance due to phenomena like Förster resonance energy transfer from RK1 to Au and plasmon enhanced electron transfer from gold to TiO_2. The pico-second resolved fluorescence transient of RK1_TiO_2 shows the presence of a faster component of ~0.1 ns representing an excellent electron transfer property of the organic dye RK1 whereas fluorescence transient studies on RK1_Al_2O_3_Au system confirm the FRET. The occurrence of enhanced photocatalytic process due to the presence of several phenomena i.e. faster electron transfer, wide absorbance window and FRET at hybrid junctions could provide promising aspects regarding new plasmon coupled solar light harvesting techniques. The fact to be noticed here is that an ultrafast femtosecond-resolved electron injection component of 10 ps has been observed from the excited state of RK1 to TiO_2, which here plays a crucial role in enhanced photocatalytic activity through ROS generation. We have used a femtosecond laser pulse of 3.5 ps to excite the samples in the visible region and monitored the excited state dynamics in a femtosecond-resolved streak camera setup. Our work will open up further directions toward robust, stable, and high-efficiency photocatalysis using D-π-A type sensitizer nanohybrids.

References

[1] A. Aldalbahi, M. E. El-Naggar, M. H. El-Newehy, M. Rahaman, M. R. Hatshan, T. A. Khattab, Effects of technical textiles and synthetic nanofibers on environmental pollution, *Polymers*, 13 (2021) 155.

[2] S. Xenarios, Water at time of war, *Nat. Sustain.*, 6 (2023) 485.

[3] J. Xu, M. Akhtar, M. Haris, S. Muhammad, O. J. Abban, F. Taghizadeh-Hesary, Energy crisis, firm profitability, and productivity: An emerging economy perspective, *Energy Strat. Rev.*, 41 (2022) 100849.

[4] M. Mofijur, T. M. I. Mahlia, A. S. Silitonga, H. C. Ong, M. Silakhori, M. H. Hasan, N. Putra, S. A. Rahman, Phase change materials (PCM) for solar energy usages and storage: An overview, *Energies*, 12 (2019) 3167.

[5] S. Licht, Multiple band gap semiconductor/electrolyte solar energy conversion, *J. Phys. Chem. B*, 105 (2001) 6281.

[6] C. Zou, Q. Zhao, G. Zhang, B. Xiong, Energy revolution: From a fossil energy era to a new energy era, *Nat. Gas Ind. B.*, 3 (2016) 1.

[7] C. S. Lai, Y. Jia, L. L. Lai, Z. Xu, M. D. McCulloch, K. P. Wong, A comprehensive review on large-scale photovoltaic system with applications of electrical energy storage, *Renew. Sustain. Energy Rev.*, 78 (2017) 439.

[8] D. Joly, L. Pellejà, S. Narbey, F. Oswald, J. Chiron, J. N. Clifford, E. Palomares, R. Demadrille, A robust organic dye for dye sensitized solar cells based on iodine/iodide electrolytes combining high efficiency and outstanding stability, *Sci. Rep.*, 4 (2014) 4033.

[9] S. S. Park, Y. S. Won, Y. C. Choi, J. H. Kim, Molecular design of organic dyes with double electron acceptor for dye-sensitized solar cell, *Energy Fuels*, 23 (2009) 3732.

[10] Y. Tachibana, L. Vayssieres, J. R. Durrant, Artificial photosynthesis for solar water-splitting, *Nat. Photon.*, 6 (2012) 511.

[11] S. Ezendam, M. Herran, L. Nan, C. Gruber, Y. Kang, F. Gröbmeyer, R. Lin, J. Gargiulo, A. Sousa-Castillo, E. Cortés, Hybrid plasmonic nanomaterials for hydrogen generation and carbon dioxide reduction, *ACS Energy Lett.*, 7 (2022) 778.

[12] H. Wen, S. Lin, C. Zhao, E. Wang, Nanoparticle surface charge-enhanced heat capacity in molten salt phase change materials for thermal energy storage, *Sol. Energy Mater. Sol. Cells*, 243 (2022) 111795.

[13] H. Huang, J. Zhao, B. Weng, F. Lai, M. Zhang, J. Hofkens, M. B. Roeffaers, J. A. Steele, J. Long, Site-sensitive selective CO_2 photoreduction to CO over gold nanoparticles, *Angew. Chem.*, 134 (2022) e202204563.

[14] L. A. Ortiz-Rodríguez, S. J. Hoehn, A. Loredo, L. Wang, H. Xiao, C. E. Crespo-Hernández, Electronic relaxation pathways in heavy-atom-free photosensitizers absorbing near-infrared radiation and exhibiting high yields of singlet oxygen generation, *J. Am. Chem. Soc.*, 143 (2021) 2676.

[15] L. He, M. X. Li, F. Chen, S. S. Yang, J. Ding, L. Ding, N. Q. Ren, Novel coagulation waste-based Fe-containing carbonaceous catalyst as peroxymonosulfate activator for pollutants degradation: Role of ROS and electron transfer pathway, *J. Hazard. Mater.*, 417 (2021) 126113.

[16] Z. Liu, W. Gao, L. Liu, S. Luo, C. Zhang, T. Yue, J. Sun, M. Zhu, J. Wang, Work function mediated interface charge kinetics for boosting photocatalytic water sterilization, *J. Hazard. Mater.*, 442 (2023) 130036.

[17] W. Yu, L. Zhao, F. Chen, H. Zhang, L. H. Guo, Surface bridge hydroxyl-mediated promotion of reactive oxygen species in different particle size TiO_2 suspensions, *J. Phys. Chem. Lett.*, 10 (2019) 3024.

[18] M. T. Islam, A. Dominguez, B. Alvarado-Tenorio, R. A. Bernal, M. O. Montes, J. C. Noveron, Sucrose-mediated fast synthesis of zinc oxide nanoparticles for the photocatalytic degradation of organic pollutants in water, *ACS omega*, 4 (2019) 6560.

[19] A. Banerjee, R. Ghosh, T. Adhikari, S. Mukhopadhyay, A. Chattopadhyay, S. K. Pal, Development of nanomedicine from copper mine tailing waste: A pavement towards circular economy with advanced redox nanotechnology, *Catalysts*, 13 (2023) 369.

[20] J. Li, X. Lv, B. Weng, M. B. Roeffaers, H. Jia, Engineering light propagation for synergetic photo-and thermocatalysis toward volatile organic compounds elimination, *Chem. Eng. J.* , 461 (2023) 142022.

[21] B. Yıldız, E. Güzel, D. Akyüz, B. S. Arslan, A. Koca, M. K. Şener, Unsymmetrically pyrazole-3-carboxylic acid substituted phthalocyanine-based photoanodes for use in water splitting photoelectrochemical and dye-sensitized solar cells, *Sol. Energy* 191 (2019) 654.

[22] F. Li, K. Fan, B. Xu, E. Gabrielsson, Q. Daniel, L. Li, L. Sun, Organic dye-sensitized tandem photoelectrochemical cell for light driven total water splitting, *J. Am. Chem. Soc.*, 137 (2015) 9153.

[23] N. Tomar, A. Agrawal, V. S. Dhaka, P. K. Surolia, Ruthenium complexes based dye sensitized solar cells: Fundamentals and research trends, *Sol. Energy*, 207 (2020) 59.

[24] V. Maffeis, H. Dogan, E. Cassette, B. Jousselme, T. Gustavsson, Role of electronic relaxation in the injection process of organic push–pull dyes in complete dye-sensitized solar cells, *J. Phys. Chem. Lett.*, 10 (2019) 5076.

[25] F. Bureš, Fundamental aspects of property tuning in push–pull molecules, *RSC Adv.*, 4 (2014) 58826.

[26] S. Mei, W. Shao, S. Huang, X. Kong, Z. Hu, M. Yang, W. Wu, H. Tan, Novel D–A− π–A organic dyes with phenoxazine as a donor unit for dye-sensitized solar cells: The effect of an ethynyl group on performance, *Energy Fuels*, 35 (2021) 19748.

[27] H. Chen, Y. Gong, A. l. Vázquez-Mayagoitia, J. Zhang, J. M. Cole, Dye aggregation, photostructural reorganization and multiple concurrent dye $\cdots TiO_2$ binding modes in dye-sensitized solar cell working electrodes containing benzothiadiazole-based dye RK-1, *ACS Appl. Energy Mater.* , 3 (2019) 423.

[28] S. Haid, M. Marszalek, A. Mishra, M. Wielopolski, J. Teuscher, J. E. Moser, R. Humphry-Baker, S. M. Zakeeruddin, M. Grätzel, P. Bäuerle, Significant Improvement of dye-sensitized solar cell performance by small structural modification in π-conjugated donor–acceptor dyes, *Adv. Funct. Mater.*, 22 (2012) 1291.

[29] J. Patwari, H. Joshi, H. Mandal, L. Roy, C. Bhattacharya, P. Lemmens, S. K. Pal, Exciton dissociation in an NIR-active triohybrid nanocrystal leading to

efficient generation of reactive oxygen species, *Phys. Chem. Chem. Phys.*, 21 (2019) 10667.

[30] S. Sardar, S. Ghosh, H. Remita, P. Kar, B. Liu, C. Bhattacharya, P. Lemmens, S. K. Pal, Enhanced photovoltage in DSSCs: Synergistic combination of a silver modified TiO_2 photoanode and a low cost counter electrode, *RSC Adv.*, 6 (2016) 33433.

[31] Z. S. Seddigi, S. A. Ahmed, S. Sardar, S. K. Pal, Ultrafast dynamics at the zinc phthalocyanine/zinc oxide nanohybrid interface for efficient solar light harvesting in the near red region, *Sol. Energy Mater. Sol. Cells*, 143 (2015) 63.

[32] N. Pan, T. K. Maji, S. Bandyopadhyay, P. Biswas, A. Chatterjee, M. Mitra, A. Chatterjee, S. K. Pal, A combined spectroscopic and theoretical analysis of plasmonic silver nanoparticle sensor towards detailed microscopic understanding of heavy metal detection, *Plasmonics*, 17 (2022) 223.

[33] A. Bera, M. N. Hasan, A. Chatterjee, D. Mukherjee, S. K. Pal, Dual sensitization via electron and energy harvesting in a nanohybrid for improvement of therapeutic efficacy, *ACS Phys. Chem. Au*, 2 (2021) 171.

[34] F. Su, T. Wang, R. Lv, J. Zhang, P. Zhang, J. Lu, J. Gong, Dendritic Au/TiO_2 nanorod arrays for visible-light driven photoelectrochemical water splitting, *Nanoscale.*, 5 (2013) 9001.

[35] P. Kar, T. K. Maji, P. K. Sarkar, S. Sardar, S. K. Pal, Direct observation of electronic transition–plasmon coupling for enhanced electron injection in dye-sensitized solar cells, *RSC Adv.*, 6 (2016) 98753.

[36] H. Choi, Y.-S. Chen, K. G. Stamplecoskie, P. V. Kamat, Boosting the photovoltage of dye-sensitized solar cells with thiolated gold nanoclusters, *J. Phys. Chem. Lett.*, 6 (2015) 217.

[37] J. V. Vaghasiya, K. K. Sonigara, K. B. Fadadu, S. S. Soni, Hybrid AgNP–TiO_2 thin film based photoanode for dye sensitized solar cell, *Perspect Sci* . 8 (2016) 46.

[38] W. Hou, P. Pavaskar, Z. Liu, J. Theiss, M. Aykol, S. B. Cronin, Plasmon resonant enhancement of dye sensitized solar cells, *Energy Environ. Sci.*, 4 (2011) 4650.

[39] M. Ihara, M. Kanno, S. Inoue, Photoabsorption-enhanced dye-sensitized solar cell by using localized surface plasmon of silver nanoparticles modified with polymer, *Physica E Low Dimens. Syst. Nanostruct.* , 42 (2010) 2867.

[40] E. Aslan, M. Karaman, G. Yanalak, H. Bilgili, M. Can, F. Ozel, I. H. Patir, Synthesis of novel tetrazine based D-π-A organic dyes for photoelectrochemical and photocatalytic hydrogen evolution, *J. Photochem. Photobiol. A: Chem.*, 390 (2020) 112301.

[41] H. Ding, M. Xu, S. Zhang, F. Yu, K. Kong, Z. Shen, J. Hua, Organic blue-colored DA-π-A dye-sensitized TiO_2 for efficient and stable photocatalytic hydrogen evolution under visible/near-infrared-light irradiation, *Renew. Energy*, 155 (2020) 1051.

[42] S. A. Ahmed, N. Pan, H. M. Altass, J. Patwari, R. J. Obaid, H. Alessa, R. S. Jassas, S. K. Pal, Broad light harvesting under restricted environment: Photophysical understanding leading to enhanced reactive oxygen species generation, *J. Photochem. Photobiol. A: Chem.*, 418 (2021) 113422.

[43] Z. Zhang, J. T. Yates Jr, Band bending in semiconductors: chemical and physical consequences at surfaces and interfaces, *Chem. Rev.*, 112 (2012) 5520.

[44] C. S. Ponseca Jr, P. Chabera, J. Uhlig, P. Persson, V. Sundstrom, Ultrafast electron dynamics in solar energy conversion, *Chem. Rev.*, 117 (2017) 10940.

[45] X. Zarate, S. Schott-Verdugo, A. Rodriguez-Serrano, E. Schott, The nature of the donor motif in acceptor-bridge-donor dyes as an influence in the electron photo-injection mechanism in DSSCs, *J. Phys. Chem. A*, 120 (2016) 1613.

[46] N. Pan, S. Ghosh, M. N. Hasan, S. A. Ahmed, A. Chatterjee, J. Patwari, C. Bhattacharya, J. Qurban, A. S. Khder, S. K. Pal, Plasmon-coupled donor–acceptor type organic sensitizer-based photoanodes for enhanced photovoltaic activity: Key information from ultrafast dynamical study, *Energy Fuels*, 36 (2022) 9272.

[47] S. El-Sherbiny, F. Morsy, M. Samir, O. A. Fouad, Synthesis, characterization and application of TiO_2 nanopowders as special paper coating pigment, *Appl. Nanosci.*, 4 (2014) 305.

[48] K. Thamaphat, P. Limsuwan, B. Ngotawornchai, Phase characterization of TiO_2 powder by XRD and TEM, *Agric. Nat. Resour.*, 42 (2008) 357.

[49] M. Neupane, S. Lee, I. Park, M. Lee, T. Bae, Y. Kuboki, M. Uo, F. Watari, Synthesis of gelatin-capped gold nanoparticles with variable gelatin concentration, *J. Nanoparticle Res.*, 13 (2011) 491.
[50] J. Wu, B. M. Murphy, N. S. Gould, C. Wang, L. Ma, B. Xu, A FTIR study of the acidity of in situ generated brønsted sites on NaY via displacement reactions, *ChemCatChem*, 11 (2019) 3253.
[51] S. A. Ahmed, M. N. Hasan, H. M. Altass, A. Bera, R. I. Alsantali, N. Pan, A. Y. Alzahrani, D. Bagchi, J. H. Al-Fahemi, A. S. Khder, S. K. Pal, Tetracycline encapsulated in Au nanoparticle-decorated ZnO nanohybrids for enhanced antibacterial activity, *ACS Appl. Nano Mater.*, 5 (2022) 4484.
[52] L. Andrade, R. Cruz, H. A. Ribeiro, A. Mendes, Impedance characterization of dye-sensitized solar cells in a tandem arrangement for hydrogen production by water splitting, *Int. J. Hydrog. Energy*, 35 (2010) 8876.
[53] N. Pan, L. Roy, M. N. Hasan, A. Banerjee, R. Ghosh, M. A. Alsharif, B. H. Asghar, R. J. Obaid, A. Chattopadhyay, R. Das, S. A. Ahmed, S. K. Pal, Unraveling an ultrafast electron transport mechanism in a photocatalytic "micromachine" for their potential light harvesting applications, *Micromachines*, 14 (2023) 980.
[54] M. Umar, H. A. Aziz, Photocatalytic degradation of organic pollutants in water in Organic pollutants-monitoring, risk and treatment, *InTech*, Rijeka, 2013.
[55] M. N. Hasan, A. Bera, T. K. Maji, D. Mukherjee, N. Pan, D. Karmakar, S. K. Pal, Functionalized nano-MOF for NIR induced bacterial remediation: A combined spectroscopic and computational study, *Inorganica Chim. Acta*, 532 (2022) 120733.
[56] W. Wu, Y. Zhou, J. Li, C. Wan, Shape memory and self-healing behavior of styrene–butadiene–styrene/ethylene-methacrylic acid copolymer (SBS/EMAA) elastomers containing ionic interactions, *J. Appl. Polym. Sci.*, 137 (2020) 48666.
[57] J. Patwari, A. Chatterjee, S. Sardar, P. Lemmens, S. K. Pal, Ultrafast dynamics in co-sensitized photocatalysts under visible and NIR light irradiation, *Phys. Chem. Chem. Phys.*, 20 (2018) 10418.

CHAPTER 7

Spectroscopic Studies on Quantum Dot Based Hybrid Nanomaterials for Manifold Applications

7.1. Introduction:

Photovoltaic technology has been a promising technique for developing and utilizing solar energy and is considered a clean strategy for addressing the world's energy crisis [1-4]. Amongst them, photoelectrochemical (PEC) water splitting is regarded as one of the most favourable methods for H_2 production, which relies on the most abundant source, i.e. solar light [5, 6]. Designing photoanodes for full solar-spectrum PEC water-splitting applications has gained significant research interest among fundamental nanoscience researchers [7, 8]. Thus, harvesting near-infrared region (NIR) of the solar spectrum is crucial for enhancing photovoltaic performance since it accounts for almost 50% of total solar energy and generally remains unharvested [9]. In addition, with the high penetrating power compared with ultraviolet (UV) and visible (Vis) light, NIR light is beneficial for applications such as bio-markers and biosensors and also for maintaining sufficient contact between solid-liquid interfaces in photocatalytic devices [10, 11]. General strategies involving NIR-driven PEC photovoltaics include using NIR absorbing sensitizers, rare-earth doped-up conversion materials, photoactive narrow bandgap semiconductors, etc. [12, 13]. In this regard, colloidal lead sulphide quantum dots (PbS QDs) have emerged as a potential candidate due to their size-dependent, easily tuneable optical and electronic properties, which paved the way for their manifold applications, including light-emitting devices, photoswitches, photodetector and as a biosensor other than NIR based PEC water splitting and quantum dot solar cells [14]. However, insufficient separation of excitons and faster charge carrier mobility have become increasingly significant problems in NIR photovoltaics [15]. In this regard, the attachment of PbS QDs with wide band gap

semiconductors such as TiO_2 could be a possible pathway and has been shown to provide a better charge separation [16-18].

TiO_2 photoanodes, being cost-effective and earth-abundant since the first demonstration of water splitting by Honda and Fujishima[19], have opened the area of extensive research on such wide bandgap semiconducting materials such as $BiVO_4$, Fe_2O_3, WO_3 etc. [20, 21]. Furthermore, modification of TiO_2 with a dopant, noble metals and narrow band gap semiconductors has arisen due to its practical implementation in broadband energy harvesting [22].

Carbon, one of the most abundant elements, exhibits excellent charge transport properties superior to its inorganic counterparts [23]. It is not surprising that graphene sheets in their low-dimensional form, i.e., carbon nanotubes (CNTs), whether single walled or multiwalled, exhibit a wide range of applications owing to their delocalized π-electrons, exceptional electrical and thermal conductivity, hollow, high surface area, and stability [23-25].

Additionally, coupling TiO_2 with CNT can be advantageous because of improved visible activity and efficient charge transport characteristics [26]. A built-in electric field in the TiO_2-CNT heterojunction forms the Schottky junction, further promoting the smooth flow of electrons by reducing the kinetic energy barrier and preventing the e^--h^+ pair recombination [27, 28]. At the same time, QDs-CNT nanocomposites have recently emerged as a new field in nanotechnology due to the interfacial effect between them and their application in large-scale miniaturization [29, 30]. Therefore, before such nanocomposites can be utilized efficiently, it is necessary to understand their surface engineering, functionalization, and synthesis. Typically, prior to the preparation of the QD-CNT nanocomposites, ligand exchange is the widely used method in PbS QDs. Otherwise, a long insulating ligand covering the surface of QD would restrict the interfacial interaction between QD and the substrate [31, 32]. However, these methods involve lengthy synthesis procedures and can reduce QD stability [33]. Therefore, adsorbing QDs on the surface of TiO_2-CNT nanohybrid can serve the

two-in-one purpose, which colocalizes the QD with CNT on the surface of TiO_2 and would resolve the problem of rigorous ligand exchange to get better attachment affinity with CNT. Nevertheless, a NIR active QD, exhibiting a dual charge transfer channel with efficient exciton separation, high charge transportation mobility, along with broadband light harvesting from UV to NIR in a nanocluster, could provide an efficient pathway towards NIR light harvesting.

We, herein, report a PbS QD-TiO_2-MWCNT tri-hybrid combining the factors related to efficient NIR PEC water splitting. PbS QDs act as a NIR active material combined with TiO_2-MWCNT nanohybrid to provide additional benefits over its pristine hybrid combinations in terms of e^- - h^+ pair separation, charge carrier transportation and full solar spectrum harvesting. Incorporation of MWCNT in combination with TiO_2 not only provides an extra charge transfer route for PbS QD, but reduces the electron-hole recombination route at MWCNT-TiO_2 heterojunction due to increased electrical double layer capacitance. The formation of tri-hybrid has been characterized with the help of UV-Vis-NIR absorption, emission spectroscopy, Raman spectroscopy and transmission electron microscopy (TEM). The photon harvesting capability of the tri-hybrid at the NIR range has been confirmed by higher reactive oxygen species (ROS) under IR lamp irradiation. To explore the inherent charge transportation dynamics, time-resolved fluorescence decay transients of the tri-hybrids have been measured and each of the time components have been analyzed along with other prepared hybrid combinations. The electronic structure and mechanism of charge transfer dynamics in the tri-hybrid has been further investigated by using the first principles DFT computational methods to understand their experimental findings and shift of fermi energy levels. The PEC results, electrochemical impedance, and Mott-Schottky analysis of the hybrids under IR lamp irradiation signify that MWCNT introduces faster charge carrier transportation in the tri-hybrid. Thus, the fundamental studies on the tri-hybrid would be equally beneficial for the future development of NIR active material.

7.2. Results and Discussion:

7.2.1. Near-Infrared Active Tri-nanohybrid for Enhanced Energy Harvesting [34]: The characterization of the pure MWCNT, TiO_2 and TiO_2-MWCNT has been performed with the help of transmission electron microscopy (TEM) and diffuse reflectance spectra (DRS). The TEM micrographs of MWCNT shown in Figure 7.1a illustrate that the MWCNT consist of folded graphene sheets forming the cylindrical shape. The Selected Area Electron Diffraction (SAED) shown in the upper inset of Figure 7.1a reveals the non-crystallinity of the nanotubes; however, the existence of several nanotube walls may mislead to the fringe-like pattern. The net outer and inner diameter of the nanotube is around 17 nm and 4.21 nm, respectively as depicted from high-resolution TEM (HRTEM) image (lower inset of Figure 7.1a). The spherical nature of TiO_2 nanoparticles with an average diameter of ~ 24 nm is shown in Figure 7.1b. The interplanar distance of the nanoparticles has been calculated from the reconstruction of the inverse FFT of the brightest dot corresponding to the FFT of the HRTEM micrograph shown in the inset of Figure 7.1b. The calculated fringe distance of 0.34 nm [35] equals 110 planes of TiO_2. Further from the TEM micrograph shown in Figure 7.1c, the formation of the TiO_2-MWCNT hybrid is evident, and there is no significant change in the morphology of the individual components. The carboxylic group functionalized MWCNT has a higher attachment affinity towards TiO_2 than that of bare MWCNT since the attachment happens through the carboxylic group, passivating the oxygen vacancy states of the TiO_2 surface. The HRTEM micrograph in a magnified scale (inset of Figure 7.1c) portrays the attachment of TiO_2 on the wall of MWCNT. The UV−vis diffuse reflectance spectra (DRS) are shown in Figure 7.1d. Pure TiO_2 exhibits the characteristic absorption edge at ~395 nm, confirming its absorption in the ultraviolet region. Evidently, the absorption in the visible region increases with the addition of CNT in the composite. Also, the red-shift towards a higher wavelength by TiO_2-MWCNT is attributed to the electronic interaction between TiO_2 and MWCNT. However, in the case of MWCNT only, no absorption edge has been observed due to the

shielding effect of MWCNT caused by excessive light absorption by MWCNT itself.

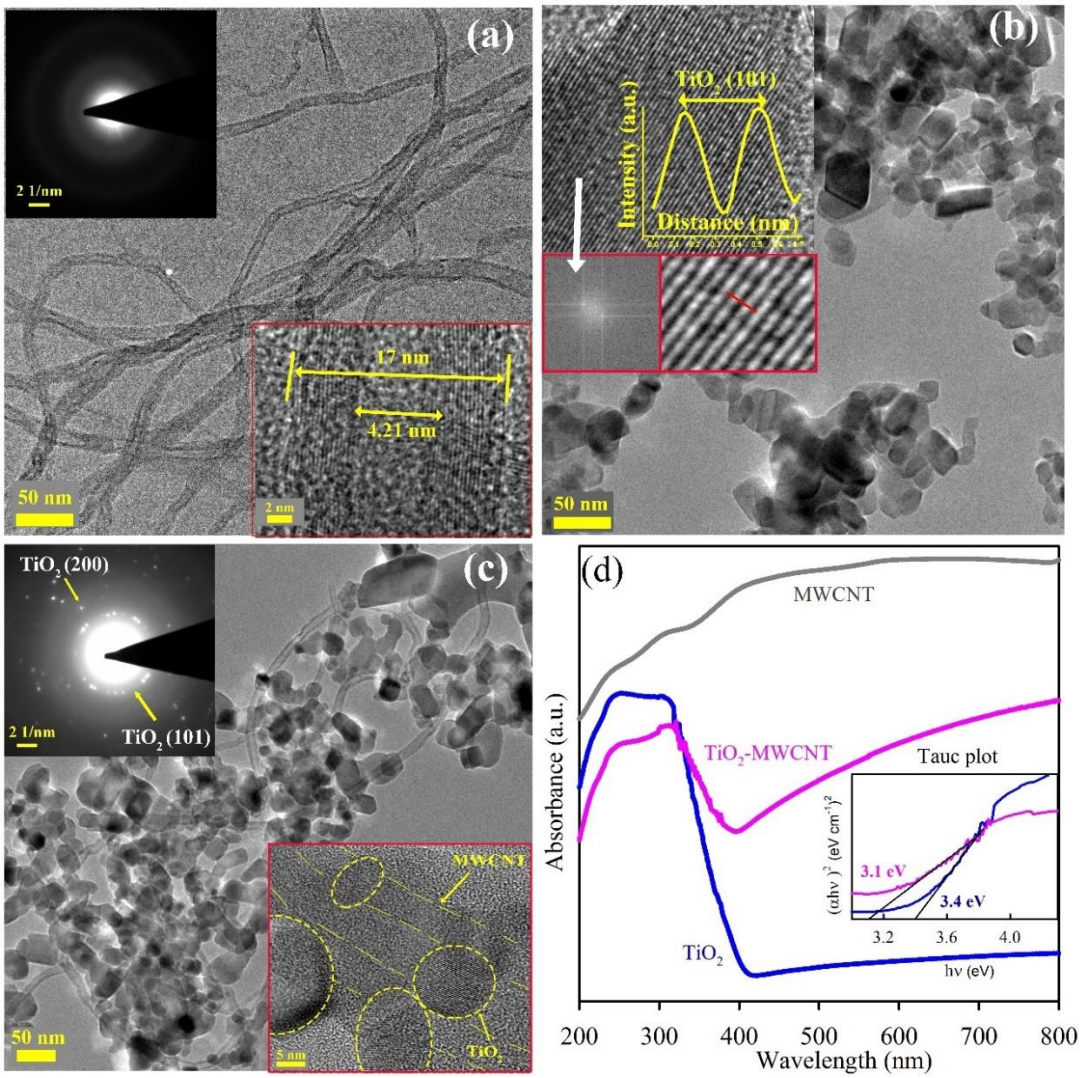

Figure 7.1: *Characterization of TiO_2-MWCNT nanohybrid (a) TEM image of the MWCNT. Upper inset: shows the SEAD pattern. Lower inset: HRTEM image of MWCNT. (b) TEM image of TiO_2 nanoparticle. Inset: HRTEM image and corresponding FFT and fringe distance of TiO_2 (110) plane. (c) TEM image of TiO_2-MWCNT nanohybrid. Upper inset: SEAD pattern of the nanohybrid. Lower inset: HRTEM image of TiO_2-MWCNT nanohybrid. (d) UV–Vis Diffuse Reflectance spectra of MWCNT, TiO_2 and TiO_2-MWCNT nanohybrid. Inset: Tauc plot for TiO_2 and TiO_2-MWCNT hybrid.*

The energy band gap calculated from the Tauc plot (inset of Figure 7.1d) of pure TiO_2 is 3.4 eV [36]. Whereas for the TiO_2-MWCNT hybrid, it is 3.1 eV. It is inferred that the band gap of TiO_2 decreases in the TiO_2-MWCNT hybrid, suggesting that TiO_2-MWCNT hybrid efficiently absorbs light in the visible region. The near-infrared (NIR) active sample comprises oleic acid-capped colloidal PbS quantum dots. The structural and optical characterization of

colloidal PbS QDs have been represented in Figure 7.2. PbS QD dispersed in toluene, as depicted in Figure 7.2a has the lowest energy (1S) absorption and emission peak at 755 nm and 820 nm, respectively. It is evident from the absorbance spectra that the QD sample exhibits a bandgap (1.6 eV) in the NIR region and is thereby suitable for NIR light harvesting. As shown in Figure 7.2b, the TEM spectrum confirms the uniform spherical distribution of QDs, which have a mean diameter of around 2.45 nm, as calculated from size distribution statistics.

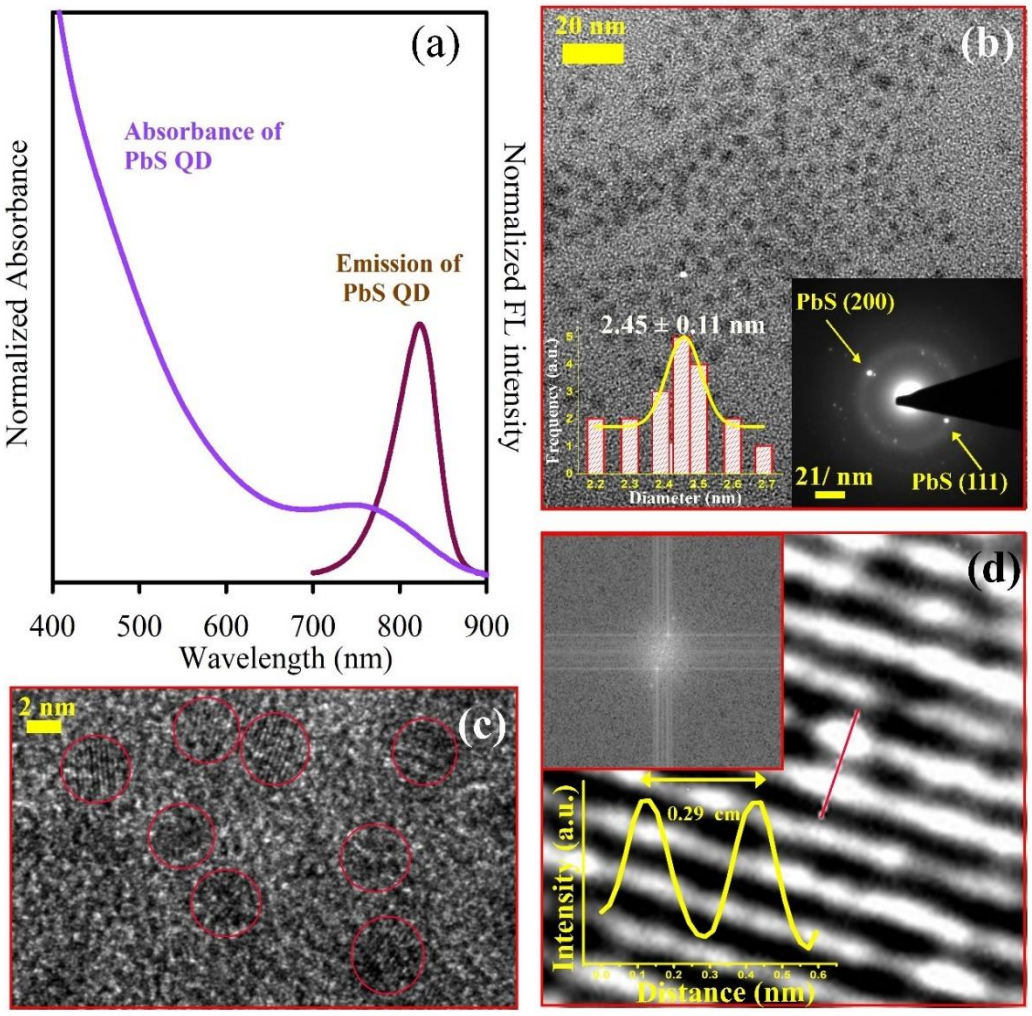

Figure 7.2: *(a) Normalized absorbance and emission of PbS QDs in toluene, (b) TEM image of PbS QDs. Inset (left): shows the size distribution of PbS QDs. Inset (right): shows the SEAD pattern. (c) HRTEM image of PbS QDs. (d) Fringe distance of PbS QD.*

The discrete rings obtained from the SAED pattern show the crystallinity of the semiconducting PbS QDs. The positions of two bright spots, as clearly shown in the inset of Figure 7.2b, refer to the crystal planes of 200 and 111. Further, the

HRTEM image reveals the existence of the lattice fringe (Figure 7.2c). The corresponding fast Fourier transformation (FFT) and reconstruction of inverse FFT from a particular dot in FFT (Figure 7.2d) indicate the lattice spacing to be ~0.29 nm, coming from the contribution of 200 crystal plane of PbS QD. As exhibited from the TEM image, the PbS QDs are uniformly decorated on the surface of the TiO_2-MWCNT hybrid. The spherical darker spots visible from the HRTEM image (inset of Figure 7.3a) clearly indicate the surface adsorption of PbS QDs on the surface of TiO_2.

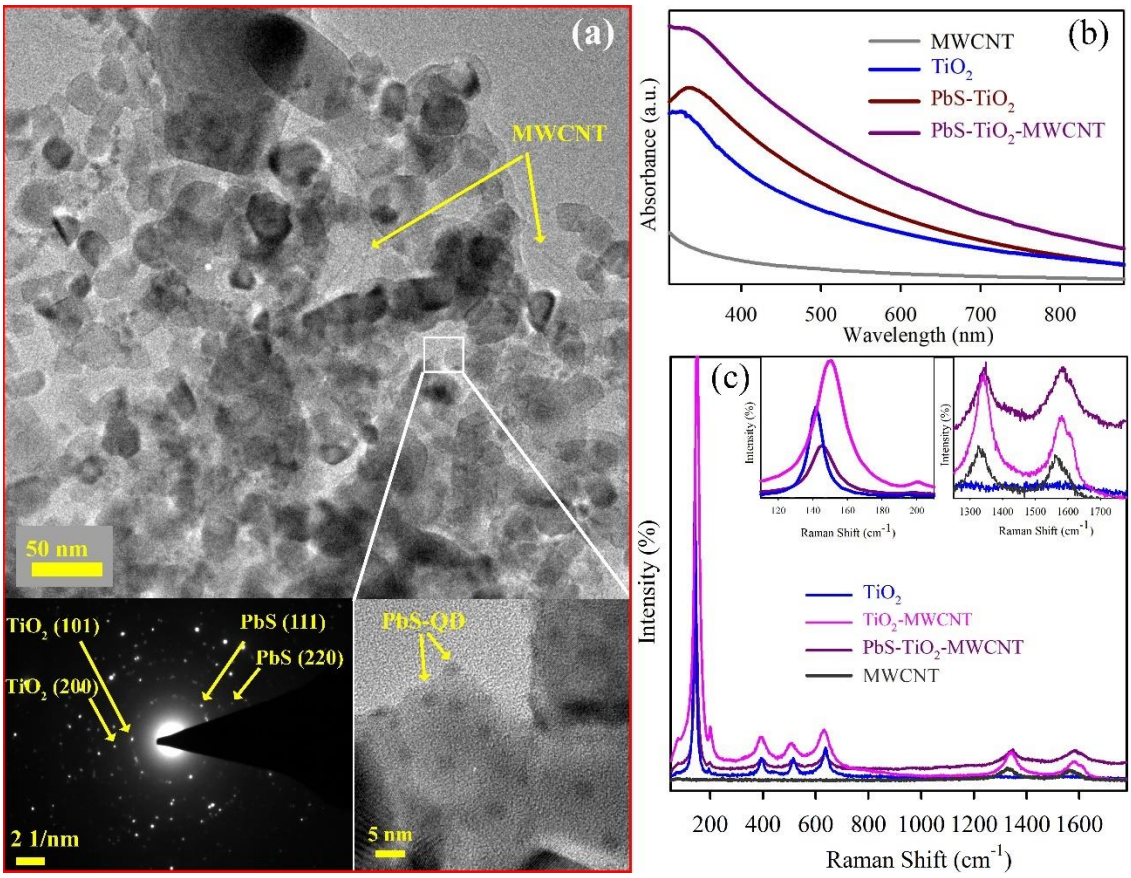

Figure 7.3: *Characterization of PbS-TiO_2-MWCNT tri-hybrid. (a) TEM image of the PbS-TiO_2-MWCNT tri-hybrid. Lower right-side inset: shows the enlarged part of the selected area of PbS-TiO_2-MWCNT tri-hybrid. Lower left-side inset: shows the SEAD pattern. (b) UV–Vis Diffuse Reflectance spectra of MWCNT, TiO_2, TiO_2-MWCNT nanohybrid, and PbS-TiO_2-MWCNT tri-hybrid. (c) Raman spectra of TiO_2, TiO_2-MWCNT nanohybrid, and PbS-TiO_2-MWCNT tri-hybrid. Inset left: Zoomed at lower scale. Inset right: zoomed at higher scale.*

The simultaneous existence of PbS QDs and TiO_2-MWCNT can further be proved with the help of dotted rings corresponding to TiO_2 (101), PbS (111), TiO_2 (200) and PbS (220) as evident from the SAED pattern. Besides TEM analysis, UV-Vis spectra of the hybrids have also been recorded to analyze their nature.

TiO_2 has a characteristic absorbance peak at 330 nm in the UV region, whereas no significant absorbance peak for MWCNT is observed. The absorbance peak of PbS when absorbed on the surface of TiO_2 and TiO_2-MWCNT hybrid is not visible due to the high scattering from TiO_2 as well as MWCNT. For a better understanding of the hybrid formation, Raman spectra of pure TiO_2, pure MWCNT, TiO_2-MWCNT and the tri-hybrid are shown in Figure 7.3c. The pure TiO_2 shows firm Raman peaks distinctively at 141.1, 395.4, 514.8, and 637.5 cm^{-1}, they are assigned to $Eg^{(1)}$, $B_1g^{(1)}$, A_1g + $B^{(2)}{}_1g$, and $Eg^{(2)}$ vibration modes respectively corresponding to anatase phase of TiO_2 [35, 37]. Unsurprisingly, TiO_2-MWCNT displayed characteristic bands of both pure TiO_2 and MWCNT. As exhibited, the two distinct bands at 1342.1 and 1575.0 cm^{-1} (inset of Figure 7.3c), which were absent in bare TiO_2 and due to the D and G bands of disordered sp^2 carbon and degree of defects in MWCNT [38]. Also, the D and G bands related to MWCNT were originally at 1337.1 and 1560.0 cm^{-1} in the composite, which were relatively blue-shifted, indicating a strong interaction between TiO_2 and MWCNT. Also, the I_D/I_G ratio decreased from 1.47 for the TiO_2-MWCNT hybrid to 1.11 for the pure MWCNT. Further, I_D/I_G decreased to 1.03 for the tri-hybrid PbS-TiO_2-MWCNT with increased FWHM of both the D and G band peaks, inferring the changes due to attachment with PbS. Referring to the $E_g^{(1)}$ band of TiO_2 (inset of Figure 7.3c), there is a significant red shift in the peak position of the $E_g^{(1)}$ band, which is at 145.3 cm^{-1} for trihybrid and 150.0 cm^{-1} for TiO_2-MWCNT hybrid [39]. The band at 141.6 cm^{-1} for pure TiO_2 is responsible for the symmetric vibration of O–Ti–O stretching, attachment of carboxylic group at oxygen vacancy state and surface adsorption of PbS on TiO_2-MWCNT surface led to a significant shift in the Ti-O stretching frequency, indicating strong interaction between TiO_2, MWCNT and PbS.

The band position NIR-sensitive PbS QDs is such that is favourable for photoinduced electron transfer (PET) to the conduction band of TiO_2. The approximate idea of the HOMO and LUMO states can be guessed based on the existing literature [40]. As the size of QD decreases due to the quantum confinement, the energy gap increases and the corresponding LUMO (E_1) shifts

towards the more positive side. In contrast, the HOMO (H_1) shifts towards more negative side of the energy scale [14, 40]. Here, QD has band gap of ~1.6 nm, the E_1 must be > -4.0 eV and H_1 < -5.40 eV, facilitating the possibility of charge transfer to the conduction band of wide band gap semiconductor TiO_2 (-4.0 eV) [41] as well as directly to the conduction band of MWCNT (-4.3 eV) [42]. The photoinduced electron transfer from PbS QD to TiO_2, MWCNT and the hybrid TiO_2-MWCNT under excitation of 510 nm has been observed from steady-state emission data shown in Figure 7.4a.

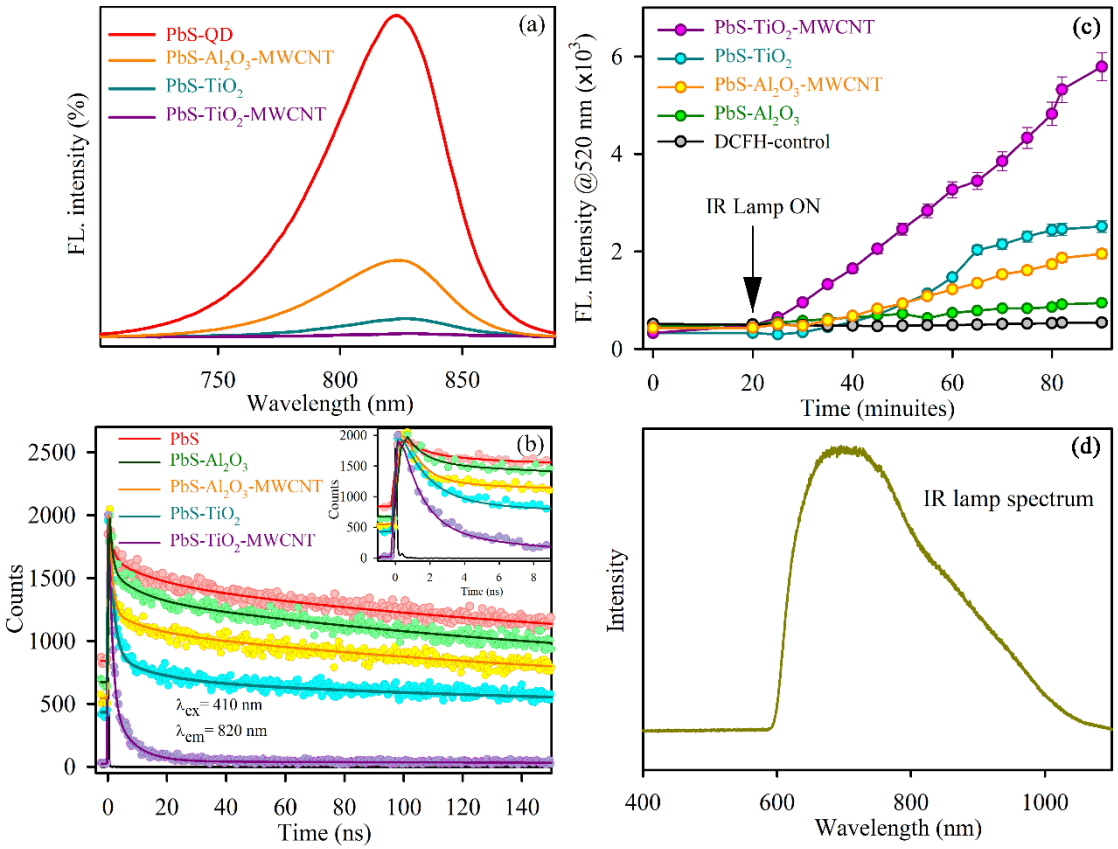

Figure 7.4: *Quenching in steady state emission of PbS QD after attachment with (a) TiO_2, Al_2O_3-MWCNT and TiO_2-MWCNT. Time resolved photoluminescence of (b) PbS QD (red) and the changes in the decay profiles after attaching with Al_2O_3 (green), Al_2O_3-MWCNT (orange), TiO_2 (cyan) and TiO_2-MWCNT (violet). Inset: Shows the faster PL decay profiles of the corresponding systems, magnified at lower scale. (c) Time dependent oxidation of DCFH under IR illumination, monitored at 520 nm, in presence of PbS-TiO_2-MWCNT tri-hybrid (violet), PbS-TiO_2 (cyan) and PbS-Al_2O_3-MWCNT (orange), PbS-Al_2O_3 (red), and time dependent oxidation of only DCFH as control (black). (d) represents the IR lamp spectra.*

The steady-state emission of PbS QD at 820 nm was gradually quenched in the presence of TiO_2 and TiO_2-MWCNT. We have attached the PbS QDs on the surface of an insulator Al_2O_3, and a significant quenching can clearly be observed

(Figure 7.4a), signifying our assumption of electron transfer from PbS QD to MWCNT by bringing them in close proximity at the surface of TiO_2. The fasted ground state recovery of photoexcited charge carriers of PbS QD (i.e. short lifetime) is expected in the tri-hybrid due to the formation of Schottky junctions and the availability of dual channel electron transportation channels. Whereas, in PbS-MWCNT the electron transportation from PbS QD to MWCNT occurs (Al_2O_3 in this case) on the host surface, rather than the direct attachment of PbS QD with MWCNT, which is reflected as a comparatively slower ground state recovery. Furthermore, the PET rate from PbS DQ to the individual and hybrid systems has been further observed with the help of photoluminescence (PL) decay transients, as illustrated in Figure 7.4b. The PL decays of all the systems have been fitted and tabulated in Table 7.1.

Table 7.1: *Dynamics of time-resolved photoluminescence transients of the PbS QD and the hybrids PbS-TiO_2 and PbS-TiO_2-MWCNT and PbS-MWCNT at excitation wavelength 0f 410 nm and emission monitored at 820 nm.*

System	τ_1 (ns)	τ_2 (ns)	τ_3 (ns)	τ_{avg} (ns)
PbS-QD	1.1 ± 0.4 (31%)	12.3 ± 2.0 (16%)	193.0 ± 5.0 (53%)	105.0
PbS-QD-Al_2O_3	1.0 ± 0.6 (42%)	12.0 ± 4.0 (15%)	193.0 ± 6.0 (42%)	85.0
PbS-QD-Al_2O_3-MWCNT	1.5 ± 1.0 (60%)	12.3 ± 3.0 (10%)	193.0 ± 6.0 (30%)	59.0
PbS-TiO_2	1.3 ± 0.3 (64%)	7.6 ± 2.5 (20%)	193.0 ± 4.0 (15%)	31.3
PbS-TiO_2-MWCNT	1.1± 0.1 (80%)	8.3 ± 2.0 (20%)		2.7

From the fitted results, the PL decay of PbS QD consists of several time components with 105 ns of average life, out of which 192 ns components contribute the highest percentage and are solely due to the radiative recombination of the photoexcited carriers. The other shorter lifetime components may be attributed to the vibrational relaxation trapping of photogenerated electron to the defect states and have contributed a significant

percentage may be due to the longer time taken to record the PL decay. A faster component of 1.1 ns having 64% contribution in the PbS-TiO_2 hybrid system is undoubtedly coming due to PET from PbS QD to the conduction band of TiO_2. On the other hand, PbS QD has PET possibility to the conduction band of MWCNT, as confirmed by the PL decay of QD in PbS-Al_2O_3-MWCNT. The observed slight change of decay transient of PbS QD on the Al_2O_3 surface can be justified by the presence of surface trap states. As expected, a 60% contribution from the faster component (~1 ns) is observed, with a 30% contribution from the usual ground state recovery of photoexcited charge carriers. However, the PET rate is higher in TiO_2 than in MWCNT. The highest charge transfer ~1 ns (80%) has been observed from PbS QDs to the TiO_2-MWCNT hybrid system. Also, as depicted from the fitting results, almost all of the photoexcited charge carriers participated in the process of PET as no contribution from 193.0 ns lifetime has been observed and resulted in an overall reduction in the baseline, thereby reflected as faster ground state recovery. Due to the dual charge transfer pathway to TiO_2 and MWCNT, the overall charge transfer rate in the hybrid system has increased significantly. Enhanced charge transfer from QD to the hybrid could be associated with the additional advantages of MWCNT as it provides an overall band alignment due to the formation of Schottky junction in the presence of MWCNT, which is reflected as reduced back electron-hole recombination. Along with this, it provides faster carrier mobility, which is the characteristic property of graphene-based structures [25].

In order to investigate the activity of the tri-hybrid system in the NIR region, we carried out reactive oxygen species generation (ROS) experiments using DCFH assay under IR light illumination and correlated the amount of ROS generated to the tri-hybrid performance. The ROS generation capability of the different hybrid samples through the probe DCFH has been shown in Figure 7.4c. The IR lamp by which the samples have been irradiated has a wavelength span that starts from 590 nm and lasts up to 1000 nm, as shown in Figure 7.4d. DCFH assay is a well-established technique for overall quantitate ROS detection; however

exact nature of ROS cannot be predicted through this method. A distinct ROS generation ability of the samples, i.e. PbS-TiO_2, PbS-Al_2O_3-MWCNT, can be observed. Upon IR lamp irradiation, the excitons from CB of PbS QD get separated by the mechanism of transferring electrons to the CB of TiO_2 in PbS-TiO_2 hybrid whereas directly to CB MWCNT in PbS-Al_2O_3-MWCNT hybrid. The overall isolated electron and hole react with water and oxygen and contribute to generating ROS in the media. Compared to their parent hybrids, a ~3 times higher ROS generation is observed in the tri-hybrid PbS-TiO2-MWCNT sample. The enhanced ROS response in tri-hybrid compared to PbS-TiO_2 can be related to the fact that the introduction of MWCNT would improve the transport of the majority of photoinduced carriers in the CB of TiO_2 so that the back recombination of photoexcited electron-hole pairs could be reduced.

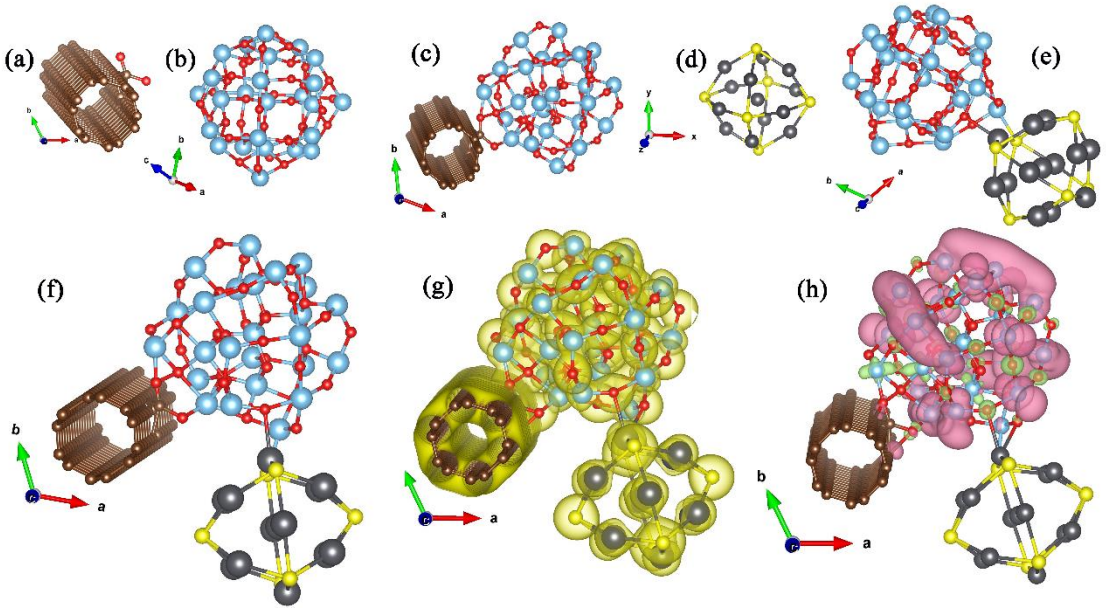

Figure 7.5: *Ground state configuration of different structures (a) carboxylic functionalized single wall carbon nanotube (CNT), (b) TiO_2 nanoball, (c) TiO_2-CNT, nanohybrid, (d) PbS nanoball, (e) TiO_2–PbS nanohybrid and (f) PbS-TiO_2-CNT (Tri-hybrid). The charge and spin density plot of the tri-hybrid.*

To investigate the details of electronic property and the mechanism of enhanced charge transfer in the tri-hybrid system, we have performed first-principles density functional theory (DFT) calculations. To model the tri-hybrid system, we have used a single wall carbon nanotube (SWCNT) instead of a multiwalled tube and functionalized it by a carboxylic group (COO^-) at the metallic armchair (3,3)

carbon nanotube as shown in Figure 7.5a. TiO_2 (anatase phase) and PbS nanoballs have been constructed after making 10 × 10 × 10 supercells and appropriately keeping a 63-atom and 19-atom cluster of average diameter 1 nm for TiO_2 and PbS, respectively (Figure 7.5b, d). As discussed earlier, the attachment of the TiO_2 nanoball has occurred through the dangling carboxylic group of CNT after passivating the oxygen vacancies of the TiO_2 surface, and the attachment corresponding to TiO_2-CNT hybrid has been shown in Figure 7.5c. Before the formation of a tri-hybrid, it is necessary to investigate the lowest energy configuration of PbS with TiO_2, and it is found that attachment of PbS with TiO_2 stabilizes through the formation of Pb-O and Ti-S (Figure 7.5e) covalent bonds. The constructed tri-hybrid (PbS-TiO_2-CNT) has been shown in Figure 7.5f, where the attachment of PbS and CNT in the tri-hybrid has occurred through TiO_2. The significant charge overlap between the individual systems can be seen from the charge density plot (Figure 7.5g) of the hybrid system, which facilitates the possibility of net charge transfer among them. The spin density plot of the hybrid system, shown in Figure 7.5h, represents the asymmetric charge distribution, which may be due to the mutual interaction of the pristine systems within the hybrid. The atom and orbital projected density of states (APDOS & OPDOS) and the corresponding energy eigenvalues of the tri-hybrid, along with their control hybrid and individual systems, have been illustrated in Figure 7.6a-f. The total DOS and corresponding highest occupied molecular orbital (HOMO) and lowest unoccupied molecular orbital (LUMO) levels, as demonstrated from Figure 7.6a, a broadband gap nature of TiO_2 nanoball with 1.8 eV band gap is observed along with few gap states in between which may be attributed to the unbound dangling bonds at the TiO_2 surface due to formation of nanoball. The results obtained from DFT are consistent with earlier DFT calculations using the Perdew-Burke-Ernzerhof (PBE) functional [43], and bandgap calculation using this useful usually underestimates the exact value [5]. The asymmetry of the upper and down channels of DOS of TiO_2 is due to the asymmetric spin distribution as previously observed from the spin density plot at the TiO_2 surface. CNT shows a usual metallic nature (Figure 7.6b).

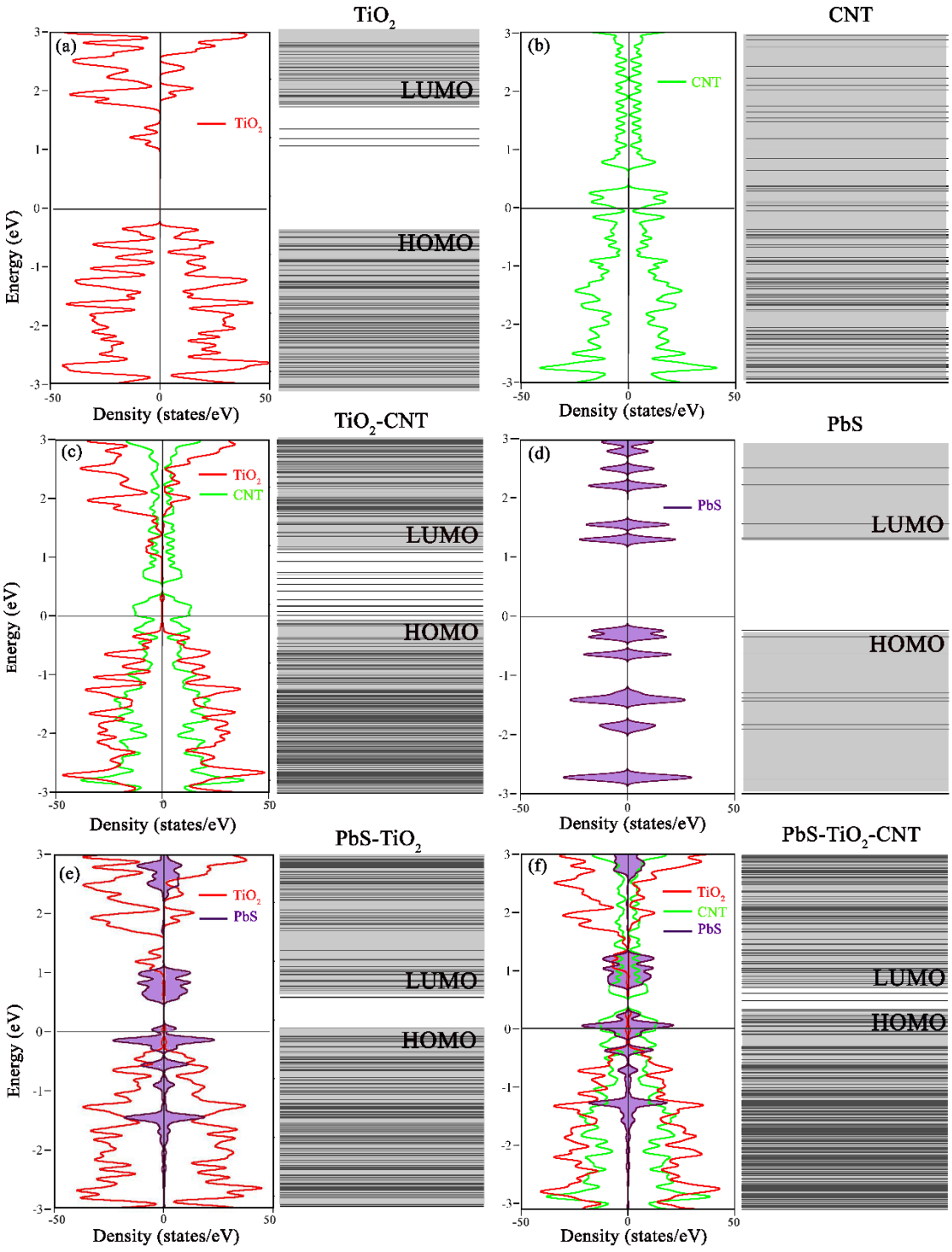

Figure 7.6: *Atom (APDOS) and orbital (OPDOS) projected density of states (DOS) and the corresponding energy eigen values of (a) pure TiO_2 nanoball, (b) pure CNT, (c) TiO_2-CNT nanohybrid, (d) pure PbS nanoball, (e) TiO_2–PbS nanohybrid and (f) PbS-TiO_2-CNT (Tri-hybrid).*

In contrast, the introduction of CNT with TiO_2 enhances its visible activity as the redistribution of states reduces the band gap, as is evident in Figure 7.6c, which is also consistent with our experimental DRS findings. The formation of the Ti-

O-C bond may have introduced interbands before the CB of TiO_2 and caused the VBM CBM redistribution.

The band gap of 1.0 eV is calculated from the total DOS and HOMO-LUMO levels of pristine PbS nanoball (Figure 7.6d). As illustrated in Figure 7.6e, E_F of PbS-TiO_2 shifts (0.23 eV) towards VB with an overall bandgap of 0.4 eV, manifesting the experimental findings of net charge transfer from PbS to TiO_2. Whereas, upon tri-hybrid formation, further bandgap reduction (0.2 eV) of PbS towards NIR with a change in E_F of 0.5 eV towards VB is evident from the total DOS and HOMO-LUMO energy level (Figure 7.6f). As compared to PbS-TiO_2, the PbS-TiO_2-CNT system unveils the maximum E_F shift towards VB, implying the huge charge transfer property of PbS in the tri-hybrid.

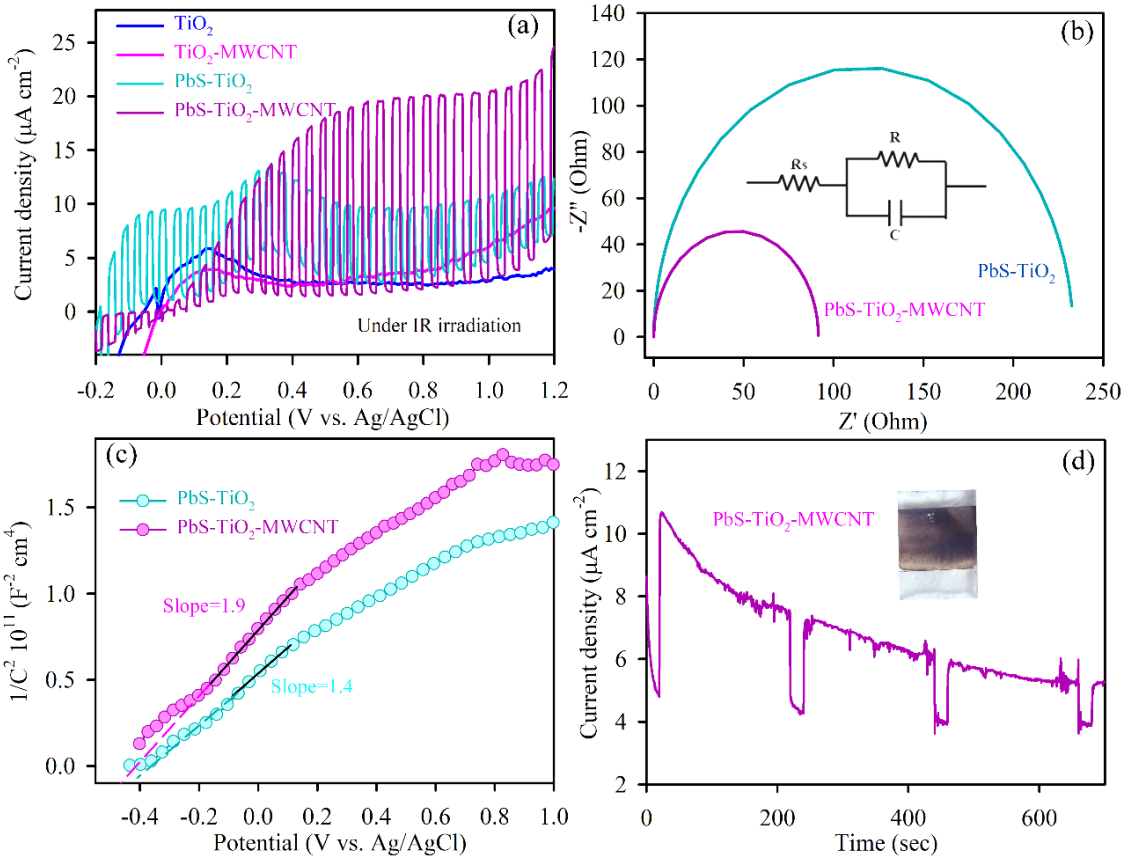

Figure 7.7: *(a) Shows linear sweep voltammetry (LSV) plots for TiO_2, TiO_2-MWCNT nanohybrid, PbS-TiO_2 and PbS-TiO_2-MWCNT electrodes in 0.1 M Na_2SO_4 and their comparative plots under infrared (IR) illumination. (b) Nyquist plots of PbS-TiO_2 and PbS-TiO_2-MWCNT tri-hybrid. (c) Mott−Schottky plots of nanohybrid PbS-TiO_2 and PbS-TiO_2-MWCNT electrodes in 0.1 M Na_2SO_4 solution and at 1000 Hz frequency. (d) Chronoamperometry stability plot of PbS-TiO_2-MWCNT electrode under IR-light illumination for 700 s. Inset shows the image of the prepared PbS-TiO_2-MWCNT photoanode.*

Additionally, the number of trap states between the HOMO-LUMO of tri-hybrid has also been reduced after hybrid formation compared to bare CNT. Furthermore, the photoelectrochemical (PEC) measurement was carried out to explore the hybrid system's NIR light harvesting capability. PEC cells consist of an anode of photoactive material and a Pt cathode in contact with the electrolyte solution. We have used PbS-TiO_2-MWCNT, PbS-TiO_2, TiO_2-MWCNT and TiO_2 only as working photoanodes for PEC measurements. In brief, during the PEC process, photo-electrons from photoexcited QDs transfer to the CB of TiO_2 and subsequently to the MWCNT. The photoexcited electrons later move to the FTO and then to the counter-electrode. The anodic reaction (oxidation) takes place through the holes at the H_1 level of the PbS, and the cathodic reaction occurs at the Pt counter-electrode, which is responsible for hydrogen gas production.

In PEC, LSV is one of the prominent methods used to determine the oxidation and reduction process of water through water splitting and gives an idea about the electron transfer during chemical reactions. The LSV results presented in Figure 7.7a were obtained in consecutive light and dark illumination (20 s of on/off) with a scan rate of 10 mV/s from −0.4 to 1.2 V potential range versus Ag/AgCl. The photocurrent density of the PbS-TiO_2-MWCNT ($J \sim 20\ \mu A\ cm^{-2}$) is almost two times higher than that of PbS-TiO_2 ($J \sim 9.01\ \mu A\ cm^{-2}$) under IR light illumination, indicating the enhanced activity of the tri-hybrid. Whereas pure TiO_2 and TiO_2-MWCNT photoanodes without NIR active PbS QDs do not show significant responses in the NIR range. The immediate fall and rise of the photocurrent density with periodic light illumination indicate that the photocurrent density arises only due to photogenerated charge carriers and not due to thermal excitation.

The PbS-TiO_2 composite shows significant photocurrent even at a much lower potential region (<0.2V vs. Ag/AgCl), indicating its efficacy towards PEC water-splitting applications. However, the material suffers loss in performance at higher potentials with prolonged exposure to light due to faster recombination of photogenerated charge carriers. The presence of MWCNT in the composite

influences the overall performance of the photoanode through the separation of charge carriers with favourable transport of charges (i.e., h^+) across the semiconductor-electrolyte interface towards the electrolyte. This results in the migration of the photogenerated electrons towards the FTO back-contact. Moreover, the idealized behaviour of I−V curves implies an improved fill factor for the water oxidation reaction, indicating better catalytic behaviour of the composite materials toward photoassisted oxidation processes. The appearance of photocurrent in the LSV plot at 0.2 V vs Ag/AgCl under periodic illumination further substantiates its photocatalytic role.

Table 7.2: *Resistance and capacitance values estimated from simulated fitting of EIS spectra of different samples.*

Sample	Rs (Ohm)	Rct (Ohm)	C_{EDL} (F)
PbS-TiO_2	46	2.234E+5	3.54E-6
PbS-TiO_2-MWCNT	47	9100	5.90E-6

Now, to get an idea about charge transportation impedance across the heterojunctions, the electrochemical impedance spectra of the two photoelectrodes were measured through Nyquist plots (Figure 7.7b). Table 7.2 shows the summarised EIS parameters obtained from the fitted equivalent RC circuit shown in the inset of Figure 7b. The series resistance (R_s) value represents the low electrical resistance at the electrolyte junction, while charge transfer resistance (R_{ct}) is 9.1 kΩ for the PbS-TiO_2-MWCNT electrode, which is comparatively low for the PbS-TiO_2 electrode (223 kΩ). The results well agree with the fact that MWCNT introduces a significant improvement in the electrical conductivity charge storage capacity at the heterojunction [44]. On the other hand, the electrical double layer capacitance (C_{EDL}) across the electrolyte-semiconductor junction is higher (5.9 μF) for the trihybrid photoelectrode, which is 3.5 μF the PbS-TiO_2 photoanode. The higher C_{EDL} value indicated the prevention of back electron-hole recombination, i.e. accumulation of a larger number of charge carriers across the junction. This is an obvious phenomenon in metal-semiconductor junctions due to the charge redistribution by the

formation of the Schottky junction, thereby preventing the faster back electron-hole recombination. The variation of the capacitive response with potential in the form is presented in Figure 7.7c. The charge accumulation, in addition to the charge carrier (donor) densities (N_d) can further be calculated from the slope of the $1/C^2$ versus potential plot (equation 1). Tri-hybrid has a charge carrier density of 5.8 $\times 10^{19}$ $cm^{-3,}$ which is higher compared to 4.32 $\times 10^{19}$ cm^{-3} for the PbS-TiO_2 junction. The increment of donor densities of the tri-hybrid photoanode is in cobordance with our explanation of less electron-hole recombination hence improvement in the PEC response. The chronoamperometry results show moderate activity of the sample. The stability of the tri-hybrid photoanodes under NIR irradiation is one of the crucial aspects. PbS-TiO_2-MWCNT photoanode has further been irradiated with the IR lamp for the duration of 700 seconds and it is observed from Figure 7.7d that almost 60 % of the trihybrid is still active for PEC. Earlier experiments on other semiconductor photoanodes for photoelectrochemical applications also suggest a such stability response [45].

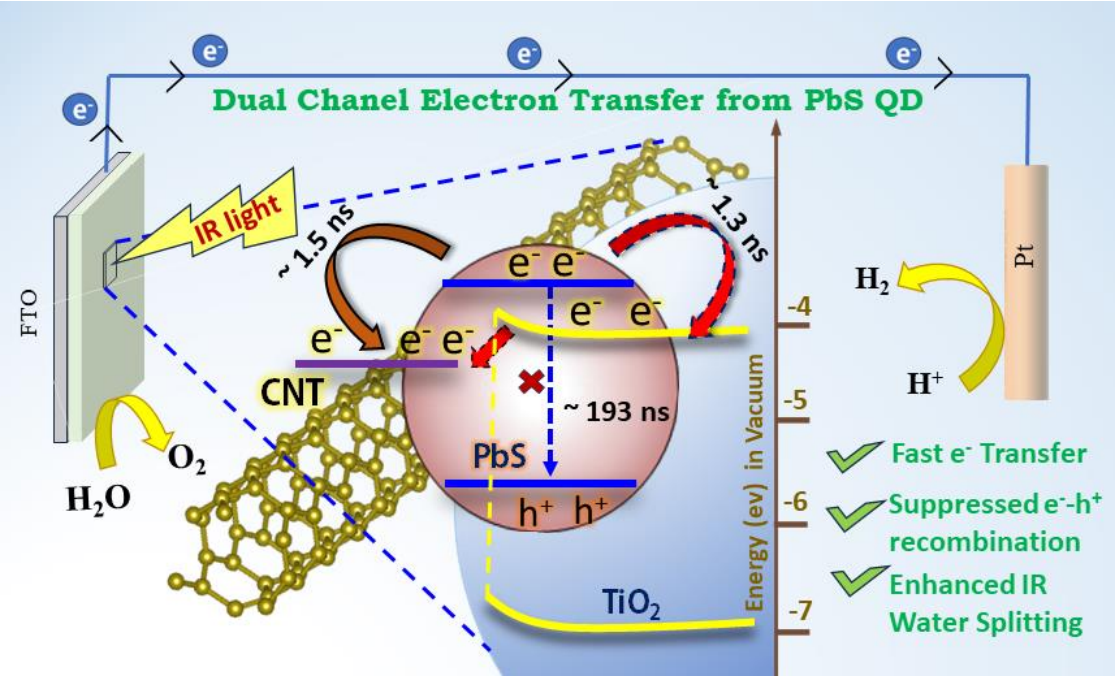

Scheme 7.1: *The proposed electron transfer from PbS QD mechanism of PEC water splitting under IR light illumination.*

Schematic for the proposed mechanism of PEC water splitting under IR light illumination is represented in Scheme 7.1. The proposed current flow and charge

separation direction based on the corresponding energy level diagram depicting that photoinduced electron from CB of PbS QD moves to CB of MWCNT directly and via CB of TiO_2 by the formation of Schottky junction and then moves towards FTO. Due to the high conductivity of the MWCNT, it behaves as a tunnel for electron transportation from the sample. Overall, the tri-hybrid shows the highest PEC performance in the NIR region.

7.3. Conclusion:

NIR absorbing PbS QDs sensitized TiO_2-MWCNT photoanodes were found to give the highest performance in PEC water splitting under IR lamp irradiation compared to its control PbS-TiO_2 photoanodes. The experimental findings suggest that the attachment of carbon nanotubes with TiO_2 not only provides additional visible activity, low interfacial series resistance, and high carrier mobility but also builds metal/semiconductor induced electric field at the TiO_2-MWCNT junction, modulates the charge carrier transportation, helps in preventing of intrinsic or photo induce electron-hole recombination. Along with it, avoiding the rigorous ligand exchange process for attachment with carbon nanotubes, PbS QDs colocalizing by adsorption on the surface of TiO_2 bring forth additional charge transfer pathway to MWCNT, which provides enhanced excitation dissociation probability. The nanosecond resolved transient analysis indicates the fastest ground state recovery in the tri-hybrid system and a dual charge transport pathway from PbS QD to TiO_2 and MWCNT. The highest charge transportation activity of the tri-hybrid system has also been confirmed by DFT results. Consequently, a higher ROS generation has been observed in the PbS-TiO_2-MWCNT compared to PbS-TiO_2, PbS-MWCNT nanocomposites. Overall, the higher PEC activity of the tri-hybrid could provide promising aspects towards designing UV to NIR full spectrum active photoanodes.

References

[1] X. Zhang, Y. Yu, X. Xia, W. Zhang, X. Cheng, H. Li, Z. L. Wang, T. Cheng, Multi-mode vibrational triboelectric nanogenerator for broadband energy harvesting and utilization in smart transmission lines, *Adv. Energy Mater.* 13 (2023) 2370179.

[2] K. Barnham, M. Mazzer, B. Clive, Resolving the energy crisis: Nuclear or photovoltaics?, *Nat. Mater* 5 (2006) 161.

[3] H. Bahrampour, A. K. Beheshti Marnani, M. B. Askari, M. R. Bahrampour, Evaluation of renewable energies production potential in the middle east: Confronting the world's energy crisis, *Front. Energy Res.* 14 (2020) 42.

[4] B. Jiang, J. Zhu, Z. Xia, J. Lyu, X. Li, L. Zheng, C. Chen, S. Chaemchuen, T. Bu, F. Verpoort, S. Mu, J. Wu, J. Wang, Z. Kou, Correlating single-atomic ruthenium interdistance with long-range interaction boosts hydrogen evolution reaction kinetics, *Adv. Mater.* 36 (2024) 2310699.

[5] J. M. Yu, J. Lee, Y. S. Kim, J. Song, J. Oh, S. M. Lee, M. Jeong, Y. Kim, J. H. Kwak, S. Cho, C. Yang, J. W. Jang, High-performance and stable photoelectrochemical water splitting cell with organic-photoactive-layer-based photoanode, *Nat. Commun.* 11 (2020) 5509.

[6] K. H. Ng, S. Y. Lai, C. K. Cheng, Y. W. Cheng, C. C. Chong, Photocatalytic water splitting for solving energy crisis: Myth, fact or busted?, *J. Chem. Eng.* 417 (2021) 128847.

[7] S. Tang, W. Qiu, S. Xiao, Y. Tong, S. Yang, Harnessing hierarchical architectures to trap light for efficient photoelectrochemical cells, *Energy Environ. Sci.* 13 (2020) 660.

[8] G. B. Bodedla, V. Piradi, M. Imran, J. Zhao, X. Zhu, W. Y. Wong, Visible-to-near-infrared light-harvesting A-π-D-π-A porphyrins for boosted photocatalytic hydrogen evolution, *J. Mater. Chem. A* 11 (2023) 1473.

[9] X. Xia, N. Deng, G. Cui, J. Xie, X. Shi, Y. Zhao, Q. Wang, W. Wang, B. Tang, NIR light induced H_2 evolution by a metal-free photocatalyst, *Chem. Commun.* 51 (2015) 10899.

[10] F. Wu, Y. Ma, Y. H. Hu, Near infrared light-driven photoelectrocatalytic water splitting over p-doped g-C_3N_4, *ACS Appl. Energy Mater.* 3 (2020) 11223.

[11] Y. Li, J. Ma, L. Xu, T. Liu, T. Xiao, D. Chen, Z. Song, J. Qiu, Y. Zhang, Enhancement of charge separation and NIR light harvesting through construction of 2D–2D $Bi_4O_5I_2$/BiOBr: Yb^{3+}, Er^{3+} Z-scheme heterojunctions for Improved full-spectrum photocatalytic performance, *Adv. Sci.* 10 (2023) 2207514.

[12] C. K. Chen, H. M. Chen, C.-J. Chen, R.-S. Liu, Plasmon-enhanced near-infrared-active materials in photoelectrochemical water splitting, *Chem. Commun.* 49 (2013) 7917.

[13] D. Meng, R. Zheng, Y. Zhao, E. Zhang, L. Dou, Y. Yang, Near-infrared materials: The turning point of organic photovoltaics, *Adv. Mater.* 34 (2022) 2107330.

[14] N. Reilly, M. Wehrung, R. A. O'Dell, L. Sun, Ultrasmall colloidal PbS quantum dots, *Mater. Chem. Phys.* 147 (2014) 1.

[15] L. Jin, H. Zhao, Z. M. Wang, F. Rosei, Quantum dots-based photoelectrochemical hydrogen evolution from water splitting, *Adv. Energy Mater.* 11 (2021) 2003233.

[16] S. B. Bubenhofer, C. M. Schumacher, F. M. Koehler, N. A. Luechinger, R. N. Grass, W. J. Stark, Large-scale synthesis of PbS–TiO_2 heterojunction nanoparticles in a single step for solar cell application, *J. Phys. Chem. C* 116 (2012) 16264.

[17] H. Zhang, Y. Gao, G. Zhu, B. Li, J. Gou, X. Cheng, Synthesis of PbS/TiO_2 nano-tubes photoelectrode and its enhanced visible light driven photocatalytic performance and mechanism for purification of 4-chlorobenzoic acid, *Sep. Purif.* 227 (2019) 115697.

[18] J. Patwari, H. Joshi, H. Mandal, L. Roy, C. Bhattacharya, P. Lemmens, S. K. Pal, Exciton dissociation in an NIR-active triohybrid nanocrystal leading to efficient generation of reactive oxygen species, *Phys. Chem. Chem. Phys.* 21 (2019) 10667.

[19] A. Fujishima, K. Honda, Electrochemical photolysis of water at a semiconductor electrode, *Nature* 238 (1972) 37.

[20] M. Tayebi, B. K. Lee, Recent advances in $BiVO_4$ semiconductor materials for hydrogen production using photoelectrochemical water splitting, *Renew. Sustain. Energy Rev.* 111 (2019) 332.

[21] T. K. Maji, M. N. Hasan, S. Ghosh, D. Wulferding, C. Bhattacharya, P. Lemmens, D. Karmakar, S. K. Pal, Development of a magnetic nanohybrid for multifunctional application: From immobile photocatalysis to efficient photoelectrochemical water splitting: A combined experimental and computational study, *J. Photochem. Photobiol. A: Chem.* 397 (2020) 112575.

[22] P. He, L. Zhang, S. Xiao, W. Jiang, Y. Wu, C. Yan, X. Li, Z. Chen, L. Wu, T. Duan, Dual charge-transfer channels harmonize carrier separation for efficient U(VI) photoreduction, *Inorg. Chem.* 62 (2023) 4705.

[23] A. Hirsch, Functionalization of single-walled carbon nanotubes, *Angew. Chem. Int. Ed.* 41 (2002) 1853.

[24] W. Feng, C. Qin, Y. Shen, Y. Li, W. Luo, H. An, Y. Feng, A layer-nanostructured assembly of PbS quantum dot/multiwalled carbon nanotube for a high-performance photoswitch, *Sci. Rep.* 4 (2014) 3777.

[25] Y. Hou, F. Zuo, A. Dagg, P. Feng, Visible light-driven α-Fe_2O_3 nanorod/graphene/BiV1–x Mo_xO_4 core/shell heterojunction array for efficient photoelectrochemical water splitting, *Nano lett.* 12 (2012) 6464.

[26] K. Woan, G. Pyrgiotakis, W. Sigmund, Photocatalytic carbon-nanotube–TiO_2 composites, *Adv. Mater.* 21 (2009) 2233.

[27] V. P. Prasadam, A. M. H. Flores, N. Bahlawane, CNT–TiO_2 core–shell structure: Synthesis and photoelectrochemical characterization, *RSC Adv.* 11 (2021) 33169.

[28] S. Bellamkonda, N. Thangavel, H. Y. Hafeez, B. Neppolian, G. R. Rao, Highly active and stable multi-walled carbon nanotubes-graphene-TiO_2 nanohybrid: An efficient non-noble metal photocatalyst for water splitting, *Catal. Today* 321 (2019) 120.

[29] V. Veeramani, Y. H. Chen, H. C. Wang, T. F. Hung, W. S. Chang, D. H. Wei, S. F. Hu, R. S. Liu, CdSe/ZnS QD@CNT nanocomposite photocathode for

improvement on charge overpotential in photoelectrochemical Li-O_2 batteries, *Chem. Eng. J.* 349 (2018) 235.

[30] J. E. Weaver, M. R. Dasari, A. Datar, S. Talapatra, P. Kohli, Investigating photoinduced charge transfer in carbon nanotube−perylene−quantum dot hybrid nanocomposites, *ACS Nano* 4 (2010) 6883.

[31] B. Ge, C. Nie, J. Shen, A hybrid photodetector of graphene/TiO_2/inorganic PbS quantum dots for fast response, *Jpn. J. Appl. Phys.* 61 (2022) 040903.

[32] J. K. Baral, A. Sharma, D. Wang, D. Ma, V. V. Truong, R. Izquierdo, Enhanced photovoltaic conversion efficiency in bulk heterojunction solar cells upon incorporating nanohybridized PbS quantum dots/multiwall carbon nanotubes, *Eur. Phys. J. Appl. Phys.* 65 (2014) 10201.

[33] D. Voigt, G. Primavera, H. Uphoff, J. A. Rethmeier, L. Schepp, M. Bredol, Ternary chalcogenide-based quantum dots and carbon Nanotubes: Establishing a toolbox for controlled formation of nanocomposites, *J. Phys. Chem. C* 126 (2022) 9076.

[34] N. Pan, M. N. Hasan, S. Ghosh, L. Roy, C. Bhattacharya, D. Karmakar, S. K. Pal, Near-infrared active tri-nanohybrid for enhanced energy harvesting, *ChemistrySelect* 9 (2024) e202400968.

[35] J. O. Olowoyo, M. Kumar, S. L. Jain, J. O. Babalola, A. V. Vorontsov, U. Kumar, Insights into reinforced photocatalytic activity of the CNT–TiO_2 nanocomposite for CO_2 reduction and water splitting, *J. Phys. Chem. C* 123 (2018) 367.

[36] P. Makuła, M. Pacia, W. Macyk, How to correctly determine the band gap energy of modified semiconductor photocatalysts based on UV–Vis spectra, *J. Phys. Chem. Lett.* 9 (2018) 6814.

[37] D. Chaudhary, S. Singh, V. Vankar, N. Khare, A ternary Ag/TiO_2/CNT photoanode for efficient photoelectrochemical water splitting under visible light irradiation, *Int. J. Hydrogen Energy.* 42 (2017) 7826.

[38] P. Eklund, J. Holden, R. Jishi, Vibrational modes of carbon nanotubes; spectroscopy and theory, *Carbon* 33 (1995) 959.

[39] R. Palomino-Merino, P. Trejo-Garcia, O. Portillo-Moreno, S. Jiménez-Sandoval, S. Tomás, O. Zelaya-Angel, R. Lozada-Morales, V. Castaño, Red shifts of the Eg (1) raman mode of nanocrystalline TiO_2: Er monoliths grown by sol–gel process, *Opt. Mater.* 46 (2015) 345.

[40] G. Itskos, P. Papagiorgis, D. Tsokkou, A. Othonos, F. Hermerschmidt, S. P. Economopoulos, M. Yarema, W. Heiss, S. Choulis, Size-dependent charge transfer in blends of PbS quantum dots with a low-gap silicon-bridged copolymer, *Adv. Energy Mater.* 3 (2013) 1490.

[41] J. I. Fujisawa, T. Eda, M. Hanaya, Comparative study of conduction-band and valence-band edges of TiO_2, $SrTiO_3$, and $BaTiO_3$ by ionization potential measurements, *Chem. Phys. Lett.* 685 (2017) 23.

[42] H. Mustafa, Y. Yu, A. Zafar, Y. Liu, S. Karim, S. Javed, S. Mehboob, H. Sun, S. Hussain, A. U. Shah, MWCNT synergy for boosting the electrochemical kinetics of V_2O_5 cathode for lithium-ion batteries, *New J. Chem.* 46 (2022) 3417.

[43] Y. Dong, M. Abbasi, J. Meng, L. German, C. Carlos, J. Li, Z. Zhang, D. Morgan, J. Hwang, X. Wang, Substantial lifetime enhancement for Si-based photoanodes enabled by amorphous TiO_2 coating with improved stoichiometry, *Nat. Commun.* 14 (2023) 1865.

[44] A. Q. H. Le, N. N. T. Nguyen, H. D. Tran, V.-H. Nguyen, L.-H. Tran, A TiO_2@ MWCNTs nanocomposite photoanode for solar-driven water splitting, *Beilstein J. Nanotechnol.* 13 (2022) 1520.

[45] S. Shyamal, P. Hajra, H. Mandal, J. K. Singh, A. K. Satpati, S. Pande, C. Bhattacharya, Effect of substrates on the photoelectrochemical reduction of water over cathodically eectrodeposited p-Type Cu_2O Thin Films, *ACS Appl. Mater. Interfaces.* 7 (2015) 18344.

List of Publications

(Peer-reviewed journals)

1. **N. Pan**#, S. A. Ahmed#, H. A. Altass, J. Patwari, R. J. Obaid, H. Alessa, R. S. Jassas and S. K. Pal
   "Broad light harvesting under restricted environment: Photophysical understanding leading to enhanced reactive oxygen species generation"
   J. Photochem. Photobiol. :A 418 (2021) 113422. (#contributed equally)

2. **N. Pan**, T. K. Maji, S. Bandyopadhyay, P. Biswas, A. Chatterjee, M. Mitra, A. Chatterjee and S. K. Pal
   "A combined spectroscopic and theoretical analysis of plasmonic silver nanoparticle sensor towards detailed microscopic understanding of heavy metal detection"
   Plasmonics, 17 (2022) 223–236 (2022).

3. **N. Pan**, N. Bhattacharyya, A. Banerjee, P. Biswas, L. Roy, A. Chatterjee, R. Bhattacharjee, S. Singh, S. A. Ahmed, A. Chattopadhyay, M. Mitra and S. K. Pal
   "Paper based plasmonic nanosensor monitors environmental lead pollution in real field"
   New J. Chem., 46 (2022) 8177-8184.

4. **N. Pan**, S. Ghosh, M. N. Hasan, S. A. Ahmed, A. Chatterjee, J. Patwari, C. Bhattacharya, J. Qurban, A. S. Khder, and S. K. Pal
   "Plasmon-coupled donor-acceptor type organic sensitizer based photoanodes for enhanced photovoltaic activity: Key information from ultrafast dynamical study"
   Energy Fuels 16 (2022) 9272–9281.

5. **N. Pan**, R. Ghosh, D. Mukherjee, N. Bhattacharyya, L. Roy, A. Banerjee, S. Singh, R. T. Goswami, M. Mitra, A. Chattopadhyay and S. K. Pal
   "A nanosensor-based prototype development for heavy metal detection: A combined spectroscopic and theoretical study"
   IEEE Sens. Lett. 7 (2023) 3.

6. **N. Pan**, L. Roy, M. N. Hasan, A. Banerjee, R. Ghosh, M. A. Alsharif, B. A. Asghar, R. J. Obaid, A. Chattopadhyay, R. Das, S. A. Ahmed and S. K. PaL
"Unraveling an ultrafast electron transport mechanism in a photocatalytic 'micromachine' for their potential light harvesting applications"
Micromachines 14 (2023) 980.

7. **N. Pan**, Md. N. Hasan, S. Ghosh, L. Roy, C. Bhattacharya, D. Karmakar and S. K. Pal,
"Near-infrared active tri-nanohybrid for enhanced energy harvesting"
ChemistrySelect, 9 (2024) e202400968.

8. * L. Roy, **N. Pan**, S. Mondal, R. Ghosh, M. N. Hasan, N. Bhattacharyya, S. Singh, K. Bhattacharyya, A. Chattopadhyay, and S. K. Pal
"Ultrafast spectroscopic studies on the interaction of reactive oxygen species with a probe impregnated in nanoscopic and microscopic matrix formulation"
Spectrochim. Acta A Mol. Biomol. Spectrosc. 308 (2024) 123671

9. * A. Chatterjee, **N. Pan**, T. K. Maji, S. S. Pasha, S. Singh, S. A. Ahmed, J. T. Al-Thakafy, and S. K. Pal
"Highly sensitive optical sensor for selective detection of fluoride level in drinking water: Methodology to fabrication of prototype device"
ACS Sustain. Chem. Eng. 9 (2021) 7160−7170.

10. * S. Mondal, **N. Pan**, R. Ghosh, A. Bera, D. Mukherjee, T.K. Maji, A. Adhikari, S. Ghosh, C. Bhattacharya, and S. K. Pal
"Interaction of a jaundice marker molecule with redox modulatory nano-hybrid: A combined electrochemical and spectroscopic study towards development of a theranostics Tool",
ChemMedChem 17 (2022) e202100660.

11. * T. K. Maji, D. Bagchi, **N. Pan**, A. Sayqal, M. Morad, S. A. Ahmed, D. Karmakar and S. K. Pal
"A combined spectroscopic and Ab initio study on transmetalation of a polyphenol for potential purification strategy of food additive"
RSC Adv. 10 (2020) 5636.

12. * A. Bera, M. N. Hasan, **N. Pan**, R. Ghosh, R. Alsantali, H. M. Altass, R J. Obaid, S. A. Ahmed and S. K. Pal
"Implementation of surface functionalization of MnS nanoparticle for achieving of novel optical properties and improving therapeutic potential"
RSC Adv. 12 (2022) 20728-20734.

13. * M. N. Hasan, F. Sorgenfrei, **N. Pan**, D. Phuyal, M. Abdel-Hafiez, S. K. Pal, A. Delin, P. Thunstrom, D. D. Sarma, O. Eriksson and D. Karmakar
"Re-dichalcogenides: Resolving conflicts of their structure-property relationship"
Adv. Phys. Res. 1 (2022) 2200010.

14. * M. N. Hasan, A. Bera, T. K. Maji, D. Mukherjee, **N. Pan**, D. Karmakar and S. K. Pal "Functionalized nano-mof for nir induced bacterial remediation: A combined spectroscopic and computational study"
Inorg. Chim. Acta 532 (2022) 120733.

15. * S. A. Ahmed, M. N. Hasan, H. M. Altass, A. Bera, R. I. Alsantali, **N. Pan**, A. Y. A. Alzahrani, D. Bagchi, J. H. Al-Fahemi, A. S. Khder and S. K. Pal
"Tetracycline encapsulated in Au nanoparticle-decorated ZnO nanohybrids for enhanced antibacterial activity"
ACS Appl. Nano Mater. 5 (2022) 4484–4492.

16. * L. Roy, **N. Pan**, R. Ghosh, Md. N. Hasan, S. Mondal, A. Banerjee, M. Das, O. Sen, K. Bhattacharyya, A. Chattopadhyay, and S. K. Pal,
"A mutagen acts as a potent reducing agent of glycated hemoglobin: A combined ultrafast electron transfer and computational studies"
ChemBioChem 25 (2024) e202300721

17. * R. Ghosh, L. Roy, S. Sarker, D. Mukherjee, **N. Pan**, Md. N. Hasan, A. Chattopadhyay, A. Adhikary, M. Bhattacharyya, A. K. Mallick, R. Biswas, R. Das, and S. K. Pal,
"Structurally dynamic monocyte-liposome hybrid vesicles as an anticancer drug delivery vehicle: A crucial concertion of microscopic elasticity and ultrafast dynamics"
J. Phys. Chem. Lett. 5 (2024) 3078–3088

(Book Chapters)

1.* L. Roy, S. Mondal, R. Ghosh, M. Das, M. N. Hasan, A. Banerjee, **N. Pan**, A. Chattopadhyay, and S. K. Pal
"Recent progress in the synthesis of nanozymes and their functionalization"
Edited by Ravi Mani Tripathi, Ramesh Namdeo Pudake, Peng Huang, Nesrin Horzum, Nanozymes - Approachable bio-applications, Elsevier, Chapter 4, ISBN: 9780443137891.

* Not included in the thesis.

List of National/International Conference/Workshop

1. **Poster presentation** delivered on "Frontiers in materials for technological applications (FIMTA-2021)" at CSIR-IMMT, Bhubaneswar, India, August 4th to 6th, 2021, Virtual.

2. **Oral presentation** delivered on "Spectroscopic studies and numerical modeling on nanoparticle-based toxic heavy metal sensor for the development of a low-cost prototype in field use" in an international conference, IEEE Applied Sensing Conference (APSCON 2023) Bengaluru, India, January 23rd to 25th, 2023.

3. **Oral presentation** delivered on "A new series of magnetic layered metal hydroxide semiconductors" in an international conference, Divergent Quantum Materials, Methods and Applications (DQMMA2023) Goa, India, February 2nd to 4th, 2023.

4. **Oral presentation** delivered on "Hydroxide semiconductors: New series of van der waals magnets" in the APS March Meeting 2023, Las Vegas, Nevada, USA, March 20th to 22th, 2023, Virtual.